Universiteit Antwerpen

Faculty of Science

Department of Bioscience Engineering

Photoactive Nanostructures: from Single Plasmonic Nanoparticles to Self-assembled Films

Dissertation submitted to obtain the doctorate in Bioscience Engineering at the University of Antwerp to be defended by

Rituraj Borah

Promoters:
Prof. Dr. Ir. Sammy Verbruggen, Dept. of Bioscience Engineering, UAntwerp
Prof. Dr. Silvia Lenaerts, Dept. of Bioscience Engineering, UAntwerp

Members of the jury:
Prof. Dr. Sara Bals (President), Dept. of Physics, UAntwerp
Prof. Dr. Ir. Rob Ameloot, cMACS, KU Leuven
Prof. Dr. Dirk Lamoen, Dept. of Physics, UAntwerp
Prof. Dr. Ir. Siegfried Denys, Dept. of Bioscience Engineering, UAntwerp

Antwerp, 21st June 2022

Samenvatting

Fotoactieve nanodeeltjes en hun lichtgedreven toepassingen hebben enorme wetenschappelijke aandacht gekregen voor het aanpakken van de wereldwijde milieuproblemen, het voldoen aan de vraag naar alternatieve energie en andere nieuwe technologische ontdekkingen. Het onderzoekswerk dat in dit proefschrift wordt gepresenteerd, omvat een fundamenteel onderzoek naar dergelijke nanodeeltjes om diepere inzichten te verkrijgen die uiteindelijk hun toepassing ten goede zullen komen. In het bijzonder is de studie van plasmonische metaalnanodeeltjes en metaaloxidenanodeeltjes voor lichtgedreven toepassingen het hoofdthema van dit werk. Het onderzoek begint met geïsoleerde plasmonische Au- en Ag-nanodeeltjes, gevolgd door een logische uitbreiding naar kleine clusters van nanodeeltjes en vervolgens naar volledige films van nanodeeltjes. Voor de computationele studies van de plasmonische nanostructuren wordt een klassiek elektromagnetisch raamwerk geïmplementeerd. Vervolgens wordt de toepassing van dergelijke plasmonische nanodeeltjesfilms voor gasfasedetectie van vluchtige organische stoffen onderzocht. Ten slotte wordt filmvorming van metaaloxide-nanodeeltjes onderzocht met het oog op de fabricage van fotoactieve functionele oppervlakken.

Ten eerste vergelijkt de studie met geïsoleerde bimetallische Au-Ag-nanodeeltjes kern-schil en legeringsnanodeeltjes in termen van hun optische eigenschappen. Hoewel Ag een zeer sterke plasmonische respons heeft, is het chemisch onstabiel en ligt de plasmonresonantie van Ag-nanostructuren bij kortere golflengten in het UV-zichtbare gebied. Hoewel Au een sterk gedempte plasmonische respons heeft, maakt de chemische stabiliteit van metallish Au het alsnog nuttig in echte toepassingen. Bimetallische Au-Ag-nanodeeltjes laten toe om de optische respons en chemische stabiliteit te tunen door variatie van hun samenstelling. In dat opzicht worden Ag-Au-legeringen, Ag@Au kern-schil en Au@Ag kern-schil bimetallische plasmonische nanodeeltjes van zowel sferische als anisotrope (nanodriehoek en nanostaafjes) vormen vergeleken, na zorgvuldige validatie van de computationele elektromagnetische modellen. Hoewel zowel Au-Ag-kern-schil als legeringsnanodeeltjes een intermediaire optische respons vertonen tussen die van pure Ag- en Au-nanodeeltjes, zijn er merkbare verschillen in de spectrale kenmerken. Ook is het effect van de bimetallische samenstelling in anisotrope nanodeeltjes sterk verschillend van dat in sferische nanodeeltjes vanwege de afwezigheid van interbandovergangen voor Au in het eerste geval. Over het algemeen gaat de verbeterde chemische stabiliteit van Ag-nanodeeltjes door het incorporeren van Au in hun structuur gepaard met een verlaging van de plasmonische versterking, die in mindere mate ook van toepassing is op anisotrope nanodeeltjes. Een fotothermische warmteoverdrachtstudie bevestigt dat verhoogde absorptie door de incorporatie van Au in sferische Ag-nanodeeltjes ook resulteert in een verhoogde evenwichtstemperatuur. Aan de andere kant absorberen anisotrope nanodeeltjes beter het licht, en vormed dus sterkere fotothermische bronnen. Hun

fotothermische eigenschappen worden blijkbaar niet sterk beïnvloed door de incorporatie van het ene metaal in het andere.

Bij het theoretisch voorspellen van de optische eigenschappen van colloïdale plasmonische nanodeeltjes, met name Ag-nanodeeltjes, wordt vervolgens de kloof tussen experiment en theorie verder gedicht. Het effect van verschillende factoren waarvan wordt aangenomen dat ze de optische respons van colloïdale nanodeeltjes beïnvloeden, zoals polydispersiteit (grootteverdeling), scheefheid van de grootteverdeling en oppervlakteruwheid, worden onafhankelijk van elkaar onderzocht. Hiervoor werden nanodeeltjespopulaties gesimuleerd met grootteverdelingen gebaseerd op gewenste statistische parameters, door middel van een bottom-up benadering voor een constant aantal (of mol) atomen. Er werd slechts een zwak effect van de statistische parameters waargenomen en de LSPR-positie (lokale oppervlakteplasmonresonantie) blijkt bijna uitsluitend te worden bepaald door de gemiddelde nanodeeltjesgrootte. De nauwkeurigheid van de theoretische voorspelling van de optische respons hangt grotendeels af van de optische constanten die in de literatuur zijn beschreven en die zonder meer worden gebruikt als input voor de theoretische modellen. In dit opzicht wordt de meest geschikte set optische constanten voor Ag geïdentificeerd om in de latere studies te worden gebruikt.

Van geïsoleerde nanodeeltjes is het uitbreiden van het onderzoek naar eindige nanodeeltjesclusters een logische overgang, aangezien de plasmonische licht-materie-interactie in clusters wordt verbeterd als gevolg van plasmonische koppeling. In de context van zelf-geassembleerde nanodeeltjesstructuren worden dicht opeengepakte tweedimensionale clusters (clusterafmetingen < golflengte van invallend licht) van sferische Au-nanodeeltjes onderzocht. De collectieve optische eigenschappen met toenemend aantal nanodeeltjes in de cluster (tot 61 nanodeeltjes) en de resulterende fotothermische eigenschappen worden bestudeerd om de effecten van de clustergrootte, de afstand tussen de deeltjes en de deeltjesgrootte te bepalen. De plasmonische koppeling van 'kleinere' (d.w.z. 20 nm) nanodeeltjes en 'grotere' (dwz 40 nm) nanodeeltjes wordt besproken in termen van near-field en far-field interacties. Er wordt een maximale lichtabsorptie per deeltje gevonden voor een optimale clustergrootte van 19 nanodeeltjes, waarvoor ook verhoogde fotothermische effecten zijn aangetoond. Een sterke afhankelijkheid van de stationaire temperatuur van de nanodeeltjes van de clustergrootte, de positie van de deeltjes in de cluster, de polarisatie van invallend licht en de afstand tussen de deeltjes geeft nieuwe inzichten in de lokale temperatuurregeling van plasmonische nanostructuren. Aan de andere kant wijst de sterke near-field-versterking in de clusters op mogelijke toepassing in oppervlakteversterkte spectroscopietechnieken (SERS, SEIRA, enz.).

Verder gaand van eindige clusters, worden oneindige nanodeeltjesfilms (filmafmetingen >> golflengte van invallend licht) van Au- en Ag-nanodeeltjes zowel theoretisch als experimenteel onderzocht. Au- en Ag-nanodeeltjesfilms worden verkregen door zelfassemblage aan de lucht-ethyleenglycol interfase en zijn gekarakteriseerd door TEM-beeldvorming. De experimentele optische respons van deze

films wordt vergeleken met berekende spectra voor de validatie van de full-field elektromagnetische modellen. Het is bekend dat in een gesloten gepakte film de individuele plasmonmodi van de individuele nanodeeltjes met elkaar koppelen om roosterresonantiemodi te vormen. De optische eigenschappen van de nanodeeltjes worden bestudeerd met toenemende afstand tussen de deeltjes (dus verzwakking van de plasmonische koppeling). Het is aangetoond dat het dempingsmechanisme van nanodeeltjes verandert van niet-stralingsgedreven demping naar stralingsgedreven demping, wanneer de interdeeltjeskoppeling toeneemt. De optische eigenschappen van de nanodeeltjesfilms in de Kretschmann-configuratie (ook bekend als de Attenuated Total Reflection (ATR)-configuratie) worden bestudeerd om de implicaties te begrijpen van de excitatie van de roosterresonantie door het voorbijgaand veld dat wordt gegenereerd door totale interne reflectie. Het is aangetoond dat de optische eigenschappen van de nanodeeltjesfilms voor *p*-gepolariseerde (TM) en *s*-gepolariseerde (TE) invallende straling in de ATR-configuratie sterk verschillen.

Vervolgens wordt, als een veelbelovende toepassing van de zelf-geassembleerde plasmonische nanodeeltjesfilms, de detectie van vluchtige organische stoffen (VOC) in de gasfase experimenteel gedemonstreerd, met een rigoureuze theoretische achtergrond. Ten eerste zijn films aangemaakt van een relatief grote oppervlakte (d.w.z. enkele cm^2), bestaande uit met-oleylamine-afgedekte Au-nanodeeltjes (10 nm), verkregen door zelfassemblage op een lucht-ethyleenglycol interfase. Het is aangetoond dat door gecontroleerde verdamping van het colloïdale oplosmiddel, tolueen, zelf-geassembleerde films met een groot oppervlak kunnen worden verkregen. De sensorische eigenschappen van deze films zijn gebaseerd op de gevoeligheid van de optische respons op de lokale brekingsindexveranderingen die worden geïnduceerd door de adsorptie van de probemoleculen. Door de aanwezigheid van oleylamine-liganden vormt de film een netwerk van nanodeeltjes en liganden dat de adsorptie van de probe-VOC-moleculen vergemakkelijkt, in dit werk van methanol. Hoewel geïsoleerde nanodeeltjes met een grootte van 10 nm in wezen niet-verstrooiend zijn, resulteert de plasmonische koppeling in sterke optische intensiteiten (reflectie, absorptie of transmissie) wanneer ze zijn georganiseerd als een dicht gepakte film. Met variërende dampfaseconcentratie van methanol worden continue optische metingen *in situ* uitgevoerd. Sensor-experimenten worden uitgevoerd via *in-situ* UV-Vis transmissie-intensiteitsmetingen van de film en *in-situ* ellipsometrie van de film in de Kretschmann-configuratie. *In-situ* ellipsometrie van de zelf-geassembleerde films in de Kretschmann-configuratie toont verbeterde gevoeligheid in de ψ (amplitudeverhouding van *s*- en *p*-gepolariseerd licht) en Δ (faseverschil) parameters met een betere signaalomkeerbaarheid.

Ten slotte wordt de focus verlegd van plasmonische metaal- naar metaaloxide-nanodeeltjes. De functionalisering van fotokatalytische metaaloxide-nanodeeltjes van TiO_2, ZnO, WO_3 en CuO met amine-getermineerde (oleylamine) en thiol-getermineerde (dodecaan-1-thiol) alkylketenliganden wordt bestudeerd onder omgevingsomstandigheden. Een hoge selectiviteit wordt waargenomen in de bindingsspecificiteit van een bepaald type ligand voor bepaalde types nanodeeltjes van

deze verschillende oxiden. Er wordt waargenomen dat oleylamine stabiel bindt aan TiO_2 en WO_3, terwijl dodecaan-1-thiol stabiel bindt aan ZnO en CuO. Op eenzelfde manier kunnen TiO_2- en WO_3-nanodeeltjes van een polaire naar een apolaire fase worden overgedragen door gebruik te maken van oleylamine, maar niet via dodecaan-1-thiol, terwijl het tegenovergestelde geldt voor ZnO en CuO. De oppervlaktechemie van ligand-gefunctionaliseerde nanodeeltjes wordt onderzocht door (ATR)-FTIR-spectroscopie, waardoor de bezetting van de liganden op de actieve plaatsen kon worden opgehelderd. De fotostabiliteit van de liganden op het oppervlak van de nanodeeltjes wordt bepaald door de fotokatalytische zelfreinigende eigenschappen van het materiaal te onderzoeken. Hoewel TiO_2 en WO_3 de liganden binnen 24 uur afbreken onder zowel UV als zichtbaar licht, blijven liganden op ZnO en CuO onaangetast. Ook vanuit toepassingsoogpunt zijn de verzamelde inzichten zeer relevant. Omdat de ligand-gefunctionaliseerde nanodeeltjes bijvoorbeeld hydrofoob van aard zijn, kunnen ze worden zelf-geassembleerd op het lucht-watergrensvlak om nanodeeltjesfilms te vormed met aangetoonde fotokatalytische en anticondenserende eigenschappen.

Samenvattend wil dit proefschrift de lezer een grondig, fundamenteel, theoretisch inzicht geven in de optische eigenschappen van lichtgevoelige plasmonische metalen nanodeeltjes. De impact van verschillende eigenschappen, waaronder het type metaal, vermenging van metalen, deeltjesgrootte, deeltjesgrootteverdeling, scheefheid van de grootteverdeling, ruwheid, clustergrootte, interdeeltjesafstand, polarisatie van invallend licht, enz., wordt nauwgezet geëvalueerd om de resulterende effecten te begrijpen met het oog op mogelijke lichtgestuurde toepassingen. Bovendien wordt in de laatste hoofdstukken een experimentele bevestiging en toepassingsdemonstratie van dergelijke op lichtgevoelige plasmonische nanodeeltjesfilms gegeven, in de hoop verdere ontwikkelingen binnen dit boeiende domein te stimuleren.

Abstract

Photoactive nanoparticles and their light-driven applications have gained tremendous scientific attention towards remediation of the global environmental problems, meeting alternative energy demands, and other new technological discoveries. The research work presented in this dissertation includes a fundamental investigation of such nanoparticles to gain deeper insights that will ultimately benefit their application. In particular, the study of plasmonic metal nanoparticles and metal oxide nanoparticles for light driven applications is the major theme of this work. The investigation begins with isolated plasmonic Au and Ag nanoparticles, followed by a natural extension to nanoparticle clusters, and then further to nanoparticle films. For the computational studies of the plasmonic nanostructures, a classical electromagnetic framework is implemented. Next, the application of such plasmonic nanoparticle films for gaseous phase sensing of volatile organic compounds is explored. Finally, film formation of metal-oxide nanoparticles is investigated with the eye on fabrication of photoactive functional surfaces.

First, the study with isolated bi-metallic Au-Ag nanoparticles compares core-shell and alloy nanoparticles in terms of their optical properties. While Ag has a very strong plasmonic response, it is chemically unstable and the plasmon resonance of Ag nanostructures lies at shorter wavelengths in the UV-visible region. Although Au has a rather damped plasmonic response, its chemical stability makes it quite useful in real applications. Bimetallic Au-Ag nanoparticles enable tuning of the optical response and chemical stability by variation of the composition. So, the most common Ag–Au alloy, Ag@Au core–shell, and Au@Ag core–shell bimetallic plasmonic nanoparticles of both spherical and anisotropic (nanotriangle and nanorods) shapes are compared upon careful validation of the computational electromagnetic models. Although both Au–Ag core–shell and alloy nanoparticles exhibit an intermediary optical response between that of pure Ag and Au nanoparticles, there are noticeable differences in the spectral characteristics. Also, the effect of the bimetallic constitution in anisotropic nanoparticles is starkly different from that in spherical nanoparticles due to the absence of interband transitions for Au in the former case. In general, the improved chemical stability of Ag nanoparticles by the incorporation of Au comes with a cost of reduction in plasmonic enhancement, also applicable to anisotropic nanoparticles to a lesser extent. A photothermal heat transfer study confirms that increased absorption by the incorporation of Au in spherical Ag nanoparticles also results in an increased steady-state temperature. On the other hand, anisotropic nanoparticles are inherently better absorbers and hence better photothermal sources, and their photothermal properties are apparently not strongly affected by the incorporation of one metal in the other.

In theoretically predicting the optical properties of colloidal plasmonic nanoparticles, especially Ag nanoparticles, the gap between experiment and theory is addressed next. The effect of different factors that are believed to influence the optical response of colloidal nanoparticles such as polydispersity (size distribution), skewness and surface roughness are investigated independently from one another. For this, nanoparticle populations with size distributions of desired statistical parameters were created by a bottom-up approach for a constant number (or mole) of atoms. Only a weak effect of the statistical parameters was observed and the LSPR (localized surface plasmon resonance) position is found to be determined almost exclusively by the mean nanoparticle size. The accuracy of the theoretical prediction of the optical response depends majorly upon the optical constants that are retrieved from literature and are used as input for the theoretical models. In this regard, the most suitable set of optical constants for Ag is identified to be used in the later studies.

From isolated nanoparticles, extending the study to finite nanoparticle clusters is a natural transition as the plasmonic light-matter interaction is enhanced in clusters due to plasmonic coupling. In the context of self-assembled nanoparticle structures, close-packed two-dimensional clusters (cluster dimensions < wavelength of incident light) of spherical Au nanoparticles are investigated. The collective optical properties with increasing number of nanoparticles in the cluster (up to 61 nanoparticles) and the resulting photothermal properties were studied to delineate the effects of the cluster size, interparticle distance, and particle size. The plasmonic coupling of 'smaller' (*i.e*. 20 nm) nanoparticles and 'larger' (*i.e*. 40 nm) nanoparticles is discussed in terms of near-field and far-field interactions. A maximum light absorption per particle is found for an optimal cluster size of 19 nanoparticles, for which enhanced photothermal effects are also demonstrated. A strong dependence of the steady-state temperature of the nanoparticles on the cluster size, particle position in the cluster, incident light polarization, and interparticle distance provides new physical insight into the local temperature control of plasmonic nanostructures. On the other hand, the strong near-field enhancement in the clusters indicates possible application in surface enhanced spectroscopy techniques (SERS, SEIRA, etc.).

Going further from finite clusters, infinite nanoparticle films (film dimensions >> wavelength of incident light) of Au and Ag nanoparticles are investigated both theoretically and experimentally. Au and Ag nanoparticle films are obtained by air-ethylene glycol interfacial self-assembly and characterized by TEM imaging. The experimental optical response of these films is compared with computed spectra for the validation of the full-field electromagnetic models. It is known that in a close packed film, the individual plasmon modes of the individual nanoparticles couple together to form lattice resonance modes. The optical properties of the nanoparticles are studied with increasing interparticle distance (thus, weakening plasmonic coupling). It is shown that the damping mechanism of nanoparticles change from non-radiative to radiative as

the interparticle coupling increases. The optical properties of the nanoparticle films in the Kretschmann configuration (also known as the Attenuated Total Reflection (ATR) configuration) is studied to understand the implications of the excitation of the lattice resonance by the evanescent field generated by total internal reflection. It is shown that the optical properties of the nanoparticles films for *p*-polarized (TM) and *s*-polarized (TE) incidence in the ATR configuration are starkly different.

Next, as a promising application of the self-assembled plasmonic nanoparticle films, volatile organic compound (VOC) sensing in the gas phase is demonstrated experimentally, with a rigorous theoretical background. First, relatively large area (*i.e.* several cm^2) oleylamine-capped Au nanoparticle (10 nm) films were obtained by self-assembly at the air-ethylene glycol interface. It is shown that by controlled evaporation of the colloidal solvent, toluene, large area self-assembled films can be obtained. The sensing by these films is based on the sensitivity of the optical response of these films to the local refractive index changes induced by the adsorption of the probe molecules. Due to the presence of oleylamine ligands, the film forms a nanoparticle-ligand network that facilitates adsorption of the probe VOC molecules, which in this work is methanol. Although isolated nanoparticles of 10 nm in size are in essence non-scattering, when they are organized as a close-packed film, the plasmonic coupling results in strong optical intensities (reflectance, absorbance or transmittance). With varying vapor phase concentration of methanol, continuous optical measurement were performed *in-situ*. Sensing experiments were conducted by *in-situ* UV-Vis transmission intensity measurements of the film and *in-situ* ellipsometry of the film in the Kretschmann configuration. *In-situ* ellipsometry of the self-assembled films in the Kretschmann configuration shows enhanced sensitivity in the ψ (amplitude ratio of *s*- and *p*-polarized light) and Δ (phase difference) parameters.

Finally, a shift of focus from plasmonic to metal-oxide nanoparticles is made. The functionalization of photocatalytic metal oxide nanoparticles of TiO_2, ZnO, WO_3 and CuO with amine-terminated (oleylamine) and thiol-terminated (dodecane-1-thiol) alkyl-chain ligands is studied under ambient conditions. A high selectivity is observed in the binding specificity of a ligand towards nanoparticles of these different oxides. It is observed that oleylamine binds stably to only TiO_2 and WO_3, whereas dodecane-1-thiol binds stably only to ZnO and CuO. Similarly, polar-to-nonpolar solvent phase transfer of TiO_2 and WO_3 nanoparticles can be achieved by using oleylamine, but not dodecane-1-thiol, whereas the opposite holds for ZnO and CuO. The surface chemistry of ligand-functionalized nanoparticles is probed by attenuated total reflectance (ATR)-FTIR spectroscopy, which enabled the occupation of the ligands at the active sites to be elucidated. The photostability of the ligands on the nanoparticle surface is determined by determining the photocatalytic self-cleaning properties of the material. Although TiO_2 and WO_3 degrade the ligands within 24h under both UV and visible light, ligands on ZnO and CuO remain unaffected. The gathered insights are also highly relevant from an application point of view. As an example, because the ligand-functionalized

nanoparticles are hydrophobic in nature, they can be self-assembled at the air-water interface to give nanoparticle films with demonstrated photocatalytic as well as antifogging properties.

Summarizing, this thesis aims to provide the reader with a rigorous, fundamental, theoretical understanding of the optical properties of light-sensitive plasmonic metal nanoparticles. The impact of various properties, ranging from the type of metal, mixing of metals, particle size, particle size distribution, skewness, roughness, cluster size, interparticle spacing, polarization of incoming light, amongst others, is meticulously evaluated to interpret the resulting effect in view of potential light-driven applications. Moreover, in the final chapters an experimental confirmation and application demonstration of such light-responsive plasmonic nanoparticle films is provided, hoping to encourage further developments in this exciting field.

Acknowledgement

It was the summer of 2012, I had the first experience of doing academic research during an internship at a research lab. In the course of two months, it was clear in my mind that I truly enjoy doing research. Fast forward to 2018 November, I joined the University of Antwerp for my PhD. The last three and a half years have been a journey full of learnings and exploration into topics that I previously had no experience in. My PhD journey would not have been an enjoyable and rewarding one without the direct and indirect contributions /support from a lot of folks. I would like to extend my sincere gratitude to all of them.

Naturally, in my word of thanks, I would start with my promoters who have made the whole thing possible. Firstly, I would like to thank my main promoter (in India, a common terms that is used is a PhD guide) Sammy, who, in the first place, recruited me from another corner of the world and planted me here. Soon, I found that Sammy's style of guidance and my approach was very compatible to work as a team. Sammy gave me enough freedom to explore new things while always checking on the progress, relevance and quality of the work I am doing. His overall guidance has been really valuable not only for my PhD work, but also to grow as a researcher. I also extend my sincere gratitude to my co-promoter Silvia for the contributions and inputs, all through her busy schedule managing at a higher level in the university. I extend my gratitude to my PhD committee and the jury for their critical and impartial evaluation of my dissertation. Special thanks to Prof. Chigrin from RWTH Aachen for the collaboration on the electromagnetic models. I also thank the department of bioscience engineering and the University of Antwerp for all the resources, all the people because of whom the places are functional, including the housekeeping department.

At the end of the day, it is the people around you that creates the experience and I was fortunate to have been surrounded by kind and helpful colleagues that made the working days enjoyable. First, my gratitude goes to Hilde and Annelize for their constant support and management that keeps the lab running. I want to thank the colleagues that made my early days in the new workplace a pleasant experience: Myrthe, Tom, Tess, Griet, Laurens, Lore, Jelle, Natan, Ramesh, from the air wing and Abbas, Janne, Weiqiang, Michiel, Sui, Rishav, Yankai, Veerle, Swetlana, Katrien, Marc, and others from the 6th floor as well as the people from the 5th floor (Especially Sarah from the 5th floor, since it was a lot of fun working for the diversity team), Thank you! It was a nice start with a lot of off the work activities, lunchtime breaks or sometimes just a casual chat (in fact sometimes these small moments matter the most!). So, my thankfulness also goes to the colleagues that joined later on: Donja, Nick, Linus, Allan, Marjan, Kobe, Hesam, Heena, Julia (it is fun to work with you in the diversity team), Marijn, Naïm, and others who have created a cool workplace vibe! Currently, in my group, it is really nice to have

you guys Fons, Rajesh and Karthick, Arno and Anthony who joined later. It's a nice team to work together, but most importantly to play darts together! ;) My special thanks to Jorid for the collaborative work and often, all the work-related discussions on teams. Then Nithin and Shahid, you guys joined for the untimely coffee at 6 pm for useless chats, Thank you!

I would like to thank Prof. Chhabra, with whom I worked during my masters, for being an inspiration. My friends and family have always been the support system. My friends back home Anil, Jeeshan, Bikram, Prasurjya, Bhawesh, and all those amazing folks with whom I had great friendships at different stages of life (and somehow lost in time), I thank you all. I thank my two brothers Jyotishmoy and Anupam, and sisters-in-law Sumi and Pratikshya, for always being supportive, for no apparent reason. I am forever grateful to my parents, mom and dad, for your unconditional and irreplaceable love and support in my life. Mein Dank gilt auch Annas Familie, besonders Gisela. Danke, dass du deine herzlichen Grüße nie vergisst, und danke für deine Unterstützung! And at last (and never the least), my love, Anna, I am just thankful that you are in my life. With you by my side, my days are full of joy, fun, stupidity, and love, and I guess that's all one mostly needs at the end of the day!

Table of contents

List of figures

List of tables

Symbols and abbreviations

ATR	Attenuated total reflectance
$\boldsymbol{B}$	Magnetic induction vector
c	Velocity of light in free space
C_p	Specific heat capacity
$\boldsymbol{D}$	Electric displacement field vector
D	Mean diameter in a frequency interval
DLS	Dynamic light scattering
$\boldsymbol{E}$	Electric field intensity vector
$\boldsymbol{E}_{inc}$	Incident electric field intensity vector
$\boldsymbol{E}_{sc}$	Scattered electric field intensity vector
$\boldsymbol{E}_{tot}$	Total electric field intensity vector
EDX	Energy Dispersive X-Ray
FDTD	Finite Difference Time domain
FEM	Finite element method
FTIR	Fourier Transform Infrared Spectroscopy
FWHM	Full width half maximum
$\boldsymbol{H}$	Magnetic field intensity vector
$\boldsymbol{H}_{inc}$	Incident magnetic field intensity vector
$\boldsymbol{H}_{sc}$	Scattered magnetic field intensity vector
$\boldsymbol{H}_{total}$	Total magnetic field intensity vector
HWHM	Half width half maximum
$\boldsymbol{J}$	Current density
k	Thermal conductivity
k_o	Wave number
LSPR	Localized surface plasmon resonance
MeOH	Methanol
n	Refractive index
$\boldsymbol{n}$	Number of nanoparticles in a frequency interval
NP	Nanoparticle
N_{Total}	Total number of nanoparticles
PML	Perfectly matched layer
S_k	Skewness factor
SPR	Surface plasmon resonance
SEIRA	Surface-enhanced infrared absorption spectroscopy
SEM	Scanning electron microscopy
SERS	Surface enhanced Raman spectroscopy
T	Temperature
TGA	Thermogravimetric analysis

TEM	Transmission electron microscopy
W_{abs}	Energy absorbed per unit time
W_{sc}	Energy scattered per unit time
$\boldsymbol{U}$	Velocity vector
VOC	Volatile organic compund
XRD	X-ray diffraction
Z	Impedance
Z_o	Free space impedance
σ_e	Electrical conductivity
σ	Standard deviation
σ^*	Shape parameter in log-normal distribution
σ_{abs}	Absorption cross section
σ_{sc}	Scattering cross section
σ_{ext}	Extinction cross section
ρ	Density
ρ_e	Free charge density
ε_e	Permittivity
μ_e	Permeability
μ_o	Permeability of free space
μ	Mean diameter of a population of nanoparticles
μ^*	Location parameter in log-normal distribution
ε_r	Relative permittivity or dielectric constant
ε_r'	Real part of complex relative permittivity or dielectric constant
ε_r''	Imaginary part of complex relative permittivity or dielectric constant
$\mu_{r,}$	Relative permeability
Δd	Frequency interval
φ	Azimuth angle of incidence
θ	Elevation angle of incidence
ν_s	Stretching vibration (symmetric)
ν_{as}	Stretching vibration (asymmetric)
δ_s	Bending vibration (symmetric)
δ_{as}	Bending vibration (asymmetric)

Chapter 1

A brief review on photoactive nanoparticles, their self-assembly and applications

Based on:

Rituraj Borah, Sammy W. Verbruggen, Self-Assembly of Colloidal Nanoparticles into Clusters, Patterns and Films: Methods and Applications. (*in preparation*)

Rajeshreddy Ninakanti, Fons Dingenen, **Rituraj Borah**, Hannelore Peeters, Sammy W. Verbruggen, Plasmonic Hybrid Nanostructures in Photocatalysis: Structures, Mechanisms and Applications. (Under review as invited article with Topics in Current Chemistry)

Research is an activity that you know you are doing right when you don't know whether you are doing it right. – Unknown.

1.1 Photoactive nanoparticles/nanostructures

A widely accepted definition of a 'nanoparticle' is a particle in the size range from 1 to 100 nm.[1] [2] Going by the same definition, a nanostructure is a structure with functional features as small as, or less than, 100 nm. For comparison, one must realize that a single human hair is 60,000 nm in thickness and the DNA double helix has a radius of 1 nm. Photoactive nanoparticles or nanostructures can be simply defined as nanoparticles/nanostructures that interact strongly with light. It is important to note that one way or the other, technically all nanoparticles interact with light. Thus, this definition of photoactive nanoparticles includes those light-matter interactions that can trigger further chemical/thermal transformations or enhance optical processes in important applications. While, historically, light-mediated processes have always drawn great scientific interest, their importance has grown tremendously in the face of the present global environmental crisis. For instance, photoactive nanoparticles or nanostructures hold great promise for the development of low-cost technologies for harvesting solar light to meet the global energy demands in a sustainable way.

In this introductory **Chapter 1**, two types of photoactive nanoparticles, namely plasmonic and metal-oxide semiconductor nanoparticles, are described briefly in **sections 1.1.1** and **1.1.2** in terms of their general physicochemical properties and potential applications. Further in **section 1.2**, the self-assembly of nanoparticles in general and its applications are discussed, followed by conclusive remarks. The brief introduction to plasmonic nanostructures and self-assembly here serves as a prelude to the original theoretical/computational and experimental results presented in **Chapters 2**, **3**, **4**, **5**, and **6**. The discussion on metal-oxide semiconductor nanoparticles is relevant to **Chapter 7** where original experimental results on the self-assembly of metal-oxide nanoparticles are reported.

1.1.1 Plasmonic nanoparticles: an introduction from electromagnetic theory

In simple terms, plasmonic nanoparticles are nanoparticles with abundant amount of free conduction electrons that exhibit resonant light-nanoparticle interactions resulting in a strong optical response. The most common plasmonic nanoparticles are composed of conductive metals such as Au, Ag, Cu, Al, etc and combinations thereof. Since light is an electromagnetic wave, when plasmonic nanoparticles are illuminated, the oscillating electric field of light induces coherent oscillation of the free electron gas of the nanoparticles, **Figure 1.1 (a)**. This energy transfer process, when described from a quantum mechanical perspective, is a coupling between photons and free electrons that gives rise to quasi-particles called plasmons. The word "plasmon" originates from plasma physics, taken to the limit of a degenerate electron gas.[3] From a first-principle viewpoint, plasmons are particular excited states that involve collective intraband excitation of electrons from the ground state to excited states.[4] The plasmon resonance by virtue of its origin in strong photon-electron coupling has drawn significant attention

over the years as a possible enhancement pathway in important light driven processes. Theoretically, the plasmonic phenomenon can be described reasonably well by the classical electromagnetic framework using the effective medium theory. At a plane metal-dielectric interface, such a resonant oscillation of conduction electrons excited by light is called surface plasmon resonance, **Figure 1.1 (b)**. In this case, the electromagnetic surface wave *i.e.* the surface plasmons (polaritons) propagates in a direction parallel to the metal-dielectric interface. In a metal nanoparticle much smaller than the wavelength of incident light, the oscillations are confined within the volume of the nanoparticle giving rise to a phenomenologically different type of resonance known as the localized surface plasmon resonance, **Figure 1.1 (c)**. The light matter interaction in both the cases results in absorption and scattering/reflection (for a thin metal film) of light accompanied by the evolution of a strong evanescent electric field at the boundary. The amplification of the electric field is often termed as near-field enhancement. Thus, from an electromagnetic point of view, this light-matter interaction is described from the variation of the electric field and the magnetic field of light in space and time as a result of varying material dielectric properties. Mathematically this is described by the Maxwell's equations as follows:

$$\nabla \cdot \boldsymbol{D}(t) = \rho_e(t) \tag{1.1}$$

$$\nabla \cdot \boldsymbol{B}(t) = 0 \tag{1.2}$$

$$\nabla \times \boldsymbol{E}(t) = -\frac{\partial \boldsymbol{B}(t)}{\partial t} \tag{1.3}$$

$$\nabla \times \boldsymbol{H}(t) = \frac{\partial \boldsymbol{D}(t)}{\partial t} + \boldsymbol{J}(t) \tag{1.4}$$

In equations (1.1) to (1.4), $\boldsymbol{E}$ and $\boldsymbol{H}$ are the electric field intensity and magnetic field intensity vectors. $\boldsymbol{D}$ and $\boldsymbol{B}$ are the electric displacement vectors and magnetic induction vectors, respectively. $\boldsymbol{J}$ is the current density. While $\boldsymbol{E}$ and $\boldsymbol{B}$ are the fundamental fields, the fields $\boldsymbol{D}$ and $\boldsymbol{H}$ account for the polarization and magnetization effects of the materials. Thus, the material dielectric properties relate $\boldsymbol{E}$ to $\boldsymbol{D}$ and $\boldsymbol{B}$ to $\boldsymbol{H}$ as:

$$\boldsymbol{D}(t) = \varepsilon_e(t) * \boldsymbol{E}(t) \tag{1.5}$$

$$\boldsymbol{B}(t) = \mu_e(t) * \boldsymbol{H}(t) \tag{1.6}$$

The equation(s) (1.5) and (1.6) are known as the constitutive relations where $\varepsilon_e(t)$ and $\mu_e(t)$ are the permittivity and permeability of the medium, respectively. Also, * denotes a convolution in equation(s) (1.5) and (1.6). These time-domain forms of the Maxwell's equations give the transient response of light's electromagnetic wave. However, the central problem in this dissertation mainly concerns the spectral response of nanomaterials in terms of the rate of energy flow and dissipation. Thus, it is convenient to rather solve the equations in the frequency domain to analyse the electromagnetic response at desired frequencies (or wavelengths). This requires the frequency domain

form of the Maxwell's equations, which can be obtained by Fourier transformation of equations (1.1 to 1.6), yielding equations (1.7 to 12):

$$\nabla \cdot \boldsymbol{D} = \rho_e \tag{1.7}$$

$$\nabla \cdot \boldsymbol{B} = 0 \tag{1.8}$$

$$\nabla \times \boldsymbol{E} = -j\omega \boldsymbol{B} \tag{1.9}$$

$$\nabla \times \boldsymbol{H} = j\omega \boldsymbol{D} + \boldsymbol{J} \tag{1.10}$$

$$\boldsymbol{D} = \varepsilon_e(\omega)\boldsymbol{E} \tag{1.11}$$

$$\boldsymbol{B} = \mu_e(\omega)\boldsymbol{H} \tag{1.12}$$

The frequency domain form from equation (1.7) to equation (1.12) now facilitates direct solution of an electromagnetic problem for any frequency. The free charge density, ρ_e is zero in the cases considered here as there is no charge accumulation. The convolutions in equation(s) (1.5) and (1.6) now become multiplications and the complex frequency-dependent dispersion relations of materials can be used. In equation (1.10), the current density $\boldsymbol{J}$ can be expressed in terms of the electric field as $\boldsymbol{J} = \sigma \boldsymbol{E}$. Thus, equations (1.9) to (1.12) can be combined to derive the wave equation that is solved numerically in the computational investigations in this dissertation:

$$\nabla \times \left[\frac{1}{\mu_r}(\nabla \times \boldsymbol{E})\right] = k_o^2\, \varepsilon_r \boldsymbol{E} \tag{1.13}$$

The magnetic counterpart of equation (1.13) can be similarly obtained as:

$$\nabla \times \left[\frac{1}{\varepsilon_r}(\nabla \times \boldsymbol{H})\right] = k_o^2\, \mu_r \boldsymbol{H} \tag{1.14}$$

Where, $k_o = \omega\sqrt{(\varepsilon_o \mu_o)}$ is the wave number. The equation(s) (1.13) and (1.14) above are applicable to general inhomogeneous materials where the dielectric properties are function of spatial coordinates. The relative permittivity ε_r in equation(s) (1.13) and (1.14) is given as $\varepsilon_r = \frac{\varepsilon_e'}{\varepsilon_o} - j\frac{\sigma_e}{\varepsilon_o \omega}$, where ε_e' is the real part of permittivity, ε_o is the permittivity of free space and σ_e is the electrical conductivity. Similarly, the relative permeability μ_r can be given as $\mu_r = \mu_e/\mu_o$, where μ_e and μ_o are the complex permeability of the material and permeability of free space respectively. For Ag and Au nanostructures as considered in this work, μ_r can be safely assumed to be unity. For the numerical solution in the frequency domain, the direct wave equation *i.e.* equation (1.13) or (1.14), or equation (1.9) to (1.12) can be implemented in a discretization scheme depending on the code. For example, in COMSOL Multiphysics, the wave equation is directly implemented in the numerical framework as indicated in the module (see below). Before the development of numerical codes and computational resources, the complete analytical treatment of spherical nanoparticle-light (of wavelength larger

than the nanoparticle) interaction was first given by Gustav Mie[5] [6] in 1908 in his analytical solution to the Maxwell's equations. However, the solution for other shapes of particles could only be obtained numerically long after Mie's work. It took more than 60 years to obtain the numerical solution for scattering by particles with a spheroidal shape. With the availability of large computational power and optimized numerical methods such as T-matrix, discrete dipole approximation, finite-difference time domain (FDTD), finite element method (FEM), *etc*, it is now possible to also solve the Maxwell's equations for complex arbitrary shapes. The numerical framework COMSOL Multiphysics used in this dissertation converts the wave equation along with the imposed boundary conditions into a set of algebraic equations by FEM (finite element method) discretization that forms a sparse matrix for numerical solution. This formulation is implemented according to the computational domain and the boundary conditions defining the plasmonic nanostructures and the surrounding dielectric environment.

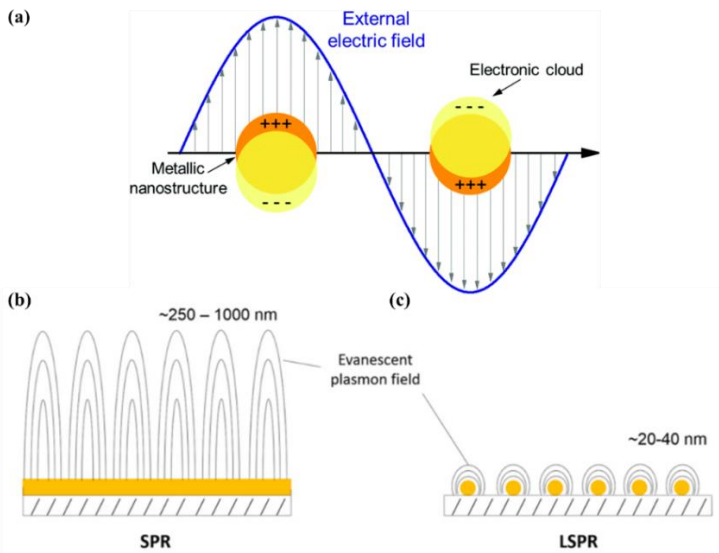

Figure 1.1 (a) Schematic representation of plasmonic oscillation of free electrons in a nanostructure by an electromagnetic field. (b) Schematic representation of surface plasmon resonance and localized surface plasmon resonance on a planar metal film and metal nanostructures respectively. Images were adapted and reproduced with permission from Bozzola *et al.*[7], Royal Society of Chemistry (©2017) and nicoyalife.com.

Plasmonic nanoparticles were known to alchemists already centuries ago, **Figure 1.2 (a)**. The famous Lycurgus cup from the 4th century AD is a common example of how colors were created in glass by using metal nanoparticles, **Figure 1.2 (b)**. The ruby red appearance of the Lycurgus cup is predominantly due to the less than 1% uniformly dispersed gold nanoparticles embedded in the glass.[8] Another splendid example of

plasmonic artwork is the rose window at the Notre Dame Cathedral, **Figure 1.2 (c)**.[9] In the 17th century, the glass-colouring process was further refined by Andreus Cassius and Johann Kunckel.[10] In the 18th – 19th century, photography by daguerreotype process relied on the formation of plasmonic Ag nanostructures from the exposure of a silver halide layer to light.[11] As shown in **Figure 1.2 (d)**, the variation and gradient of colour was created by varying the nanostructure's size and density. Even by modern imaging technology standards, the daguerreotypes could yield images of very high resolution, **Figure 1.2 (e)**.[12] On February 5, 1857, Michael Faraday delivered the historic Bakerian Lecture of the Royal Society entitled: "Experimental Relations of Gold (and other Metals) to Light" that not only spawned a new field of chemistry known as colloidal chemistry but also brought the attention of the world towards the highly light sensitive plasmonic metal nanoparticles.[13] Given the theoretical and experimental developments of his time, his intuitive observations were truly remarkable as evident from the statement "*...known phenomena appeared to indicate that a mere variation in the size of its particles gave rise to a variety of resultant colours...*". The size dependent optical properties of plasmonic nanoparticles is now a basic fact described quite accurately by classical electromagnetic theory. In the recent times, the interest in plasmonics surged in the last decades as a part of the continuous efforts towards the development of new frontiers in nanotechnology. Also, with the advanced characterization techniques of the modern times, visualization and chemical analysis of plasmonic nanostructures has become more accurate than ever, pushing the field of plasmonics rapidly towards new frontiers.

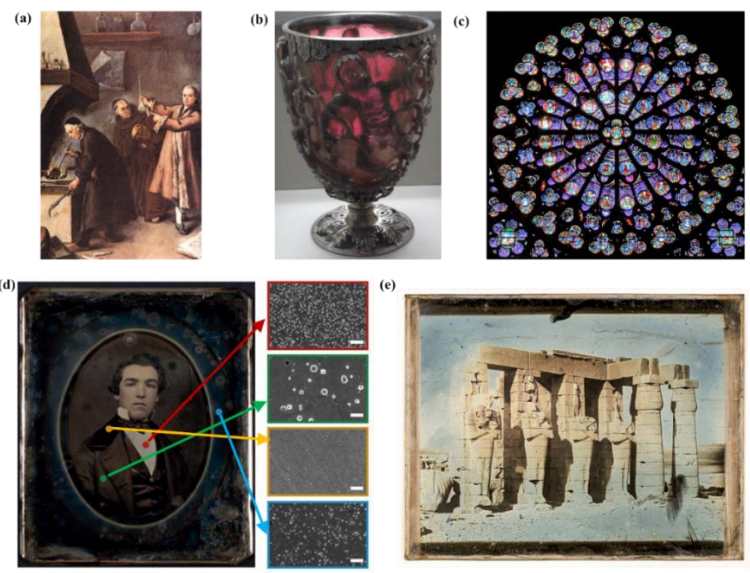

Figure 1.2. (a) Medieval alchemists at work captured in the painting "The Alchemist" by Pietro Longhi, 1661.[14] (b) Lycurgus cup from the 4th century A.D. made of glass embedded with Au nanoparticles (~1% by weight). (c) The colourful rose window of

the Notre Dame cathedral made of dichroic glass. (d) Daguerreotype image from unknown artists: the SEM images with coloured boundaries on the side corresponds to the areas marked by colour dots. [11](e) Created in 1844, this daguerreotype of Pharaoh Ramses II's mortuary temple in Thebes has the sharp clarity of a modern photograph.[12] Figure (a), (d) and (e) were re-produced from the respective publishers according to the terms and conditions. Images were adapted and reproduced with permission from the American Chemical Society (©2020), National Academy of Sciences (© 2019), and William Andrew Publishing: Oxford (© 2015).

In the recent years, the application of plasmonic nanoparticles /nanostructures has expanded to broad areas such as sensing, photocatalysis, photothermal therapy, photoacoustic imaging, solar energy harvesting, photovoltaics, amongst others.[15] A rather common application that most people are now familiar with due to the COVID 19 pandemic is the lateral flow test kit which exploits the strong light-matter interaction in plasmonic nanoparticles. For naked eye detection, Au nanoparticles are used as the optical detection agent that binds to specific locations (the usual red strips) depending upon the presence of a biomarker, **Figure 1.3 (a)**.[16] Due to the high sensitivity of the plasmon resonance to the refractive index of the surrounding medium, plasmonic nanoparticles are also promising in refractive index-based sensing of biomolecules, liquid mixtures, gas molecules, etc.[17] [18] As shown in **Figure 1.3 (b)**, an example is provided for refractive index-based sensing of glucose: The change is glucose levels is detected as a red-shift of the plasmon band *i.e*., the dip in the reflectivity with increasing glucose concentration. . In plasmon enhanced photocatalysis, plasmonic nanoparticles/nanostructures often serve as an antenna for enhanced light-matter interaction. As shown in **Figure 1.3 (c)**, Janus (i.e. two-faced) nanoparticles consisting of a TiO_2 and Au nanostructure have higher photocatalytic activity than pure TiO_2 nanoparticles in water splitting due the strong near-field enhancement induced by Au. Thus, plasmonic nanoparticle decorated photocatalytic nanostructures are promising for various light driven processes, **Figure 1.3 (d)**. The light absorbed by plasmonic nanostructures, when not utilized in subsequent reactions through accompanying quantum-level processes, dissipates as heat. By careful engineering towards maximum absorption and minimum scattering/reflection losses, solar light can be directly used for thermal processes such as seawater desalination, **Figure 1.3 (e)**. Again, as shown in **Figure 1.3 (f)**, the strong near-field enhancement induced by plasmonic nanoparticles is a common signal amplification strategy in surface enhanced processes such as SERS (surface-enhanced Raman spectroscopy), SEIRA (surface-enhanced infrared absorption spectroscopy), etc.[19]

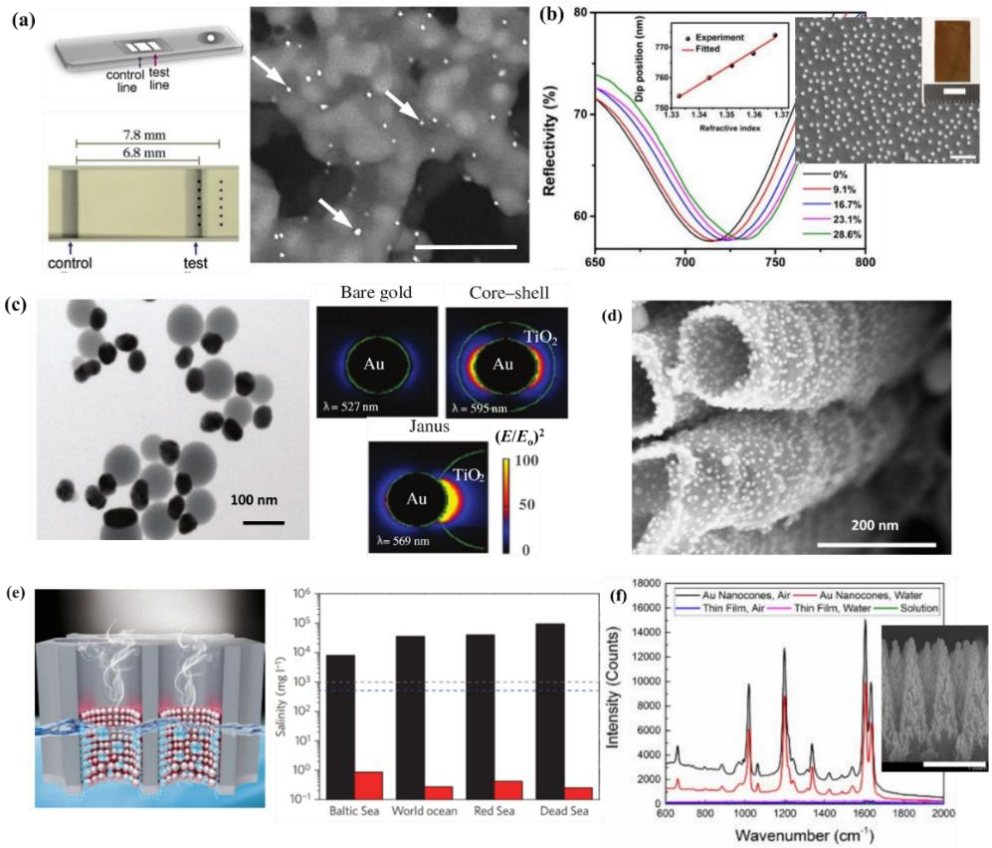

Figure 1.3 (a) Plasmonic Au-Pt nanoparticles attached to a positive test line in a later flow test (SEM image scale bar: 3 µm) .[20] (b) Glucose concentration sensing based on refractive index sensitivity of Au nanocube arrays (with L = 85 nm, h = 8 nm) with SEM image of the nanocubes (scale bar: 800 nm).[21] (c) Transmission electron microscopy (TEM) images of Janus Au-TiO_2 nanoparticles and near-field enhancement map showing maximum enhancement for Janus NPs compared to bare Au and Au@TiO_2 core-shell NPs for water splitting.[22] (d) Scanning electron microscopy (SEM) image of Au NP decorated TiO_2 nanotubes ((T)NTs).[23] (e) Plasmonic Al nanoparticles utilized for solar desalination with yield well-below permitted concentration (black column: before desalination, red column: after desalination).[24 25] (f) Au nanoparticles decorated on Si nanocones (SEM image scale bar: 1 µm) for surface enhanced raman spectroscopy (SERS).[26] Images were adapted and reproduced with permission from Elsevier (© 2021), Royal Society Chemistry (© 2019, 2017, 2009), Wiley-VCH (© 2012) American Chemical Society (© 2020), Springer Nature (© 2016).

The scientific interest around plasmonic nanostructures stems from the intense light-matter interaction as well as the accompanying quantum processes. The central questions in the plasmonic enhancement of photo-electro-chemical processes are about the generation of optically-excited energetic hot carriers *i.e.* hot electrons and holes, and

their channelling to subsequent processes. The generation of hot carriers in plasmonic nanostructures is influenced by various factors such as material optical properties, size and shape of the nanostructure, polarization of the incident light with respect to the nanoparticle's orientation (relevant to anisotropic nanoparticles) and so on[27]. The theoretical description of these processes is an area of on-going research.

1.1.2 Metal oxide nanoparticles

Formation of oxides from pure metals by spontaneous oxidation is an ubiquitous process. This makes many metal oxides abundant in the earth crust. Interestingly, the nanoparticles of many metal oxides are highly valuable due to their application in common chemical reactions in catalysis, photocatalysis, (photo)electrocatalysis, semiconductor electronics, photovoltaics, sensing, etc.[28] [29] The photoactivity of some metal oxide nanoparticles such as TiO_2, ZnO, WO_3, MoO_3, CuO, ZrO_2, etc., originates from the band gap of these materials, **Figure 1.4 (a)**. Among different oxides, TiO_2 has been the most widely explored material in the last decades of research due to its low cost and wide availability. However, the quest for better materials has only been intensified in recent years for industrially feasible technologies towards a sustainable future. The suitability of metal oxides in light driven applications is determined by both the band gap of these materials as well as the band-gap edges (shown in **Figure 1.4 (a)**), which can be determined experimentally.[30] Upon illumination of light *i.e*. photons on these materials, electrons from the valance band are excited to the conduction band forming a hole in the valence band. While a fraction of these photogenerated electrons and holes migrate to the metal oxide surface, the rest recombine together with a release of the energy in the form of heat or photons. The excited electron-hole pair *i.e*. the photoexcitons on the surface can interact with adsorbed chemical species to undergo chemical reactions. Naturally, a small band-gap with a low recombination rate is desirable so that a large portion of the visible spectrum can excite valence band electrons that can drive subsequent chemical reactions. However, the effectiveness of these photoexcitons is also dependent on the band positions with respect to the energy of the reaction. To facilitate the electron transfer from the photocatalyst to the adsorbate, the conduction band (CB) minimum of the photocatalyst must be higher than the reduction potential of the adsorbate. Similarly, the photogenerated holes could generate strong oxidizing agents like OH radicals by interacting with the adsorbed molecules on the surface. Here, the valence band (VB) maximum of the photocatalyst must be lower than the oxidation potential of the adsorbate for efficient hole transfer. For instance, as shown in **Figure 1.4 (a)**, despite having a low band gap falling within the visible range, good electron transport properties and low recombination rates, WO_3, MoO_3, CuO, Fe_2O_3, and V_2O_5 are not efficient photocatalysts due to the fact that their conduction band position is too low. Thus, the photoexcitons do not have the potential high enough to catalyse important reactions. In contrast, although TiO_2 has a large bandgap that matches only with photons in the UV range, the higher position of the conduction band

ensures high enough potential of the excited electrons to drive different reactions.[31] Also, TiO_2 being an indirect band-gap semiconductor, has slower rate of recombination due to photon-phonon coupling further enhancing the photocatalytic activity, while for Fe_2O_3, the direct band gap facilitates faster re-combination thereby reducing surface reactivity by photoexcitons.[32]

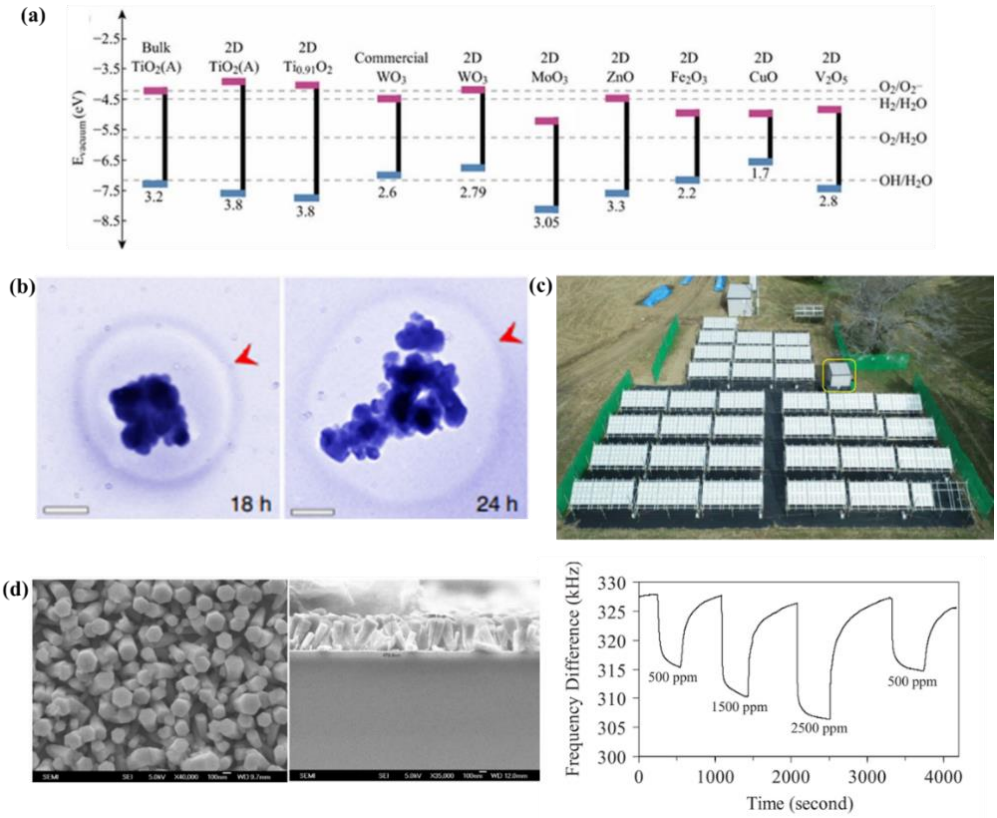

Figure 1.4 (a) Band gap and band positions of different metal oxides[31]. (b) In-situ TEM imaging of H_2 bubble formation by water splitting reaction over TiO_2 nanoparticles under UV illumination[33]. (c) Large scale (100-m^2) photocatalytic array of panel reactors for spontaneous solar hydrogen production with an STH of 0.76%.[34] (d) ZnO nanostructures for H_2 gas sensing application[35].). Images were adapted and reproduced with permission from Springer Nature (© 2009, 2018, 2021).

Metal oxide nanostructures have been going through intense fundamental investigations over the last decades for spontaneous photocatalytic water-splitting, which is considered as the holy-grail for a carbon free future. **Figure 1.4 (b)** shows *in-situ* visualization of H_2 nanobubble formation as a result of water splitting by TiO_2 under UV illumination in an environmental TEM cell. While the working of such a system was proven decades ago, the efficiencies required for an industrial scale technology still provides a challenge. Recently, however, the feasibility of a large scale (100 m^2) water-splitting

plant has been shown with a solar to hydrogen efficiency of 0.76%, **Figure 1.4 (c)**. Obviously, to meet the global energy demands, reaching much higher efficiencies is a must. Nonetheless, the surface chemistry of metal oxide nanostructures also creates possibilities to solve non-existential technological problems such as sensing. The application of metal oxide nanoparticles in gas sensing has been studied quite extensively[36]. Common metal oxide semiconductor (MOS)-based gas sensors can mainly detect a gas because of the change in electrical signal caused by the gas. When O_2 molecules are adsorbed on the metal oxide surface, conduction band electrons are trapped by the molecules to form ions. As a results, an electron depletion region forms on the surface which also results in band bending. Reaction of these oxygen species on the surface with reducing gases or the replacement of the adsorbed oxygen by other molecules by competitive adsorption can reverse the band bending resulting in an increased conductivity. **Figure 1.4 (d)** shows Pt coated ZnO nanostructures for H_2 gas sensing as an example.

1.2 Self-assembly of nanoparticles into clusters and films

1.2.1 Definition and classification

While the individual properties of nanoparticles as discussed in **Section 1.1.1** and **1.1.2** strongly determine the effectiveness of colloidal nanoparticles in different applications, the placement of the nanoparticles at a target region or interface in an optimal arrangement is equally important. In this regard, self-assembly is an efficient technique for the nanoscale organization of nanoparticles for their optimal performance. As the term itself suggests, self-assembly, broadly, is a process of autonomous organization of components into structures without human intervention. While self-organization is an ubiquitous phenomenon in nature at different length scales, in nanotechnology, self-assembly is a promising technique to build functional structures and interfaces from nanomaterials, molecules, and so on. The growing interest on self-assembly stems from the fact that it enables self-organization at the nanoscale, where mechanical intervention is not possible. Thus, apart from the access to the unique spontaneous structures, self-assembly also promises an alternative nanofabrication technology to obtain functional interfaces more economically.

Generally, self-assembly of nanoparticles has countless possibilities with regard to the structural make-up from the nano to the macro scale. Based on the present state of literature, one can divide self-assembled nanoscale structures broadly into two classes as given in Table 1. The first one comprises of finite clusters of nanoparticles resulting from assembly in 2D and 3D. The second class encompasses assemblies extending to infinity in at least one dimension. For instance, a self-assembled nanoparticle film extends is considered infinite in two dimensions. In practice, no film or structure can be *actually* extended to infinity in any dimension. Thus, it is the relative length in one dimension with respect to the size of a single nanoparticles that is being referred to here.

Table 1.1 Overview of self-assembly techniques to obtain nanoparticle clusters and films with existing important literature.

Self-assembly of colloidal nanoparticles	Nanoparticle Clusters	• Assembly by electrostatic/van-der-Waals interaction.[37] • Emulsion directed self-assembly. • Assembly by molecular binding DNA origami.[38 39] • Magnetic field directed self-assembly.[40] • Lithographic patterning.[41] • Light induced self-assembly.
	Nanoparticle films	• **Air-liquid interfacial self-assembly** • Liquid-Liquid interfacial self-assembly.[42 43] • Evaporative self-assembly. • Directed Self-assembly on functionalized substrate.

As shown in **Table 1.1**, each class of self-assembly techniques is quite broad to treat in a single discussion. Therefore, the following discussion is limited to one specific technique from the above classification namely, the air-liquid interfacial assembly, which is the technique used in this dissertation.

1.2.2 Air-liquid interfacial self-assembly

Among different self-assembly based techniques that have been developed for the fabrication of nanoparticle thin films, air-liquid interfacial assembly has been the most widely investigated approach based on which commercial technologies have also been developed. These developments have been inspired by the original Langmuir-Blodgett technique for organic molecules which is extended to nanoparticles to obtain nanoparticle films.[44] This technique simply involves trapping of nanoparticles at the liquid-air interface which form a close packed film when there are enough nanoparticles to cover the interfacial area available. For self-assembled film of nanoparticles, this technique is still being explored for further developments towards more complex nanoscale arrangements and large-scale applications.[45] The common Langmuir-Blodgett trough design has a large area container/trough (for example, Kibron

Microtrough G4 has a surface area of 930 cm^2) where the sub-phase (mostly water) is filled up to the top. The nanoparticles are introduced on the surface of this liquid to be trapped at the interface as shown in **Figure 1.5 (a)**.[46] The surface area over the liquid is then reduced by a movable barrier so that the surface area is exactly what is needed for the nanoparticles to form a close packed monolayer film. The movable barrier in this design is very important for using water as the subphase as this allows surface pressure regulation. Due to the high surface tension of water, introduction of nanoparticles onto an air-water interface with fixed surface area results in increasing surface pressure that hinders free movement of the nanoparticles to form a continuous close packed film. Thus, the barrier allows a large surface area in the beginning for a limited number of nanoparticles to move around freely like in a 2D gas, after which the molecules are gradually packed into a smaller area by the barrier sliding over the water surface. Also, the barrier allows for different packing densities in the film, **Figure 1.5 (a)**. Also, the barrier regulates the surface pressure during the transfer of the film to a substrate by vertical dipping. An alternative simpler set-up for the air-liquid interfacial assembly consists of a low surface tension liquid (e.g. ethylene glycol, diethylene glycol, etc.) contained in a container so that the liquid surface, which is of fixed area unlike the set-up discussed above, acts as the interface. This method has been used extensively by Murray *et al*. as well as other groups to obtain self-assembled films over relatively smaller areas (up to a few cm^2) but also for more complex arrays such as multilayer films, binary nanoparticle films and so on.[47] [48] [49] The low surface tension liquid facilitates easier movement of the nanoparticles at the interface in the formation of the film without requiring external arrangements for the regulation of the surface area, **Figure 1.5 (b)**. However, naturally, this method has less control over the monolayer or multilayer formation. When the number of nanoparticles introduced over the subphase is exactly equal to what is needed to cover the entire surface, the film tends to be a monolayer. With increasing number of nanoparticles over this limit, bi-layer or multilayers are formed at different locations of the films.[50] [51] Regardless of the subphase used, in air-liquid interfacial assembly procedures, the nanoparticles –that are often synthesized in aqueous medium- need to be functionalized with organic ligands in order to be dispersed in a volatile organic solvent. Naturally, use of a non-polar solvent (e.g., hexane, toluene, chloroform, etc.) as the solvent of the nanoparticle colloid is convenient as the solvent stays separate over the polar subphase (water or glycols) due to the immiscibility. For the nanoparticle synthesis procedures that are performed in a non-polar organic medium, polar to non-polar phase transfer is not required. Usually, all the excess ligands present in the non-polar phase are removed before self-assembly. Griesemer *et al*. systematically investigated the effect of the excess ligands on film formation to show that a certain excess ligand concentration inhibits the wrinkling and folding of the film during compression, **Figure 1.5 (c)**. Also, naturally, the interparticle distance increases with increasing excess ligand concentration.[52] For nanoparticles stably dispersed only in polar solvents, Nie *et al*. provided a solution by demonstrating that nanoparticles dispersed even in a polar phase (PVP coated Au nanoparticles in

ethanol) can spread over a water surface without mixing with it when the nanoparticles are introduced as an aerosol by electro-spraying, **Figure 1.5 (d).**[53] After nebulization, the solvent in the tiny colloid droplets evaporates rapidly resulting in trapping of the nanoparticles at the air-water interface. In fact, complete hydrophobization of the nanoparticles is not a requirement to trap the nanoparticles at the interface. As Moon *et al*. showed, nanoparticles can be trapped at the interface in several ways, such as by reducing the compatibility of the colloidal dispersion phase with water, increasing the particle concentration in the colloid, reducing the zeta potential of the colloidal particles, adding a salt (NaCl) to the suspension, and utilizing soft particles. Morag *et al*. showed another interesting possibility by adding elaidic acid and myristyl alcohol to the thiol coated Au nanoparticles to obtain network-like Au nanoparticle films with polygonal myristyl alcohol domains, **Figure 1.5 (e)**.[54] Elaidic acid, on the other hand, is added for solubilizing Au NPs at the air/water inter-face at the operating temperature. **Table 1.2** summarizes the set-ups used for air-liquid interfacial self-assembly in different important part studies. Although the air-liquid self-assembly is a mature technology for molecular films, its success with nanoparticles is determined by many factors. First, for a well-ordered film, size and morphological uniformity of the nanoparticles is important. Again, the colloidal synthesis procedures determine the feasibility of further ligand functionalization of the nanoparticles in order to be compatible with the self-assembly procedure. For example, the replacement of a polar thiol ligand on Au nanoparticles with a non-polar ligand can be difficult due to the strong thiol-Au bond. Such modifications can be more complicated in hybrid nanoparticles (for example, janus nanostructures) with multiple surface compositions. On the other hand, among the techniques listed in **Table 1.1** for nanoparticle films, the air-liquid self-assembly technique is the most evolved for obtaining closed-packed arrays with adequate control over nanoscale dimensions. Among other techniques, for instance, the liquid-liquid interfacial assembly has seen little progress regarding the control of the interfacial pressure during the self-assembly process. Also, transfer of large area (*i.e.* several cm^2) nanoparticle films from the liquid-liquid interface to a substrate has been proven to be extremely difficult. Again, both the evaporative assembly and directed assembly on functionalized substrates are techniques still at early stages. The primary challenge of the evaporative self-assembly has been to avoid the coffee ring effect which results in concentration of nanoparticles at the outer edges of a drying colloidal droplet on a flat surface. On the other hand, directed assembly on functionalized substrate requires compatible surface chemistry to bind the nanoparticles to the substrate by inter-molecular bonding.

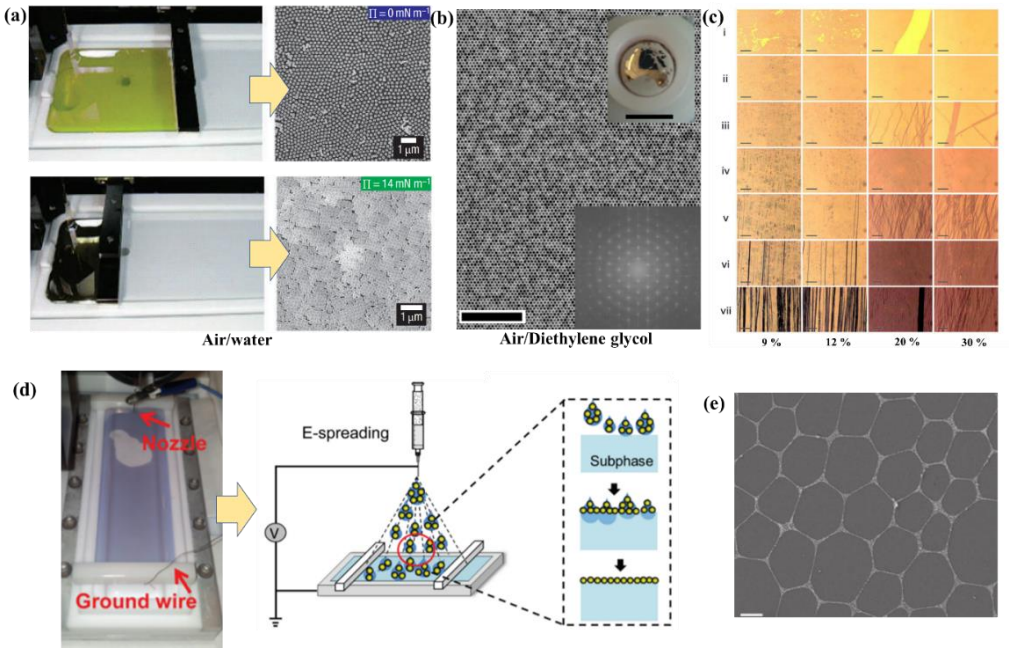

Figure 1.5 (a) Ag nanoparticles self-assembled at the air-water interface in Langmuir Blodgett trough set up.[46] The movable barrier can compress the film towards higher packing density. (b) Au nanoparticles self-assembled at a fixed air- diethylene glycol interface. (SEM image scale bar: 500 nm, digital image scale bar: 1 cm) [55] (c) The presence of excess ligands at the interface inhibits wrinkling and folding of the nanoparticle film during compression (scale bar: 40 μm).[52] (i-vii: different stages of compression for different ligand concentrations) (d) Nie *et al*. showed that nanoparticle dispersed in polar solvents (e.g. ethanol) can also be trapped at the air-water interface by nebulization with electro-spreading.[53] (e) Network-like assemblies can be obtained by adding myristyl alcohol that forms its polygonal domains (scale bar: 10 μm).[54] Images were adapted and reproduced with permission from Royal Society Chemistry (© 2017), Wiley-VCH (© 2011) American Chemical Society (© 2015), Springer Nature (© 2007, 2020).

Table 1.2 Summary of air-liquid interfacial self-assembly procedures reported in selected literature.

Literatu -re	**Subphase**	**Nanoparticle/shape/A -pprox. size/capping ligand**	**Nanoparti -cle solvent**	**Set-up description/uniqu-e feature**	**Film quality**
Kim *et al*.[56] (2001)	water	$BaCrO_4$/nanorod/20 nm length, 5 nm dia./dioctyl sodium sulfosuccinate (AOT or Aerosol-OT)	isooctane	Commercial Nima Technology M611 LB trough with surface pressure regulation.	Unidirecti--onal Nanorod monolayer

Song *et al.*[57] (2005)	water	Pt/nanocubes, cuboctahedra, and octahedra/9-10 nm/	Chloroform	Commercial Nima Technology M611 LB trough	Randomly packed monolayer
Tao *et al.*[46] (2007)	water	Ag/truncated cubes, cuboctahedra, and octahedra/120, 150 and 250 nm/PVP	Ethanol-chloroform (1:100 ratio)	Commercial KSV Nima 611 LB trough	Several cm^2 close packed film
Dong *et al.*[48] (2010)	Diethylene glycol	Binary mixture of Fe_3O_4 and FePt/ nanospheres/15 and 6 nm/oleylamine	Hexane	A Teflon well with glass cover for slow evaporation	Binary nanocrystal superlattices.
Martin *et al.*[58] (2010)	Toluene (droplet)	Au/nanospheres/3.2 to 5.2 nm/1-dodecanethiol	Hexane	A droplet of Toluene on substrate was used as a subphase.	Close packed monolayers of several mm^2 area.
Moon *et al.*[59] (2011)	Water	Polystyrene, SiO_2, pNIPAm, Ag, Au /nanospheres/ 500, 700, 45,40/PS, SiO_2, pNIPAM: no ligand, Ag, Au: PVP	Ethanol, Butanol, Isopropanol	Water contained in a petri dish was used as an interface. The nanoparticles were introduced carefully on the surface.	Close packed large area (several cm^2) films
Xiong *et al.*[60] (2013)	Water	Au and Fe_2O_3 binary mixture/nanospheres/ 5 nm and 13.4 nm/1-dodecanethiol	Toluene with dissolved PMMA	A PMMA polymer layer over water induces contact line pinning for the formation of close packed assembly.	Close packed binary lattice.
Nie *et al.*[53](2015)	Water	Au/nanosphere/50 nm/PVP	Ethanol	Nebulization of nanoparticle colloid by electrospraying on water surface (LB trough).	Several cm^2 monolayer films.
Schulz *et al.*[55]	Diethylene glycol	Au nanoparticles/spheres/25 nm/Thiolated polystyrenes (PSSH)	Toluene	A HDPE well (ID ~1.1 cm, max. vol 1.0 ml) to containing the subphase and glass cover for slow evaporation.	Several mm^2 films

*The content in the third column separated by / is in the respective order in the cases where two or more kinds of nanoparticles are included.

In the recent years, the air-liquid interfacial assembly has been successfully demonstrated also for the fabrication of more complex structures. One main advantage

of this method is the control over monolayer film formation. Thus, multi-layered structures can be obtained by a layer-by-layer approach with desired structural properties in each layer.[61] Similarly, complex multicomponent nanocrystal assemblies have also been successfully obtained by this technique[62].

1.2.3 Towards applications

The growing interest in the self-assembly of nanoparticles is driven by the application potential of assembled structures and the process of the self-assembly itself. Broadly, bottom-up construction at nanoscale with functional nanoparticles can realize complex structures that are not possible to fabricate by a top-down approach. For instance, the fabrication of self-assembled thin film of bi-functional plasmonic-photocatalytic core-shell nanoparticles is only possible using a self-assembly process. In fact, otherwise sophisticated thin-film techniques can also be replaced by self-assembly based techniques for certain applications. For an overview, **Table 1.3** outlines the known applications of nanoparticle clusters and films. In this dissertation, **Chapters 4** to **7** include results on nanoparticle clusters and films. In **Chapter 4** and **5**, where optical properties of plasmonic nanoparticle clusters and films are included from a fundamental perspective, the implications of the new results on different applications as outlined in **Table 1.3** are discussed wherever relevant. In **Chapter 6** and **7**, applications of nanoparticle films are demonstrated experimentally accompanied by theoretical insights.

Table 1.3: Summary of known applications of nanoparticle clusters and films reported in selected literature.

Application of self-assembly of colloidal nanoparticles	Nanoparticle clusters	• Broadband light harvesting[63] **(Chapter 4)** • Emulsion clustering for micro reactor[64 65] • Synthesis of Janus particles[66] • Photothermal effect[67] **(Chapter 4)** • Porous materials[68] • Sensing[69 70] • Surface-enhanced spectroscopy[71] **(Chapter 4)**
	Nanoparticle films	• Functional thin films of nanoparticles for photo catalysis, electrocatalysis, self-cleaning surface, etc.[72 73] (**Chapter 7**) • Sensing[74] **(Chapter 6)** • Surface Enhanced Spectroscopy[75] **(Chapter 5)** • Broadband Light harvesting[76] **(Chapter 5)** • Photonic crystals[77] (**Chapter 5**)

*the highlighted points in bold indicate applications on which the theoretical and experimental results in this dissertation have direct implications.

1.3 General conclusions and outlook

The importance of light-mediated processes in nanotechnology has been growing exponentially. Colloidal synthesis of photo-active nanoparticles and their self-assembly for the formation of functional interfaces is a promising area of development for large scale applications. Apart from facile synthetic procedures, colloidal synthesis is specifically advantageous for the control of nanostructure dimensions down to a very small scale (<10 nm) that is out of reach for traditional lithographic techniques. In the last decades, synthetic chemists have unravelled significant insights into the structural control of nanostructures in wet chemical procedures and such developments continue to grow at a fast pace. This progress in the development and understanding of plasmonic nanoparticles, which is an important class of photo-active nanoparticles, is quite important as the optical properties of plasmonic nanoparticles are strongly dependent on the size and shape of the nanoparticles. Most of the advancement on the synthetic front has been made on Au and Ag nanostructures. Over the years, synthetic procedures for various structures such as nanorods, nanostars, nanowires, nanotriangles, nanocubes, etc., have been established. Also, combination of two or more metals in the form of alloys, core-shell, janus structures, etc., has been shown to be possible with relatively simple procedures. While, Ag is known to have excellent plasmonic response, its chemical instability often poses difficulties in applications. Chemically stable Au, on the other hand, is expensive and its plasmonic response is damped by interband transitions. Other metals such as Cu, Al, Pd, Pt, etc., have also been explored for plasmonic applications. But meeting all the important criteria together has still been a challenge. Thus, design and synthesis of plasmonic or hybrid plasmonic nanostructures with tailored properties is critical for their application in different light-driven processes.

On the other hand, the developments on self-assembly techniques are quite complementary to the progresses on wet-chemical synthesis as ordered arrangement of colloidal nanostructures to form functional arrays or films is important in many applications. The combination of colloidal synthesis and self-assembly is a unique nano-fabrication procedure where the building blocks (*i.e*. the nanostructures) can be designed and synthesized for a specific application. This allows desired complexity and tailoring of the individual nanostructures, before they are arranged to form a bulk phase by self-assembly. Such flexibility can simply not be offered by conventional thin-film techniques. Again, self-assembly of plasmonic nanoparticles have a further advantage as these nanoparticles' interaction with light is significantly enhanced when they are arranged closely as arrays. This makes self-assembly even more important in the case of plasmonic nanoparticles for their application in light-mediated processes. Thus, colloidal synthesis of nanoparticles and their self-assembly altogether show a new direction towards the nano-fabrication of advanced functional materials.

In view of the existing literature and the important current trends, this dissertation aims to meet primarily three objectives as follows:

Objective 1: To gain fundamental insight into plasmonic noble metal nanostructures through computational electromagnetic models, going from individual nanoparticles to infinite particle assemblies, and bridging the gap between theoretical and experimental optical properties of plasmonic nanostructures.

Objective 2: To bridge the gap between theoretical and experimental optical properties of plasmonic nanostructure arrays by investigating the self-assembly of plasmonic nanoparticles and their applications.

Objective 3: To experimentally study the functionalization of metal oxide nanoparticles for self-assembly and related applications.

.

Chapter 2

Single silver-gold bimetallic plasmonic nanoparticles for light enhanced processes: alloy *vs*. core-shell nanoparticles

Based on:

Rituraj Borah,; Sammy W. Verbruggen, S. W. Silver–Gold Bimetallic Alloy versus Core–Shell Nanoparticles: Implications for Plasmonic Enhancement and Photothermal Applications. *J. Phys. Chem. C* 2020, *124* (22), 12081–12094.

Contribution:

R.B. formulated the problem, carried out the investigation, and wrote the article.

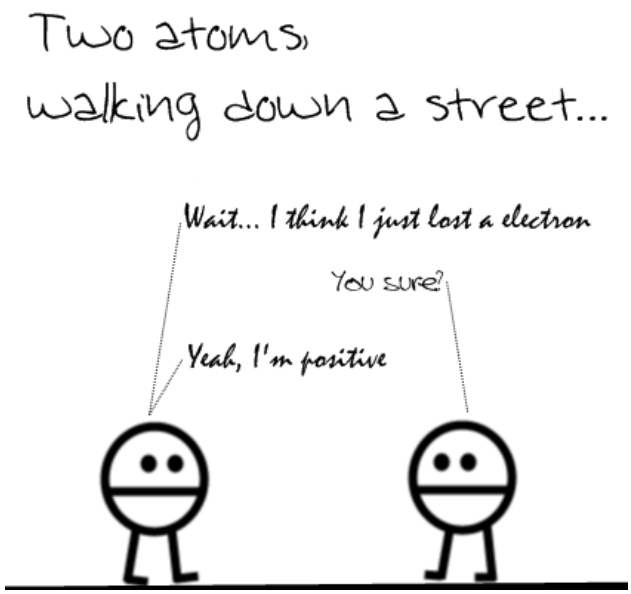

Courtesy: www. www.deviantart.com

2.1 Introduction

While the search for better plasmonic materials continues, most of plasmonic research so far has been based on Ag and Au nanostructures due to their excellent optical properties and ease of fabrication.[78] Both elements have their own benefits and shortcomings. The low interband transition energy of Au (2.3 eV) leads to energy loss by such transitions, whereas the larger energy gap of Ag (3.7 eV) does not allow this interband transition, thus implying more efficient use of incident light energy for hot electron generation.[79] Thus, while Ag experiences less interband transition loss in the visible and near-infrared (NIR) range, Au is more resistant to oxidative degradation. For comparable sizes, Ag nanostructures have a Localized Surface Plasmon Resonance (LSPR) wavelength shorter than that of Au with stronger near field enhancement. [80] [81] Also, Ag nanoparticles have narrower and more symmetric plasmon absorption bands compared to Au.[82] While starkly different in optical response as pure metal nanoparticles, bimetallic Ag-Au nanoparticles show the possibility to tune the optical features tailored to specific applications by regulating the composition and structure.[83] Both core-shell and alloy nanoparticles of Ag-Au bimetallic systems have been shown to exhibit spectral characteristics that lay between those of pure Au and Ag nanoparticles.[84] [85] [86] [87] Thus, bimetallic nanoparticles, constituted as both alloy and distinct core-shell phases, have been explored extensively, not just with Ag and Au, but also using other metals such as Cu, Pt and Pd, amongst others.[88] Considerable efforts have been devoted towards controlled synthesis of both core-shell and alloy nanoparticles with desired compositions. Generally, wet chemical synthesis of Au@Ag core-shell nanoparticles is straightforward and proceeds by the controlled reduction of an Ag precursor in the presence of Au nanoparticles, or seeds, that facilitate crystallization of Ag as a shell around the Au cores.[89] Conversely, Ag@Au core-shell nanoparticles are difficult to synthesize in a similar way. In the presence of Ag nanoparticles, Au^{3+} ions trigger a galvanic replacement reaction that results in hollow structures.[90] It has been shown that by controlling the relative kinetics of the galvanic replacement and the reduction by a reducing agent, growth of Au shells on silver nanoparticles can be achieved with smooth morphology.[91] [92] [93] While several studies have reported direct synthesis methods for Ag-Au alloy nanoparticles by co-reduction of Ag and Au precursors,[85] [94] recent work shows that traditional co-reduction methods do not necessarily lead to fully homogeneous alloys.[95] Conversion of a hybrid Ag-Au nanostructure such as core-shell nanoparticles to alloys simply by heat treatment at temperatures as low as 250°C has also been shown to be a promising and facile synthesis route.[96] [97] [98] The intrinsic aspect that sets alloy nanoparticles apart from bimetallic core-shell nanoparticles is the overlapping of energy bands of the constituting elements in the alloy. Thus, the distinct plasmonic behavior of alloy nanostructures results from the altered dielectric properties of the mixed material.[99] In contrast, core-shell nanoparticles exhibit plasmonic behavior that is a hybrid of the individual plasmon modes of the core and the shell.[100]

This intrinsic difference and the ease of switching from core-shell to alloy naturally raises a question: Which is the better plasmonic configuration, alloy or core-shell? The answer clearly is subject to the intended application. In general, gold nanoparticles are preferred over silver nanoparticles for photothermal applications due to higher stability and absorption intensity of gold.[101] [102] Espinosa *et al*. recently showed that silver nanoparticles lose their photothermal properties with time due to chemical degradation inside human mesenchymal stem cells; but with a thin Au shell surrounding the Ag core, the nanoparticles can be stabilized completely.[101] On the other hand, spectral tunability of Ag-Au alloy nanoparticles enables wider coverage of the visible light spectrum for plasmon-assisted photocatalysis.[81] Similarly, the bimetallic constitution facilitates spectral tunability for SERS-based sensing.[103] [104] While spectral tunability is an advantage, plasmonic hot carrier generation is strongly dependent on the nanoparticle composition.[79]

The objective of the current chapter is to draw a comparative picture of Au-Ag core-shell vs. alloy nanoparticles in view of different light-mediated applications. In particular, the numerical results compare the far-field and near-field properties of Ag–Au alloy, Ag@Au core–shell, and Au@Ag core–shell bimetallic plasmonic nanoparticles of both spherical and anisotropic (nanotriangle and nanorods) shapes. By studying both spherical and anisotropic (with LSPR in the near-infrared region) shapes, cases with and without interband transitions of Au can be decoupled.

In the first part of this chapter, the problem at hand is specified with a brief description of the numerical methods implemented. These numerical models are then validated with existing experimental results and the optical constants to be used for different Au–Ag alloy compositions are examined by careful comparison among different literature sources. In the results, spherical nanoparticles are treated first in terms of the far-field optical spectra and near-field optical properties. Then, anisotropic nanorods and nanotriangles are dealt with in a similar manner. Overall, the far-field optical spectra of alloy and core-shell nanoparticles are significantly different qualitatively (features and shapes), but quantitatively, the optical intensities are similar. In general, the improved chemical stability of spherical Ag nanoparticles by incorporation of Au comes with a cost of reduction in plasmonic enhancement, which is also applicable to anisotropic nanoparticles, but with a much weaker effect. The implications of the optical intensities on the photothermal properties are investigated in the conduction heat-transfer regime as the convection is too weak to have any significant effect. The increased absorption by the incorporation of Au in spherical Ag nanoparticles also results in an increased steady-state photothermal temperature. On the other hand, anisotropic nanoparticles are inherently better absorbers and hence better photothermal sources, and their photothermal properties are apparently not strongly affected by the incorporation of one metal in the other. This chapter on the optical/spectral and photothermal characteristics

of bimetallic Au–Ag alloy versus core–shell nanoparticles provides detailed physical insight for development of new taylor-made plasmonic nanostructures.

2.2 Problem specification and numerical methodology

The present study involves electromagnetic simulations of isolated bimetallic spherical and anisotropic nanoparticles with a core-shell configuration as well as an alloy configuration of Ag and Au. **Figure 2.1** shows schematics of spherical nanoparticles with corresponding Transmission Electron Microscopy (TEM) images and Energy Dispersive X-Ray (EDX) analysis maps reproduced from literature. Since scattering is low for small nanoparticles (<50 nm), the size of the nanoparticles in this chapter was fixed at 60 nm, so that both absorption and scattering are significant over the entire range of studied compositions in order to draw meaningful comparisons. Similarly, the studied nanotriangles in this chapter are of 60 nm each side and 7 nm in thickness, and the nanorods are 20 nm in diameter and 80 nm in length. The implications for smaller nanoparticles are discussed briefly in the later sections for the completeness of the results.

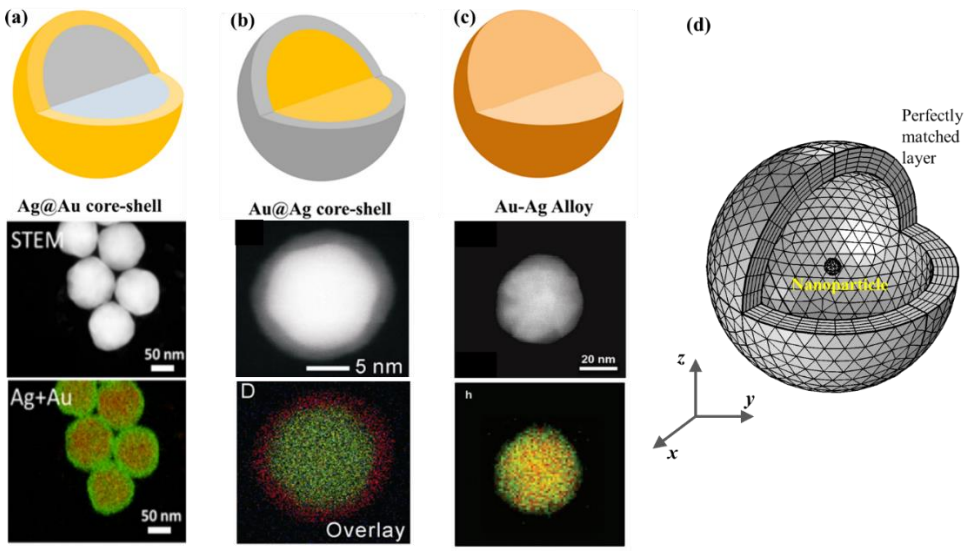

Figure 2.1 Schematic of spherical bi-metallic Au-Ag nanoparticles in different configurations: (a) Ag@Au core-shell, (b) Au@Ag core-shell and (c) alloy with their TEM images and EDX mappings taken from references[92] [89] [94]. The images were adapted and reproduced with permission from American Chemical Society (© 2017), IOP Publishing (© 2012), Wiley-VCH (© 2019).

As discussed in **Chapter 1**, the classical electromagnetic framework is quite efficient in describing optical properties of metal nanostructures. This reduces this rather huge quantum mechanical problem (*w.r.t* the computational capacities of present times) involving a sea of electrons to a much simpler electromagnetic problem based on

Maxwell's equations that involves only Newtonian mechanics. Thus, the study of any complex plasmonic nanostructures, for which analytical solutions are impractical, is possible by rigorous numerical solution of the Maxwell's equations subjected to appropriate boundary/initial conditions. In the study of plasmonic nanoparticles, it is the spectral response that is important rather than the time-varying optical response. Thus, the frequency domain form of the Maxwell's equation as given below was solved numerically in all the different cases:

$$\nabla \times (\mu_r{}^{-1} \nabla \times \boldsymbol{E}_{sc}) - k_o{}^2 (\varepsilon_r^{'} - j \frac{\sigma_e}{\omega \varepsilon_o}) \boldsymbol{E}_{sc} = 0 \tag{2.1}$$

In equation (2.1), μ_r, ε_o and σ_e denote material properties namely relative permeability, permittivity of free space and electrical conductivity respectively, and k_o denotes the wavenumber. The relative permeability in this case is assumed to 1 as the present work does not concern with magnetic response. Now, $\varepsilon_r^{'}$ is the real part of the complex relative permittivity (or dielectric constant) and importantly, σ_e is directly connected to the imaginary part of the dielectric constant as $\sigma_e = \varepsilon_r^{''} \omega$, where $\varepsilon_r^{''}$ is the imaginary part of the dielectric constant. Equation (2.1), as specified in COMSOL Multiphysics, is the representation of equation (1.13) in **Chapter 1** in terms of the scattered electric field. Thus, the problem at hand can be completely specified with only the complex dielectric constants as the input material optical properties. Also, the optical properties of different materials in literature are reported in the form of both dielectric constants and refractive index. The conversion from one to the other is simple by well-known mathematical relations. For the numerical solution of Equation (2.1), the computation domain containing the nanoparticle in the middle and the surrounding medium enclosed by a spherical shell is shown in **Figure 2.1 (d)**. In the numerical model, these model components are represented in terms of the spatial coordinates in 3D. The spherical shell, also known as the PML (perfectly matched layer), is a numerical construct that imposes a complete absorption condition on the walls of the computational domain so no electromagnetic wave is reflected back from domain boundaries. The size of the computational domain surrounded by the PML should be large enough so that the evanescent near-field around the nanostructure does not touch the domain boundaries. A spherical domain of radius 15 times the radius of the nanoparticle at the center is sufficiently large for these computations. The scattered field solution of equation (2.1) is obtained in terms of the local scattered electric field, $\boldsymbol{E}_{sc}$ in the presence of a background electric field which is the incident electromagnetic wave, $\boldsymbol{E}_{inc}$. The total field $\boldsymbol{E}_{tot}$ is the superposition of the scattered and incident electric fields, $\boldsymbol{E}_{sc}$ and $\boldsymbol{E}_{inc}$ respectively. Upon discretization of the computational domain for the boundary value problem at hand, the FEM solver COMSOL Multiphysics implemented here converts the partial differential equation(s) into a system of linear equations to solve for $\boldsymbol{E}_{sc}$ numerically. In the meshing scheme, the PML was discretized by prismatic elements, while the computational domain including the nanoparticle was discretized by tetrahedral elements. While for plain spherical nanoparticles this

discretization scheme has been proven to work well,[105] to ensure that it is also valid for the core-shell nanoparticles with a shell thickness as thin as 2.14 nm, a grid independence test was carried out. Comparing a 199043 elements grid (minimum element size: 1.08 nm, maximum element size: 25 nm) with a 594120 elements grid (minimum element size: 0.144 nm, maximum element size: 14.4 nm) in **Figure A2.4 (Appendix)** makes it clear that even distinctly different grid geometries provide excellent agreement in the spectra. This grid independence test validates the accuracy of the present numerical results.

After the solution, the magnetic field can be directly obtained from the electric field by the relationship:

$$\boldsymbol{H}_{inc} = \frac{1}{Z} k \times \boldsymbol{E}_{inc} = \sqrt{\frac{\varepsilon}{\mu}} k \times \boldsymbol{E}_{inc} \tag{2.2}$$

or,

$$\boldsymbol{H}_{inc} = \frac{1}{Z_o} \sqrt{\frac{\varepsilon_r}{\mu_r}} k \times \boldsymbol{E}_{inc} \tag{2.3}$$

Where, Z is the complex impedance of the medium/material. In equation 2.2, ε and μ are the permittivity of the medium. For the consistency with equation (2.1), the impedance is expressed in terms of relative permittivity (ε_r), relative permeability (μ_r) and free space impedance (Z_o).

From the numerical solution of the electric field and magnetic field, the optical intensities are obtained by mathematical post-processing. The energy absorbed per unit time, W_{abs}, and energy scattered per unit time, W_{sc}, by the nanoparticle are given by the following equations:

$$W_{abs} = \frac{1}{2} \iiint_V Re[\,(\sigma_e \boldsymbol{E} + j\omega \boldsymbol{D}) \cdot \boldsymbol{E}^* + j\omega \boldsymbol{B} \cdot \boldsymbol{H}^*] dV \tag{2.3}$$

$$W_{sc} = \frac{1}{2} \oiint_s Re[\,\boldsymbol{E}_{sc} \times \boldsymbol{H}_{sc}^*] \cdot \boldsymbol{n} dS \tag{2.4}$$

The volume integration and the surface integration in the above equations are applied over the volume and outer surface of the nanoparticle respectively, with $\boldsymbol{n}$ being the unit normal vector. The superscript * and $\boldsymbol{D}$ stand for complex conjugate and displacement currents respectively. The absorption cross section, σ_{abs}, and scattering cross sections, σ_{sc}, for a nanoparticle can be defined as:

$$\sigma_{abs} = \frac{W_{abs}}{I} \tag{2.5}$$

$$\sigma_{sc} = \frac{W_{sc}}{I} \tag{2.6}$$

In equation (2.5) and (2.6), I is the intensity of incident light which can be expressed in terms of the incident field as:

$$I = \frac{1}{2} c\varepsilon |\boldsymbol{E}_{inc}|^2 \tag{2.7}$$

The heat transfer analysis for the evaluation of the photothermal effect of nanoparticles in water medium requires solving the steady state form of the heat equation:[106 107]

$$\rho C_P \, \boldsymbol{U} \cdot \nabla T = k\nabla^2 T + q \tag{2.8}$$

Here, $\boldsymbol{U}$ and T are the velocity vector and temperature, respectively. While, k, ρ, and C_p denote thermal conductivity, density and specific heat capacity, respectively. In equation (2.8), q is the rate of heat generation per unit volume due to absorption obtained as in equation (2.3). For a given set of values of these parameters, the problem is essentially simplified to the numerical solution of the conduction equation, as the velocity vector U in equation (2.8) for the convective velocities of water can be neglected since convection will not be significant for an object of extremely small dimensions, also indicated by a very small Rayleigh number, *Ra*, (in the order of 10^{-14}).[108] The insignificance of the convective terms in equation (2.8) was further ascertained by comparing the results from the solution of the complete heat equation *i.e.* equation (2.8) and the conduction equation to find negligible difference in the temperature. The inspection of the isotherm contours with perfectly circular concentric patterns also suggests the absence of convective heat transfer contributions. While, the convection does not influence the development of the temperature field, the investigation of the convective velocities, however small they are, is also important for applications in micro-environments. This aspect is not included in this dissertation. A suitably large domain is chosen that imitates an infinite medium. In practice, the boundaries have to be extremely far as the temperature spatial decay scales as $1/r$, where r is the distance from the nanoparticle.[109] A spherical domain of size 2000 nm in diameter was found to be suitable as an infinite medium. The thermophysical properties were taken from relevant literature sources.[110 111] Since the thermal conductivity of water is significantly low as compared to Au and Ag, the variability of the thermal conductivity of Au and Ag with temperature does not impact the conductive heat transfer characteristics. This is also implicit from the low value of the Biot number (*Bi*) meaning the lump capacitance approximation is valid for both cases.

2.3 Results and discussion

2.3.1 Model validation

First, the present numerical model was validated using past experimental results. For alloy nanoparticles, the literature on reliable optical constant data is scent. Also, not all of the handful of such studies cover a wide spectral range or, more importantly, can reproduce experimental results accurately.[112 113] Reliance on weighted average values

as shown in some past literature is a too simplistic approach as the energy of the transitions changes with the alloy composition. [8, 86, 114] In view of the literature available on this topic, Rioux *et al*. provides a rigorous model for the optical constants of Au-Ag alloys based on critical point analysis of the band structure of Au and Ag to show close agreement between theoretical and experimental values.[99] Their model overcomes the unphysicality of the simple Drude-CP model reported by Etchegoin *et al*.[115 116] in spite of the good quality of the fit obtained. In this model the summation of Lorentzian oscillators representing individual (interband) transitions in the Drude-Lorentz model has been replaced by an integration of the joint density of states (jDOS). The two functions CP1 and CP2 defined by Rioux *et al*. for the interband transitions were obtained by the approximation of the joint density of states (jDOS). Upon defining this 10 parameter model of Ag and Au, the composition dependence of each parameter in the alloy has been modeled as a second-order polynomial giving rise to 3 sub-parameters. Thus, a 30 parameter model combined with the Drude free electron term was obtained for the composition dependent dielectric functions of Ag-Au alloy that overcomes the shortcomings of the previous literature. For the fitting of this model to experimental data, they implemented a genetic algorithm suited for multi-parameter optimization based on least square error.

Nonetheless, it is useful to compare the values reported in different studies, as presented in **Figures A1.1, A1.2 and A1.3 (Appendix).**[99 117 118 119] For Ag-Au alloys, the agreement of Nishijima *et al*. and Peña-Rodríguez *et al*. with Rioux *et al*. is considerably better than Gong *et al*. over the visible light range, **Figure A2.3**. Further assessment of these data is done by comparing computed normalized scattering cross section spectra with experimental results reported by Patskovsky *et al*. in **Figure 2.2(a)**.[120] Clearly, optical constants predicted by the theoretical model of Rioux *et al*. work well in estimating the extinction spectra of both pure as well as alloy nanoparticles. Au generally shows a better agreement than Ag using optical constants from different literature sources, as illustrated in **Figures A1.5 and A1.6 (Appendix).** When compared for 60 nm pure Ag nanoparticles, optical constants from Palik[121] appear to give large deviations from the rest, **Figure A2.5**. Also, the sharp quadrupolar peak in the absorption cross section is absent when optical constants from Palik were used. Apart from the experimental errors in the optical constants, the deviation of the computed spectral peak position from the experimental one, may also arise from the sensitivity to the surrounding environment, morphological irregularity of nanoparticles, instrumental errors and so on.[122] The effect of nanoparticle polydispersity and morphology on the optical properties is treated in detail in **Chapter 3**. In **Figure 2.2 (b)**, computed extinction spectra using the dielectric constants of Rioux *et al*. are compared with experimental UV-Vis spectra of Ag nanocubes with a thin shell of Au reported by Yang *et al*.[123] The simulated results match the experimental data both quantitatively and qualitatively. With this overview of the available literature on the optical constants of Au and Ag alloy, it is reasonable to proceed with the model of Rioux *et al*. as it estimates

the constants for any arbitrary composition and the agreement with experiments is shown to be the most satisfactory.

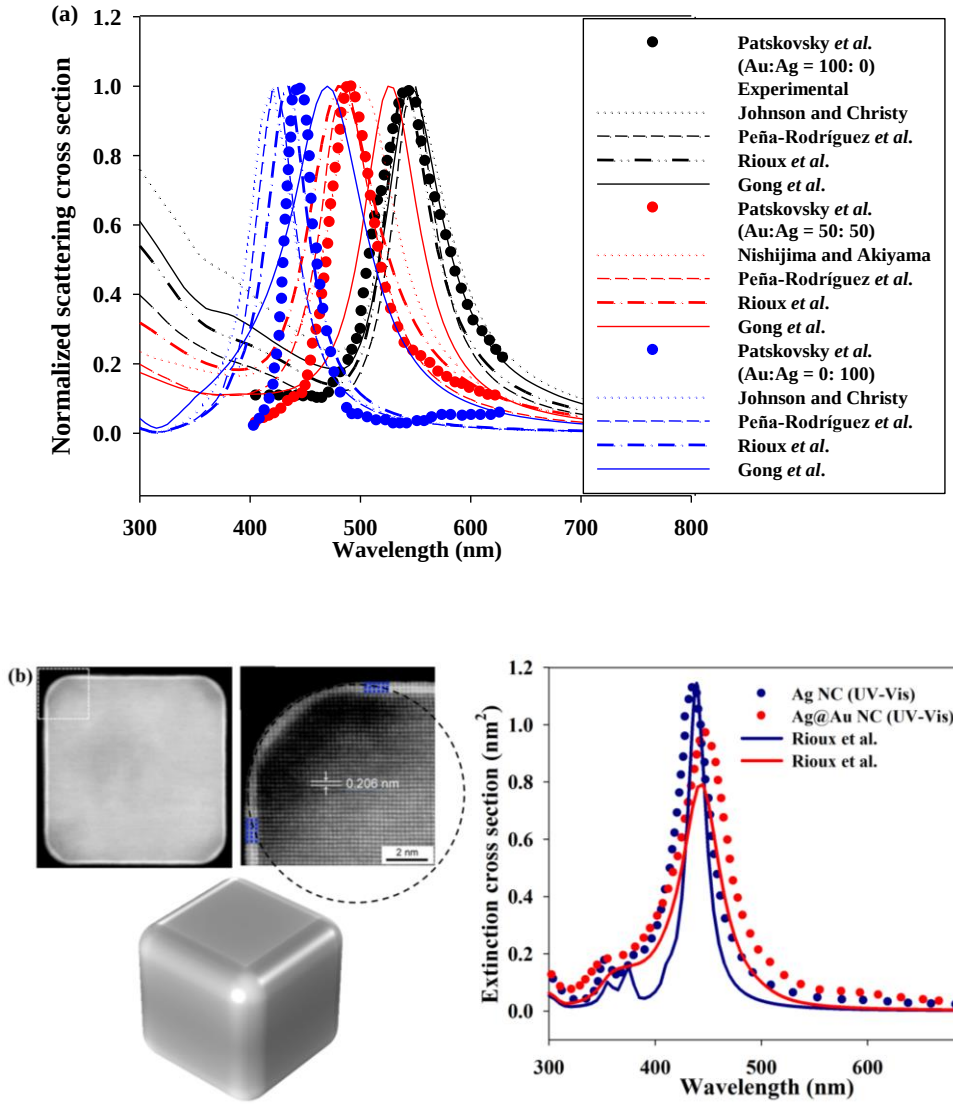

Figure 2.2 (a) Comparison of experimental scattering spectra of Patskovsky *et al*. [120] with computed spectra for optical constants from different literature sources: Johnson and Christy[124], Peña-Rodríguez *et al*.[118], Rioux *et al*.[99] and Gong *et al*.[119] for pure Au, pure Ag and 50:50 alloy Au:Ag **(**Note: Optical constants from Peña-Rodríguez *et al*. ae for 48:52 molar ratio of Au to Ag). Color codes: black for Au:Ag=100:0, red for Au:Ag=50:50, blue for Au:Ag=0:100 (b) TEM images of Ag nanocubes (AgNC) with thin Au protecting layer[123], visualization of 3D nanocube model in the present study, comparison of experimental extinction spectra with calculated spectra with constants from and Rioux *et al*. The TEM images are adapted and reproduced from American Chemical Society (© 2014).

2.3.2 Comparison of plasmonic properties: spherical nanoparticles

2.3.2.1 Absorption and scattering behavior

Before delving into bi-metallic nanoparticles, it is useful to analyze the role of the interband transitions and that of free electrons that eventually results in plasmonic excitation. As mentioned earlier, Au introduces such interband transitions, while Ag can be approximated as an entirely free electron contributor in the visible range. While the free electrons result in plasmonic excitation, with consequent radiative and non-radiative damping, the interband transition contributes to "non-plasmonic" light capture and consequent thermalization. Discriminating between both effects is possible by using a mathematical model for the wavelength dependent dielectric constants, where the parameters concerning individual effects can be selectively dropped. For this, the Drude-CP model from Etchegoin *et al.* that exploits critical point (CP) analysis[115 116] has been shown to fit well with the dielectric constants of Au reported in Johnson and Christy[124], **Figure 2.3 (a)** and **(b)**. **Figures 2.3 (c)** and **(d)** compare optical spectra obtained by separately considering the interband transitions (CP terms) and the free electrons (Drude term) in the dielectric constants with the spectrum that is obtained by considering the complete dielectric function. The position and the intensity of the LSPR is an outcome of these two effects coupled together. For a 60 nm nanosphere, the Drude free electron part in the absence of interband transitions yields plasmonic excitation that results in large radiative damping (scattering) and small non-radiative damping (absorption) at the LSPR. It is important to note that this purely plasmonic excitation is strongly dependent on nanoparticle's shape and size. In the presence of the interband transition, however, the LSPR is red-shifted significantly, and the scattering component is drastically reduced with a proportionate enhancement in the absorption. Thus for 60 nm Au nanoparticles, the absorption cross section has a significant contribution from the interband transitions. However, whether it is the dominant contributor cannot be concluded directly. In contrast, the small size of a 20 nm nanoparticle facilitates strong non-radiative damping of the plasmons contributing to the absorption cross section far more significantly than interband transitions, **Figure 2.3 (e)** and **(f)**. Thus, while in the absence of interband transitions, the plasmonic excitation is remarkably strong as evidenced by the sharp absorption and scattering peaks; taking interband transition into account results in a drastic drop of the plasmonic excitation and the consequent optical cross sections. When interband transitions are excluded, the plasmon band broadening by the retardation effect in the 60 nm nanoparticle is quite strong in contrast to the smaller 20 nm nanoparticle for which the retardation effect is much smaller. The competing effects of free electrons and interband transitions combined with the size and shape factors will also determine the optical response of Ag-Au bimetallic nanoparticles, as will be shown further.

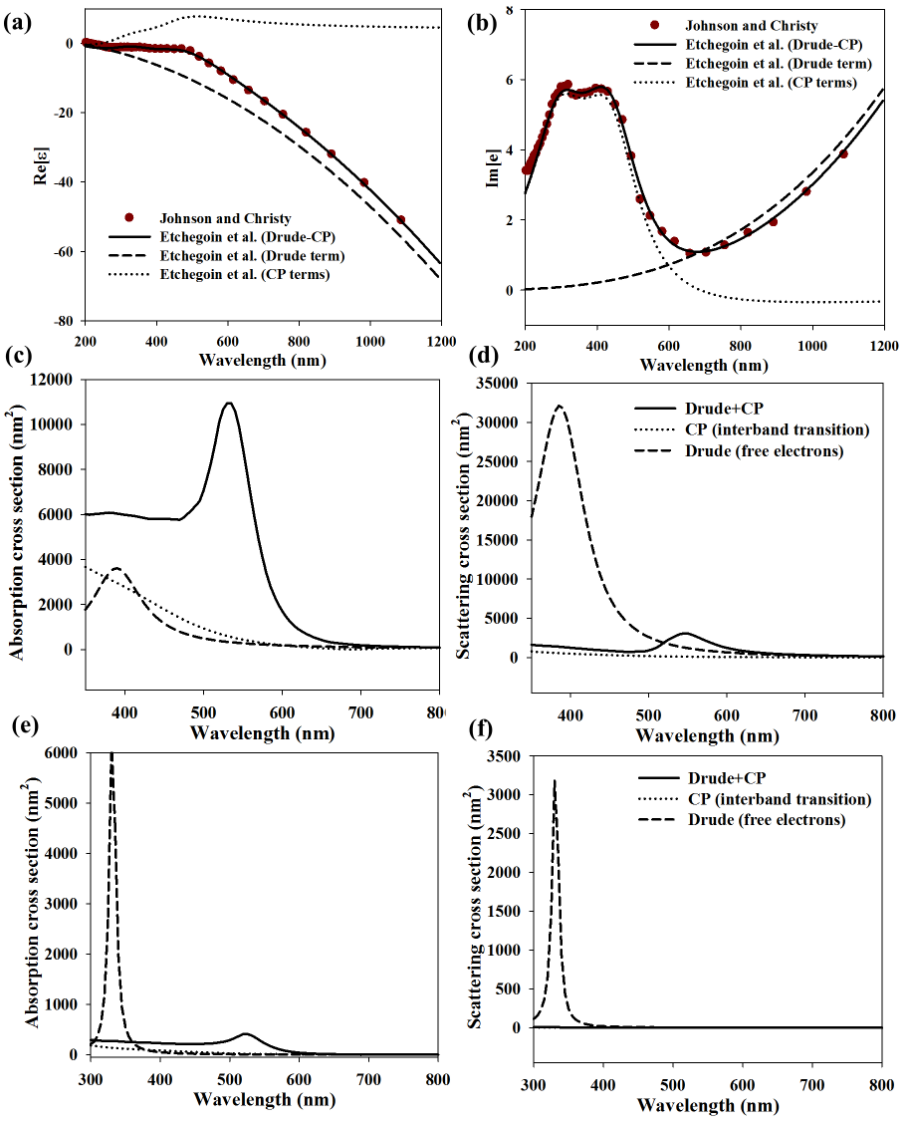

Figure 2.3 (a) Comparison of Johnson and Christy[124] dielectric constants for Au with Drude-CP model as reported by Etchegoin *et al.*[115 116]. The dielectric functions only considering the free electron Drude term and the interband transition CP term are also shown. (c, d) Comparison of absorption and scattering cross sections of a 60 nm Au nanoparticle with those calculated considering the Drude term and the CP terms alone. (e, f) Comparison of absorption and scattering cross sections of a 20 nm Au nanoparticle with those calculated considering the Drude term and the CP terms alone.

Figures 2.4 to **2.6** compare spherical Au-Ag alloy nanoparticles, Ag@Au core-shell nanoparticles, and Au@Ag core-shell nanoparticles, respectively, all of 60 nm in diameter and different compositions. The general trends of the bimetallic constitution are discussed first before delving into the specific cases. In general, incorporation of Au

in Ag nanoparticles induces a red-shift of the plasmon band accompanied by a reduction in scattering, and an increase in absorption as seen for both alloy and core-shell structures. From the discussion related to **Figure 2.3**, it can be attributed to the interband transitions in Au. Incorporation of even 20% Au significantly increases the absorption cross section for both alloy and core-shell nanoparticles accompanied by a corresponding drastic reduction in the scattering component. It is useful to note that the absorption component of the total energy extinction dissipates thermally while the scattered part is re-radiated to the surroundings. The absorption in Au is contributed by interband transitions from the *d*-band and plasmon decay, both resulting in hot carrier generation that eventually thermalize if not utilized in some other way.[125] [126] Zheng *et al*. showed that hot carriers from plasmon decay are more energetic than those from interband transitions and are able to cross a ~1 eV Schottky potential barrier more efficiently. While in silver, the interband transitions are absent.[127] The resulting optical intensities are a cumulative effect of these mechanisms (resulting in absorption) and radiative damping of the plasmons *i.e.* scattering. A 60 nm Ag nanoparticle is characterized by a strong radiative decay of plasmons (large scattering component) and weaker absorption. Incorporation of Au in Ag consequently introduces new interband transitions and reduction of the plasmonic excitation of the pure Ag state. The net result is an increase in the absorption component and a decrease in scattering. It is important here to bring up the case of 20 nm nanoparticles, for which Ag exhibits significantly higher absorption at LSPR than Au, as a consequence of strong non-radiative decay of plasmons and weak scattering limited by the small size. In this case, since the absorption is primarily from plasmon decay, incorporation of interband transitions via addition of another material would be detrimental to the absorption. Thus, incorporation of Au into (small) 20 nm Ag nanoparticles reduces the plasmonic excitation of the pure Ag state as Au introduces new interband transitions. The net result of this is reduced absorption as the dominating mechanism behind the high absorption is strongly damped. This is in contrast to 60 nm Ag nanoparticles as discussed above, for which much of plasmonic excitation is lost to radiative decay *i.e.* scattering instead of thermalization, addition of even a small amount of Au only increases the absorption cross section due to increased interband transitions and radiative losses by scattering is also reduced. The resulting decrease in the overall extinction intensity upon introduction of Au in Ag is also clear from **Figure A2.7**. Importantly, this effect of interband transition is not seen in the case of anisotropic nanoparticles as will be discussed later. The change of optical intensities with the amount of Au incorporated does not seem to follow a continuously increasing trend. While for alloy nanoparticles, it can be attributed to the changes in the optical properties with different alloy compositions; for core-shell nanoparticles, it is rather attributed to the coupling of different sizes of the core and the shell.[23]

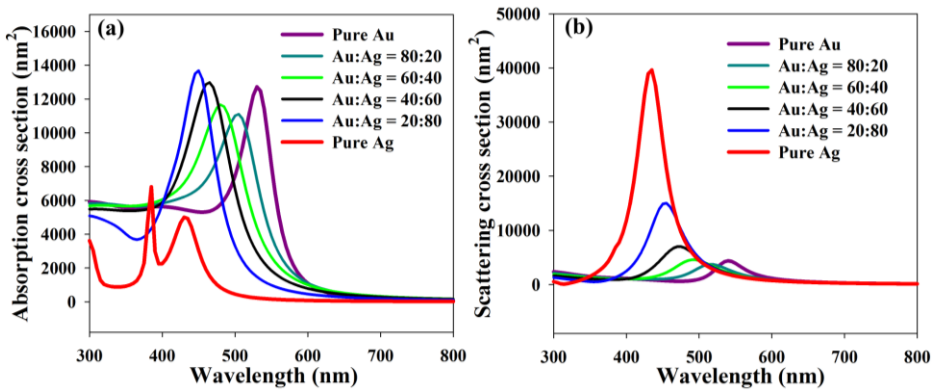

Figure 2.4 Absorption and scattering cross section of spherical Ag-Au alloy nanoparticles with varying composition and fixed size of 60 nm in diameter. From pure Ag (in red), Au is incorporated as alloy increasingly up to100% Au (in purple).

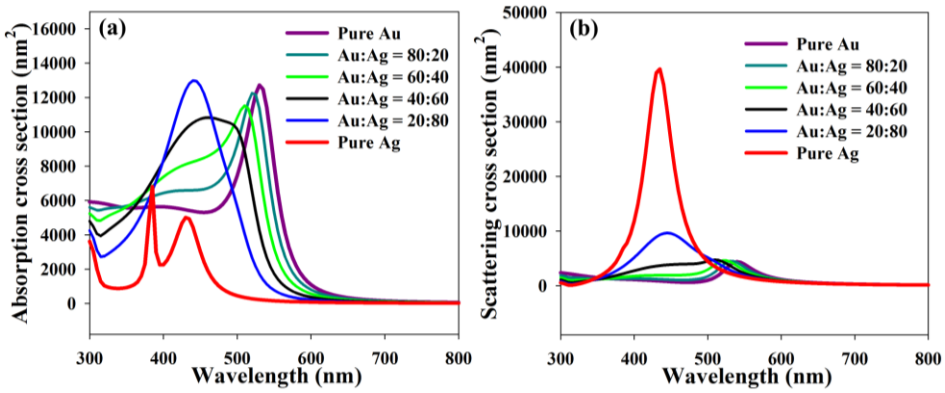

Figure 2.5 Absorption and scattering cross section of spherical Ag@Au core-shell nanoparticles with varying composition and fixed size of 60 nm in diameter. From pure Ag (in red), Au is incorporated as a shell increasingly up to 100% Au (in purple).

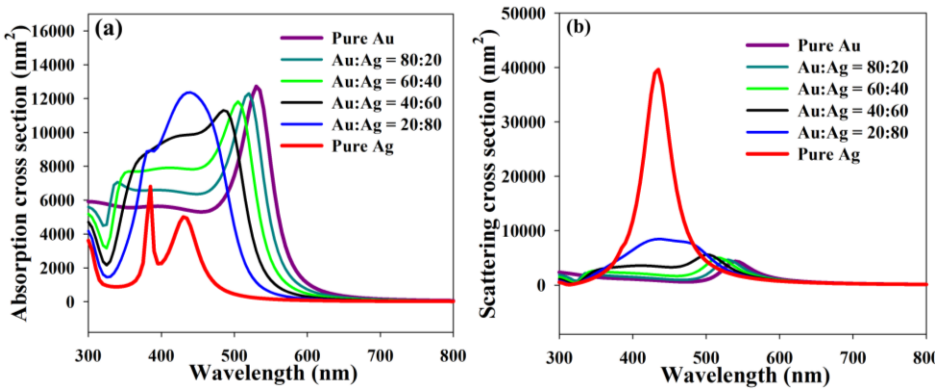

Figure 2.6 Absorption and scattering cross section of spherical Au@Ag core-shell nanoparticles with varying composition and fixed size of 60 nm in diameter. From pure Ag (in red), Au is incorporated as a core increasingly up to 100% Au (in purple).

Further comparison of alloy with core-shell constitutions shows that the optical spectra of the alloy nanoparticles, **Figure 2.4**, are generally sharper (with one characteristic LSPR peak) than the core-shell ones, **Figures 2.5** and **2.6**. Experimental evidence of these trends has been reported in literature by means of UV-Vis data of bimetallic nanoparticles.[128] [129] The asymmetric broadening of the LSPR peaks of core-shell nanoparticles with different intermediate Ag:Au compositions, shown in **Figure 2.5** and **2.6**, is also in agreement with experimental observations for Au@Ag core-shell nanoparticles.[130] [131] [132] According to the plasmon hybridization theory, the hybrid plasmon modes expressed in the asymmetrical optical spectra that are constituted by individual plasmon modes of core and shell are strongly dependent on the core and shell sizes. In contrast, an alloy nanoparticle has a homogeneous composition with its optical properties determined by the composition. Alloys exhibit optical properties that are intermediary between pure Ag and Au.[133] [134] [86] [87] It is noteworthy that recent research on Au-Ag alloy nanoparticles has shown that similar single dipolar LSPR peaks are also obtained for inhomogeneous bimetallic nanoparticles that attain a core-shell-like architecture.[94] These differences in the spectral characteristics between core-shell and alloy are well supported by experimental results.[130] It is important to note that the diffusion of one metal to the other in the core-shell nanoparticles is a spontaneous process which is extremely slow at room temperature. Thus, this slow spontaneous conversion from core-shell to alloy configuration at room temperature is not expected to become apparent in the optical properties in a short period of time (*i.e.* a few months, as for our study).

Considering the use of bimetallic nanoparticles for the tuning of the LSPR wavelength by variation of the composition, it is useful to understand the dependence of the spectral shift on the composition for both alloy and core-shell configurations. As apparent from **Figure 2.7**, the spectral shift upon introduction of Au in Ag is considerably different for all three configurations, Ag@Au, Au@Ag and alloy, taking into consideration the dipolar resonance peak. For alloy nanoparticles, the red-shift is proportionate to the amount of Au as alloy when moving from pure Ag to Au, also supported experimentally.[87] [85] For core-shell nanoparticles, the red-shift is not gradual. For instance, in **Figure 2.7 (a)**, going from 40% to 60% Au in the Ag@Au core-shell nanoparticle, the red-shift of the absorption spectra is significantly larger than that while going from 60% to 80%. Also, core-shell nanoparticles have irregular and wider spectra. For both absorption and scattering components in **Figure 2.7 (a)** and **(b)**, the LSPR peaks for the Au@Ag core-shell nanoparticle are located at longer wavelengths than those for the alloy nanoparticles of the same overall composition.

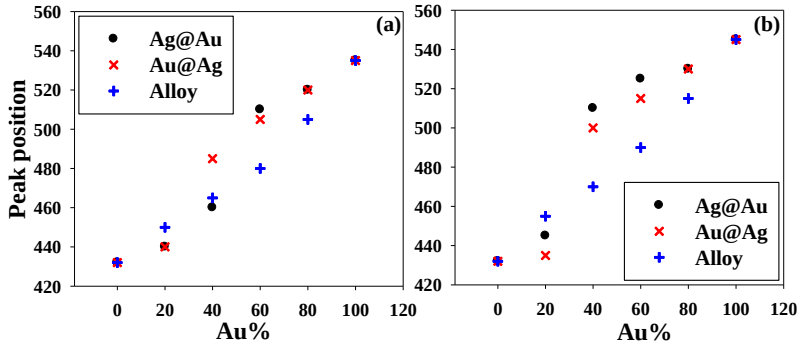

Figure 2.7 Shift of the plasmon band in the absorption (a) and scattering (b) cross section spectra with the incorporation of Au in Ag as a shell in the Ag@Au structure, as a core in the Au@Ag structure and as a homogeneously mixed element in alloy nanoparticles. The diameter of the nanoparticles is fixed at 60 nm.

2.3.2.2 Near-field enhancement

Despite the reduction of plasmon induced hot carriers upon introduction of Au in Ag, the chemical stabilization of Ag by Au is often quite useful. The result of energy consumption by interband transition is reduced plasmonic excitation. Zheng *et al*. quantified the hot carrier generation by plasmon decay separated from that by interband transitions and showed good correspondence with experiments.[125] Generally, for spherical nanoparticles, the near-field enhancement is always weaker in gold nanospheres than in silver due to the contribution by interband transitions, **Figure A2.8**. **Figure 2.8** shows that addition of 20% Au in Ag also significantly weakens the near-field enhancement around the thus-obtained alloy or core-shell nanoparticles when compared to the near-field enhancement of pure Ag nanoparticles. The alloy nanoparticle does not seem to be significantly different from the core-shell particle in terms of the attenuation of the near-field enhancement. Thus, stabilization of Ag nanoparticles in atmospheric environment by adding a thin Au shell has strong consequences with respect to the plasmonic properties.

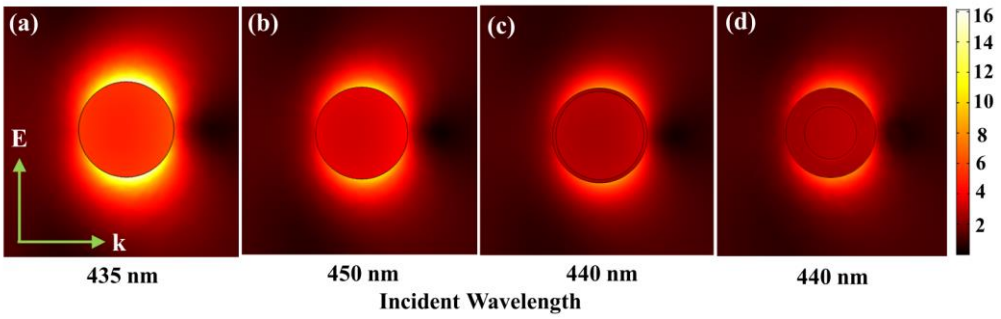

Figure 2.8 The near-field enhancement with respect to the incident field around (a) pure Ag nanoparticle compared with 20% Au (rest 80% Ag) nanoparticles of (b) alloy (c)

Ag@Au core-shell (d) Au@Ag core-shell configuration. The near-field enhancement is shown at their dipolar plasmon resonance. The diameter of the nanoparticles is 60 nm.

Importantly, while 20% Au addition significantly alters both the spectral and near-field characteristics of a pure Ag nanoparticle, the thin shell of Au around Ag is only 2.14 nm in that case. Since the preceding comparisons were for a constant 60 nm nanoparticle size, incorporation of Au as the shell material entails a corresponding reduction of the Ag core size. To show that the drastic reduction in scattering and increase in absorption is not due to the shrinking of the core, optical spectra for a 60 nm Ag nanoparticle with a 2.14 nm Au shell around it (total diameter: 64.28 nm) were evaluated, **Figure 2.9**. Clearly, the effect of a slightly shrunk core is insignificant compared to that of the addition of the thin shell, resulting in strong changes in the optical spectra for a 2.14 nm thick shell surrounding a 60 nm particle core. The resulting optical response of the 64.28 nm nanoparticle differs from that of the 60 nm nanoparticle primarily due to the overall enlargement of the particle size.

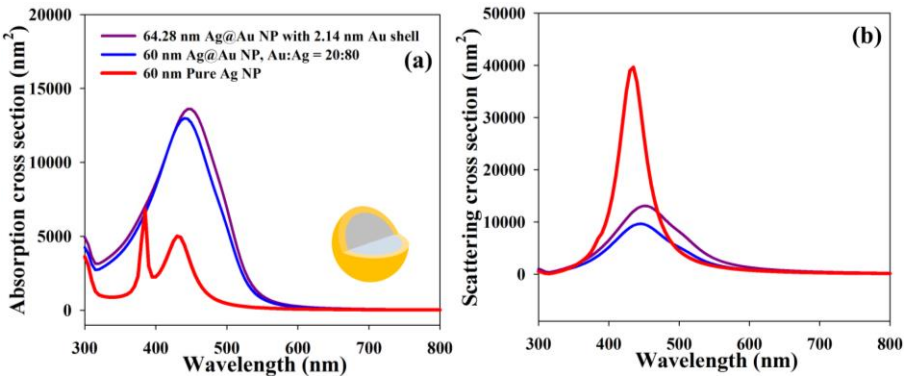

Figure 2.9 The Effect of extra 2.14 nm thick Au shell on a 60 nm Ag nanoparticle compared to Au incorporation as shell (2.14) in a 60 nm nanoparticle for 20:80 molar composition of Au:Ag. (a) Absorption cross section (b) scattering cross section. An Au shell around Ag is grown to protect Ag against oxidation.

2.3.3 Comparison of optical properties: anisotropic nanoparticles

2.3.3.1 Absorption and scattering behavior

The discussion so far concerned nanospheres for which the LSPR wavelength falls in the wavelength range in which Au exhibits interband transitions. Thus, it is interesting to investigate the effect of bimetallic constitutions when the LSPR is in the near-infrared or infrared region where Au does not have interband transitions. In that regard, synthesis of anisotropic nanoparticles such as nanorods and nanotriangles, which exhibit LSPR in the near-infrared and infrared region, has seen considerable progress in the recent years.[135]

In continuation of the preceding discussion, the effect of incorporating 20% Au in an anisotropic Ag nanoparticle as a shell or alloy on the optical response is shown in **Figure 2.10** and **Figure 2.11**. In this case the LSPR is located in the near-infrared and infrared region. The effect of addition of 20% Au in Ag in this case is interestingly different from the behavior that was observed in the case of nanospheres. In the absence of interband transitions, the absorption with the consequent thermalization is only caused by non-radiative plasmon decay. Thus, apart from the obvious shift in plasmon band position, both the LSPR absorption and scattering intensities of an Ag nanorod, **Figure 2.10**, and a nanotriangle, **Figure 2.11**, are not significantly altered after adding an Au shell. Interestingly, when Au is added as alloy, the absorption is reduced a bit more, but the scattering is reduced dramatically. This rather strong change in the plasmonic response can be attributed to the altered band structure of the alloy. Experiments comparing the plasmonic hot carrier generation in Ag@Au core-shell and alloy nanorods or nanotriangles would thus provide useful insight into these observations. Regarding the spectral shift, while the Ag@Au core-shell nanorods and nanotriangles both exhibit a blue shift, in the case of alloying only the nanotriangles shows a blue shift but not the alloy nanorods. At this point it is also important to inspect the effect of corner sharpness changes even by addition of a thin layer, which for nanotriangles is obviously significant. **Figure 2.12 (a)** and **(b)** show that layer by layer uniform enlargement of nanotriangles smoothens the corners leading to a blue shift of the spectra accompanied by an increase in both absorption and scattering. While for nanorods, adding uniform layers results in a usual red-shift due to elongation and remains unaffected by any edge effect, **Figure 2.12 (c, d)**. Thus, it is clear that the edge smoothening also has a significant role in the LSPR blue shift of nanotriangles when 20% Au is added as shell or alloy.

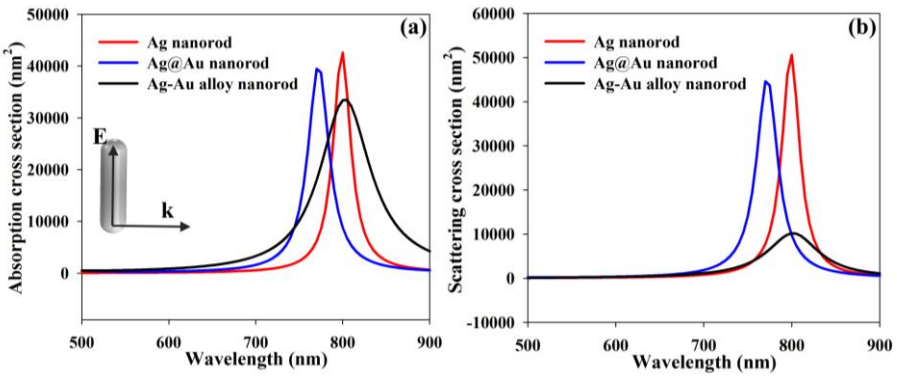

Figure 2.10 The Effect of addition of 20% Au to an Ag nanorod (diameter: 20 nm, aspect ratio: 4) as a thin shell or alloy: (a) absorption cross section (b) scattering cross section.

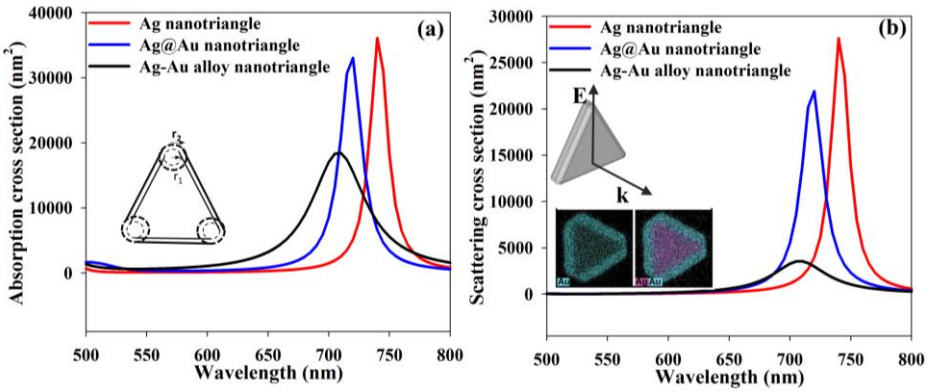

Figure 2.11 The effect of addition of 20% Au to an Ag nanotriangle (diameter: 20 nm, aspect ratio: 4) as a thin shell or alloy: (a) absorption cross section (b) scattering cross section. Inset (a): schematic of a core-shell nanotriangle with corner curvatures r_1 and r_2 for the core and shell respectively. Inset (b): EDX mapping of synthesized Ag@Au core-shell nanotriangle reproduced from reference[93] with permission from Wiley-VCH (© 2019).

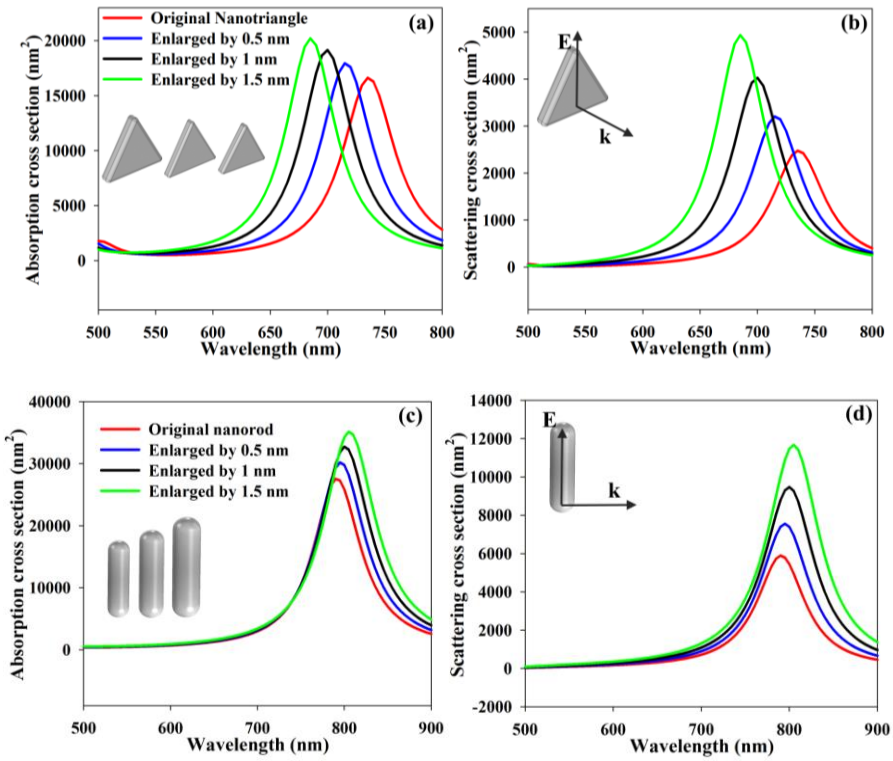

Figure 2.12 The effect of enlargement of Au:Ag = 20:80 alloy nanotriangle (a, b) and nanorod (c, d) by uniform addition of thin layers of the same 20:80 composition ratio that reduces corner sharpness. Original Nanotriangle size: ~60 nm each side, 7 nm thick; original nanorod size: 20 nm in diameter, 80 nm in length.

It is also useful to look further into the effect of alloying of nanorods and nanotriangles for a fixed volume, hereby excluding the geometrical effects. **Figure 2.13** and **Figure 2.14** compare the optical spectra of alloy nanorods and nanotriangles, respectively, showing that Ag exhibits both stronger absorption and scattering than Au in the infrared region. Interestingly, absorption and scattering intensities of alloy nanoparticles are lower than for both pure Ag and Au nanoparticles. Although the LSPR is red shifted for Au, the shift has been found to be rather discontinuous when moving from pure Ag to Au.

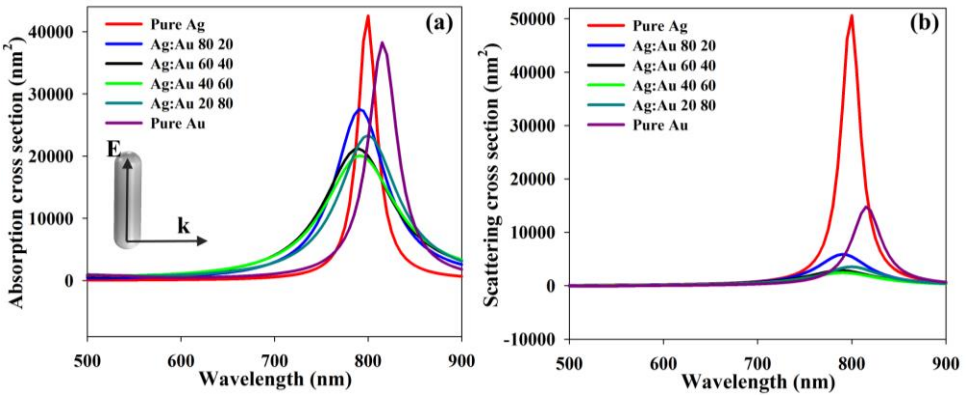

Figure 2.13 Absorption (a) and scattering (b) cross section of Ag-Au alloy nanorods with varying composition and fixed size of diameter 20 nm and aspect ratio 4. From pure Ag (in red), Au is incorporated as a shell increasingly up to 100% Au (in purple).

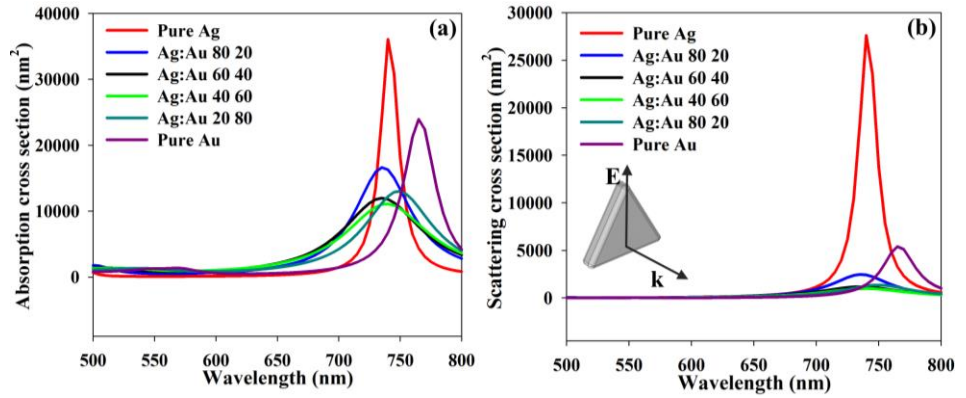

Figure 2.14 Absorption (a) and scattering (b) cross section of Ag-Au alloy nanotriangles with varying composition and fixed size of ~60 nm side length and 7 nm thickness. From pure Ag (in red), Au is incorporated as a shell increasingly up to 100% Au (in purple).

The above analysis for anisotropic nanoparticles considered the direction of the incident electric field to be parallel with the nanorod's axis *i.e.*, longitudinal, while for nanotriangles the electric field is parallel to the triangular plane as shown in the Figures

above. However, the alignment of the nanorods and nanotriangles with respect to the incident light has a significant effect on the plasmonic enhancement.[136] [137] While the plasmonic enhancement is dependent on the incident angle, the dependence is proportional. For instance, slight deviations from the longitudinal excitation for nanorods also results in slight reduction in the LSPR excitation.[137] Similarly, for nanotriangles, all the other orientations with respect to the incident irradiation results in strong plasmonic extinction and the intensity is still more than half of that for the most favorable orientation.[136] Most importantly, the LSPR wavelength is independent of the orientation in all cases. Thus, the above results are still applicable in all different situations with varying degree of optical intensity. Also, certain applications of anisotropic nanoparticles particularly exploit this orientation dependence of plasmonic response.[137] [138] [139] It is useful to state that the problem of orientation dependence in other applications can be solved with nanostars which exhibit strong LSPR at large wavelength irrespective of the orientation.[140]

2.3.3.2 Near-field enhancement

In the absence of interband transition of Au, it is also interesting to observe the near-field characteristics of nanorods and nanotriangles in **Figure 2.15**. Clearly, due to edge effects, nanotriangles have significantly stronger near-field enhancement than nanorods. Overall, the optical cross sections in **Figure 2.10** and **2.11** suggest that more light is captured by the nanorod. However, the sharper corners of the nanotriangles facilitates concentration of light over a smaller volume resulting in stronger near-field enhancement. So, one must also keep in mind that uniform layer by layer enlargement of the nanorod will also strongly affect the near-field enhancement.

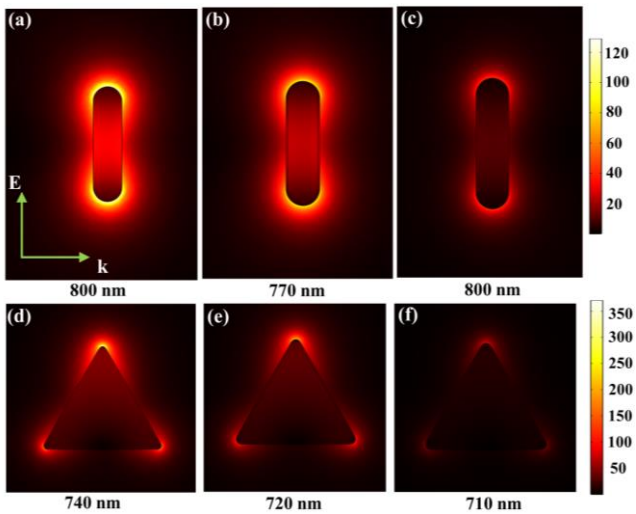

Figure 2.15 Near-field enhancement with respect to the incident radiation around nanorods of (a) pure Ag (b) Ag@Au (c) Alloy, and nanotriangles of (d) pure Ag (e) Ag@Au (f) Alloy. In correspondence to **Figure 2.10** and **2.11**, the Ag@Au core-shell

(b,e) and alloy (c,f) nanoparticles are modifications of pure Ag nanoparticles in (a, d) by addition of 20% Au as a thin shell or as alloy. Nanotriangle size: ~60 nm each side, 7 nm thick; nanorod size: 20 nm in diameter, 80 nm in length. The near-field enhancement is shown at the plasmon resonance.

It is clear from **Figure 2.15** that the near-field enhancement is weakened by the addition of an Au shell to both the Ag nanorods and Ag nanotriangles, implying an overall reduction in plasmonic near-field enhancement. Importantly, addition of Au as alloy weakens the near-field enhancement to a much greater extent. This along with the corresponding strong decrease in the scattering component (**Figure 2.10** and **2.11**) confirms a significant reduction in plasmonic excitation.

2.3.4 Photothermal effect of spherical and anisotropic nanoparticles

For spherical nanoparticles, while weakening of the optical response (scattering and near-field enhancement) is generally disadvantageous for applications such as SERS, plasmonic phototcatalysis, *etc*.; the enhanced absorption and reduction of scattering due to Au incorporation is certainly advantageous for photothermal applications.[141] Likewise, the widening of the spectra in the case of core-shell nanoparticles provides a wider window of usable wavelengths. A large 60 nm Ag nanoparticle with high radiative loss and low absorption does not reach a maximum photothermal steady state temperature as high as a pure Au nanoparticle of the same size. In **Figure 2.16**, the steady state temperature of 45.5^{o}C of a 60 nm silver nanoparticle, **Figure 2.16 (a)**, is increased by ~70% to 77.2^{o}C simply by growing a thin gold shell of 2.14 nm around it, **Figure 2.16 (b)**. Also, the LSPR band does not exhibit any significant shift, **Figure 2.9**. The steady-state temperature for a 60 nm Au nanoparticle under the same irradiation conditions is low (47.5^{o}C at 435 nm), unless the incident wavelength is changed to 530 nm in order to achieve a similar steady-state temperature of 78^{o}C, **Figure 2.16 (c, d)**. Such enhancement of the photothermal response of Ag nanoparticles by the incorporation of a thin shell of Au is an interesting aspect as the chemical stabilization of Ag nanoparticles by Au in cellular environments has already been demonstrated.[101] It is worth noting that the nanoparticle size is an important factor. For a smaller size of 20 nm, Ag exhibits strong non-radiative decay of plasmons that leads to considerably higher absorption than Au (for which the absorption also has contributions from interband transitions). In this case, the temperature of Ag will be considerably higher than that of Au. Also, incorporation of Au in Ag in this case will reduce the absorption of pure Ag. However, due to smaller absolute absorption for smaller nanoparticles, the steady state temperature is in turn significantly lower than for large nanoparticles.

The disadvantages of silver nanoparticles in the context of biomedical applications are the LSPR being in the high frequency region and small bandwidth (FWHM ~ 9 nm). Thus, LSPR tuning of silver nanostructures over a wide wavelength range is important for their utility in different applications. This is enabled by anisotropic nanoparticles

such as nanoplates, nanotriangles, nanorods, *etc*.[135] For comparable sizes, **Figure 2.17** shows that Ag nanotriangles and nanorods have significantly higher photothermal steady state temperature than spherical nanoparticles. Since the same color map scale of **Figure 2.16** is used in **Figure 2.17**, one can see a much larger >75 ^{o}C region around the nanotriangle and nanorod. The implications of addition of Au as alloy or a protective layer around Ag nanorods and nanotriangles on the absorption are evident from **Figure 2.10** and **Figure 2.11**. A thin protective layer of Au does not reduce the absorption greatly, implying a similar steady state temperature. On the other hand, addition as alloy results in a greater reduction in the absorption. However, the peak broadening provides a wider window of useful wavelengths.

Using the renewed physical insights from the present study, one may envisage the possibility of chemically stabilizing such anisotropic Ag nanostructures with a thin gold shell.[101] In view of the present trends of bimetallic nanoparticle synthesis and photothermal applications of nanoparticles, the present results open up new avenues for further investigation.

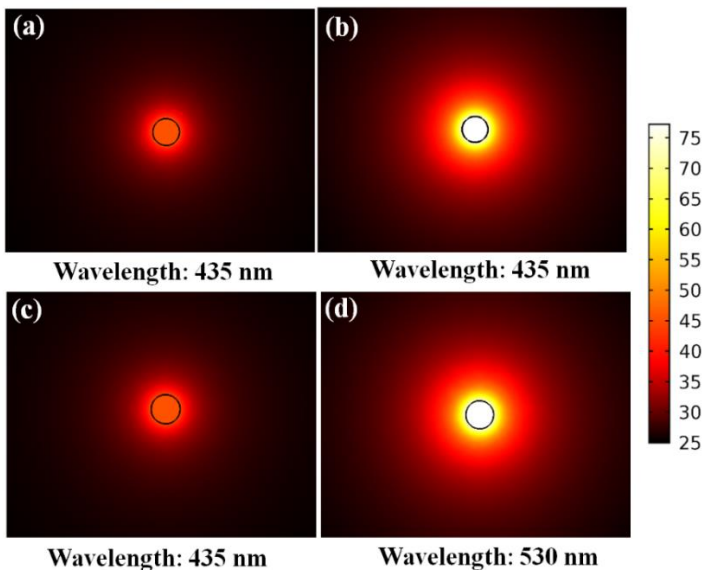

Figure 2.16 Steady state temperatures (^{o}C) of (a) 60 nm Ag nanoparticle (b) 60 nm Ag nanoparticle with a 2.14 nm thin Au shell (c,d) 60 nm Au nanoparticle. The intensity of incident radiation is 1 mW/μm^2 for all the cases. The nanoparticles are embedded in an infinite water medium. In Figure (a), (b) and (d), the nanoparticles are excited at their plasmon resonance wavelength.

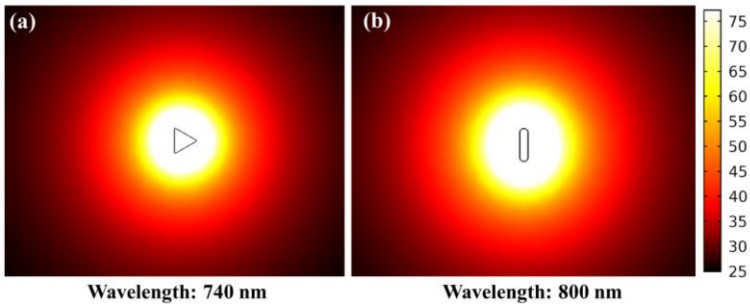

Figure 2.17 Steady state temperatures (°C) of an Ag nanotriangle (~60 nm each side, 7 nm thick) and Ag nanorod (20 nm in diameter, 80 nm in length). The intensity of incident radiation is 1 mW/μm^2 for all the cases. Note: the temperature scale is defined with respect to nanospheres in **Figure 2.16** to make a visual comparison between the two. The nanoparticles are embedded in an infinite water medium. The nanoparticles are excited at their plasmon resonance wavelength.

2.4 Conclusions

Chapter 2 compares the plasmonic properties of isolated Ag−Au alloy and core−shell bimetallic nanoparticles and shows the implications on the optical response and the photothermal effect. The comparison includes spherical as well as anisotropic nanoparticles (rods and triangles) to cover structures with and without the contribution of interband transitions of Au, respectively. The effects of bimetallic constitutions for these two cases are starkly different from each other. For 60 nm spherical nanoparticles, the LSPR band shifts proportionally with changing composition in the alloy constitution, while for the core−shell constitution, the shift does not follow a proportional trend. Alloy nanoparticles display sharper spectral features with a characteristic LSPR peak in contrast to the widened spectra of core−shell nanoparticles. Incorporation of even a small amount of Au (20%) in Ag (60 nm nanoparticles) as alloy or core−shell significantly increases the absorption cross section due to interband transitions in Au. On the other hand, scattering is drastically reduced by the incorporation of the same amount of Au. Apart from the spectral characteristics, the optical intensities of alloy and core−shell nanoparticles are comparable. For nanorods and nanotriangles of comparable sizes, incorporation of Au in Ag results in a reduction of both absorption and scattering. While this reduction is not significant in a core−shell constitution, absorption and scattering are reduced dramatically in alloy nanoparticles. In particular, the drastic reduction in scattering suggests changes in the band structure by alloying that are detrimental to plasmonic enhancement. Also, unlike spherical particles, there is not a proportionate shift of the LSPR band with changing alloy composition from pure Ag to pure Au. In addition, for nanotriangles, the edge effects play a pivotal role in the LSPR intensity and spectral position. Thus, in anisotropic nanoparticles, geometrical effects become crucial while determining the plasmonic response. An increase in absorption and peak widening due to incorporation of Au in

Ag improves the photothermal characteristics of 60 nm nanoparticles. In general, nanotriangles and nanorods are significantly better for photothermal applications due to much higher absorption in their optimal orientation. Addition of a thin Au shell around Ag nanorods or nanotriangles does not reduce the absorption intensities; thus, the photothermal effect is well retained, while the Ag structure is chemically stabilized. At room temperature, the diffusion of one metal from the shell towards the core (and from core to shell) is a slow kinetic process. Thus, the stabilization of Ag nanoparticles by a Au shell is a practical strategy for low temperature applications. However, the kinetics can be accelerated at elevated temperature (for instance already at 200 ^{o}C) to obtain homogeneous alloy nanostructures in just a few hours. In anisotropic nanoparticles, an accompanying effect of the alloying at elevated temperature is the reshaping of the nanoparticles towards a more energetically favourable geometry *i.e.* sphere. As the optical properties of the alloy and core-shell nanoparticles have been shown to be different in many aspects, thermal conversion of a nanoparticle's configuration can be useful depending on the application. The numerical results and the obtained physical insights show interesting possibilities for the use and adaptation of bimetallic nanoparticles according to the required function.

Chapter 3

Bridging the gap between theoretical and experimental optical properties of colloidal plasmonic nanoparticles

Based on:

Rituraj Borah, Sammy W. Verbruggen, Effect of Size Distribution, Skewness and Roughness on the Optical Properties of Colloidal Plasmonic Nanoparticles. Colloids and Surfaces A: Physicochemical and Engineering Aspects 2022, 640, 128521.

Contribution:

R.B. formulated the problem, carried out the investigation, and wrote the article.

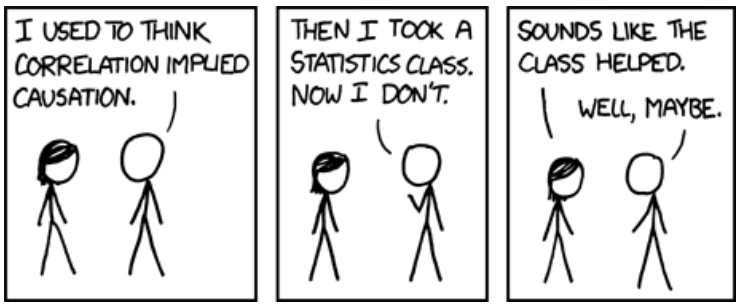

Courtesy: www.xkcd.com

3.1 Introduction

In **Chapter 2**, the optical properties of single plasmonic nanoparticles were compared elucidating the effect of nanoparticle bimetallic composition (Au and Ag), shape and size, and the implications in different applications. In general, the application potential of plasmonic nanostructures in various areas such as solar energy harvesting[142], photocatalysis[143], sensing[144], photothermal therapy[145 146], *etc.*, have been growing over the years. Thus, well-controlled (with respect to dimensions) as well as economical fabrication of such nanostructures has emerged as an important field of research. For this reason, wet chemical synthesis of plasmonic nanoparticles has gained considerable attention over the years[147 148]. The wet chemical route is advantageous due to its facile procedures, cost-effectiveness and high throughput when compared to clean-room fabrication techniques (**also see Chapter 1**) [149 150]. The wet-chemical route can even facilitate synthesis of nanoclusters of a few hundreds of atoms or less,[151 152] prompting considerable efforts towards the development of large-scale continuous reactor systems for the synthesis of nanoparticles.[153 154] A major challenge in the wet chemical route, however, is the lack of full control over all nanoparticle characteristics. Due to the inherent randomness in the nucleation and the subsequent growth process, the size distribution of the nanoparticles is difficult to control.[155] Polydispersity is also a challenge in the synthesis of nanoparticles by pulsed laser ablation.[156 157] Thus, the minimization of the polydispersity is one of the important challenges of this synthesis route as highly polydisperse or irregular particles pose difficulties for further applications.[158 159 160] It is widely believed and accepted that the optical properties of plasmonic nanoparticles strongly depend on the size, polydispersity and non-uniformity of the particle morphology.[161 162 163 164]It has also been shown that polydispersity has a strong effect on the total energy absorption and thus, on the plasmonic heat generation.[165] However, after a detailed analysis, the effect of particle polydispersity seems to be rather speculative as no study can be found elucidating the exact role of the size distribution in determining the optical spectral response.

For nanoparticles of 10 nm in size or bigger, the classical electromagnetic theory can be used with sufficient accuracy to calculate the optical properties, as the quantum size effects are not significant enough for larger clusters. This requires an accurate set of optical constants determined experimentally for the given metal or the alloy composition with similar crystal properties. The high optical absorbance obtained at the resonance frequency in the optical spectra of the nanoparticles, resulting from Localized Surface Plasmon Resonance (LSPR), is captured quite realistically by solving Maxwell's equations as elaborated in the previous chapters. While for Au, the agreement between the calculated spectra of single isolated nanoparticles using classical Mie theory, which is the analytical solution of the Maxwell's equations, and the experimental spectra of the colloidal nanoparticles is often satisfactory[166], the same is not at all the case for Ag. Often, the simulated optical spectra are blue shifted by over

10 nm, accompanied by a much smaller bandwidth (characterized by the full width half maximum, FWHM) relative to the experimental spectra.[167] Apart from the general deviation of the theoretical LSPR wavelength and bandwidth from the experimental ones, the higher order resonance peaks are not visible in the optical spectra of large Ag nanoparticles (>100 nm).[149] Apart from the uncertainty in the experimental optical constants used in the calculations and polydispersity, morphological irregularities are also often stated to explain the large difference between experimental spectra and theoretical optical spectra obtained for perfectly spherical and monodisperse nanoparticles.[168] [169] The Ag optical data from two highly cited literature sources, Palik[170] and Johnson and Christy[171], show significant differences in the imaginary part of the refractive index, possibly due to the difference in the sample preparation methods that determine the crystallinity. Generally, such discrepancies are observed across various experimental data sets.[172] [173] [174] [158] Thus, with many possible factors such as particle crystallinity, morphology, particle size distribution, *etc*., to be playing their roles, it is our aim to understand the effects of these factors independently from one another. Further insight into these factors will be helpful in the accurate prediction of the optical response of Ag nanostructures in general, which is in turn important for many application scenarios. For instance, the determination of the particle size of plasmonic nanoparticles from their optical spectra is promising for fast characterization. Commonly used dynamic light scattering (DLS) measurements are influenced by morphological features (surface ligand, nanoparticle shape, roughness, *etc*.), deconvolution models for the correlation function and so on.[176] In contrast, determination of the particle size from the plasmonic response can be fast and straightforward[177], and has been studied in some previous works, especially for Au.[178] [179] In order to obtain detailed information about a population of colloidal nanoparticles, the effect of all the different factors discussed above needs to be understood individually.

In **Chapter 3**, first, the effect of the particle size distribution is established explicitly by varying the standard deviation for a constant mean size while keeping the total number of atoms constant in a normal distribution. This is achieved by a bottom-up statistical approach to generate nanoparticle size distributions from a fixed number of atoms as described in **section 3.2**. Apart from the plasmon band broadening and the expression of the multipolar modes, this also clarifies the effect of a higher volume contribution by larger nanoparticles for sizes larger than the mean. As shown in **section 3.3.1**, the effect of polydispersity increases with increasing mean size. However, the position of the plasmon band is not altered significantly by the polydispersity as long as the mean is constant. Then, a normal distribution was converted to a log-normal distribution to study the effect of the skewness in the distribution. Overall, for the range of polydispersity observed in colloidal synthesis, the difference between normal and log-normal distributions in terms of the optical spectra appears little significant. Further, the effects of surface roughness and different optical constants from different literature are

compared, **section 3.3.2**. The comparisons of theoretical results with experimental results are validated by reproducing the simple experiments of Bastús *et al*.[149] to synthesize Ag nanoparticles, and their optical spectra were recorded for comparison. Also, the most suitable set of optical data for Ag is identified. Finally in **section 3.3.3**, the implication of the present results in the DLS intensity distribution measurements is discussed. It is shown that the intensity distribution band inherently shift towards larger values as the polydispersity increases while keeping the mean fixed. For plasmonic nanoparticles, since the mean is determined by the LSPR position, the DLS can indicate how polydisperse the population is. In short, it is clear that the mean particle size is the most important parameter, while the standard deviation and skewness only exert a minor influence on the prediction of theoretical spectra with appropriate optical constants.

3.2 Theoretical formulation

3.2.1 Mie analytical solution for a distribution of nanoparticles

Normal distribution. The size distributions based on constant mass were obtained by a bottom-up approach with considerations to the colloidal reduction methods. Although a top-down synthesis method like pulsed laser ablation is conceptually completely different, the particle size distribution still follows similar trends owing to the universality of the central limit theorem.[180] For the calculations based on a fixed atomic population, the number of Ag atoms was fixed at 1.5055 x 10^{19} (based on 1 ml of 25 millimolar $AgNO_3$ Ag-precursor solution) according to a generic one-pot synthesis procedure reported by Bastús *et al*.[149] The reproducibility of the protocol was tested experimentally in order to ensure the validity of the theoretical assumptions and comparisons. Thus, this method emulates colloidal plasmonic nanoparticles of concentrations at the Beer Lambert limit in contrast to previous works on planar particle arrangement on a substrate.[181] [182] The formation of polydisperse nanoparticles from the given number of metal atoms is described in the schematic in **Figure 3.1 (a)**. Regardless of the reducing agent and accompanying stabilizing reagents, the basic principle of the formation of the nanoparticles remains the same. For a fixed number of atoms, desired mean and standard deviation, the particle size distribution was obtained by an iterative procedure as shown in the flow chart in **Figure 3.1 (b)**. In the second step of this iterative process, the assumption for the number of nanoparticles has to be made judiciously towards obtaining a number of atoms as close to the initial fixed number as possible. For comparisons, the mean particle diameter was fixed and the standard deviation was varied which also obviously results in variation in the total number of nanoparticles. Assuming a normal distribution of the particle size, the Gaussian function for the particle size distribution for a fixed number of particles is:

$$\boldsymbol{f}(D) = \frac{N_{Total}}{\sqrt{2\pi}\sigma} exp\left[-\frac{1}{2}\left(\frac{\boldsymbol{D}-\mu}{\sigma}\right)^2\right] \tag{3.1}$$

The number of nanoparticles, *n*, in a predefined frequency interval, Δd, can thus be obtained from equation (1) as:

$$\boldsymbol{n} = \Delta d \times f(D)$$

or

$$\boldsymbol{n} = \Delta d \times \frac{N_{Total}}{\sqrt{2\pi}\sigma} exp\left[-\frac{1}{2}\left(\frac{\boldsymbol{D}-\mu}{\sigma}\right)^2\right] \quad (3.2)$$

In equation (3.1) and (3.2), N_{Total} is the number of total nanoparticles, D is the mean diameter in the interval, μ is the mean diameter of all the nanoparticles and, σ is the standard deviation. The particle size distribution for specific values of μ and σ was obtained by the iterative procedure. The number of particles, N_{Total} had to be first estimated with different values until the total number of atoms calculated from the entire distribution of nanoparticles with the given μ and σ results in 1.5055 x 10^{19}. The molar mass and density values used in the calculations were 107.9 g/mole and 10.5 g/cm^3.

Log normal distribution. In order to study the effect of asymmetry in the distribution leading to skewness, the number of particles in a frequency interval, Δd in a lognormal distribution can be given as:

$$\boldsymbol{n} = \Delta d \times \boldsymbol{f}(D) \quad (3.3)$$

where, $\boldsymbol{f}(D) = \frac{N_{Total}}{D\sqrt{2\pi}\sigma^*} exp\left[-\frac{1}{2}\left(\frac{ln\,\boldsymbol{D}-\mu^*}{\sigma}\right)^2\right]$ is the lognormal distribution function. The location parameter μ^* and shape parameter σ^* in equation (3.3) are related to the mean and standard deviation of the distribution as:

$$\sigma^* = \sqrt{ln\left(\frac{\sigma^2}{e^{2\boldsymbol{ln}\mu}} + 1\right)} \quad (3.4)$$

$$\mu^* = ln\,\mu - \frac{\sigma^{*2}}{2} \quad (3.5)$$

Thus, for a given mean diameter, μ and standard deviation, σ, defined for a standard normal distribution, a corresponding lognormal distribution can be obtained whose skewness can be given as:

$$Sk = (exp(\sigma^{*\boldsymbol{2}}) + 2)\sqrt{exp(\sigma^{*\boldsymbol{2}}) - 1} \quad (3.6)$$

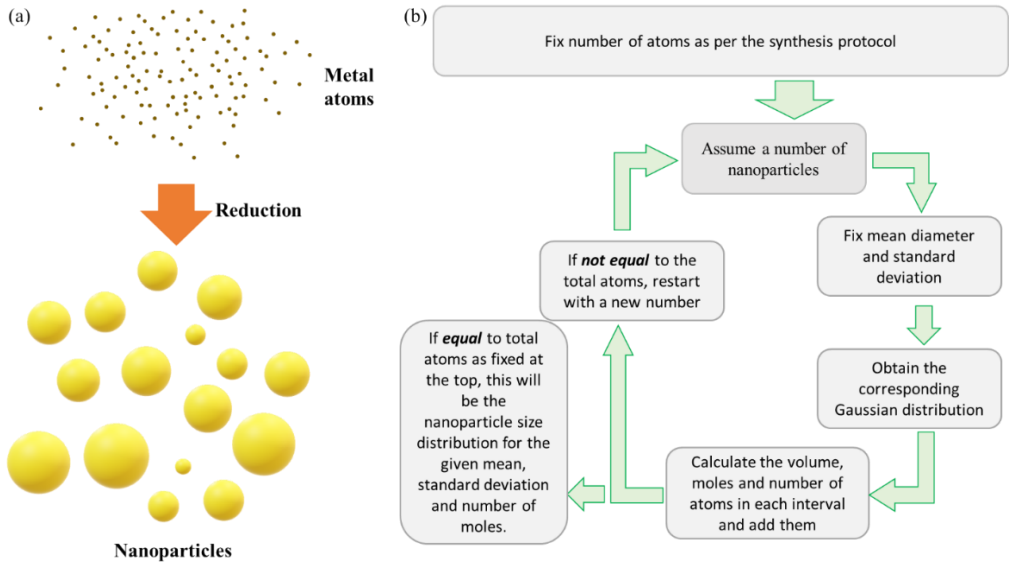

Figure 3.1 (a) Schematic describing the general colloidal synthesis route for plasmonic nanoparticles: formation of a distribution of nanoparticles from fixed number of atoms. (b) Flow chart describing how, for a fixed mole of atoms, distributions of different mean and standard deviation were obtained assuming a normal distribution. In this work, the total number of atoms is fixed at 1.5055 x 10^{19} (based on 1 ml of 25 millimolar $AgNO_3$ Ag-precursor solution).

Mie theory calculations for a distribution of nanoparticles. Upon obtaining the particle size distribution, the optical cross sections were calculated using a MATLAB script (see **Appendix A2**). The underlying equations for the optical cross sections from the Mie analytical solution for spherical nanoparticles are well-known and are documented elsewhere.[177 183] For each set of wavelengths, corresponding complex optical constants of Ag and refractive index of the medium (n = 1.33 for water), the extinction, absorption and scattering cross sections were computed for the entire particle population normally distributed about the mean size as shown in **Figure A3.1 (appendix)**. Specifically, the optical cross section computed for a given size (interval size: 0.1 nm) was multiplied with the number (frequency) of the nanoparticles in that interval/bin. Finally, the optical cross sections for each frequency interval were added in order to obtain the total optical cross sections for a specific wavelength. The important condition for the addition of the optical intensities of individual particles of the distribution is that the concentrations should be at the Beer-lambert limit so that the intensity is proportional to the concentration.

3.2.2 Calculation of optical response by numerical simulation

In order to investigate the effect of particle surface morphology, Maxwell's equations were solved for the scattered field in the frequency domain. The computational details can be found in **section 2.2** of **Chapter 2**.

3.2.3 Experimental section

For the verification of the literature data used herein, Ag nanoparticles were also synthesized experimentally following the protocol of Bastús *et al.*[149] All the chemicals were obtained from Sigma Aldrich. Briefly, 1 ml of 25 mM $AgNO_3$ solution was injected into a 100 ml boiling solution of sodium citrate (5 mM) and tannic acid under vigorous stirring. The concentration of tannic acid determines the mean size of the nanoparticles. Thus, for 15 nm and 36 nm nanoparticles, the tannic acid concentrations were 0.1 and 1 mM respectively. After the addition of $AgNO_3$, the solution was left to boil for another 10 minutes before rapid cooling in an ice bath. The nanoparticles were then centrifuged twice at 10000 rpm for 30 minutes for the removal of excessive citrate and tannic acid. The UV-Vis spectra of the nanoparticle colloids were recorded by a Shimadzu spectrophotometer (UV 2600).

3.3 Results and discussion

3.3.1 Effect of particle size distribution for fixed number of Ag atoms

When the number of Ag atoms is fixed, for instance when starting from 1 mL of 25 mM $AgNO_3$ as in the experimental synthesis protocol by Bastús *et al.*[149], different scenarios for the particle size distribution can be envisaged. The mean size and the standard deviation are commonly reported as the primary indicative parameters of the distribution. Thus, naturally, a normal distribution is the first basic assumption for the size distribution. The deviations from the normal distribution will be discussed in the later sections. It is expected that with increasing standard deviation, *i.e*. widening of the size distribution, the collective plasmon band should also be widened as the contribution of the smaller and larger nanoparticles relative to the mean size will enhance the extinction intensities around the LSPR of the mean. In **Figure 3.3** to **3.5**, the effect of standard deviation in the normal distribution of nanoparticles with mean sizes of 20, 60 and 100 nm is delineated. It is important to note that a symmetric size distribution around a mean implies that the volume distribution will be skewed towards right due to bigger sizes. Since the optical absorption and scattering increase with increasing size, one may expect that with increasing standard deviation, the LSPR might red-shift due to a more dominant effect by the larger nanoparticles. However, it is clear that for 20 and 60 nm particles as the mean, the effect of standard deviation, in general, does not have a significant effect on the LSPR band position (**Figure 3.2** and **3.3**). Even a standard deviation of 33% of the mean did not result in any significant shift of the LSPR although the volume distribution is strongly shifted towards particles of larger

diameters. While the band position remains constant, the effect of the standard deviation on the right-HWHM (half width at half maximum) is relatively stronger for the 60 nm average distributions than 20 nm average distributions (**Figure 3.2** and **3.3**). The LSPR position is determined by the condition at which the generalized multipolar resonance frequency, $\omega_l'(D)$, for a diameter D and different Eigenmodes $\{l = 1, 2\ldots\}$, is equal to the incident wave frequency. Derkachova and Kolwas show by numerically solving the dispersion relation for sodium that $\omega_l'(D)$ decreases first slowly (starting from radius: 0 nm) leading to a faster fall up to >200 nm, then to eventually become slow again.[184] This trend is particularly strong for the dipolar mode *i.e.*, $l = 1$ which is also the strongest in the extinction spectrum of smaller nanoparticles. Thus, it is expected that the effect of size distribution on the optical spectra will also exhibit an increasing trend with increasing mean size at least up to 150 nm. For the 60 nm mean, the quadrupolar mode ($l = 2$) is also quite visible as a shoulder on the left side of the spectra that gets smeared out with increasing polydispersity (**Figure 3.3**).

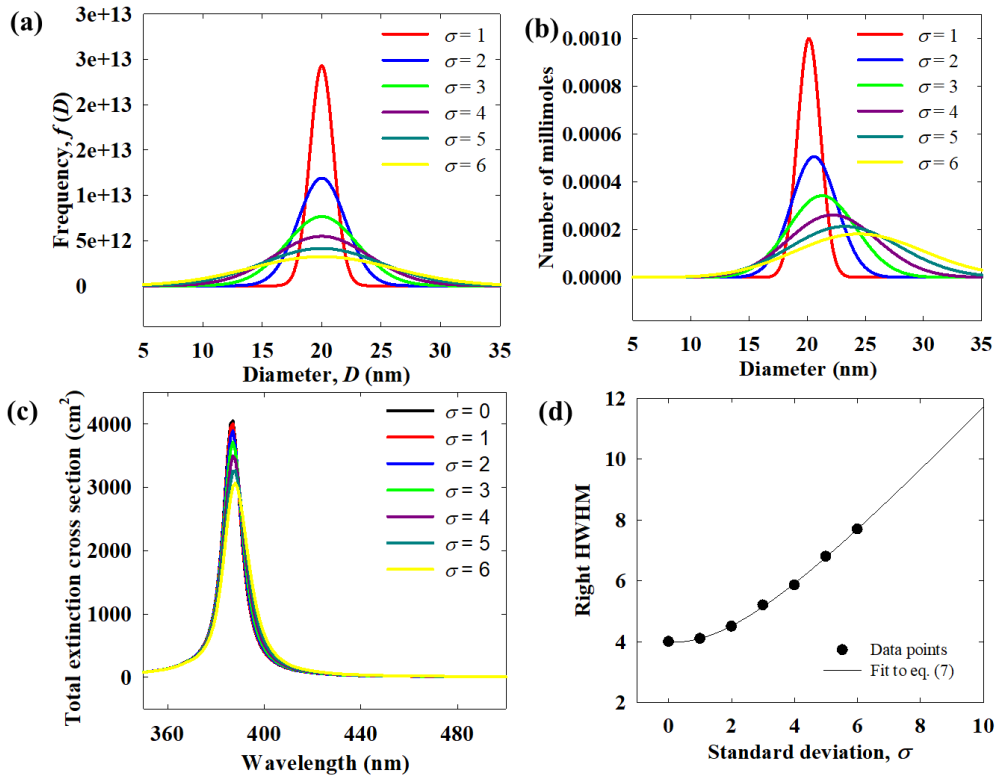

Figure 3.2 For a constant number of Ag atoms (0.025 mmol): (a) nanoparticle size distribution from equation (3.1) for a fixed mean, μ = 20 nm and different values of standard deviation, σ (b) corresponding atomic distribution with respect to size (c) total extinction cross section of the entire population of nanoparticles for μ = 20 nm and different values of σ (in cm^2) (d) variation of the right-half width half maximum (HWHM) with increasing σ, fitted to the empirical correlation in eq. (3.7).

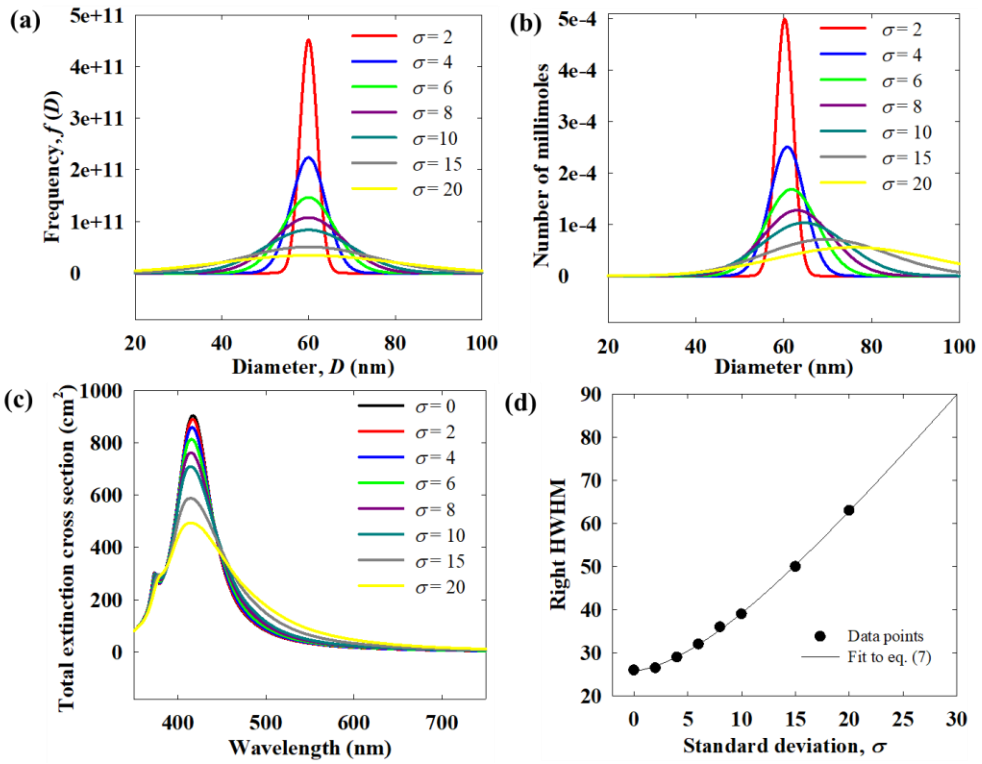

Figure 3.3 For a constant number of Ag atoms (0.025 mmol): (a) nanoparticle size distribution from equation (3.1) for a fixed mean, μ = 60 nm and different values of standard deviation, σ (b) corresponding atomic distribution with respect to size (c) total extinction cross section of the entire population of nanoparticles for μ = 60 nm and different values of σ (in cm^2) (d) variation of the right half width half maximum (HWHM) with increasing σ, fitted to the empirical correlation in eq. (3.7).

For particles with a large mean diameter (for example, 100 nm, **Figure 3.4**), apart from the stronger size dependence of the LSPR shift in this size regime, the peaks due to both the dipolar (Eigenmode, l = 1) and the quadrupolar modes (l = 2) are strong.[185] Thus, for the distributions with 100 nm as the mean, both these bands play a role in the overall spectra of the population. The effect of both of these aspects is clear from **Figure 3.4**, where the LSPR band is significantly influenced by the increasing standard deviation, thus resulting in weakening of both the modes to eventually become indistinguishable from one another. Importantly, similarities between these theoretical spectra and experimental ones also strongly depend on the correctness of the optical constants used in the theoretical simulations, which will be discussed in later sections. It is convenient to correlate the dependence of the LSPR bandwidth (right HWHM) and the polydispersity, σ for the prediction of the band-broadening for any standard deviation. An exponential growth function describes this relation empirically but with sufficient

accuracy as given in equation (3.7), where Y_{HWHM} and σ are right-HWHM and standard deviation:

$$Y_{HWHM} = c_o + c_1 x + c_2 \exp(c_3\sigma + c_4) \quad (3.7)$$

In equation (3.7), c_o, c_1, c_2 and c_4 are empirical coefficients. The statistical parameters in **Table A2.1** show that the correlation fits the data points satisfactorily.

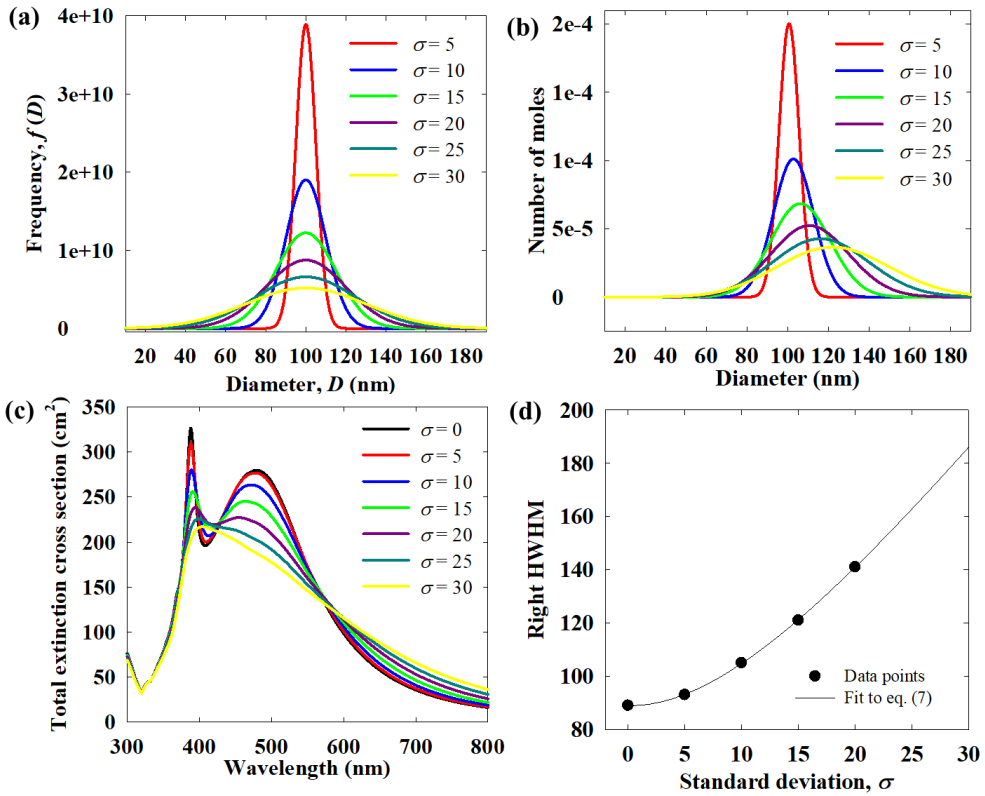

Figure 3.4 For a constant number of Ag atoms (0.025 millimole): (a) nanoparticle size distribution from equation (3.1) for a fixed mean, μ = 100 nm and different values of standard deviation, σ (b) corresponding atomic distribution with respect to size (c) total extinction cross section of the entire population of nanoparticles for μ = 100 nm and different values of σ (in cm^2) (d) variation of the right-half width half maximum (HWHM) with increasing σ, fitted to the empirical correlation in eq. (3.7).

While the normal distribution is a simple approximation, it is known that in reality the formation of smaller clusters is actually favored, which leads to a skewness towards smaller sizes.[186187] As per the coagulation model of Smoluchowski[188], this is a self-preserving size distribution during Brownian coagulation which takes place at the nucleation and crystallization stages of nanoparticle formation. In an alternative modeling approach, Kriss *et al*. showed that distribution of growth time determines the skewed lognormal distribution.[189] For smaller standard deviations, a normal and a

lognormal distribution are indistinguishable. However, with increasing polydispersity, a lognormal distribution tends to be progressively skewed with respect to a normal distribution with the same mean and standard deviation. As shown in **Figure 3.5** (a), for a mean of 60 nm, the distribution with a standard deviation of 20 nm is significantly skewed towards left with a skewness factor, *Sk*, of 1.037 in contrast to standard deviation of 10 (*Sk* = 0.5045). It is, however, clear that even for highly polydisperse particles, the spectra for the lognormal distribution do not deviate much from those for the normal distribution. Even for a standard deviation of 33.3% of the mean, which can be described as a highly polydisperse population in view of the present literature on nanoparticle synthesis, the spectrum is only slightly blue shifted for the lognormal distribution. In case of the protocol reported by Bastús *et al.*, a normal distribution is thus a satisfactory assumption as the standard deviations are too low to have any significant effect. It is clear that in general under typical colloidal synthesis conditions, the mean size is the most important statistical parameter that determines the optical spectrum, while polydispersity and skewness only have a minor influence.

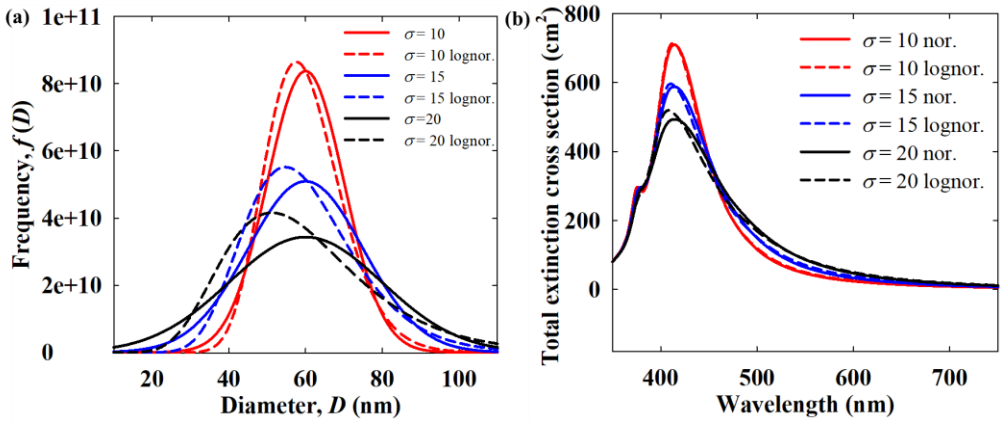

Figure 3.5 For a fixed NP mean diameter of 60 nm: (a) comparison between normal distribution from equation (3.1) and lognormal particle size distribution from equation (3.3) for three different values of σ (solid lines: normal distribution, dashed line: lognormal distribution) (b) corresponding total extinction spectra comparing normal and lognormal distributions. The skewness factor for the three values of σ = 10, 15, 20 are 0.5045, 0.7656 and 1.037 respectively. (all calculations were done for a constant number of Ag atoms: 0.025 millimoles)

3.3.2 The deviation of theoretical predictions from experimental optical spectra

Another important aspect that determines the optical properties of plasmonic nanoparticles is the surface morphology, as the optical response is strongly influenced by the surface characteristics as well as the shape.[190] González *et al*. demonstrated moderately pronounced effect of the surface morphology on the optical spectra for small Ag nanoparticles from 4 to 13 nm in size.[191] In the larger particles synthesized by Bastús

et al.[149], high morphological irregularities can be observed (**Figure A3.2**) and it is possible that they might be playing a significant role in shaping the optical spectra. In order to study the effect of such surface irregularities, the optical spectrum of an ideal spherical nanoparticle was compared to that of roughened nanoparticles, **Figure 3.6**. Although the artificially induced roughness resulted in a reduction of the total volume and irregularities on the surface, the LSPR position and the bandwidth do not change enough to drastically alter the spectrum. This is in line with the work of Linge *et al.*, defining plasmon length for Au nanoparticles as the determining parameter of a plasmonic particle's optical spectrum, which is a characteristic path length of plasmon oscillation independent of the surface morphology.[192] Also, for larger sizes, the edge effects become progressively less important.

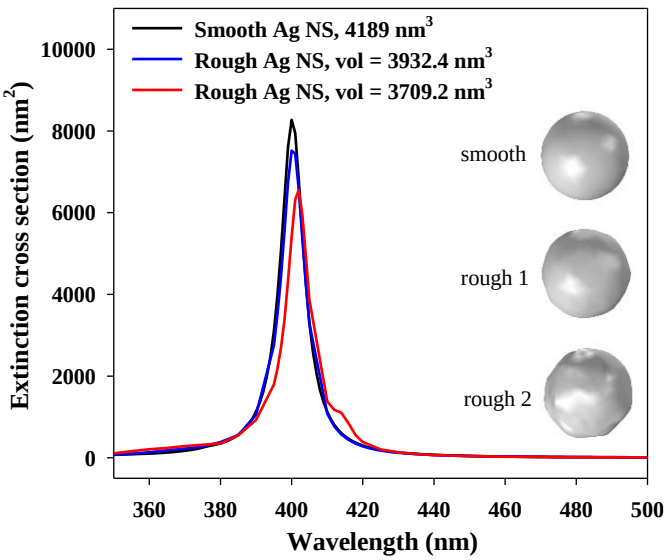

Figure 3.6 The effect of surface roughness on the optical spectra of Ag nanoparticles of diameter ~ 36 nm. The surface roughness was artificially introduced. (Optical constants used from Johnson and Christy)

The preceding discussion has shown that, in general, for a fixed mean particle size, varying polydispersity of the population as well as moderate surface irregularities do not influence the optical spectra significantly. In view of the reference synthesis protocol for this study by Bastús *et al.*[149], the polydispersity, skewness and morphological irregularities are low enough to not be playing any significant role in spectral characteristics. Thus, the remaining primary factor deemed to be determining the spectral characteristics in theoretical simulations is the suitability of the optical constants used in the calculations. While the optical constants data from Johnson and Christy[171] work well for Au nanoparticles (**Figure A3.3**), there is a major mismatch for Ag nanoparticles, **Figure 3.7 (a)** and **A3.4**. In comparison, the constants from Rioux *et al.*[174] and Palik[170] have a much better performance in predicting the LSPR position. The

complete spectra in **Figure 3.7 (b)** show that, except from Palik[170], all the other optical data result in much narrower spectral bands as well as differences in the LSPR position. Since the recent data from Wu *et al.*[173] were obtained for monocrystalline Ag thin films, this difference is consistent with the existence of several crystalline domains even in colloidal Ag clusters of sizes as small as 5 nm.[193] Hence, the important factor here appears to be the degree of polycrystallinity or defects in the thin film samples that were used for the measurement of the optical constants, and the extent to which this matches the crystallinity of the colloidal Ag nanoparticles. From the comparisons done in this work, the optical constants from Palik[170] seem to be the best for the theoretical prediction of the optical spectra both in terms of LSPR position and plasmon bandwidth, **Figure 3.7 (c)** and **(d).** For the legitimization of the comparisons reported in **Figure 3.7**, the experiments of Bastús *et al.*[149] were successfully reproduced for this chapter and excellent agreement was obtained with the UV-Vis absorbance spectra for both a target average diameter of ~15 and ~36 nm. The standard deviation calculated out of a population of 500 nanoparticles remains within 15% of the diameter as they claim that the protocol yields highly monodisperse particles. Clearly, for 15 nm average size, the standard deviation has almost no effect on the spectra, while also for 36 nm average size, even a standard deviation much larger than their reported value does not lead to any significant qualitative/quantitative change, which is fully consistent with our findings above.

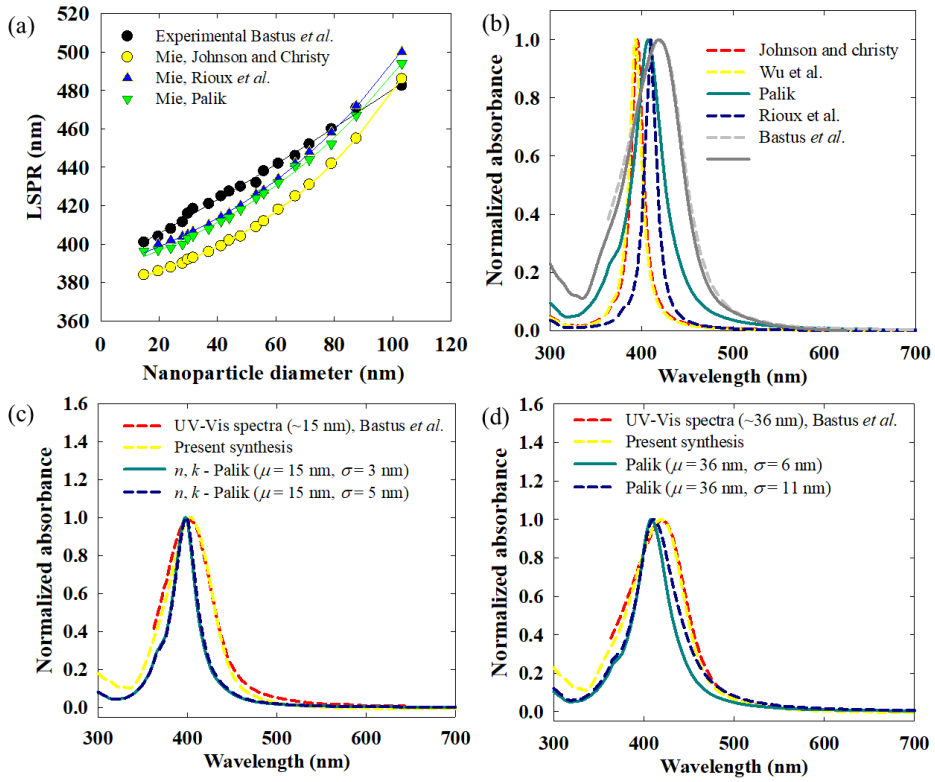

Figure 3.7 (a) Comparison between experimental (Bastús *et al*.) and theoretical LSPR wavelength of single Ag nanoparticles of different sizes (only mean). The data is fitted to the empirical correlation in equation (3.7) for the convenience in representation. (b) Comparison of different optical data from literature in terms of Mie spectra of a 36 nm nanoparticle. (c, d) Comparison of Bastús *et al*. data and present experimental spectra with theoretical spectra computed using Palik's optical data for 15 and 36 nm mean diameter.

In **Figure 3.4 (c)**, for 100 nm mean distributions, the quadrupolar mode is quite strong in spectra calculated using the optical data of Johnson and Christy[171], especially for narrow distributions. It also smears the dipolar band in wider distributions, resulting in a plateauing effect between the quadrupolar and the dipolar peaks. However, in experimental spectra, such high intensities for the multipolar modes are not observed.[149] [194] In **Figure 3.8**, the expression of the dipolar and quadrupolar modes by the Palik's optical data in spectra obtained by applying Mie theory, is shown for different standard deviations and a constant mean diameter of 100 nm. While the quadrupolar mode is relatively weaker in this case, the experimental spectra still show a much weaker intensity resulting only in a faint shoulder. For wider distributions, the plateauing of the spectra due to equal intensities of the two modes is also quite strong. Nonetheless, the familiarity between the experimental spectra for 103.1 ± 7.4 particles and theoretical particles assert the overall suitability of Palik's data.

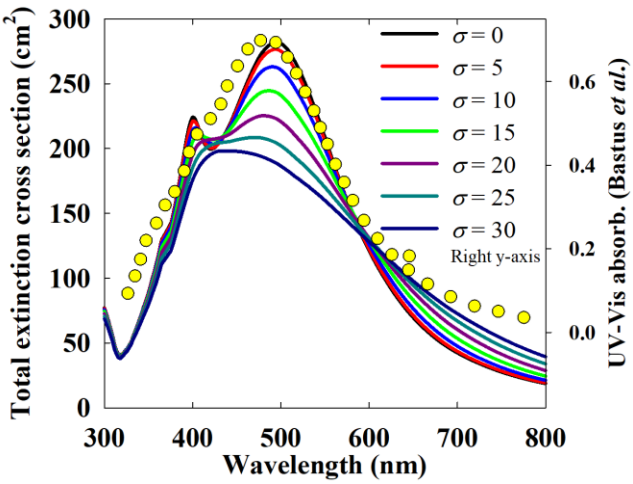

Figure 3.8 Performance of Palik's optical data in resolving the dipolar (at around ~500 nm) and quadrupolar modes (the shoulder at ~400 nm) of 100 nm mean distributions with varying polydispersity and comparison with the experimental extinction spectra of 103.1 ± 7.4 nm average diameter Ag nanoparticles reported by Bastús *et al*.[149]

In order to correlate the dependence of the theoretical LSPR position with the size of Au nanoparticles, Haiss *et al*. implemented an exponential function, which despite being purely empirical, fits experimental data almost perfectly.[178] Since it is the mean that

determines the LSPR position with minimal influence of the polydispersity and skewness, such a correlation allows one to predict the mean nanoparticle size directly from the optical spectra. The usefulness of such a correlation only obtained from theoretical results is, however, dependent on the suitability of the optical constants used. For Au, the theoretical predictions are quite satisfactory even with the commonly used Johnson and Christy's[171] optical data (**Figure A3.3**). Based on the present work, a similar correlation can now also be defined for Ag nanoparticles, where c_o, c_1 and c_2 are empirical constants:

$$\lambda_{LSPR} = c_o + c_1 \exp(c_2 D) \tag{3.8}$$

or

$$D = ln[(\lambda_{LSPR} - c_o)/c_1]/c_2 \tag{3.9}$$

In equation (3.8) and (3.10), λ_{LSPR} is the LSPR position and *D* is the particle diameter. The quality of the fit for the different data sets given in **Table 3.1** shows that equation (3.8) correlates the wavelength dependence of LSPR quite well. Thus, equation (3.9) can be used along with the appropriate empirical constants to predict the mean particle size simply based on the LSPR position. However, due to the larger differences between the theoretical and the experimental results for Ag nanoparticles (**Figure 3.7**), the correlations from theoretical Mie solution in **Table 3.1** can predict mean sizes (*D*) that are slightly off from the real (experimental) mean. In this regard, the correlations from Rioux *et al*. and Palik's optical data are better in terms of the closeness to the experimental data. One can also use the first correlation, which is based on the experimental data, directly rather than the theoretical size-LSPR dependence. In this context, it would be interesting to have a standard set of experimental data available, with complete characterization correlating the mean size to the LSPR position, to be used as a universally accepted reference for the practical implementation of the equation (3.8) for the estimation of mean size from optical spectra.

Table 3.1. Fitting parameters with statistics correlating mean size and LSPR position in **Figure 3.7** (a) with equation (3.8).

	parameters			Statistics	
data	c_o	c_1	c_2	R^2	Adj. R^2
Bastús *et al*. (experimental)	~0	388.75	0.0021	0.9954	0.9948
Mie (Johnson & Christy)	355.6469	21.2390	0.0176	0.9996	0.9995
Mie (Rioux *et al*.)	354.0039	33.5452	0.0143	0.9993	0.9992

Mie (Palik)	349.5965	35.9518	0.0135	0.9976	0.9973

While the theoretical data in **Figure 3.7 (a)** follow a clear exponential trend over the reported size range, the experimental data tend to be more linear over this range although a very slow exponential growth also results in a decent fit. For comparison, the data from Agnihotri et *al*.[194] were inspected (**Figure A3.5**) and a similar size dependence was observed. Since the mean largely determines the LSPR position, this experimental trend is unlikely to be false due to any reason other than a wrongly estimated mean particle size. Given that both Bastús *et al.*[149] and Agnihotri *et al*.[194] characterized the size by TEM, these estimations depend on how representative the sample is with respect to the whole population. Based on the observed trends above, it appears that the experimental LSPR position-size relationship for Ag nanoparticles has a more linear tendency than that the theoretically predicted LSPR position-size relationship (**Figure 3.7 (a)**). Thus, the problem of theoretical prediction of optical spectra of Ag nanoparticles trickles down to finding the right optical constants. In this regard, Palik's data exhibit quite some differences from those from other sources[195], but also out-perform others in matching the experimental results. While the physical aspects down from the atomic level behind these observations is not in the scope of this study, the need for better experimental optical data capturing the crystallinity real colloidal nanoparticles remains.

3.3.3 Implications for dynamic light scattering (DLS)

The fact that for moderate polydispersity the assumption holds of a normal particle distribution, has interesting implications for particle size analysis with dynamic light scattering (DLS). Dynamic light scattering is a non-intrusive technique to estimate the particle size distribution. However, it is often difficult to estimate the true size distribution of nanoparticles with DLS as the hydrodynamic diameter strongly depends on the particle morphological features. Even for particles with a perfect spherical shape and smooth morphology, fundamentally, the intensity distribution given by DLS as the raw data for a fixed mean size shifts towards larger sizes with increasing polydispersity, **Figure 3.9 (a)** and **(b)**. Thus, it is difficult to measure the true mean of the nanoparticle population as the polydispersity always leads to larger values than the real. For instance, as reported by Bastús *et al*.[149], the mean from DLS for the 36.9 nm expected mean diameter (from TEM) population is 48.6 nm; a much higher value. Generally, the DLS mean is at least 25% above the expected TEM mean. One cannot also rely completely on TEM data as during imaging one may tend to select the more monodisperse part of the population for better representation, while leaving out the extremes. In addition, one needs to ensure that the ensemble of particles studied by TEM is representative for the entire nanoparticle population. The fundamental disadvantage of DLS measurements is

besides the draw-back that the hydrodynamic diameter is estimated from the diffusivity, which in turn depends on the surface ligands.

Since it has been established that the normal distribution is a decent approximation for polydisperse particles obtained via colloidal synthesis methods and the mean can be approximated directly from the LSPR position, the standard deviation can be estimated from how much the intensity distribution peak obtained in DLS deviates from the mean due to the polydispersity. For instance, the intensity distribution peak in DLS for the 36.9 nm mean particles from Bastus *et al*.[149], lies at 43 nm (**Figure A3.6**). In contrast, the optical absorption spectrum suggests that the true mean diameter is ~ 34 nm, which is close to the reported mean of 36.9 nm from direct TEM analysis. The difference between the DLS intensity distribution peak and the true mean, 9 nm, is therefore indicative of the polydispersity. The larger this difference, the more polydisperse the sample. As shown in **Figure 3.9 (b)**, the relationship between the population standard deviation and the theoretical intensity distribution peak can be correlated empirically with the following equation in analogy with equation (3.7):

$$Y_{int.\ dist.\ peak} = c_o + c_1\sigma + c_2 \exp(c_3\sigma + c_4) \tag{3.10}$$

In equation (3.10), $Y_{int.\ dist.\ peak}$ and σ are the scattering intensity distribution peak position and the standard deviation respectively, and c_o, c_1, c_2 and c_4 are empirical parameters. The goodness of the fit for the different data sets given in **Table 3.2** shows that equation (3.10) correlates the σ dependence of $Y_{int.\ dist.\ peak}$ quite well. The relationship in **Figure 3.9 (b)** is an example of how for a fixed mean, the intensity distribution peak depends on the standard deviation correlated by equation (3.10). Such a relationship can be derived for any mean size after the mean has been estimated from the LSPR position.

Table 3.2. Fitting parameters with statistics correlating intensity distribution peak, $Y_{int.\ dist.\ peak}$ and standard deviation, σ (**Figure 3.9 (b)**) for distributions with 36 nm as the mean.

Parameters					Statistics	
c_o	c_1	c_2	c_3	c_4	R^2	Adj. R^2
10.7299	3.0545	2.6707	-0.119	2.2463	0.9997	0.9996

It is important to note that the accuracy of the direct conversion of the intensity distribution to a volume or population distribution is again subject to the accuracy of the optical constants used in the Mie theory calculations.[196] This is shown in **Figure 3.9 (c)**, by using two different optical datasets yielding two different size distributions (FWHM). The higher frequency for Palik's[170] data is because of the fact that at 52 nm particle size (intensity distribution peak), the scattering cross section obtained using Palik's[170] data is 757 nm^2, higher than that obtained from Johnson and Christy[171], 620

nm^2. However, the position of the intensity distribution peak is not influenced by the quality of the data. Thus, the estimation of the standard deviation from **Figure 3.9 (b)** is unaffected by the choice of optical constants. Also, these trends also apply to any other solid nanoparticle or even emulsion droplet populations. **Figure 3.9 (d)** further corroborates the theoretical formulation of the size distribution by showing that the intensity distribution is not dependent on the wavelength of laser used in the DLS, as the laser type varies from manufacturer to manufacturer. Thus, the relationship between the intensity distribution peak and standard deviation shown in **Figure 3.9 (b)** is independent of the choice of optical constants and wavelength of illumination. It is however useful to use a wavelength closer to the LSPR, which is 530 in this case, so that the strength of the signal is higher.

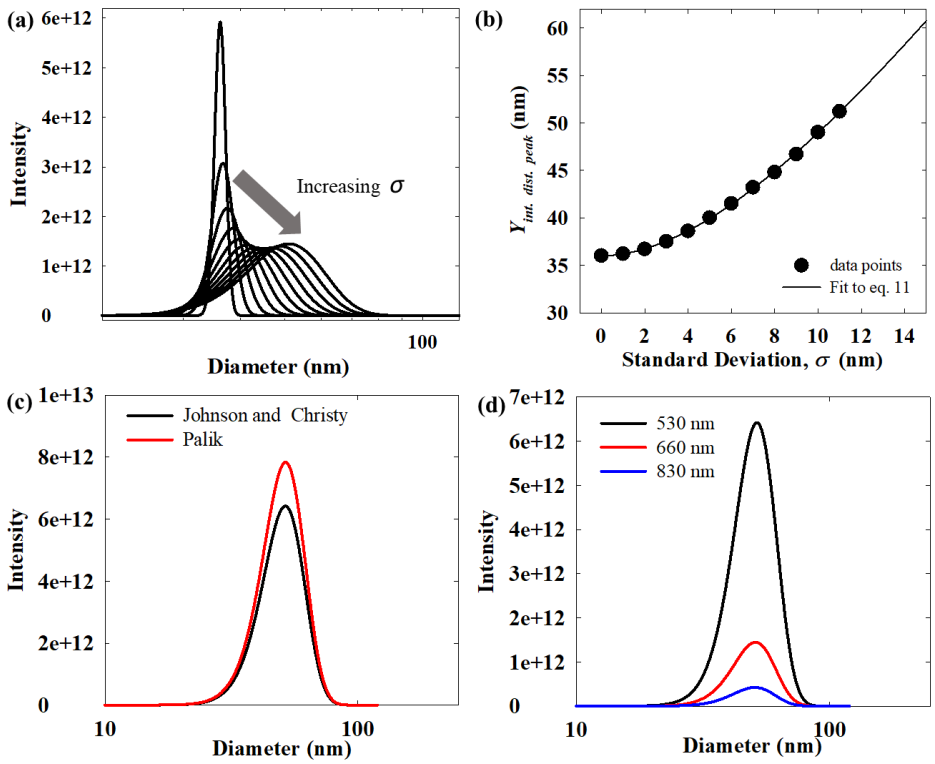

Figure 3.9 (a) The effect of polydispersity *i.e.* standard deviation, σ on the theoretical scattering intensity distribution (theoretical raw DLS data) at 660 nm incident laser for a fixed mean of 36 nm. (b) Intensity distribution peak vs. σ fitted to equation (3.10). (c) The dependence of the theoretical scattering intensity distribution from optical data source. (d) The dependence of the theoretical scattering intensity distribution from incident laser wavelength. Figures (c) and (d) confirm the validity of the intensity distribution results.

3.4 Conclusion:

With the above results in **Chapter 3**, the ambiguity around the role of particle size distribution, intrinsic optical properties and particle surface morphology in determining the collective optical response of colloidal plasmonic nanoparticles is resolved. The rather insignificant contributions of the polydispersity and the skewness for smaller colloidal Ag nanoparticles (~60 nm or less) synthesized via standard protocols in literature have been established. Generally, the mean size is the most important statistical parameter and determines the optical spectrum. The insignificance of the other statistical parameters implies that one only needs the suitable optical constants for theoretical calculations of the spectra. Also, it works well to assume a normal particle distribution as far as the optical spectra are concerned, since the tendency towards a lognormal distribution has no significant impact. It is possible that polycrystallinity plays a big role and Ag nanoparticles are mostly polycrystalline. It is shown that the position of the LSPR wavelength is not influenced by the particle size standard deviation when the mean is fixed, although the volume distribution shifts towards larger values as the standard deviation increases. For larger nanoparticles, however, the polydispersity and skewness become increasingly important as the size dependence of the LSPR increases with size. Also, the expression of the multipolar modes leads to broadening of the overall spectra. Based on the fact that the LSPR position is determined by the mean diameter, the mean diameter can indeed be accurately estimated from the optical spectra. For that, either carefully obtained standard experimental data can be used as universal reference, either theoretical calculations with suitable optical constants are required. Relying on the dependence of the DLS intensity distribution mean on the standard deviation, it is also possible to estimate the polydispersity from the difference between the mean size and the intensity distribution peak. While the results in **Chapter 3** clear all the ambiguity regarding the primary factors determining the optical spectra of colloidal plasmonic nanoparticles, these findings pave way for the studies in later chapters (**Chapter 5** and **6**) where experimental and computational results are compared for further insights.

Chapter 4

Finite two dimensional Au nanoparticle clusters: optical properties for light enhanced processes

Based on:

Rituraj Borah, Sammy W. Verbruggen, Coupled Plasmon Modes in 2D Gold Nanoparticle Clusters and Their Effect on Local Temperature Control. J. Phys. Chem. C 2019, 123 (50), 30594–30603.

Contribution:

R.B. formulated the problem, carried out the investigation, and wrote the article.

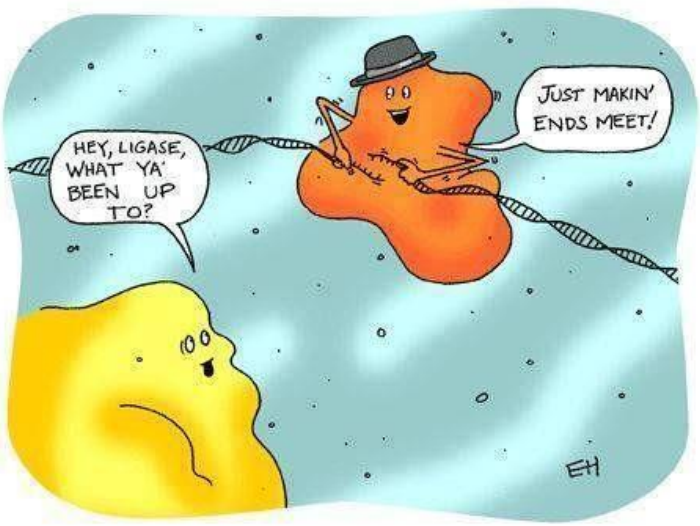

Courtesy: www.si.edu

4.1 Introduction

In **Chapter 2** and **3**, optical properties of individual Au and Ag nanoparticles were discussed. In **Chapter 4**, two dimensional clusters of Au nanoparticles are discussed, whose optical properties are enhanced due to the plasmonic coupling among the nanoparticles.[197] [198] The interaction among the plasmon modes of individual nanoparticles of a cluster or assembly gives rise to interesting optical characteristics such as higher order modes, magnetic resonance[199] and fano-like resonance[200] that are promising for various applications.[201] [202] For instance, the fano-like resonance can be useful in chemical and biological sensing, electro-optics, switching, etc.[203] Thus, considerable efforts have been devoted towards the understanding and fabrication of such composite nanostructures. [204] [205] [206] [207] Obviously, the discussion on collective plasmonic behavior starts with simple dimers for which many past studies have shed light on relevant aspects such as the polarization dependence, near-field enhancement, spectral shift, and the effect of interparticle distance.[208] [209] [210] [211]Apart from the classical electromagnetic field theory, the analogy of molecular hybridization theories with the interaction of plasmon modes has yielded an alternative approach to explain the collective plasmonic behavior of composite nanostructures.[212] [213] Importantly, the spectral red-shift and the significant enhancement of the near-field between the particles are striking features of dimers. As one adds more nanoparticles to a linear arrangement, the red-shift gets stronger with increasing chain length.[214] [215] On the other hand, it is interesting to note that an equilateral 2D arrangement of three nanoparticles exhibits little dependence on the in-plane polarization angle of incident light. This planar symmetry is even further extended to 3D isotropy for 3D symmetric tetramers. One important aspect of many particle systems is the interaction among the radiative modes that results in constructive and destructive interference often indicated by the Fano-like characteristic dip in the scattering spectra. In the discussion of nanoparticle clusters, an obvious question arises regarding the infinity limit beyond which the cluster size becomes insignificant. The formalism given by Modinos *et al*. for the estimation of the optical response of infinite arrays of nanoparticles is based on the methods developed in relation to electron scattering by two-dimensional atomic layers.[216] [217] [218] The estimated optical spectra from this formulation have been shown to agree reasonably well with the experimental spectra for gold nanoparticle lattices. An alternative approach among others is the Korringa–Kohn–Rostoker (KKR) method which has been demonstrated as a robust approach for electromagnetic waves in a periodic dielectric medium in their full complexity.[219] [220] Zundel and Manjavacas discussed this infinity limit for large 100 nm nanoparticles arranged in a square array, a system with strong far-field coupling.[221] Infinite nanoparticle films are discussed in the next **Chapter 5**, while in the present chapter finite arrays of Au nanoparticle will be discussed whose overall size is smaller than the exciting wavelength.

For the fabrication of nanoparticle/nanostructure oligomers or clusters, techniques like e-beam lithography or ion beam milling are widely used due to their high controllability.[222] [223] However, these techniques are expensive and inefficient at small dimensions. On the other hand, formation of nanoparticle clusters with precise dimensions by self-assembly techniques is a challenging task and an important area of investigation.[224] [225] [226] [227] The thermo-plasmonic effect and resulting phenomena such as plasmo-fluidic convection, phase transition, vapor generation, etc., in nanoparticles and nanoparticle arrays have gained considerable attention over the years.[228] [229] [230] [231] [232] [233] [234] [235] [236] In view of the immense possibilities and rapid advances in the area of nanostructure design and applications, promising research avenues are continuously emerging.

Pertaining to self-assembled structures, plasmonic response of clusters of small (<50 nm) nanoparticles is an important unexplored aspect of investigation as such systems promise many applications. Particularly due to low scattering and high absorption, small nanoparticle systems are very relevant to photothermal applications as well as hot electron mediated processes. Based on rigorous validation of the numerical methods used, in this **Chapter 4**, the collective plasmonic properties and the resulting photothermal effects in 2D close packed nanoparticle clusters of small (20 and 40 nm in diameter) Au nanoparticles is discussed. Clusters of varying size and interparticle distance were considered in order to delineate the effect of these structural aspects on the collective plasmonic (optical) behavior. The results compare the optical response of clusters of different sizes ranging from a single nanoparticle up to large assemblies of 61 nanoparticles. Increasing the cluster size induces significant changes to the spectral position and optical intensities. The effect of the particle size and interparticle distance is investigated to elucidate the nature of plasmonic interaction in terms of near-field and far-field coupling. Apart from the optical response, the steady state temperatures of the nanoparticles in an aqueous medium were calculated in order to evaluate the photothermal characteristics of these clusters. A strong dependence of the steady state temperature of the nanoparticles on the cluster size, particle position in the cluster, incident light polarization, and interparticle distance was observed. Based on these outcomes, an optimal cluster size for maximum absorption per nanoparticle is also determined for enhanced photothermal effects.

4.2 Problem specification and numerical methodology

The results included in this chapter involve electromagnetic simulations of close packed 2D assemblies of Au nanoparticles with varying number of nanoparticles and interparticle distance (**Figure 4.1**). The details of the numerical methodology are described in **Section 2.2** of **Chapter 2.** For the models, the optical constants for Au were taken from Johnson and Christy.[237] Similar to **Chapter 2**, equation (2.1) is to be solved for the scattered field in a homogeneous medium in the presence of a plane polarized incident electric field. The minimum interparticle distance considered in this

study is 1 nm for which quantum tunneling effects can be neglected.[238] The computational domain was discretized with tetrahedral elements in the physical domain *i.e.*, the nanoparticles and the surrounding medium. While the perfectly matched layer was discretized by prismatic elements. The optical cross sections were calculated by post processing of the numerical results as given in **section 2.2**. Similarly, equation 2.8 was solved for the photothermal studies with the convection contribution neglected as at such an extremely small length scale *i.e.* extremely small Grashof number, *Gr*, the contribution of convection to heat-transfer is negligible. The thermophysical properties of Au and water are taken from Chen *et al.*[110] Considering the strong variation of the thermal conductivity of Au as a function of the thickness of the film used for measurement, the temperatures for k = 110 W/m.K and k = 317 W/m.K were compared to show that the variability of the thermal conductivity has little effect on the steady state temperature profile (**Table A4.1** and **Figure A4.2**). Since the thermal conductivity of water is significantly low as compared to Au, this variability does not impact the conductive heat transfer characteristics. From dimensional considerations, for both the values of k, the value of the Biot number is very low implying that a lump capacitance approximation is valid for both the cases.[239]

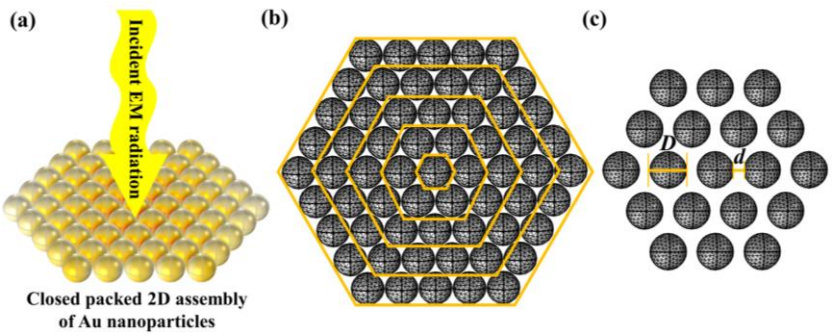

Figure 4.1 Schematic representation of (a) nanoparticle 2D nanoparticle cluster irradiated with plane polarized electromagnetic wave in normal incidence, (b) top view of nanoparticle cluster with hexagonal yellow boundaries defining different cluster sizes considered. The yellow boundaries starting from the outermost one define clusters of 61, 37, 19, 9 and single nanoparticle(s), respectively. (c) A cluster of 19 nanoparticles with the definition of particle diameter D and interparticle distance d.

4.3 Results and discussion

The reliability of the present computational method is established upon previous literature that has shown good agreement between COMSOL Multiphysics numerical solutions, analytical solutions, as well as with experimental results.[105 240] Even for more complex nanostructures, good agreement between the computational method and experimental data has been obtained. [223 241 8] For the present work, **Figure A4.1** and **A4.2** illustrates the validation of the numerical models used in this study by comparing them to existing numerical as well as experimental results.[241 238] Since the photothermal

effect is a direct consequence of the optical characteristics of the nanostructures considered, the optical behavior is discussed in detail in section 4.3.2, followed by the discussion on the thermal effects of the important cases in section 4.3.3.

4.3.1 Model validation

Reproduction of the results by Fan *et al*.[62] and Barrow *et al*.[58] is useful as their experimental results for Au nano-shell heptamers and nanoparticle trimers, respectively, are in excellent agreement with numerical results (**Figure A4.1**). Fan *et al*. also showed experimentally that the effect of a silica substrate on the optical output of a nano-shell heptamer is weak. Despite using the same numerical framework, the minor deviation of present results from the numerical results of Barrow *et al*. can be attributed to the dissimilarities in mesh quality, PML or domain size. Nonetheless, the spectral features are in complete agreement. Importantly, the agreement between experimental and theoretical results from classical electromagnetic theory when the interparticle gap is as small as 0.5 to 1 nm validates the exclusion of quantum tunneling effects. Additionally, the results reported by Baffou *et al*. for an array of 15 nanospheres were also compared with the present results to compare BEM and FEM based computations (**Figure A4.2**). At this point, it is concluded that the electromagnetic models of nanoparticle clusters built in COMSOL Multiphysics are successful in reproducing various sets of experimental and numerical data from literature, and will from hereon be used to study clustering effects in more detail.

As even small clusters with 3 equilaterally placed nanoparticles exhibit polarization independence for in-plane polarized incident light, it is naturally expected that bigger clusters will also exhibit similar planar isotropy and the results in **Figure 4.2 (a)** illustrate this for a 37 nanoparticle cluster. To understand this polarization independence *i.e*. axial symmetry, it is more convenient to work with a simple system like an equilateral trimer for which, using plasmon hybridization theory, nine hybrid plasmon modes (or Eigen modes) can be derived.[205 242] The excitable planar modes for an equilateral trimer are symmetric linear combinations of the individual plasmon modes, basically meaning that plasmons mix into each other with the same symmetries that they exhibit at infinite separation.[243] Thus, the symmetry in a larger cluster can be explained using the same principle. However, such an analysis for a 37 nanoparticle cluster would be much more complicated. **Figure 4.2 (b)** shows for the same cluster that the system also has 2-fold symmetry in terms of individual optical spectra about the dotted axes shown in the diagram in the inset, due to which the individual spectra of corresponding nanoparticles from each quarter coincide completely. Thus, the cluster can be divided into four equal sections equivalent to one another. **Figure A4.4** presents the absorption spectra of individual nanoparticles in a 61 nanoparticle cluster. It is clear from both **Figure A4.4** and **Figure 4.2** that the absorption spectra for individual nanoparticles vary strongly with the position in the cluster implying that similar position dependence of the

photothermal effects can also be expected. This aspect is discussed further in the later sections addressing the near-field and thermal effects.

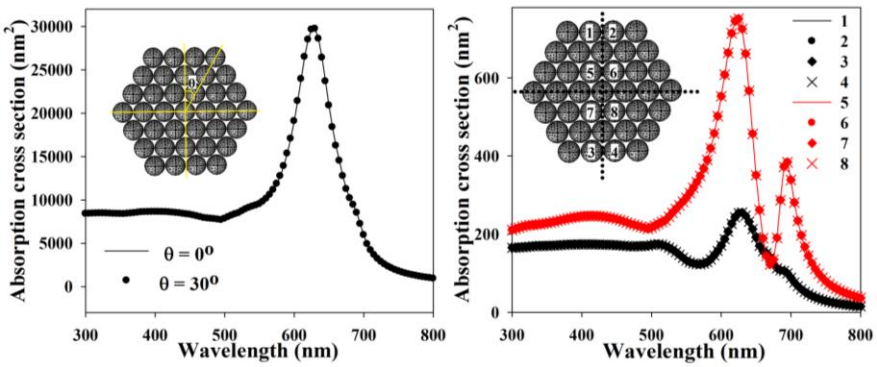

Figure 4.2 (a) The effect of in-plane polarization angle of incident light on the total absorption cross section in a 37 nanoparticle cluster with d = 1 nm of interparticle gap. (b) The comparison of absorption cross section of individual nanoparticles in a similar 37 nanoparticle cluster to show the 2-fold symmetry for a 0° polarization angle. The diameter of the nanoparticles is 20 nm.

4.3.2 Effect of cluster size for strongly interacting nanoparticles

In order to delineate the effect of cluster size, spectra for close packed nanoparticle clusters were compared by varying the number of nanospheres from 1 to 61. Since the individual radiative damping is very small for 20 nm nanoparticles, the interparticle distance considered was 1 nm so that there is strong interaction among the near-field generated by individual nanoparticle. As apparent from **Figure 4.3**, the LSPR is red-shifting for both absorption and scattering spectra with increasing number of nanoparticles. Obviously, increasing the number of particles will increase the total optical intensity. However, from the perspective of efficiency , it is more important to quantify the intensity as the "average intensity per particle". Thus, the comparison in **Figure 4.3** is shown in terms of average absorption and scattering cross section per nanoparticle. It is rather intuitive to expect that in the limit of an infinite number of nanoparticles, the average optical cross section per nanoparticle will remain unchanged upon further expansion of the cluster. This is quite clear for the average absorption cross section while varying the cluster size from 1 to 61 nanoparticles in **Figure 4.3**. It is worth noting that in the infinity limit, it is the average optical intensity, absorption or scattering, that remains constant upon addition of nanoparticles as the total absorption and scattering will obviously increase with more nanoparticles. While, although the average scattering cross section continually increases untill 61 nanoparticles, the rate of increase becomes smaller implying that at a certain number it will reach a plateau or a maximum. Thus, the optimal cluster size is not the same for absorption and scattering. Interestingly, 20 nm nanospheres have a significantly large average scattering cross section per particle in the cluster in contrast to their diminishingly small scattering cross

section when isolated (**Figure 4.3 (b)**). Since an isolated 20 nm nanoparticle is essentially "non-scattering", this enhancement in scattering can be attributed to near-field coupling of the nanoparticles.[198] [244] If the collective optical response of the nanoparticles in a cluster is due to the interaction of near-fields, the cluster can behave like a single entity bridged together by inter-connected near-fields (see further, **Figure 4.7**). Since the radiative modes of individual particles become strong in cluster, the coupling of these strengthened radiative modes is also possible. Thus, the collective response is a correlative effect of near-field and far-field interactions. However, the relative strength of these two interaction modes is an important aspect discussed later in this work, **Figure 4.5**, **4.6** and **4.7**. Another interesting way to view this collective behavior is a hybridized plasmon mode of constituent individual plasmon modes analogous to a molecular orbital from the hybridization of individual atomic orbitals in molecular orbital theory.[212] [100] [245] Interestingly, akin to the red-shift of optical cross sections with increasing size for an isolated nanostructure, the collective optical spectra for clusters also red-shift with increasing cluster size. Also, the scattering is greatly enhanced for bigger clusters. An important feature of a nanoparticle cluster is that as the cluster size increases, even to the macro-scale, the localized plasmons remain intact. In contrast, a single nanoparticle is known to lose its optical properties derived from localized surface plasmon resonance if the size increases beyond a certain point, as the localized plasmons give way to bulk plasmons. The LSPR wavelength *vs*. number of nanoparticles in the cluster is plotted in **Figure 4.4** and clearly evidences that the red-shift tends to become weaker and weaker with increasing cluster size. Thus, after a certain limit, there will not be any red-shift upon addition of more nanoparticles implying that the infinite limit is reached. While extending the present numerical model to find this infinite limit is a coveted aspect, the increase in the required computational power with increasing cluster size unfortunately limits this endeavor. Thus, the use of theoretical formalisms of Modinos *et al*. or KKR method will be more practical in this regard.[33-37] The coupled dipole method is an alternative approach to tackle this problem, but it is based upon assumptions that significantly simplify the model.[221] [246] Use of a theoretical formalism for infinite arrays of nanoparticle remains an important objective of our future research.

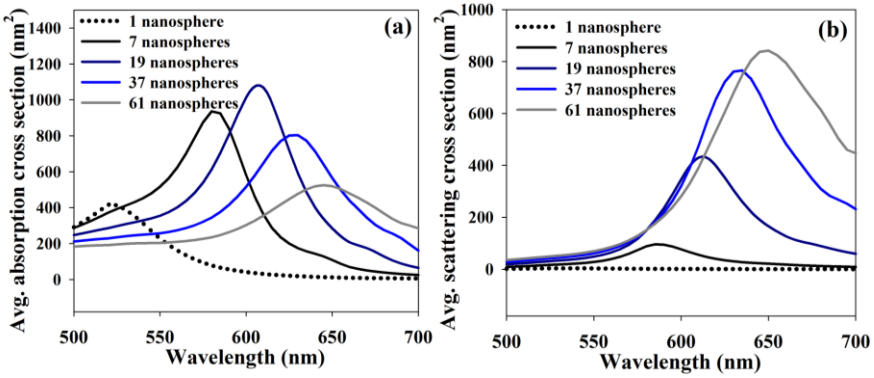

Figure 4.3 (a) Average absorption cross section per nanoparticle and (b) average scattering cross section per nanoparticle for varying cluster size with interparticle gap of 1 nm. The diameter of the nanoparticles is 20 nm.

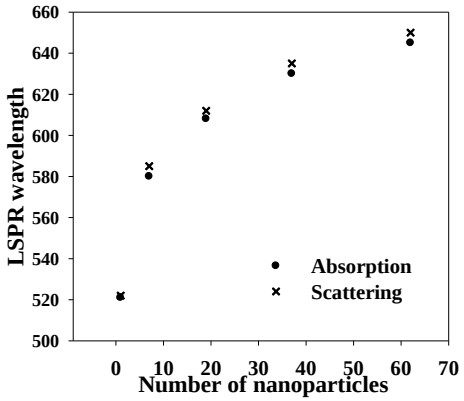

Figure 4.4 Absorption and scattering spectral peak wavelength variation with number of nanoparticles in the cluster from 1 to 61 particles. The interparticle gap *d* is 1 nm and the nanoparticle diameter *D* is 20 nm.

4.3.3 Effect of interparticle gap and particle size

As discussed above, **Figure 4.3 (a)** and **(b)** show that the absorption per particle increases (then decreases) with cluster size and otherwise non-radiative 20 nm nanoparticles have significant 'per particle' average scattering cross sections when they are clustered together. To further understand the nature of this interaction, it is instructive to study the effect of interparticle distance in a cluster with particles with different individual scattering power.

To start with, the effect of interparticle distance was studied for a 19 nanoparticle cluster, as it has been shown for closely packed (d = 1 nm) 20 nm nanoparticles that the average absorption cross section per nanoparticle is the highest in that case. Now in **Figure 4.5 (a)** and **(b)**, both absorption and scattering spectra red-shift with increasing intensity as the interparticle distance decreases. These trends are consistent with the hypothesis that the interparticle interaction happens primarily through overlapping near-fields as the spectral features are intact. Thus, with decreasing gap, the cluster tends to show a collective optical response like an integrated large nanostructure. The interparticle interaction in clusters is understood further by analyzing the effect of the interparticle gap in a cluster of 40 nm nanoparticles for which the individual scattering power is higher (**Figure 4.6**). The interaction among these bigger nanoparticles is enabled through both overlapping of the near-fields *i.e.*, near-field coupling and the interference of the radiative modes *i.e.*, far-field coupling. Importantly, when 40 nm nanoparticles are clustered, the characteristic resonance peak in the absorption spectra loses its sharp feature and intensity, while the scattering intensity increases. The

evidence of the strong interference of the radiative modes is the fano-like characteristic resonance in the scattering spectra resulting from super-radiant and sub-radiant modes for an interparticle gap of 2 and 4 nm.[247] It is interesting to note here that the fano-dip is also dependent on the interparticle gap. This intensification of the radiative damping through the interference of scattered radiation may be connected to the loss of spectral characteristics in the absorption spectra. Evidently, the larger nanoparticles require a larger interparticle distance to be free from interparticle interaction. **Figure 4.7** shows the difference in the strength of interparticle interaction for a 1 nm and a 16 nm interparticle gap by comparing the near-fields. As expected for the 1 nm gap, the strength of the electric field between the particles is significantly higher than that for a 16 nm gap. Also, for 16 nm gap the dipolar plasmon modes of individual nanoparticles are dominant with weak enhancement of the near-field in the interparticle gap. In contrast, for the 1 nm gap individual dipolar modes are lost as they couple together to form hybridized modes. These hybridized modes result in strong near-field enhancement in specific locations of the cluster.

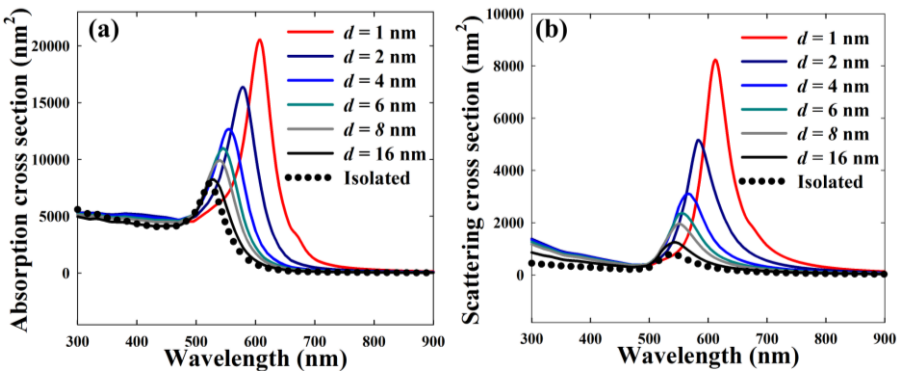

Figure 4.5 Variation of (a) absorption and (b) scattering cross section of a 19 nanoparticle cluster with varying interparticle distance *d*. The nanoparticle diameter *D* is 20 nm.

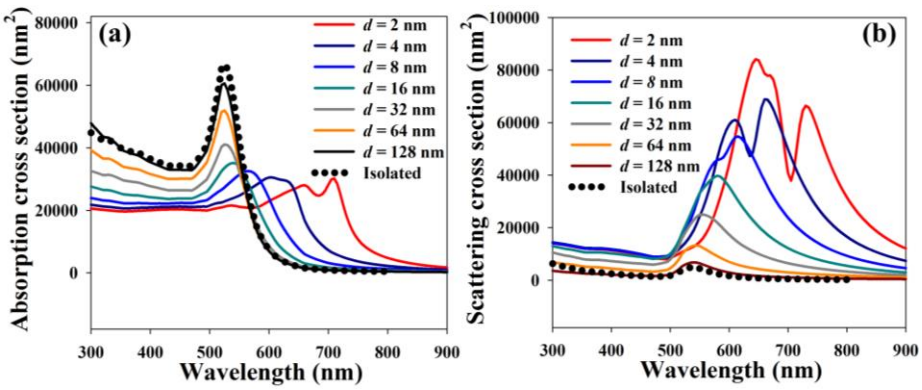

Figure 4.6 Variation of (a) absorption and (b) scattering cross section of a 19 nanoparticle cluster with varying interparticle distance *d*. The nanoparticle diameter *D* is 40 nm.

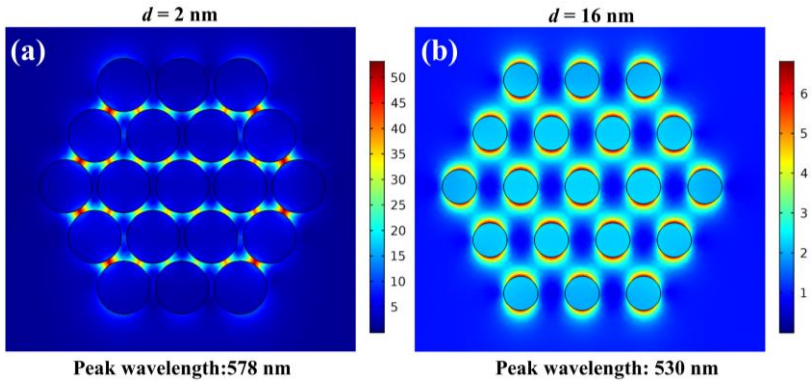

Figure 4.7 Near-field enhancement in 19 nanoparticle clusters with interparticle distance (a) d = 2 nm and (b) d = 16 nm for a nanoparticle size of 20 nm. The enhancement of the scattered field with respect to the incident field is shown. The direction of the wave is from left to right and the polarization of the electric field is along the vertical direction.

The near-field enhancement at specific locations in a cluster for a certain incident wavelength corresponds with the fact that individual nanoparticles in a cluster have significantly different absorption characteristics. Apparently in **Figure A4.4**, the absorption spectra of individual nanoparticles in a 61 nanoparticle cluster differ one to another greatly with varying peak positions in the spectrum. Thus, the near-field enhancement corresponding to these individual absorption peaks also varies with the location of each individual particle in the cluster. **Figure A4.5** shows the near-field enhancement in a 61 nanoparticle cluster for different incident wavelengths. For 645 nm incident wavelength, the near-field enhancement is along the nanoparticles at the left and right boundaries of the cluster. But at 720 nm wavelength, the near-field enhancement is now in the core of the cluster. This spatial variability of near-field enhancement is an interesting observation with regard to many applications of plasmonics. For instance, it has been found that strong near-field enhancement and hot-electron injection catalyzes certain reactions, photocatalytic processes, etc. Local control of these processes is possible due to this spatial variability of near-field enhancement.

4.3.4 Photothermal effect of clusters

The inevitable consequence of energy absorption is thermal dissipation and thus, temperature rise of the nanoparticle cluster and its surrounding, while the scattered energy is simply radiated away. Thus, the absorption spectra of the nanoparticles and their assemblies readily correspond with the resulting temperature fields. Since the

absorption characteristics are dependent on the nanoparticle position in a cluster, individual nanoparticles will exhibit different steady state temperatures according to their relative position and polarization angle, **Figure 4.8 (a)** to **(d)**. Interestingly, the number of nanoparticles strongly influences the steady state temperature of the cluster due to enhanced absorption in hybridized plasmon modes in a cluster and containment of heat by the outer spheres of the cluster. Thus, absorption and heat containment simultaneously influence the steady state temperatures of the particles.

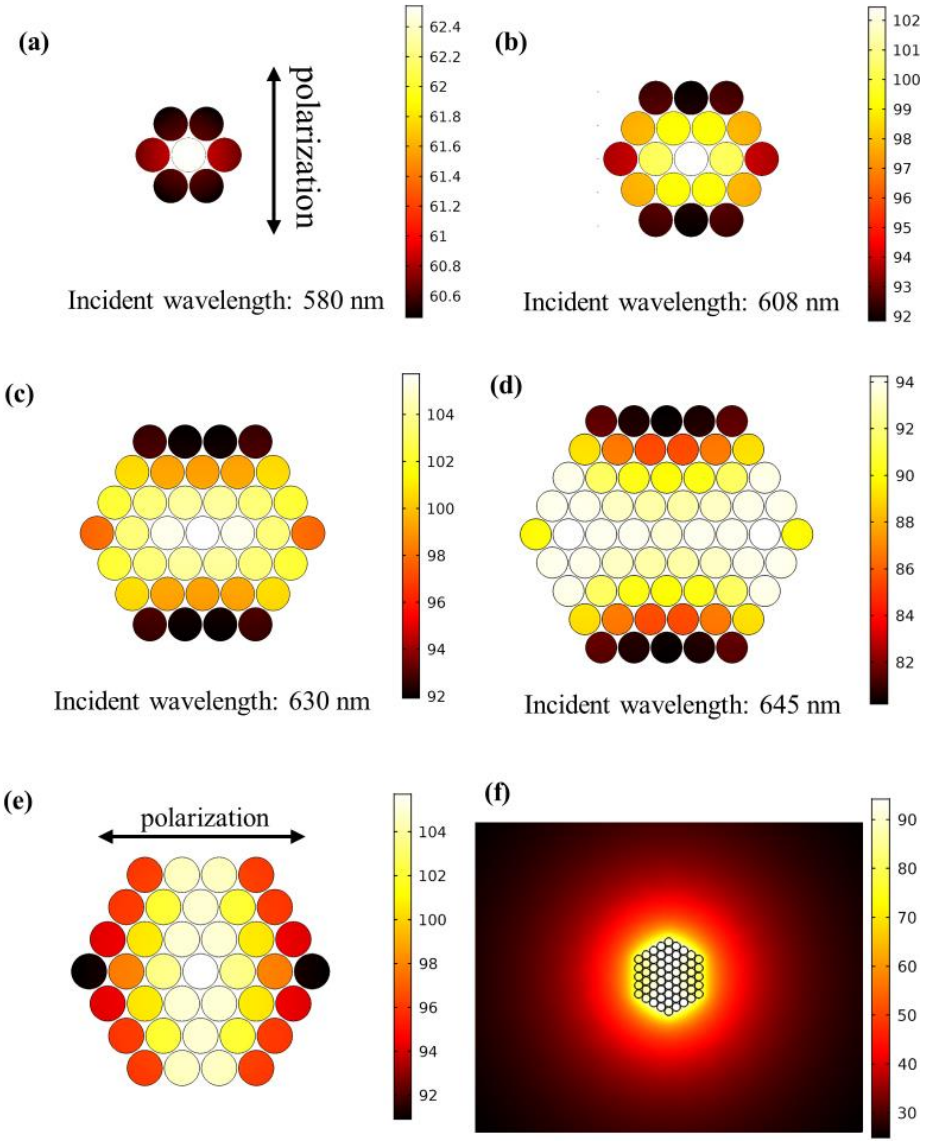

Figure 4.8 Steady state temperatures (°C) of nanoparticles in a cluster: (a) 7 nanoparticles (b) 19 nanoparticles (c) 37 nanoparticles (d) 61 nanoparticles upon EM irradiation of respective peak wavelength in infinite water medium. (e) Temperature profile in a 37 nanoparticle cluster when the incident radiation polarization is horizontal.

(f) Temperature field around a 61 nanoparticle cluster. The intensity of incident radiation is 1 mW/μm^2 for all the cases. The wavelength of incidence is the plasmon resonance wavelength.

In a water medium at 25^{o}C, a single nanosphere is heated up to only ~30^{o}C (**Figure A4.6**), while the 7 nanoparticle cluster attains a temperature over 62^{o}C when irradiated at 1 mW/cm^2. Similarly, for 19 and 37 nanoparticle clusters, the temperature of the "hottest" nanoparticle in the cluster will exceed 100^{o}C. Interestingly, the average aborption per particle is higher for a 19 nanoparticle cluster as compared to the 37 nanoparticle cluster, but the 37 nanoparticle cluster has a higher steady state temperature for the central nanoparticles than the 19 nanoparticle cluster. Clearly, although the absorption is less, the central nanoparticles in the 37 nanoparticle cluster are surrounded by more nanoparticles than a 19 nanoparticle cluster implying greater heat retention and steady state temperature in the core. However, for the 61 nanoparticle cluster, the steady state temperature of the "hottest" particles again drops to ~95 ^{o}C because the decrease in the average absorption per particle is the dominating factor. Also, for the 61 nanoparticle cluster, nanoparticles at the boundaries have high temperature in spite of lower heat retention as the high absorption compensates for the higher heat loss rate to the surrounding. The temperature variation with the position of the particles is an important aspect demonstrated here. In **Figure 4.8 (e)**, the change of the temperature profile in the 37 nanoparticle cluster is shown when the incident radiation polarization is horizontal in contrast to vertical polarization in **Figure 4.8 (c)**. This indicates the possibility of controlling the temperature profile in a cluster. The temperature field of the 61 nanoparticle cluster with the surrounding is shown in **Figure 4.8 (f)**.

It is worth mentioning that although the steady state temperature is significantly enhanced by clustering nanoparticles as compared to isolated nanoparticles, the light intensity required to achieve this heating effect is considerably high. In **Figure A4.7**, it is clear that a drop of one order of magnitude in the intensity results in a significantly lower steady state temperature. When the intensity is two orders of magnitude lower, there is almost no apparent heating. It is also important to note that the present model assumes an infinite water medium which is not an insulating material. To check the extreme limit, heat transfer analysis was also done for a 37 nanoparticle cluster in an air medium, a good insulating medium, while keeping the absorption values the same as those in water, **Figure A4.8**. For the intensity corresponding to **Figure 4.9**, the overall cluster temperature was estimated to be as high as around 900 ^{o}C, attained solely by altering the thermal properties of the medium. It is to be noted that the convective effects are excluded in this calculation. With this fundamental insight, it is clear that raising the steady state temperature is a matter of improving the energy input rate and heat retention by better optical and thermal design of the system. For instance, attaining a high temperature under sunlight would require improved heat trapping possibly by clustering in 3D and embedding in an insulating matrix as shown by Dhiman *et al*. for dendritic

plasmonic colloidosomes.[248] In contrast to 20 nm nanoparticles considered in this work for which the heating is rather weak, an isolated large nanoparticle of 100 nm diameter can induce a temperature rise >50 °C for the intensity considered in this study.[249] This promises further development in the cluster heating with larger nanoparticles. The present results demonstrate the possibilities to improve and control the thermal effects of nanoparticles by clustering in suitable configurations.

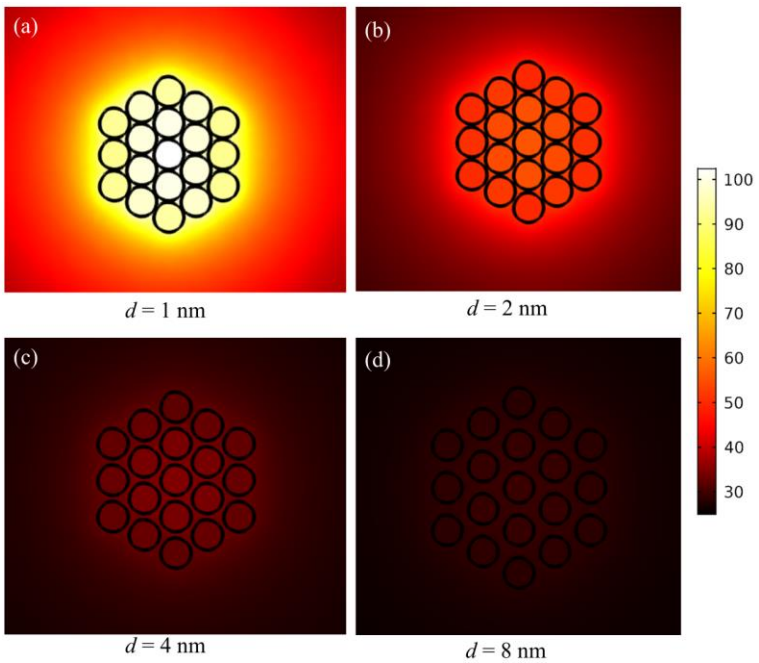

Figure 4.9 Steady state temperatures (°C) of a 19 nanoparticle cluster with varying interparticle distance, *d*. The wavelength of the incident radiation is the plasmon resonance wavelength of 608 nm for d = 1 nm. The intensity is 1 mW/μm^2 for all the cases. The cluster is embedded in an infinite water medium.

The effect of interparticle distance on the absorption spectra of clusters is another aspect that leads to interesting thermal effects. In **Figure 4.8 (b)**, it has been shown that a 19 nanoparticle cluster can attain significantly higher temperature as compared to an isolated nanoparticle when irradiated by an electromagnetic wave of their peak wavelengths. However, this temperature is for the smallest interparticle gap of 1 nm. As the interparticle gap increases, the absorption intensity as well as the spectral peak changes. The consequence of this on the thermal effect is obviously direct. In **Figure 4.9**, the steady state temperature of a 19 nanoparticle cluster with varying interparticle gap is shown. For an interparticle gap of 8 nm, the thermal effects of the nanoparticle cluster are practically gone. It is however useful to point out the difference in the representation of **Figure 4.8** and **4.9**. In **Figure 4.8**, the spatial variation of temperature only in the nanoparticles is shown, while in **Figure 4.9**, the cluster as well as the surrounding temperature field is shown. The results in **Figure 4.9** also promise

interesting applications of local temperature control and sensing. For instance, it has been shown how the interparticle gap of nanoparticle assembly embedded in a substrate can be controlled by thermal treatment, chemical modification or mechanical strain of the substrate without structural distortion.[250] [251] [252] It is important to note that demonstrated photothermal effect due to tuning the interparticle gap is only possible with 20 nm particles according to our simulation. As we have shown that the 40 nm nanoparticle cluster does not exhibit similar dependence of absorption characteristics on the interparticle gap. Due to strong coupling of radiative modes, the absorption rather decreases with smaller interparticle gap. Detailed experimental studies on 2D clusters of weakly radiant nanoparticles as small as 20 nm have not been carried out yet. Thus, experimental verification of these theoretical results is of significant practical importance with regard to the numerous possible applications.

4.4 Conclusion

In **Chapter 4**, the coupled plasmonic response and resulting photothermal effects of isolated Au nanoparticle clusters of different sizes were discussed. The collective optical response is analyzed in terms of near-field and far-field coupling among constituent nanoparticles in the cluster. Otherwise weakly radiative 20 nm Au nanoparticles, when coupled through overlapping of near-fields in a close packed 2D cluster, exhibit an optical response as an integrated structure resulting in strong absorption and scattering with a spectral shift. As optical cross sections obviously increase with increasing cluster size, it is more useful to determine average absorption/scattering per particle from an efficiency perspective. As shown for 20 nm nanoparticle clusters with small interparticle gap (1 nm) i.e. strong near-field coupling, the absorption intensity per particle increases with cluster size up to an optimal cluster size beyond which the average intensity reaches a constant value at the limit of an infinite cluster. For absorption, the optimal cluster size is 19 nanoparticles, while, for scattering the optimum could not be determined in the present study that covers cluster sizes up to a maximum of 61 nanoparticles. The spectral red-shift with increasing cluster size is apparent in all cases. Since the coupling among weakly scattering 20 nm nanoparticles is predominantly through the near-fields, increasing the interparticle gap rapidly weakens the collective modes and the individual dipolar modes of the nanoparticles become strong. However, due to their stronger radiative modes, 40 nm nanoparticles in a cluster are coupled through both near-field and far-field, enabling far reaching interparticle interaction. The effect of decreasing the interparticle gap, thus enabling stronger collective modes in a cluster, is a red-shift of the spectra. However, the contrast between 20 nm and 40 nm nanoparticles is that the absorption intensity increases for 20 nm particles while decreases for 40 nm particles with decreasing interparticle gap. Also, the absorption characteristics in a cluster vary strongly from particle to particle. Since the steady state temperature of individual particles depends upon the individual absorption intensity and the heat retention around the particle, the

steady state temperature of individual nanoparticles varies strongly in a cluster. This variation is stronger for stronger laser intensity and also dependent on the incident polarization. The effect of interparticle distance on absorption intensity leads to interesting photothermal effects in a cluster which can be controlled by varying this distance. The present study provides new theoretical insight into plasmonic behavior of close packed Au nanoparticle clusters and resulting photothermal phenomena. The photothermal effect in the clusters shows the possibility of nanoscale temperature control.

Chapter 5

Plasmonic nanoparticle films obtained by air-liquid interfacial assembly: optical properties for light mediated applications

Based on:

Rituraj Borah, Rajeshreddy Ninakanti, Sara Bals, Sammy Verbruggen, Plasmonic Lattice Resonances in Self-assembled Arrays of Silver and Gold Nanoparticles: Normal vs. ATR (Kretschmann) Configuration (*to be submitted*).

Contribution:

R.B. performed the nanoparticle synthesis/self-assembly/optical characterization experiments, carried out the computational modeling, and wrote the manuscript.

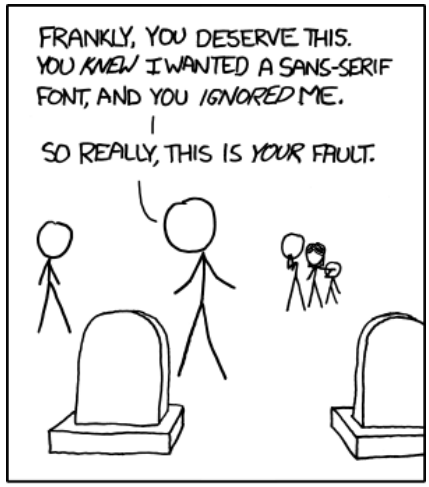

Courtesy : www.xkcd.com

5.1 Introduction

Chapter 4 dealt with finite plasmonic nanoparticle clusters (cluster dimension < wavelength of incident light). In **Chapter 5**, the study is extended to infinite films of plasmonic nanoparticles (film dimensions >> wavelength of incidence). In multiple applications of nanoparticles, ordered periodic arrays are particularly interesting since the light-matter interaction is enhanced in such periodic assemblies. Given an optimal spacing between the nanoparticles, this effect occurs due to the coupling of the individual plasmons, resulting in an amplified coherent optical response *i,e*. lattice resonances.[253] To exploit this plasmonic coupling, periodic arrays of nanostructures have gained considerable attention.[254] For instance, plasmonic nanostructure arrays have been demonstrated for light-harvesting enhancement in photovoltaic applications.[255] Furthermore, the intense near-field enhancement upon plasmonic coupling in closely packed periodic nanostructure arrays results in a significant improvement in surface-enhanced Raman spectroscopy (SERS)[256], fluorescence[257], surface-enhanced infrared absorption spectroscopy (SEIRA)[258], and photoemission and photodetection[259] signals. Self-assembly is a promising technique to obtain such periodic arrays of nanoparticles in a simple and cost-efficient way.[260] The use of tailored nanoparticles as building blocks allows application-specific functionalities in which the macro-scale interface or bulk phase properties arise from the individual nanoparticles.[261] [262] [263] In recent years, self-assembled films of nanoparticles have gained attention, both in terms of fabrication techniques and novel applications.[264] Air-liquid interfacial assembly, a technique originally devised for monolayer films of organic molecules, also provides a promising route towards nanoparticle arrays. Current approaches based on air-water interfacial assembly such as Langmuir-Blodgett troughs involve precise control of the interfacial pressure through compression and expansion of the interfacial area to tune the film morphology. An alternative liquid phase is ethylene glycol, which has been extensively used by, e.g., Murray and co-workers, for obtaining monolayer films as well as binary nanoparticle arrays with nanoparticles of two different sizes.[265] [266]

In view of the growing importance of self-assembled plasmonic nanoparticle arrays, thorough understanding of their optical properties is important for their application[253]. In this regard, Ag and Au are widely investigated metals with their known advantages and disadvantages. Apart from the direct normal incidence of light on the nanoparticle arrays, the ATR (attenuated total reflection) also known as the Kretschmann configuration is an interesting optical configuration that is commonly used in sensing applications.[267] In this **Chapter 5**, the optical properties of self-assembled arrays of Au and Ag nanoparticles in direct normal incidence and Kretschmann *i.e.* ATR configuration are investigated. The individual optical properties of nanoparticles in close packed arrays and when they are isolated are compared. The computational models are first validated with experimental results obtained for Au and Ag nanoparticle films self-assembled at the air-ethylene glycol interface. The optical properties of the nanoparticle arrays are then studied in terms of their far-field and near-field optical properties.

5.2 Materials and methods

5.2.1 Synthesis of Au nanoparticles and phase transfer

Au nanoparticles were synthesized by the well-known citrate reduction method. A 100 mL 5 mM tri-sodium citrate solution in water was brought to boil before the addition of 1 mL of 25 mM $HAuCl_4$ solution. Following the precursor addition, the solution was kept boiling for 20 more minutes for complete reduction. The as-synthesized nanoparticles were centrifuged at 12500 rpm for 30 minutes and redispersed in 10 mL Milli-Q water to obtain a 10 times more concentrated colloidal solution. The concentrated Au nanoparticles in the aqueous phase were transferred to a toluene phase by using oleylamine as a hydrophobic ligand. 3 mL of toluene were gently added onto the surface of 1 ml of aqueous Au nanoparticle colloid so that the toluene floats over the water as a separate phase. To this bi-phasic liquid, 2 mL of oleylamine in ethanol solution (200 mg in 20 mL ethanol) were added followed by gentle shaking for thorough mixing and then resting for separation of the toluene and ethanol-water phases. After resting the mixture for 24 hours, the nanoparticles appear in the toluene phase above (indicated by a distinct red color) and the ethanol-water phase below becomes transparent. The nanoparticles in the toluene phase were then carefully pipetted out for further processing

5.2.2 Synthesis of Ag nanoparticles and phase transfer

Au nanoparticles were synthesized by the well-known citrate reduction method in presence of tannic acid as reducing agent,as reported by Bastus *et al.*[268] A 100 mL 5 mM tri-sodium citrate and 0.1 mM tannic acid solution in water was brought to a boil before the addition of 1 mL of 25 mM $AgNO_3$ solution. Following the precursor addition, the boiling of the solution was continued for 20 more minutes for complete reduction of the Ag ions. The as-synthesized nanoparticles were concentrated 10 times by centrifuging at 11000 rpm for 30 minutes and re-dispersing in milli-Q water. The concentrated Ag nanoparticles in the aqueous phase were transferred to the toluene phase by a procedure similar to Au nanoparticles as described above. A higher concentration of oleylamine in ethanol (100 mg in 20 mL Ethanol) was used in this case. Also, the oleylamine solution was added first to the nanoparticle colloid before the addition of the toluene phase and mixing.

5.2.3 Self-assembly

The same self-assembly procedure was adopted for both Au and Ag nanoparticles. The nanoparticles in toluene after phase transfer (2 mL) were concentrated by centrifugation at 12000 rpm for 20 minutes to 200 µL and then introduced onto the surface of ethylene glycol contained in a glass container of 30 mm in diameter. The beaker was then immediately covered by a glass plane, allowing toluene to evaporate slowly, **Figure 5.1 (a and b)**. After the complete evaporation of toluene (in 8 hours), the nanoparticle films were transferred to the substrates for further characterization and application. The nanoparticle films were transferred to a glass substrate by careful vertical dip coating

similar to the Langmuir-Blodgett technique. The films were dried under vacuum at 40°C for 48 hours. For bi-layer films, two films were deposited sequentially one on the other.

5.2.4 Characterization

The as-obtained films on glass were characterized by UV-Vis spectroscopy in transmission mode, using a Shimadzu UV2600 apparatus. For the bright field transmission electron microscopy (TEM) of the self-assembled nanoparticles, an FEI Tecnai G2 operated at an accelerating voltage of 200 kV was used. To prepare the TEM samples, the nanoparticle films were immobilized on a hydrophobic copper grid by dip coating before vacuum drying at 100°C for 12 hours.

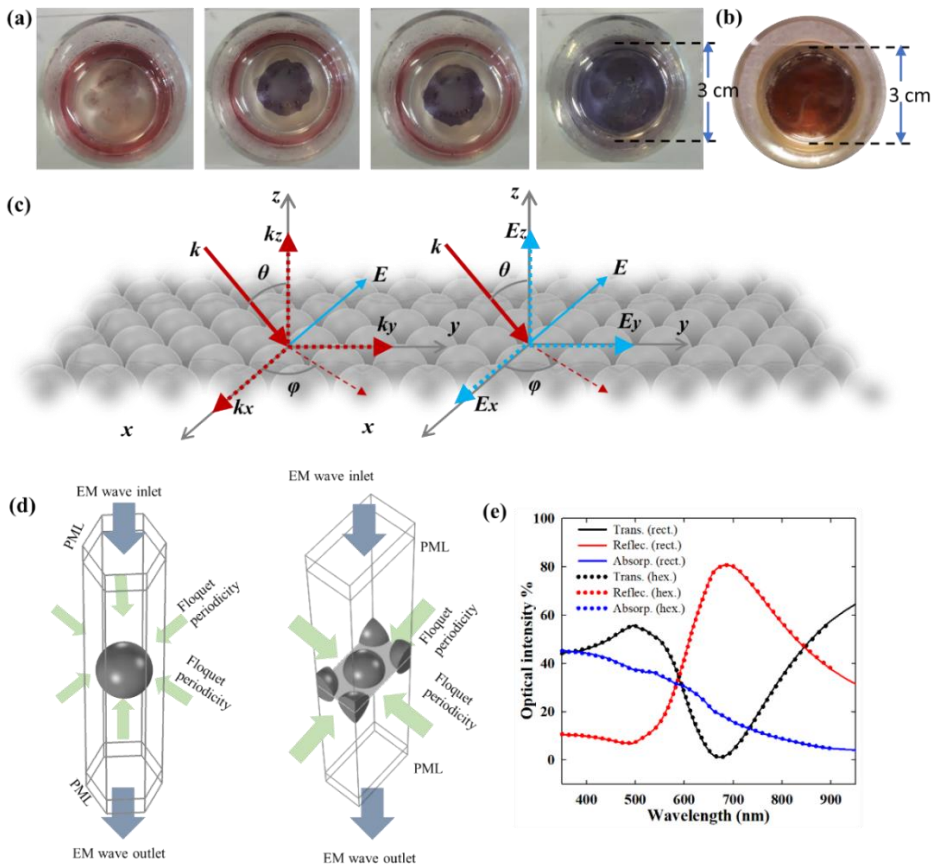

Figure 5.1 (a) Development of the nanoparticle film during the self-assembly of Au nanoparticles over ethylene glycol surface for 8 hours. (b) Self-assembled Ag nanoparticle film after solvent evaporation. (c) Schematic representation of a self-assembled nanoparticle monolayer with incident and electric field wave vectors *w.r.t.* the 3-D cartesian axes. The incident angle θ is varied only for the Krestchmann *i.e.* ATR configuration as discussed later. Otherwise, $\theta = 0^o$ *i.e.* normal incidence in all the cases and the two polarizations at normal incidence: $\varphi = 0^o$ is termed horizontal polarization $\leftrightarrow$ and $\varphi = 90^o$ is termed vertical polarization $\updownarrow$ also shown in **Figure 5.7**, **5.8** and **5.9**. (d) Hexagonal and rectangular unit cells with periodic boundary conditions

implemented as the computational domains in the electromagnetic modeling. (e) Comparison of the results obtained from rectangular and hexagonal computational domains.

5.2.5 Electromagnetic modeling

The computational electromagnetic models for the rigorous solution of the Maxwell's equations are built on an FEM solver COMSOL Multiphysics as mentioned in the previous chapters. The infinite 2D arrays were approximated by a unit cell with periodic boundary conditions on the side walls, **Figure 5.1 (c, d)**. The incident electromagnetic field was introduced from the top with the wave outlet at the bottom for the full-field solution. A perfectly matched layer (PML) was implemented on the top and the bottom boundaries to ensure total absorption of the propagating wave. To ensure the accuracy of the periodic boundary conditions, both rectangular and hexagonal unit cell models were constructed for comparison, **Figure 5.1 (d)** and **(e)**. To ensure the mesh and the domain independence of the numerical results, mesh and domain independence tests were performed with varying mesh elements and domain sizes. The computational domains and the meshing scheme in the rectangular and hexagonal unit cell are shown in **Figure A5.1** and **A5.2**.

5.3 Results and discussions

5.3.1 Characterization of the films and computational validation.

Figures 5.2 (a) and **(b)** show the self-assembled monolayer films of Au and Ag nanoparticles, respectively. The overall packing order of the films is clear from the fast Fourier transformations (FFT) of the images. The average sizes of the nanoparticles were estimated to be 10 ± 2 nm with an interparticle gap of ~2.1 nm for Au and 21 ± 3 nm with an interparticle gap of ~3 nm for Ag nanoparticles, **Figure A5.3** and **A5.4**. While the films, overall, have the hexagonal close packed structure, the lattice is highly polycrystalline with local defects and irregular particle morphology. It has been shown that the presence of excess free ligands and excess nanoparticles (*i.e.* more nanoparticles than needed to cover the complete surface with a monolayer) enhanced the degree of ordering during the self-assembly process.[269 270] Thus, after the water-to-toluene phase transfer, the nanoparticle colloids were concentrated to the desired concentration for self-assembly without further washing steps so that a certain amount of excess free ligands remained in the colloid to facilitate the ordering during self-assembly. As the number of Au nanoparticles (~2×10^{13}) introduced over the ethylene glycol surface was much higher (> 4 times) than the number required (~5×10^{12}) for covering the total surface area available, the excess nanoparticles exert pressure on the film for close packing. For this concentration of nanoparticles, the excess nanoparticles accumulate at the outer boundary of the film resulting in a predominantly monolayer film. A 3-4 times higher concentration on the other hand leads to the formation of large bilayer areas, **Figure 5.2 (a, b)**. In order to ensure a uniform bi-layer, deposition of one monolayer over another is a more effective strategy.

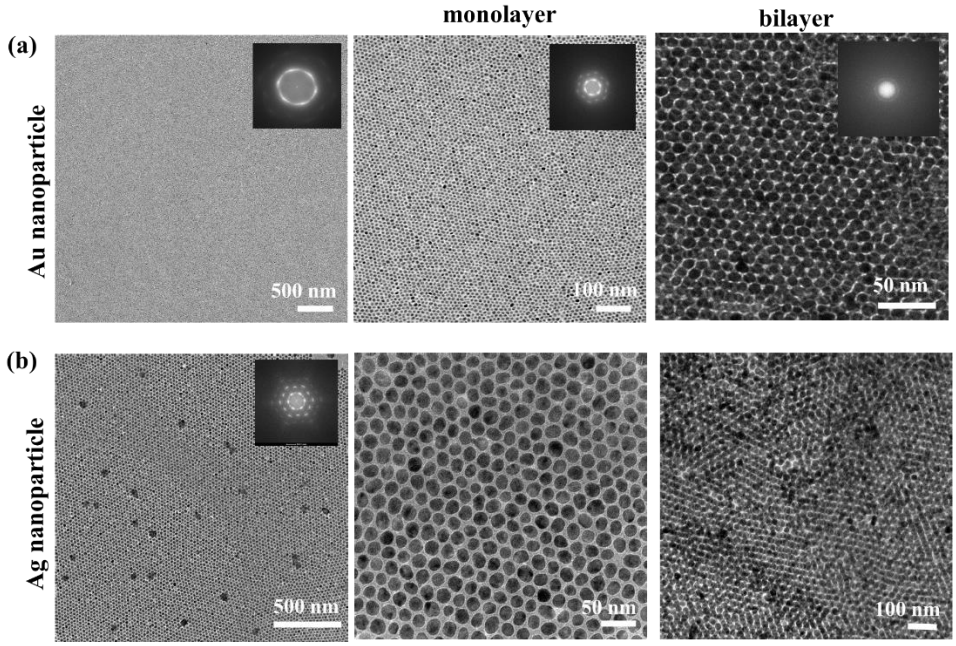

Figure 5.2 TEM images of Au (a) and Ag (b) nanoparticle self-assemblies obtained at the air-ethylene glycol interface. The films at different length scales including both monolayer and bilayer are shown. The FFT (fast Fourier transform) of the images in the inset indicates the periodicity in the Fourier space.

For the electromagnetic modeling of the self-assembled films, the average values of the nanoparticle diameter and interparticle distance in a unit cell with a hexagonal close packing were used. As shown by Schatz and co-worders, the irregularities in the 2D lattice such as polycrystallinity, small variations in the particle diameter and the interparticle gap do not lead to any dramatic changes in the optical properties.[271] Thus, average lattice parameters (given in **Figure 5.3** title) are sufficient to describe the optical properties of the films by electromagnetic models. The experimental transmittance spectra of the monolayer and bi-layer nanoparticle films were measured after immobilization of the films on glass followed by vacuum drying at 40^{o} C for 12 hours. Thus, the refractive index of the medium was assumed to attain a constant value of 1.4 to take in to account the ethylene glycol still present in the film[272]. The optical constants for Au and Ag were taken from Johnson and Christy[273], and Palik[274] respectively. While optical constants of Au reported in various literature have a general agreement, for Ag, there exist some variations, as discussed in detail in earlier chapters. The suitability of the optical constants of Palik in predicting plasmonic response of colloidal nanoparticles has been established by taking into consideration all the influencing factors such as particle polydispersity, skewness of size distribution, morphological irregularity, and so on.[275] **Figure 5.3** shows that the computed spectra largely match with the experimental spectra for all cases with respect to the lattice resonance positions and spectral features. The plasmon bands at ~600 and ~500 nm for Au and Ag nanoparticle films, respectively, are significantly red-shifted from their respective LSPR positions at ~532

and ~408 nm when isolated, confirming the findings from Chapter 4 for smaller clusters. Also, there is no significant difference in the lattice resonance position for monolayer and bilayer configurations. The near-field enhancement plots in the insets show that the films exhibit lattice resonance by strong near-field coupling. As small nanoparticles have low scattering intensity, far-field coupling is negligible or very low in these cases. For both Au and Ag, the near-field enhancement is stronger for monolayers as compared to bilayers. The suppressing effect of the lower layer of the bilayer stems from the reflection from the lower layer that interferes destructively with the field around the top layer.[253] Since the top layer of the Ag nanoparticle bi-layer is highly reflective with little transmission to the bottom layer (near-field in **Figure 5.3 (d)**), the suppressive effect on the near-field is significantly less than in the case of a Au nanoparticle bilayer film. In the simulated spectra of **Figure 5.3 (c)** for Ag nanoparticles, a mild shoulder is observed at ~400 nm, which in the experimental spectra seems to be hidden with only a mild inflection in that wavelength region. While the implication of this feature is not immediately clear at this point, some interesting implications of it in the near-field and detailed far-field (transmittance, absorptance and transmittance) spectra will be discussed in the later sections.

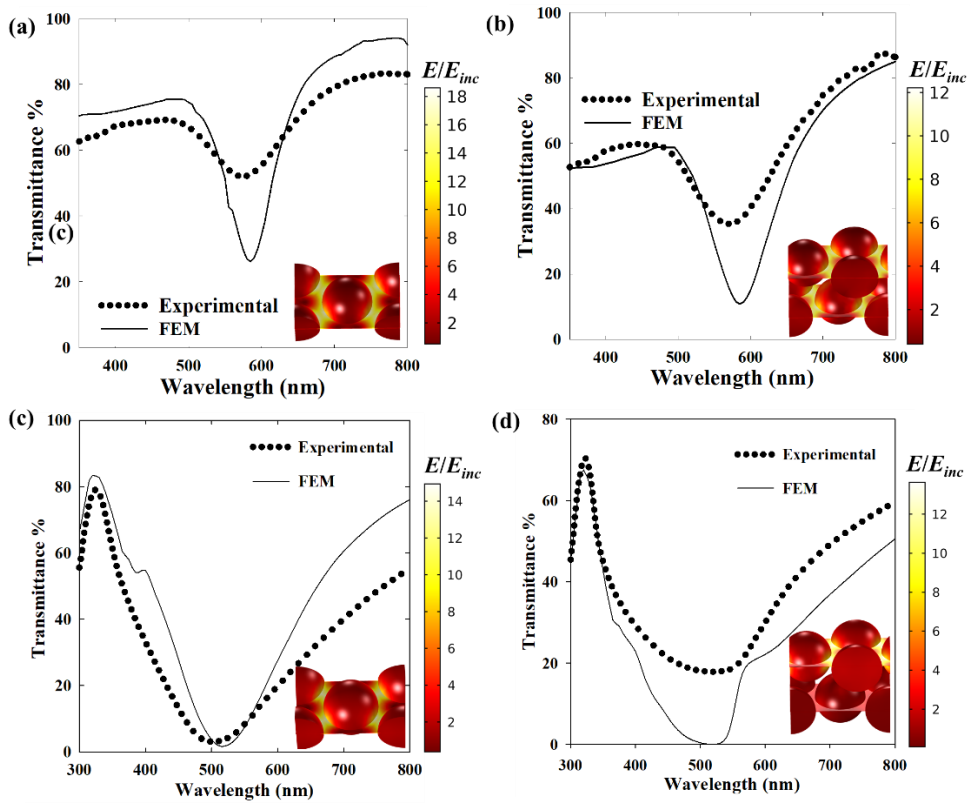

Figure 5.3 Experimental transmittance spectra compared with computed spectra for (a) Au nanoparticle monolayer (b) Au nanoparticle bi-layer (c) Ag nanoparticle monolayer (d) Ag nanoparticle bilayer. The near-field enhancement with respect to the incident field is shown in the inset of each plot. The dimensions for the electromagnetic models

were taken from the TEM images (**Figure 5.2**). Au nanoparticle diameter and interparticle gap: 10 nm and 2 nm, Ag nanoparticle diameter and interparticle gap: 20 and 2 nm. $\theta = 0^{o}$ and $\varphi = 0^{o}$ in all the cases according to the schematic **Figure 5.1**. The irradiance is from the top normal to the plane of the film.

5.3.2 Far-field optical properties in direct normal incidence

As the interparticle gap in a close packed nanoparticle array increases, the particle-particle coupling naturally weakens resulting in increasingly weaker lattice resonance. Also, gradually, the individual plasmon modes (predominantly dipolar) becomes more prominent as shown in **Figure 5.4** for Au and **Figure 5.5** for Ag nanoparticles. Thus, the plasmon band which is red-shifted due to the lattice resonance, now blue shifts as the nanoparticles become distant from one another. At a small interparticle distance, the transmittance is naturally low, **Figure 5.3 (a)**, but it is mainly the reflectance that makes the highest contribution. Thus, the plasmonic enhancement by lattice resonance is not necessarily useful in applications where radiation/reflection losses are not desirable. For instance, in solar energy harvesting, a packing too dense will lead to the reflection of most of the incident energy. For 20 nm Au nanoparticles in water, an interparticle gap of at least 32 nm is necessary to ensure minimum reflection losses while still maintaining considerable absorption for complete harvesting of the light in multiple layers. Again, at large interparticle gaps, the long wavelength light remains inaccessible. As shown in **Figure 5.4 (d)**, the individual absorption cross sections of the nanoparticles approach the Mie solution for isolated nanoparticles as the interparticle distance increases. The individual absorption cross section of 20 nm Au nanoparticles in a closely packed array is significantly lower with a weak plasmon band in contrast to isolated nanoparticles with only absorption and almost no scattering. Thus, the excitation of the plasmons in nanoparticles closely packed as an array leads to changes in the plasmon relaxation pathways with the radiative damping dominating over non-radiative damping. This has strong implications in plasmonic hot electron driven processes as the hot electrons typically result from non-radiative damping.[276]

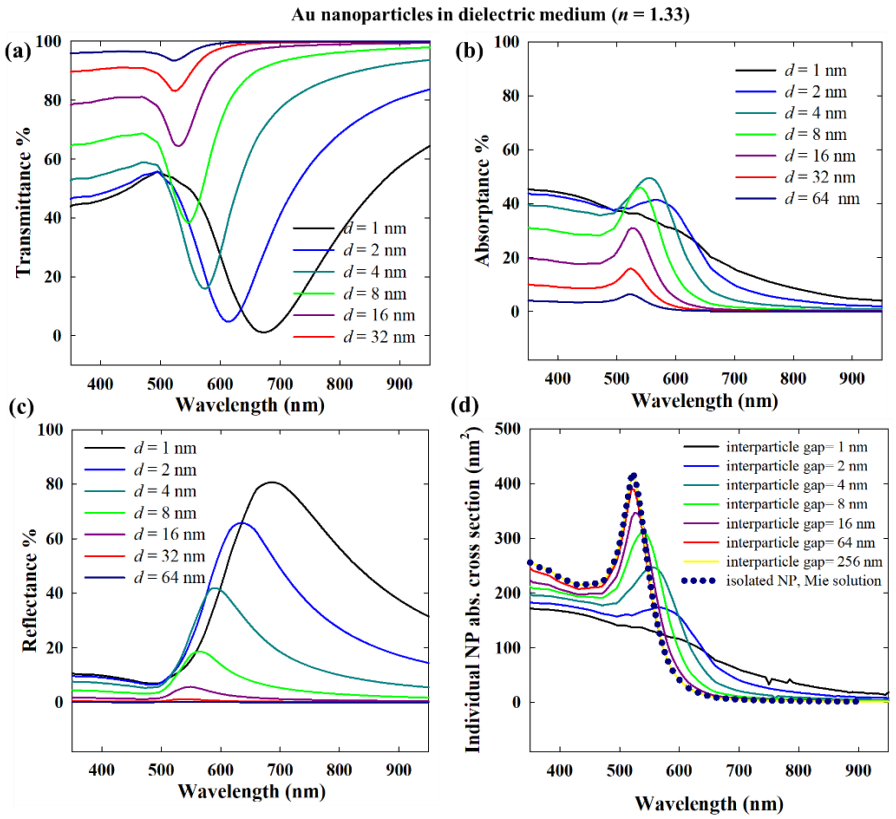

Figure 5.4 Effect of the interparticle gap in monolayer hexagonal close packed arrays of 20 nm Au nanoparticles in dielectric medium (n = 1.33): (a) transmittance (b) absorptance (c) reflectance (d) per particle absorption cross section. The incidence is normal to the plane of the film *i.e.* $\theta = 0^{o}$ and $\varphi = 0^{o}$ in all the cases.

The plasmonic response of Au nanoparticles in visible light is dampened by the interband transitions due to the low interband transition energy of Au (2.3 eV) that overlaps with the visible spectrum.[277] On the other hand, the response of Ag nanoparticles is dominated by only free electron excitation in the visible range, hence, resulting in more efficient plasmonic excitation. In 20 nm diameter nanoparticles, while Au nanoparticles have almost no radiative damping *i.e.* scattering (1%< of total extinction), Ag nanoparticles have a small contribution (~5% of total extinction) from scattering at the localized plasmon resonance. This implies that, although 20 nm Ag nanoparticles in 2D arrays will exhibit lattice resonance mainly by near-field coupling, weak far-field coupling is also present due to the interaction of the scattered fields. As Ag nanoparticles individually have significantly higher optical cross sections than Au, relatively higher optical intensities are maintained for the same interparticle gap *i.e.* packing density, **Figure 5.5 (a, b, c)**. With decreasing interparticle gap, the strengthening plasmonic coupling is evident from the large bands in transmittance (dip) and reflectance (peak). Also, as shown in **Figure 5.5 (d)**, a greater distance as compared to Au nanoparticles is required for Ag nanoparticles to become completely isolated.

This is due to the far-field coupling of the Ag nanoparticles as confirmed by the near-field plots in the following discussion. Interestingly, if **Figure 5.5 (a)** and **(b)** are compared, the transmittance and the absorption spectra for the interparticle gap = 1 nm or 2 nm show two distinct features. While the lowest transmittance dip is at 600 nm for the 1 nm interparticle gap case, the absorptance has the highest peak at around 400 nm with only a broad band at 600 nm. In the transmittance and reflectance, a small shoulder at ~400 nm is observed. Thus, the absorption peak at 400 nm also indicates a strong plasmon resonance that relaxes mainly non-radiatively. For an interparticle gap of 2 nm, this peak in all three transmittance, absorptance and reflectance, is much weaker. While the experimental transmittance spectra for 20 nm nanoparticles with 2 nm interparticle gap in **Figure 5.3 (c)** does not show this shoulder clearly, the presence of a weak inflection can be observed.

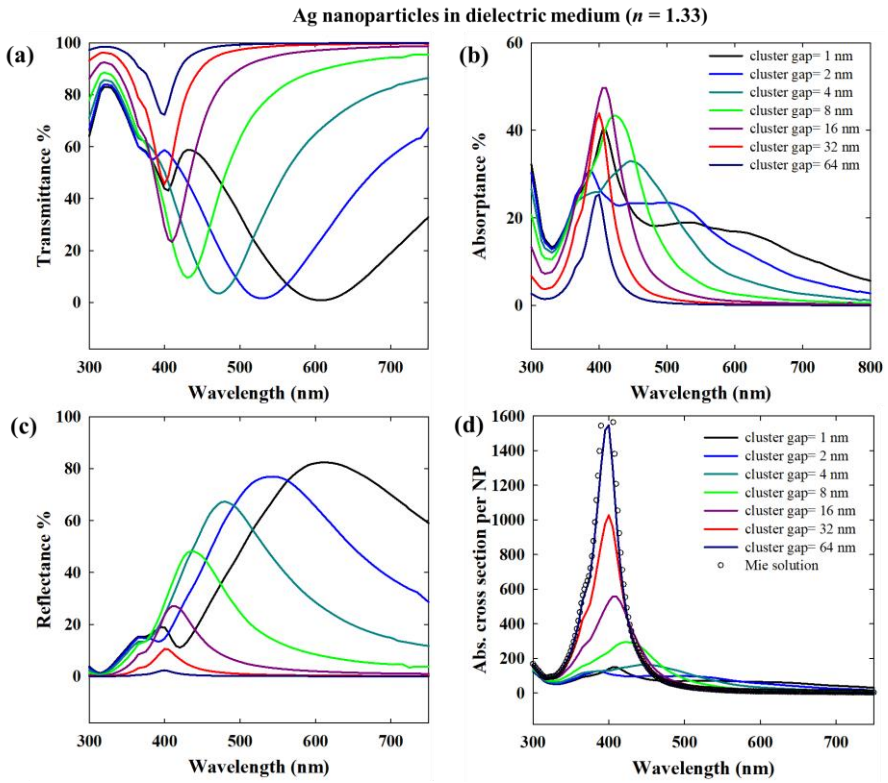

Figure 5.5 Effect of interparticle gap in monolayer 2D hexagonal close packed arrays of 20 nm Ag nanoparticles in dielectric medium (n = 1.33): (a) transmittance (b) absorptance (c) reflectance (d) per particle absorption cross section. The incidence is normal to the plane of the film *i.e.* $\theta = 0^{o}$ and $\varphi = 0^{o}$ in all the cases.

In contrast to a dielectric water medium (n = 1.33) as shown in **Figure 5.4** and **5.5**, in vacuum, the interparticle coupling is suppressed due to the absence of a dielectric environment. When the surrounding medium is a dielectric, it also polarizes with the plasmonic nanoparticles in response to the incident field, thereby enhancing the interparticle coupling.[278] [279] Thus, in vacuum (n = 1), it takes a shorter interparticle

distance for the nanoparticles to be isolated from interparticle interactions, **Figure 5.6**. Also, the individual nanoparticle absorption cross section varies differently for Au and Ag. For small interparticle gaps *i.e.* strong plasmonic coupling, the individual absorption intensity of 20 nm Au nanoparticles is significantly higher than in the isolated case. This implies stronger contribution of non-radiative damping as well as interband transitions as compared to radiative damping of the excited plasmons. In contrast, strongly coupled Ag nanoparticles have significantly lower absorption as radiative damping of the plasmons dominates as compared to non-radiative damping that leads to thermal dissipation. In the application of the Au nanoparticles in gaseous phase, strong interparticle coupling can thus enhance the photothermal processes. While for Ag nanoparticles, the implications of interparticle coupling in both gaseous and dielectric medium remains basically the same.

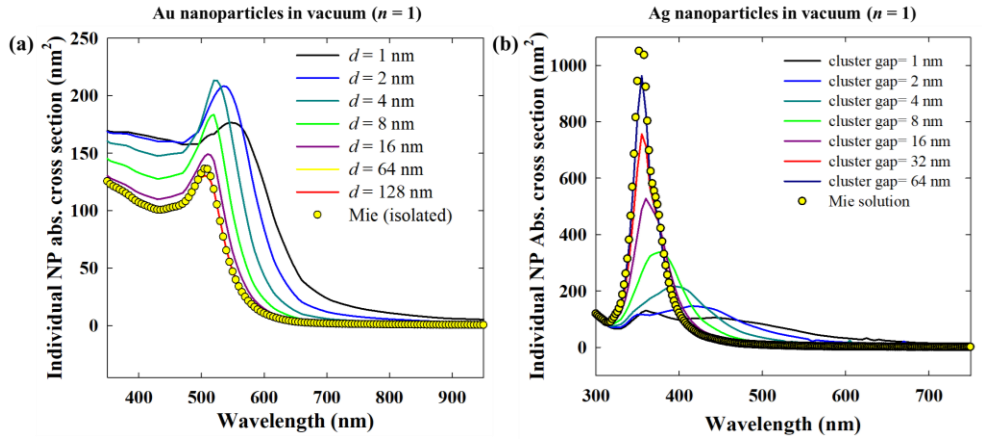

Figure 5.6 Effect of interparticle gap in monolayer 2D hexagonal close packed arrays of 20 nm Ag nanoparticles in vacuum (n = 1) comparing per particle absorption cross section. The incidence is normal to the plane of the film *i.e.* $\theta = 0^{o}$ and $\varphi = 0^{o}$ in all the cases.

5.3.3 Near-field optical properties in direct normal incidence

Strong amplification of the evanescent electric field close to the resonating plasmonic nanoparticles is a characteristic optical effect of plasmonic nanoparticles. In this section, the near-field profiles with varying interparticle gap are discussed first, followed by the near-field spectra. The effect of polarization for $\varphi = 0^{o}$ and $\varphi = 90^{o}$ is discussed as the near-field properties are polarization dependent, while far-field properties obey the rotational symmetry.

This near-field enhancement is much stronger for isolated Ag nanoparticles than for isolated Au nanoparticles, as plasmons are significantly damped by interband transitions in Au.[280] In any case, it is known that the plasmonic coupling between adjacent nanostructures results in even stronger near-field enhancement at the interparticle gap.[281] In plasmonic nanoparticle arrays, the lattice resonance by near-field interactions also results in extremely high near-field enhancement relative to isolated nanoparticles,

Figure 5.7 and **5.8**. The maximum intensity of the near-field enhancement increases with decreasing interparticle gap. However, at the same time, the enhanced near-field, which is a non-propagating standing wave, also gets limited to smaller space as the interparticle gap shortens. Such high enhancement into small space is, thus, promising for single molecule detection by signal enhancement[282]. The near-field enhancement also indicates the strength of plasmonic coupling with increasing interparticle distance. At 64 nm interparticle spacing, the 20 nm Au nanoparticles become completely decoupled from each other with near-field enhancement as strong as that for individual nanoparticle, **Figure 5.7** and **A5.5**.

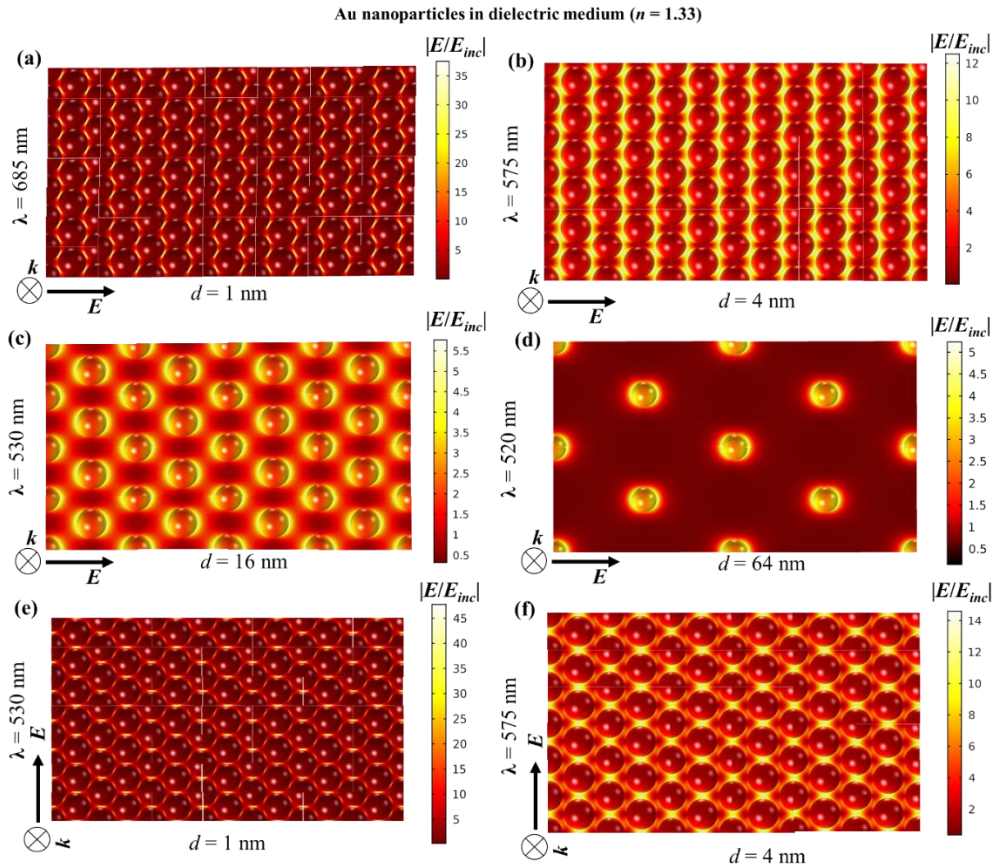

Figure 5.7 Near-field enhancement *w.r.t* the incident field for 2D hexagonal monolayer array of 20 nm Au nanoparticle in dielectric medium (n = 1.33) for different interparticle gaps: (a) 1 nm (b) 4 nm (c) 16 nm and (d) 64 nm. Figure (e) and (f) shows the near-field profiles at vertical polarization for interparticle gaps 1 and 4 nm respectively. At normal direct incidence, Figure (a, b, c, d) are for horizontal polarization *i.e.* $\varphi = 0^{o}$ and vertical polarization *i.e.* $\varphi = 90^{o}$, while $\theta = 0^{o}$ in all cases.

Although individual Ag nanoparticles have stronger near-field enhancement than Au nanoparticles, in a close packed array, this advantage vanishes. As shown in **Figure 5.8 (a, b)**, the maximum intensity of the near-field enhancement in the Ag nanoparticle

array is of the same order as that of Au nanoparticle arrays in **Figure 5.7 (a, b)**. However, as the interparticle distance increases, the difference between both cases increases and Ag nanoparticles tend to show significantly higher field enhancement. At an interparticle distance of 64 nm, Ag nanoparticles also have near-field properties similar to individual particles. Thus, for Ag nanoparticles, depending on the size, there lies an optimum interparticle distance for which the packing density is high enough for efficient surface coverage without losing the advantage of its stronger enhancement over Au. Rahmani *et al*. showed for a plasmonic oligomer that the far-field spectra (transmittance, reflectance and absorptance) are not influenced by the angle of polarization at normal incidence, while the near-field characteristics do change with the polarization.[283] It is shown that since the near-field profiles are determined by the particular mode superpositions excited by the incident field, they vary with the polarization. In contrast, due to the rotational symmetry in the oligomers, the far-field properties are unaffected by the polarization. A similar trend can also be seen in **Figure 5.7** and **5.8** for Au and Ag nanoparticles respectively, where the horizontal and vertical (*w.r.t*. the page layout) polarization gives rise to starkly different near-field profiles with different maximum values. The consequence of this can be interesting in surface enhanced spectroscopy applications of self-assembled nanoparticle films. The complete near-field spectra, the maximum value and the average values, for self-assembled nanoparticle films are discussed along with the polarization dependence in **Figure 5.9**.

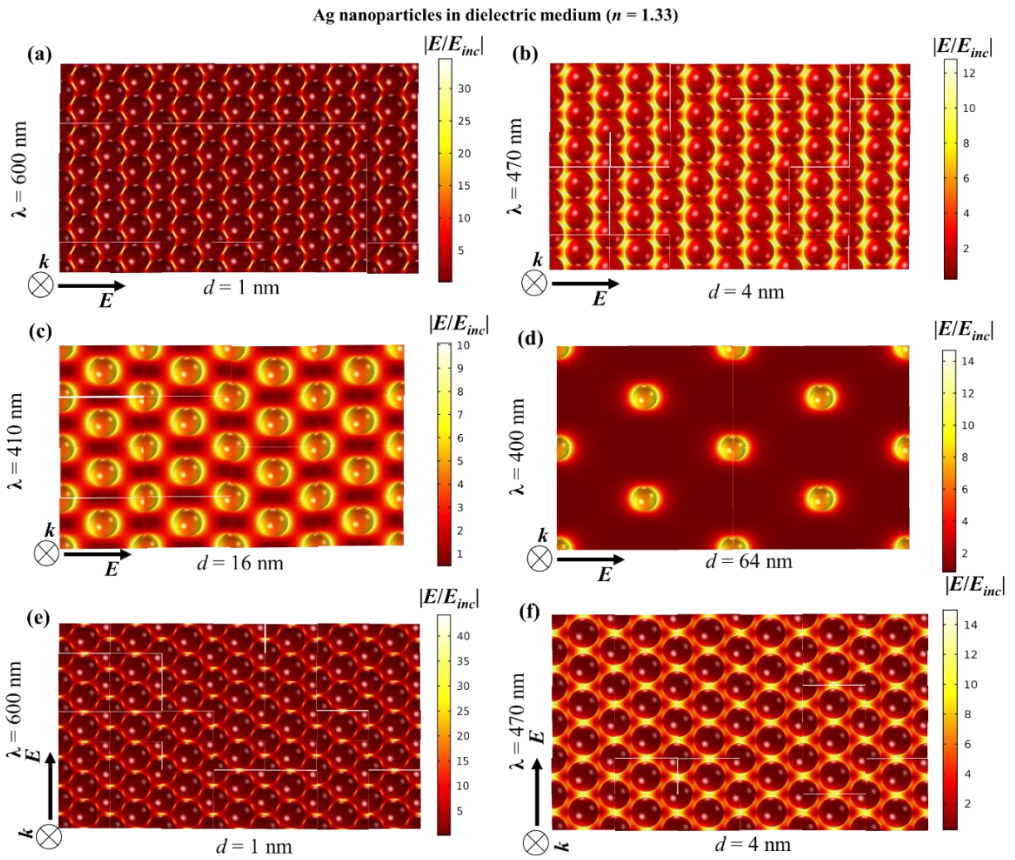

Figure 5.8 Near-field enhancement *w.r.t.* the incident field for 2D hexagonal monolayer array of 20 nm Ag nanoparticle in dielectric medium (n = 1.33) for different interparticle gaps: (a) 1 nm (b) 4 nm (c) 16 nm and (d) 64 nm. Figure (e) and (f) shows the near-field profiles at vertical polarization for interparticle gaps 1 and 4 nm respectively. At normal direct incidence, Figure (a, b, c, d) are for horizontal polarization *i.e.* $\varphi = 0^o$ and vertical polarization *i.e.* $\varphi = 90^o$, while $\theta = 0^o$ in all cases.

While the near-field profiles are different for two perpendicular polarizations, the far-field response should be polarization independent. This is obvious from **Figure 5.9 (a)** and **(b)**, where the reflectance spectra for vertical and horizontal polarization merge together for both Au and Ag nanoparticles. It has already been seen in **Figure 5.7** and **5.8** that the near-field profiles and the range are both different for the two directions of polarization. The near-field maximum spectra in **Figure 5.9 (c)** and **(d)** show the complete trend in the wavelength range. Clearly, the near-field maximum is significantly higher for the vertical polarization (*w.r.t.* to the page layout) than the horizontal polarization in the plane cutting through the centre of the nanoparticles along the plane of the film. Since the interparticle distance is also the lowest at this cut-plane, it is expected that the maximum near-field enhancement value on this cut-plane is also the maximum value overall. The near-field enhancements averaged over the cut-plane for horizontal and vertical polarization are however much closer as the near-field profiles are only differently distributed with respect to the incident polarization in the two cases and the average effect is expectedly low. **Figure 5.9 (c)** and **(d)** also show that for Au, the high near-field enhancement due to lattice resonance is observed only at wavelengths over 500 nm. However, for Ag, a peak in the near-field spectra is observed close to 400 nm. As discussed above, this resonance mode is observed in the far-field spectra also in the form a shoulder in transmittance and reflectance. While in the absorptance, a strong global maximum is observed in that region. Thus, it is interesting that an overall strong near-field enhancement is obtained over the entire visible range in the case of close packed Ag nanoparticle assemblies.

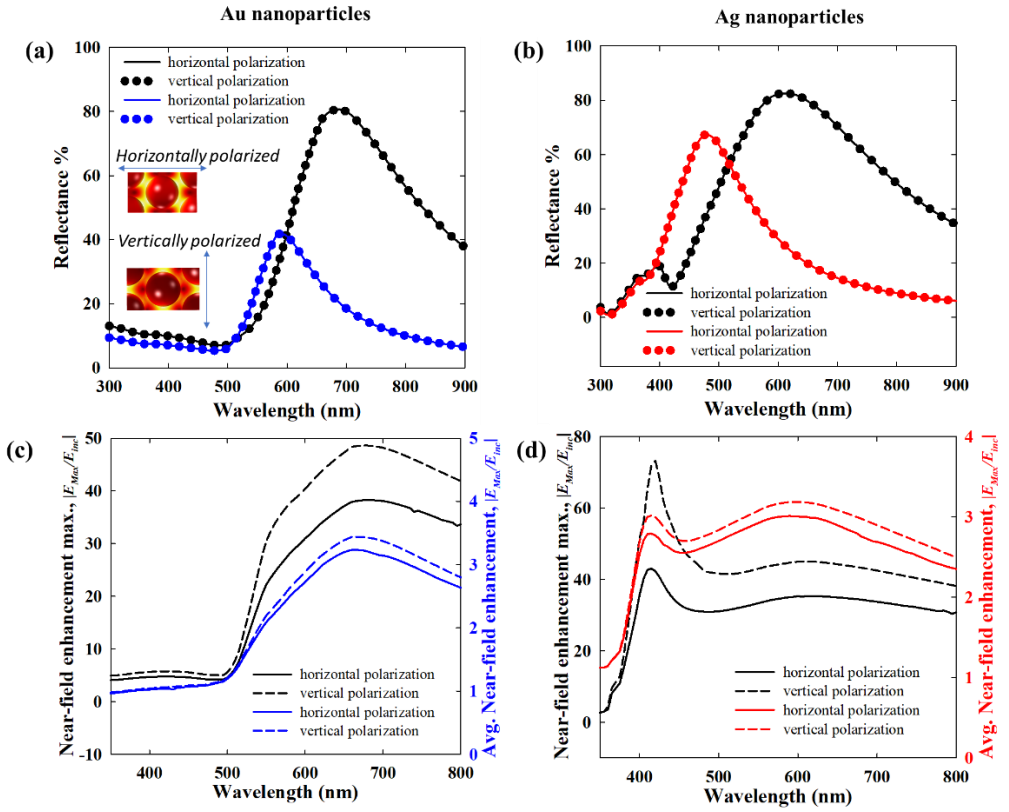

Figure 5.9 Comparison of reflectance spectra of Au (a) and Ag (b) nanoparticle assemblies under normal illumination with 1 nm and 4 nm interparticle gaps at two perpendicular polarizations. The maximum near-field enhancement spectra and average near-enhancement spectra of Au (c) and Ag (d) nanoparticle assemblies (shown only for interparticle gap of 1 nm) at two perpendicular polarizations. Figure (c): black plots are for left *y*-axis, blue plots are for right *y*-axis. Figure (d): black plots are for left *y*-axis, red plots are for right *y*-axis. From **Figure 5.1**, horizontal polarization is $\varphi = 0^{o}$ and vertical polarization is $\varphi = 90^{o}$, while $\theta = 0^{o}$ in all cases. (embedding medium, $n = 1.33$)

5.3.4 Effect of substrate in direct normal incidence

While the discussion so far involved only the nanoparticle arrays/films, in real applications the substrate onto which the films are immobilized, also plays an important role. **Figure 5.10** elucidates the effect of a substrate in terms of reflectance and near-field maximum spectra by introducing a dielectric substrate of $n = 1.5$ (**Figure 5.10 (a)**), a refractive index value typical for glassy materials. The effect of the dielectric substrate is mainly manifested in the reflectance. In the presence of the nanoparticles, the wave transmitted through the nanoparticle array undergoes reflection and transmission. This reflected wave again interacts with the nanoparticles to give rise to a net effect. Thus, it is expected that as the interparticle gap decreases *i.e.* the transmitted wave weakens, the effect of the substrate also decreases.

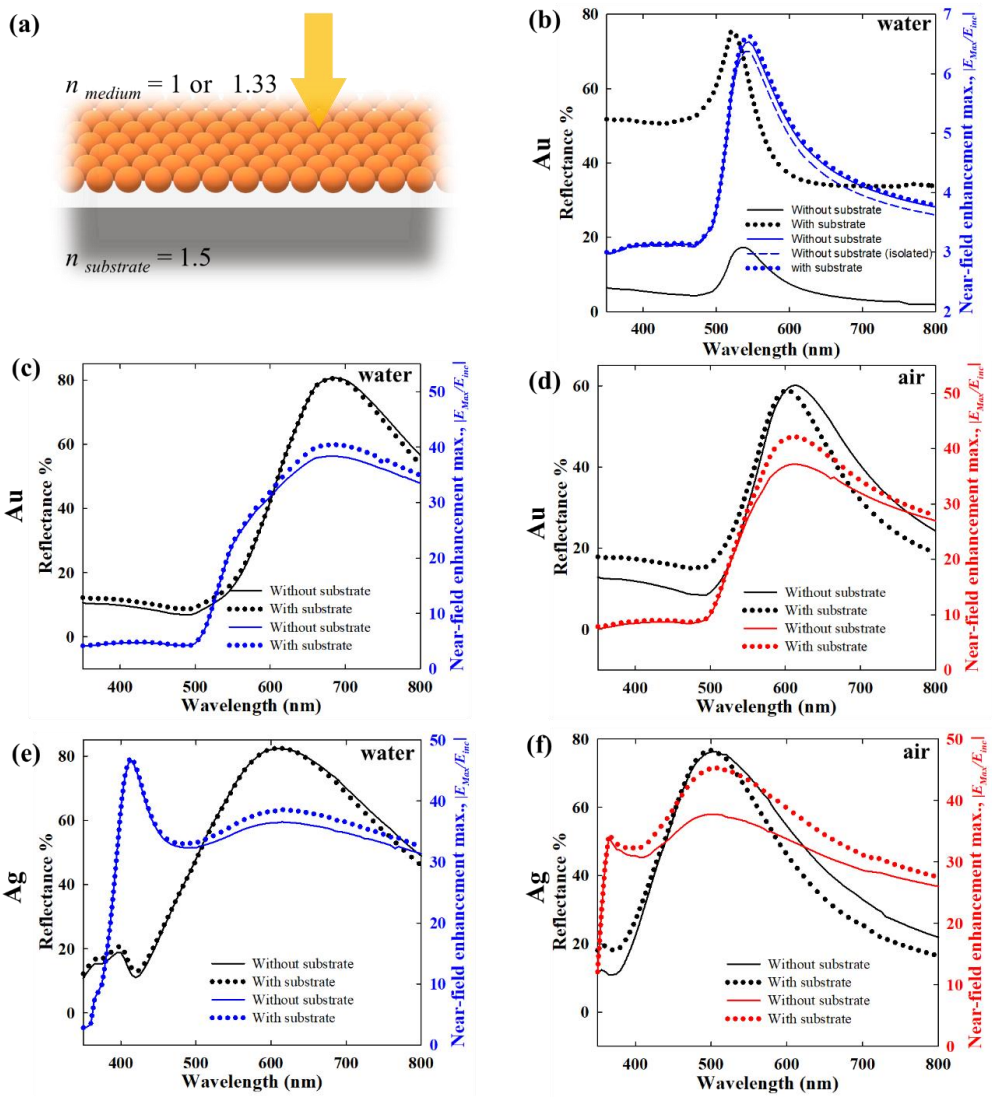

Figure 5.10 (a) Schematic of nanoparticles on substrate with normal direct incidence. (b) Effect of substrate (n_{sub} = 1.5, n_{medium} = 1.33) on reflectance and near-field enhancement maximum spectra for Au nanoparticle assembly with large interparticle distance, 64 nm. Effect of substrate for (c) n_{medium} = 1.33 and (d) n_{medium} = 1 with close packed Au nanoparticle assembly *i.e*. interparticle distance 1 nm, comparing reflectance and near-field enhancement maximum spectra. Effect of substrate for (e) n_{medium} = 1.33 and (f) n_{medium} = 1 with close packed Ag nanoparticle assembly *i.e*. interparticle distance 1 nm, comparing reflectance and near-field enhancement maximum spectra.

As shown in **Figure 5.10 (b)**, the effect of substrate for an isolated Au nanoparticle, *i.e*. interparticle distance 64 nm, is quite strong when the embedding medium is a dielectric. With substrate, the reflectance is shifted by a significant margin from that without substrate, however, without any significant change in the spectral features. On the other hand, the near-field maximum spectra show very small differences between the with-

and-without substrate cases. This corroborates the point that the effect of the substrate is majorly an enhanced reflectance, which weakly influences the plasmonic response of the nanoparticles. For close packed films as shown in **Figure 5.10 (c)** and **(d)**, irrespective of the embedding medium being air or water, the effect of the substrate remains, however, quite small. A similar trend is also observed for Ag nanoparticles as shown in **Figure 5.10 (e)** and **(f)**.

5.3.5 Far-field and near-field optical properties in the Kretschmann (ATR) configuration

As shown in **Figure 5.11 (a)**, in the Kretschmann configuration, the incident beam comes from a high refractive index medium and the nanoparticle film (or any substance of interest being probed) is on the other side where the medium has a lower refractive index. The incoming beam is incident at an angle higher than the critical angle for the given set of refractive indexes, so that it is reflected by total internal reflection at the interface. Thus, the resulting standing evanescent wave on the lighter medium interacts with the object of interest. In order to excite the surface plasmons in a planar thin film, it is necessary to implement specific geometric arrangements such as the Kretschmann *i.e*. ATR configuration to compensate for the momentum mismatch between the incident photon and the plasmon wave.[284] In contrast to a thin planar Au films, for a nanostructure array like a self-assembled film, the lattice resonance can be excited by direct illumination from a vacuum or dielectric medium. It is however interesting to investigate the excitation of the lattice plasmons in the Kretschmann configuration as many sensing applications utilize this arrangement with completely different underlying optics. Firstly, when the incident beam undergoes total internal reflection in the Kretschmann configuration, the plasmonic excitation of the nanoparticle film is only possible by the standing evanescent field on the other side of the prism coupler, **Figure 5.11 (a)**. As there is no transmission possible, the reflected intensity is only due to the absorption by the film due to the plasmonic excitation. Also, the evanescent fields due to *s* and *p*-polarized (TE and TM polarized) light have totally different directionality. In ATR-FTIR spectroscopy, it has been shown that while the *p*-polarized light can probe the vibration modes parallel and perpendicular to the sample film, the s-polarized beam probes solely the components of the vibrational modes parallel within the plane of the sample film.[285] The accuracy of the angle-resolved electromagnetic models was ascertained by comparison with analytical spectra from Fresnel coefficients. As shown in **Figure 5.11 (b)**, the computed spectra for *p* and *s*-polarized incidence in the ATR configuration without nanoparticles matches perfectly with the analytical solution. The nanoparticles were introduced in the same numerical models for further calculations. From a computational point of view, obtaining solutions for the direct incidence at different angles poses significant difficulties due to the Rayleigh Wood's anomalies.[286] [287] These surface wave anomalies occur at certain wavelengths due to the diffracted waves that arises due to the periodicity of the metallic structures, and propagate tangentially to the surface of the nanostructure array.[288] The tangential wave propagation poses difficulties with the periodic boundary conditions on the side walls of the unit-cell domain. While for the Kretschmann or ATR configuration, such

difficulties were not encountered in the numerical solution. The consistency in the computed spectra in the following discussion further corroborates this point.

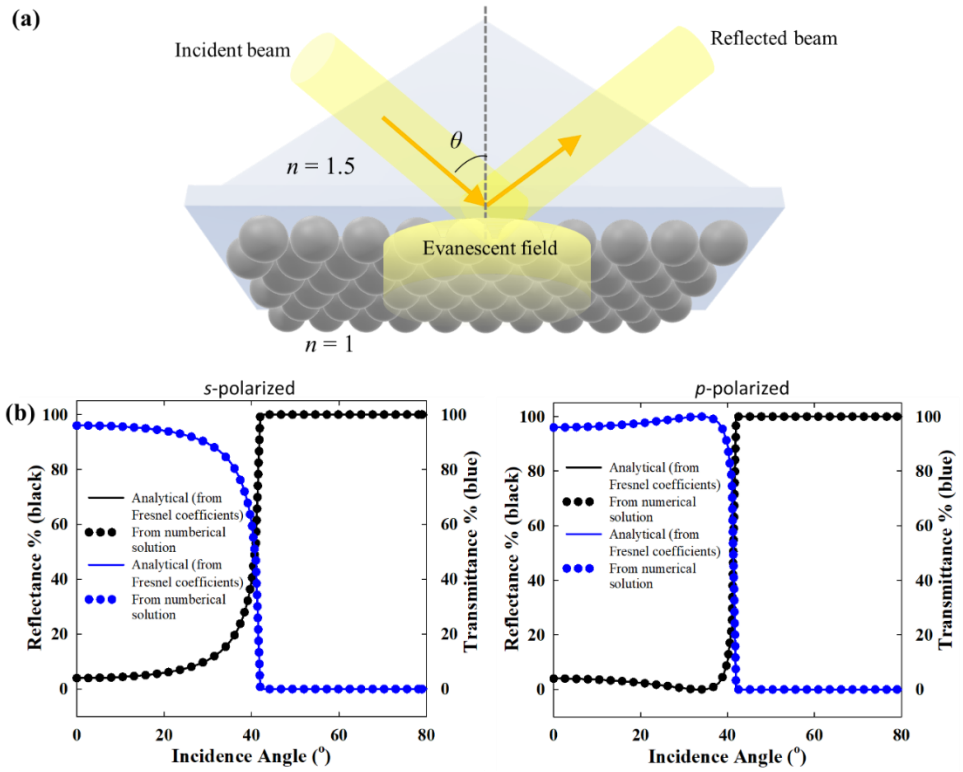

Figure 5.11 (a) Schematic representation of a plasmonic nanoparticle film in the Kretschmann *i.e.* ATR configuration. (b) Validation of the angle resolved electromagnetic models of the Kretschmann configuration (without nanoparticles) by comparison with optical spectra obtained from the Fresnel coefficients for *p*-polarized *i.e.* TM polarized and *s*-polarized *i.e.* TE polarized incidence.

Figure 5.12 and **5.13** compare the optical spectra of close packed Au and Ag nanoparticle monolayer films in the Krestchmann configuration for both *p*- and *s*-polarized incident beams at different incident angles. For the combination of a glass prism (n = 1.5) and air (n = 1) the critical angle of incidence is 41.8°. Thus, for incident angles above 41.8°, the transmittance becomes zero and the incident power goes only to absorptance and reflectance, **Figure 5.12 (a)** and **5.13 (a)**. Up to 30°, the transmittance, reflectance and absorptance spectra remain qualitatively similar to the spectra for normal direct incidence as the refracted wave that interacts with the nanoparticles has similar properties as the incident wave. At 45° incidence and onwards, the lattice plasmons are excited by the evanescent wave. The lattice resonance of the nanoparticle array (**Figure 5.12** and **5.13**) excited by the evanescent wave is marked by the reflectance dip in agreement with Manera *et al.*[289], which is red-shifted from individual LSPR of the nanoparticles (in air). Expectedly, the *p*-polarized and *s*-polarized incident waves tend to have increasing differences in the optical spectra with increasing incident

angle. Firstly, the evanescent field that decays exponentially with the distance from the interface, has a penetration depth for *p*-polarized incidence twice that for *s*-polarized incidence. Also, with increasing angle of incidence and decreasing wavelength, the penetration depth decreases strongly. Thus, at 75°, while the *p*-polarized wave has a strong absorbance, for *s*-polarized incidence, the absorbance is weak with strong reflection. The *p*- and *s*-polarized spectra in the Kretschmann configuration have qualitative similarities with the *p*- and *s*-polarised spectra of plasmonic nanostructure arrays under direct angular incidence.[290] In both the cases, the *s*-polarized incidence, overall, has a higher reflectance than *p*-polarized incidence. Hence, the absorption is stronger for *p*-polarized incidence than for *s*-polarized incidence. The strong and broadband absorptance at larger incident angle for *p*-polarized incidence can be interesting for light harvesting applications. As shown in **Figure 5.4** for a close packed *i.e*. interparticle distance = 1 nm nanoparticle array in direct normal incidence, the strong radiative damping of the plasmons excited at lattice resonance results in strong reflection and low absorptance. In contrast, in the Kretschmann configuration, the damping pathway is now switched to the non-radiative damping, which is again advantageous for light harvesting applications. The near-field enhancement of the Au nanoparticle film for *p*-polarized incidence and incidence angle of 75° in **Figure 5.12 (b)** shows that the in-plane interparticle coupling is as strong as the direct normal incidence on nanoparticles in air (over glass substrate, **Figure 5.10 (d)**). Since the in-plane lattice resonance mode is very strong, the excitation of the lattice plasmons by the in-plane component of the evanescent field (due to *p*-polarized incidence) dominates the overall response at 590 nm wavelength. At 400 nm, the interband transitions damp the near-field response *i.e*. the overall plasmonic excitation and the absorptance has a significant contribution from direct interband transitions. Again, in **Figure 5.12 (b)**, the near-field enhancement for *s*-polarized incidence at 590 nm is due to the evanescent field confined entirely in the plane of the nanoparticle array. At 475 nm, however, the near-field enhancement is significantly lower due to interband transitions. It is important to note that the near-field enhancement here is not with respect to the incoming incident field, but with respect to the resulting background evanescent field. The background evanescent electric field is weaker in the *s*-polarized case due to faster attenuation.

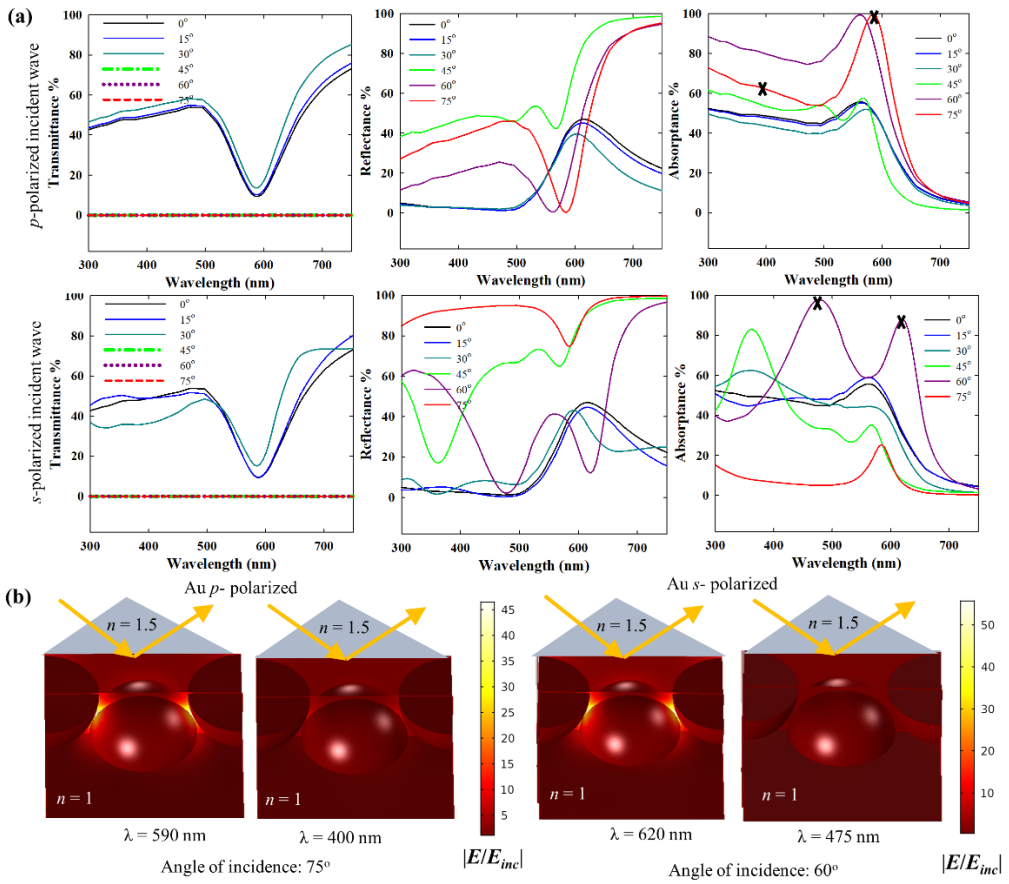

Figure 5.12 (a) Transmittance, reflectance and absorptance spectra of a close packed 20 nm Au nanoparticle film in the Kretschmann *i.e.* ATR configuration for *p*- and *s*-polarized incident wave, and varying incident angle. In the Kretschmann configuration, $n = 1.5$ for the denser medium, $n = 1$ for the lighter medium and interparticle gap: 1 nm. (b) Near-field enhancement with respect to the background evanescent field (in absence of the nanoparticles) for *p* and *s*-polarized (or TM and TE polarized) incidence.

In the optical spectra, apart from the plasmonic lattice resonance band, the features in the lower wavelength range arise from the interplay between the penetration depth of the evanescent field which depends on the polarization, angle of incidence, and wavelength, and the optical properties of the nanoparticles that depends on both intraband and interband transitions. The results in **Figure 5.13** for Ag nanoparticles also follow similar trends as Au nanoparticles. However, the absence of interband transition in Ag in the visible range alters the lattice resonance conditions as well as the overall optical properties. Up to 30° incidence angle, the optical spectra are similar to direct normal incidence, beyond which the optical spectra are due to the plasmonic excitation by the evanescent wave. The lattice resonance at 75° incidence is at around 500 nm for both *p* and *s*-polarized excitation . The weaker optical intensity for *s*-polarization can again be attributed to the faster attenuation of the evanescent field. For 60° incidence,

however, the spectra for *p*- and *s*-polarized incidence are quite different. For *s*-polarized incidence, the plasmon resonance band is at around 590 nm, while for *p*-polarized incidence the plasmon band is below 500 nm. For both Ag (and Au) nanoparticles, the reflectance and absorptance spectra in the Krestchmann configuration have multiple features due to the interplay between the variable penetration depth of the evanescent field which is dependent on the incidence angle, wavelength and polarization, and the optical properties of the materials.

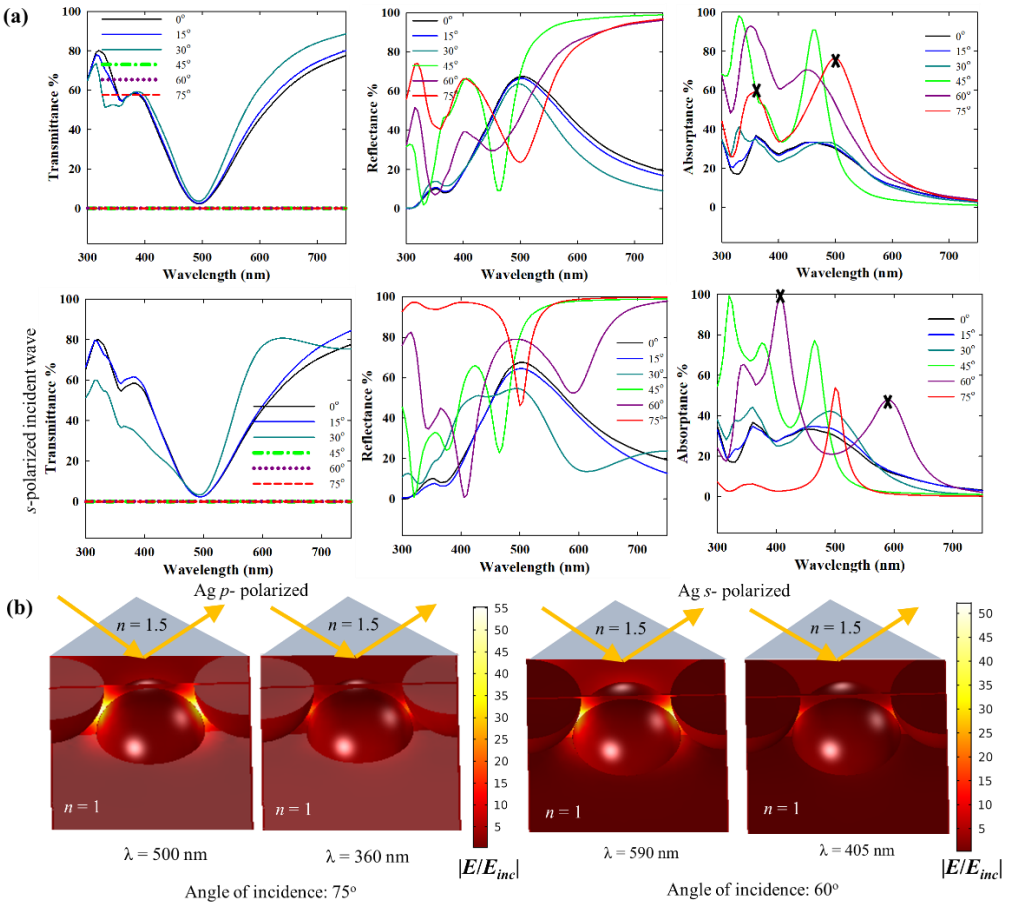

Figure 5.13 Transmittance, reflectance and absorptance spectra of a close packed 20 nm Ag nanoparticle film in the Kretschmann *i.e.* ATR configuration for *p*- and *s*-polarized incident wave, and varying incident angle. In the Kretschmann configuration, $n = 1.5$ for the denser medium, $n = 1$ for the lighter medium and interparticle gap: 1 nm. (b) Near-field enhancement with respect to the background evanescent field (in absence of the nanoparticles) for *p*- and *s*-polarized (or TM and TE polarized) incidence.

While the optical far-field spectra have a lot of influencing factors, the near-field spectra with respect to the background field (in absence of the nanoparticles) can show the position of the plasmon band unambiguously. As shown in **Figure 5.14**, the near-field maximum spectra have more well-defined plasmon bands indicated by the peaks.

Clearly, the plasmon band of Au nanoparticles for *p*- and *s*-polarized incidence as shown in **Figure 5.14 (a)** and **(b)** have corresponding bands in **Figure 5.12**. For example, the absorptance peak (or reflectance dip) at ~620 nm wavelength for 60° *s*-polarized incidence matches with the corresponding near-field enhancement peak in the similar region. However, the band at 475 nm for the same incidence conditions thus does not have a plasmonic origin as clear from the absence of any band in the near-field spectra. Similarly, also for Ag, the near-field maximum spectra in **Figure 5.14 (c)** and **(d)** resolve the plasmon band from the multiple features in the far-field spectra in **Figure 5.13**. Overall, it is evident from the near-field profiles and the near-field spectra that the lattice plasmon resonance results in strong field enhancements also in the Kretschmann configuration. These results are important for surface enhanced spectroscopy in the ATR configuration.

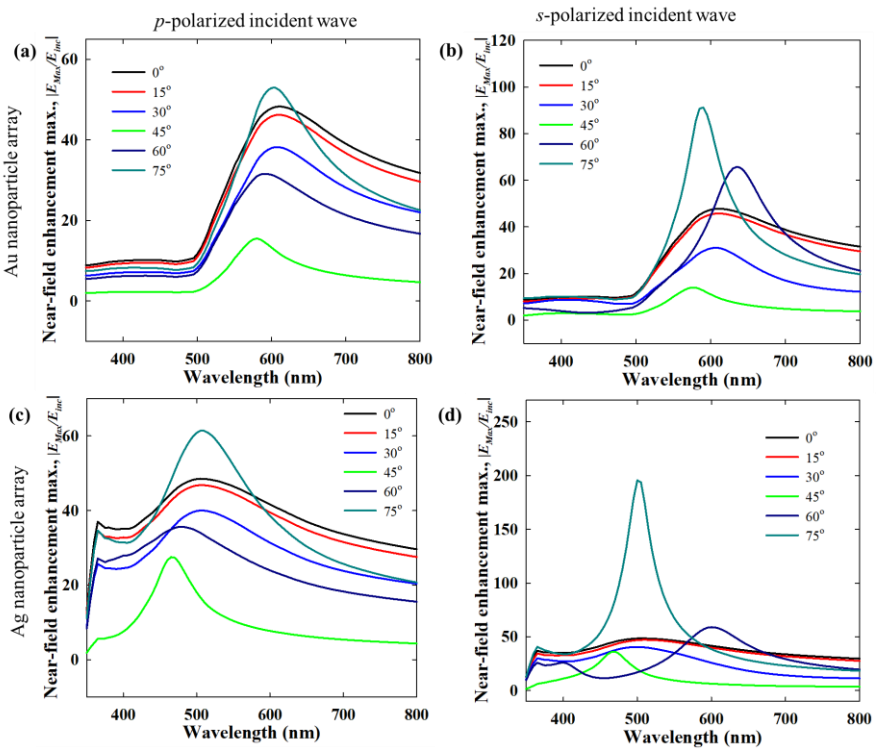

Figure 5.14 Near-field maximum spectra of close packed 20 nm Au (a, b) and Ag (c, d) nanoparticle films in the Kretschmann *i.e*. ATR configuration for *p*- and *s*-polarized (or TM and TE polarized) incident wave, and varying incident angle. In the Kretschmann configuration, $n = 1.5$ for the denser medium, $n = 1$ for the lighter medium and interparticle gap: 1 nm.

5.4 Conclusions

Chapter 5 elucidates the plasmonic lattice resonances in Au and Ag nanoparticle arrays in the direct normal incidence and the Kretschmann *i.e*. ATR configuration by numerical models validated with experimental data. For 20 nm nanoparticles, it is

shown that the interparticle coupling is almost entirely dominated by near-field coupling with a very weak contribution from radiative coupling. The damping mechanism of the plasmons in the nanoparticles at resonance changes as the interparticle coupling becomes stronger and radiative damping tends to contribute more. The changes in the plasmon relaxation mechanism have direct consequences for light-driven processes where plasmonic hot-electrons are important, as hot electrons are generated by non-radiative damping. The per-particle absorption cross-section in a close packed nanoparticle array (or film) is significantly suppressed in comparison to an isolated nanoparticle. This effect is stronger in a dielectric medium in comparison to vacuum, as the plasmonic coupling is stronger in the presence of a dielectric medium. It is also clear that for closed films, while the far-field optical properties in normal incidence are independent of polarization due to rotational symmetry, the near-field properties are strongly dependent on the polarization. Although individual Ag nanoparticles have significantly stronger near-field enhancement than Au nanoparticles, when they are closely packed as a 2D array or film, the differences become much smaller. The lattice resonance in plasmonic nanoparticle films in the Kretschmann *i.e.* ATR configuration is excited by the evanescent field with strong absorptance and near-field enhancement. The many features of the far-field optical spectra in the Kretschmann configuration hare resolved by the comparison with the near-field spectra. It is found that under suitable conditions (for example 60º or 75º angle of incidence for Au nanoparticles), close to 100% absorbance with a broad band can be achieved. The near-field and far-field optical properties thus have interesting implications for various applications, such as surface enhanced spectroscopy, as well as light-harvesting or light-driven hot carrier mediated processes.

Chapter 6

Self-assembled plasmonic nanoparticle films for refractive index based sensing

Based on:

Rituraj Borah, Jorid Smets, Rajeshreddy Ninakanti, Max L. Tietze, Rob Ameloot, Sara Bals, Silvia Lenaerts, Sammy Verbruggen, Self-assembled Ligand-capped Plasmonic (Au) Nanoparticle Films in the Kretschmann Configuration: Towards Sensing of Volatile Organic Compounds. (*to be submitted*)

Contribution:

R.B. performed the nanoparticle synthesis/self-assembly/optical characterization experiments, carried out the computational modeling and drafted the manuscript. The *in-situ* sensing experiments were performed by J.S.

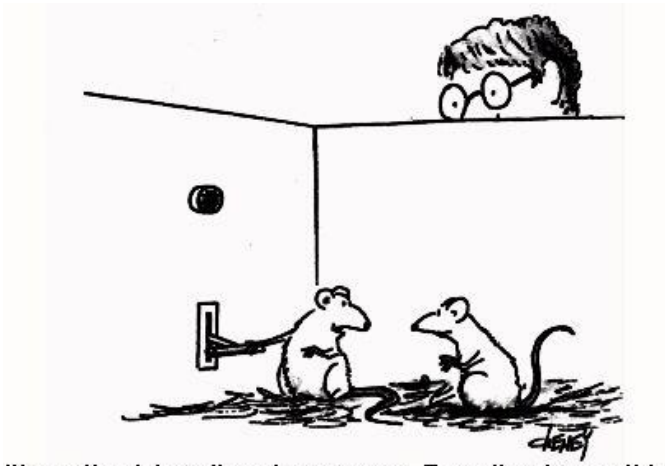

Courtesy: lovestats.wordpress.com

6.1 Introduction

In continuation of the general results on self-assembled nanoparticle arrays from **Chapter 5**, in the present **Chapter 6**, the application of self-assembled plasmonic nanoparticle films in refractive index based sensing is demonstrated. In self-assembly techniques, improved control over parameters such as the packing configuration, interparticle gap, number of layers, *etc.*, also facilitates tailoring towards specific applications.[256 291 292 293] Au thin films are interesting for sensing applications because of the high sensitivity of the plasmon excitation to the local dielectric environment.[294–296] To excite surface plasmon polaritons in planar films, the Kretschmann configuration is commonly used to compensate for the momentum mismatch between the incident photon and the plasmon wave.[297] In **Chapter 6**, self-assembled Au nanoparticle films fabricated at an air-ethylene glycol interface are used as a sensing platform. The films consist of discrete 10 nm oleylamine-capped Au nanoparticles that create a ligand-nanoparticle network and exhibit lattice resonances due to the strong interparticle coupling which can be excited by both normal EM wave incidence and incidence in the Kretschmann (*i.e.* ATR) configuration. *In-situ* measurements using optical transmission in the normal direct incidence and Kretschmann configurations were compared. In the Kretschmann configuration set-up, *in-situ* ellipsometry was integrated in order to measure the relative optical response of the film to *p*- and *s*-polarized incident waves with controlled dosing of methanol vapor. It is shown that the homogeneous ligand-capped plasmonic nanoparticle films obtained through facile wet chemical procedures hold the potential for a low-cost sensing technology for volatile organic compound (VOC) (as well as biosensing) .

6.2 Methods

6.2.1 Synthesis of Au nanoparticles and phase transfer

Au nanoparticles were synthesized by the well-known citrate reduction method. A 100 mL 5 mM tri-sodium citrate solution in water was brought to boil before the addition of 1 mL of 25 mM $HAuCl_4$ solution. Following the precursor addition, the solution was kept boiling for 20 more minutes for complete reduction. The as-synthesized nanoparticles were centrifuged at 12500 rpm for 30 minutes and redispersed in 10 mL Milli-Q water to obtain a 10 times more concentrated colloidal solution.

The concentrated Au nanoparticles in the aqueous phase were transferred to a toluene phase by using oleylamine as a hydrophobic ligand. 3 mL of toluene were gently added onto the surface of 1 ml of aqueous Au nanoparticle colloid so that the toluene floats over the water as a separate phase. To this bi-phasic liquid, 2 mL of oleylamine in ethanol solution (200 mg in 20 mL ethanol) were added followed by gentle shaking for thorough mixing and then resting for separation of the toluene and ethanol-water phases. After resting the mixture for 24 hours, the nanoparticles appear in the toluene phase above (indicated by a distinct red color) and the ethanol-water phase below becomes transparent. The nanoparticles in the toluene phase were then carefully pipetted out for further steps.

6.2.2 Self-assembly

The nanoparticles in toluene (4 mL) after phase transfer were concentrated 10 times to 400 µL by centrifugation at 12000 rpm for 30 minutes and then introduced onto the surface of ethylene glycol contained in a 40 mL glass beaker of 4 cm in diameter. The beaker was then immediately sealed with a glass cover and parafilm leaving only a tiny hole at the mouth for the toluene to evaporate. After the complete evaporation of toluene (8 hours), the nanoparticle films were transferred to the substrates for further characterization and application. For bi-layer films, two films were deposited sequentially one on the other.

6.2.3 Characterization

For the UV-Vis spectroscopy, the nanoparticle films were transferred to a glass substrate by careful vertical dip coating similar to the Langmuir-Blodgett technique. The films were vacuum dried at 100ºC for 24 hours to remove the ethylene glycol. The UV-Vis transmittance spectra for the model validation of the initial films were taken by a Shimadzu UV2600 spectrophotometer. The reflectance and transmittance of the film used in the in-situ measurements were taken by a Lambda UV/VIS 950 Perkin Elmer Spectrophotometer. The absorbance was calculated from the measured reflectance and transmittance (100% - R% - T% = A%). Bright field transmission electron microscopy (TEM) images of self-assembled nanoparticles were acquired using a FEI Tecnai G2 electrom microscope operated at an accelerating voltage of 200 kV. The self-assembled film was immobilized on a hydrophobic copper grid using the same procedure to immobilize self-assembly on glass substrates. The grid was dried at 100°C for 12h in a vacuum oven. Scanning electron microscopy (SEM) images of the films were acquired using an FEG-ESEM-EDX, FEI Quanta 250 at an accelerating voltage of 20 kV.

6.2.4 Dosing experiments

Vapor concentrations of methanol in N_2 flow were regulated in a custom-built dosing setup. Concentrations were set by controlling the liquid methanol and N_2 gas flow with mass flow controllers. Methanol was evaporated and mixed with N_2 in a controlled evaporation mixer. The methanol and N_2 gas mixture was then passed through an environmental chamber where the Au nanoparticle film was set-up for *in-situ* spectroscopic and ellipsometric measurements. During each run, different concentrations were swept alternated with a purge step to assess the reversibility of the response.

Conventional normal incidence configuration: the nanoparticle film on the glass substrate was placed on the sample holder, resulting in an upwards-facing gold nanoparticle film on which the incident beam was directed from the bottom (simplified schematic in **Figure 6.5**). An Avantes fiber optic UV-VIS-NIR spectrometer and an Avalight balanced deuterium light source were used in the *in-situ* set-up. Measurements were performed in the transmission mode using Thorlabs optical and mechanical components. A stainless-steel environmental chamber contained the set-up.

Kretschmann configuration: The Au nanoparticle film on a glass substrate was placed facing the sample holder, using thin spacers at the edges to avoid direct contact and allow gas flow to pass the particles. A right-angle prism was placed on the top of the glass slide using glycerol as a contact fluid. The beam of the ellipsometer is let in/out through fused silica glass windows of the stainless-steel environmental chamber that contains the set-up. All ellipsometry measurements were performed with an iSE Woollam Ellipsometer at an angle of 61^{o} from the normal.

6.2.5 Electromagnetic modeling

For the electromagnetic modeling of the nanoparticle films, an FEM solver COMSOL Multiphysics was used to solve the frequency domain form of the Maxwell's equations numerically as mentioned before. The infinite 2D films were approximated by rectangular unit cells with periodic boundary conditions on the side walls. The incident electromagnetic field was excited at the top (and the wave outlet at the bottom) and the discretized equations were solved for the full-field solution. A perfectly matched layer (PML) was implemented on the top and the bottom boundaries for the complete absorption of the propagating wave. The mesh and the domain independence of the numerical results were ascertained by performing mesh and domain independence tests, and comparison with existing numerical/experimental results. More details/schematics about the numerical results are provided in the results and discussions and **Figure A6.2**.

6.3 Results and discussion

6.3.1 Self-assembly

In this chapter, the air-ethylene glycol self-assembly procedure to obtain nanoparticle films is extended to several cm^2, in contrast to previously reported studies restricted to only several mm^2 films.[298 265] The advantage of ethylene glycol as a subphase is that, unlike water, there is no need for careful regulation of the surface pressure for the self-assembly of small (~10 nm) nanoparticles. Following the existing literature on large area air-water interfacial assembly with larger nanoparticles (>100 nm) over a fixed water surface[299 300], the initial experiments in this chapter with water as a subphase (and small 10 nm Au nanoparticles) failed due to apparent migration of nanoparticles to the walls, and formation of clusters of nanoparticles and oleylamine ligands in patches. Due to the relatively low polarity and surface tension, ethylene glycol slows down this process facilitating gradual re-arrangement of the nanoparticles and ligands at the interface to form close packed arrays while at the same time preventing the nanoparticles and ligands to migrate (or dissolve) into the bulk. As shown in **Figure 6.1 (a)**, a glass beaker half-filled with ethylene glycol was sealed with a small hole opening for the slow evaporation of toluene over 8-9 hours. This approach ensures well-controlled natural convection that induces slow evaporation of toluene from the opposite side, resulting in gradual film formation (**Figure 6.1 (b)**). Although the as-synthesized nanoparticle colloid is deep red in color, the film appears blue due to the interparticle coupling which red-shifts the collective plasmon resonance, indicating the formation of a close-packed assembly. Excess nanoparticles accumulate at specific locations, leaving

most of the film uniform. Importantly, excess nanoparticles or ligands in the toluene phase create an extra surface pressure at the interface that helps the formation of the well-ordered close-packed film.[301] The reproducibility of the self-assembly procedure was ascertained by repeating the experiment and using containers of different sizes, *i.e.*, varying interfacial area and nanoparticle concentrations (see **Figure 6.1(c)**). As shown in the low magnification SEM image in **Figure 6.1(d)**, the films obtained after transferring the self-assembly to a glass substrate by the Langmuir-Blodgett deposition technique have uniform morphology over large areas. The nanoparticles arrange themselves into hexagonal close packed arrays to form predominantly mono- or multi-layered films depending on the concentration of the nanoparticles in the colloid. **Figure 6.1 (b)** shows the development of a self-assembled film which is predominantly monolayer, from 20 ml (~10^{14} nanoparticles) of the as-synthesized nanoparticle colloid concentrated into 400 µl in the toluene phase.

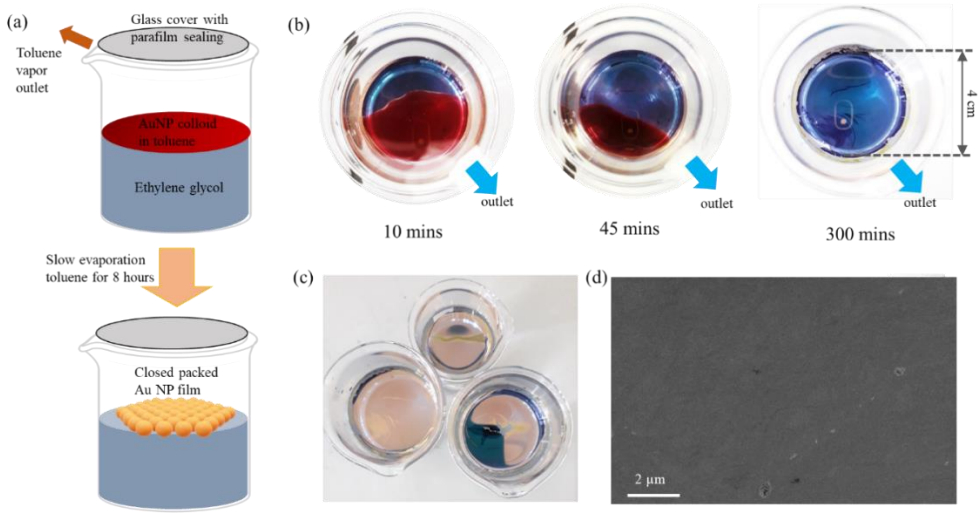

Figure 6.1 (a) Schematic representation of the air-liquid interfacial self-assembly procedure over ethylene glycol surface inside a glass beaker with a small opening at a corner of the vapor space for the evaporation of toluene. (b) The time evolution of the film-formation as the solvent toluene evaporates leaving behind the close packed Au nanoparticles. (c) Picture of beakers after film formation indicating the reproducibility of the process. (d) SEM image showing the uniformity of the films over large surface areas (scale bar: 2 µm).

6.3.2 Description of the optical configuration and modeling

The collective lattice resonance of the Au nanoparticle films can be adequately described by classical electrodynamics.[302 253] Unlike a continuous Au film, for which a specific geometric arrangement (e.g., the Kretschmann or Otto configuration) is required for the surface plasmon resonance (SPR) modes to be excited,[303] a nanoparticle film exhibits lattice resonances even at normal incidence. This phenomenon is possible since each nanoparticle has its localized surface plasmon resonance (LSPR) modes that couple together to form collective lattice resonance modes. The excitation of the lattice

resonances is strongly determined by the incident angle. As shown in **Figure 6.2 (a)**, as the incident angle θ varies, the plasmonic coupling and the optical response should also vary, depending on the E-field polarization (defined by the angle φ). For *p*-polarized ($\varphi = 90^{o}$) and *s*-polarized ($\varphi = 0^{o}$) optical incidence at an interface between two dielectric media, the reflectance and transmittance are defined by the classical law of Fresnel reflection.[304] However, the optical response for the nanoparticle film in **Figure 6.1** results from the excitation of the lattice plasmon modes. The shiny appearance of these films (**Figure 6.1 (b, c)**) when viewed at an angle indicates the reflection by a collective optical response. To simulate the optical response of the films, a unit cell is constructed as the computational domain with Floquet periodic boundary conditions on the side walls that enable the extension of the film in 2D to infinity (see **Figure 6.2(b)**). The schematic in **Figure 6.2 (c)** shows the Au nanoparticle film in the Kretschmann configuration. Since the incident beam through the prism coupler gets reflected at the inside bottom face by total internal reflection, the Au nanoparticle film on the bottom face (outside) only interacts with the standing evanescent field. Thus, only the light absorbed by the plasmonic nanoparticle film is absent in the reflectance and no light is transmitted. It is important to note that the evanescent field arising from the *p*- and *s*-polarized incident light has completely different directionalities *i.e*. in-plane (plane of the film) and out-of-plane components for *p*-polarized and only an in-plane component for *s*-polarized light.[305] To ascertain the accuracy of the used electromagnetic models, results from literature were initially reproduced. The agreement of the finite difference time domain (FDTD) results from Mueller *et al*.[306] with our FEM model for mono- and bi-layers indicates the validity of our approach for the normal incidence case (**Figure A6.2**). The electromagnetic models of the Kretschmann configuration were first validated by comparing the computed reflectance and transmittance with analytical solutions obtained from Fresnel's coefficients in the absence of the Au nanoparticles (**Figure A6.3 (a)**). Additionally, the angle-resolved reflectance of an Au thin film in the Kretschmann configuration (experimental data from Vohnsen *et al*.[307]) was reproduced through our model (**Figure A6.3 (b)**).

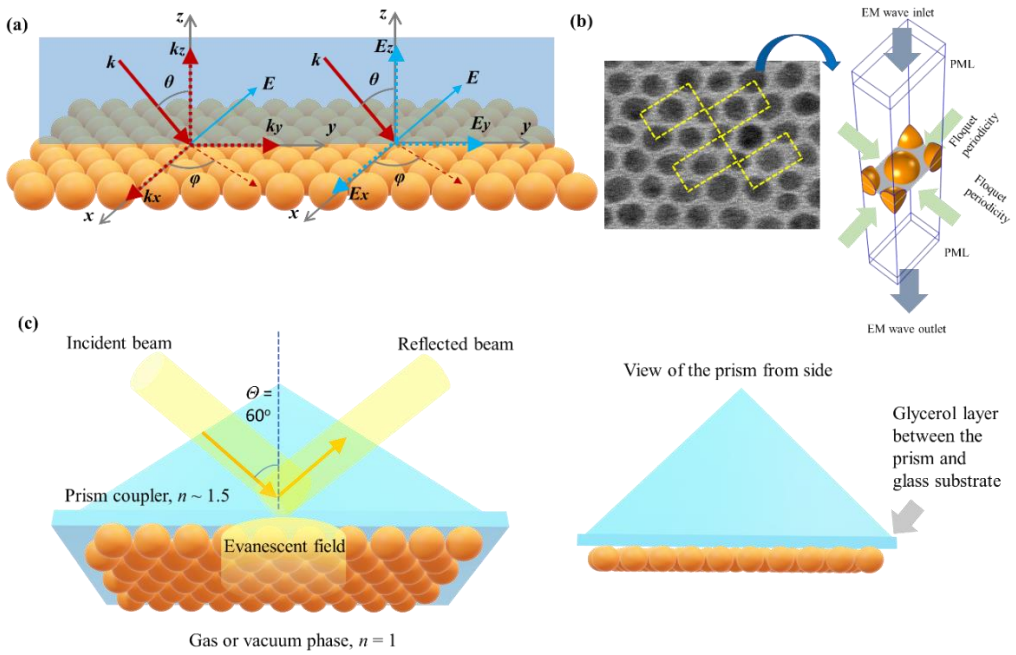

Figure 6.2 (a) Schematic representation of an Au nanoparticle self-assembled monolayer with incident and electric field wave vectors *w.r.t.* the 3-D cartesian axes and the plane of incidence (transparent blue plane). (b) The unit cell rectangular domain with periodic boundary conditions on the side walls which is implemented in the electromagnetic modeling of the self-assembled films. (c) Schematic of the Kretschmann configuration: the Au nanoparticle film on glass substrate is attached to a prism coupler with a connecting glycerol layer in between to fill the space in between.

6.3.3 Characterization of the films and computational validation

TEM measurements were performed to obtain the spatial information required for electromagnetic modeling. As shown in **Figures 6.3 (a)** and **(b)**, a well-ordered, close-packed monolayer film is observed in TEM when nanoparticle concentrations were large enough to cover the complete air-liquid interface. When the concentration is too high, bilayer or multilayers form over significant areas of the film, **Figure 6.3 (d)** and **(e)**. The nanoparticle size (~9.91 nm) and interparticle gaps (~ 2 nm) determined from the TEM images are given in **Figure A6.4**. Schatz and co-workers have shown that irregularities in the 2D lattice, such as small variations in the particle diameter and the interparticle gap, can be circumvented in the electromagnetic models by taking average values, in our case 10 nm and 2 nm, respectively.[271] Also, minor deviations from the perfect hexagonal close packing can be ignored. Experimental and modeled transmittance spectra of the monolayer and bi-layer Au nanoparticle films (measurements done after vacuum drying at 40°C for 72 hours) are compared in **Figures 6.3(c)** and **(f)**, respectively. The agreement between the experimental and theoretical resonance wavelength is clear from the position of the dip at 585 nm. The film's lattice resonance position is significantly red-shifted *w.r.t.* the resonance of isolated

nanoparticles (521 nm, *cf.* **Figure 6.3 (i)**) due to the interparticle coupling. Importantly, these ~10 nm nanoparticles almost do not scatter when isolated. However, as a close packed film, coherent scattering due to plasmonic coupling results in a significant reflectance (**Figure A6.6**). As small nanoparticles exhibit only non-radiative damping of the plasmons, the excited plasmons couple by near-field interactions among adjacent nanoparticles. Due to their non-radiative (or non-scattering) property, the 10 nm Au nanoparticle cannot couple by far-field or radiative coupling.

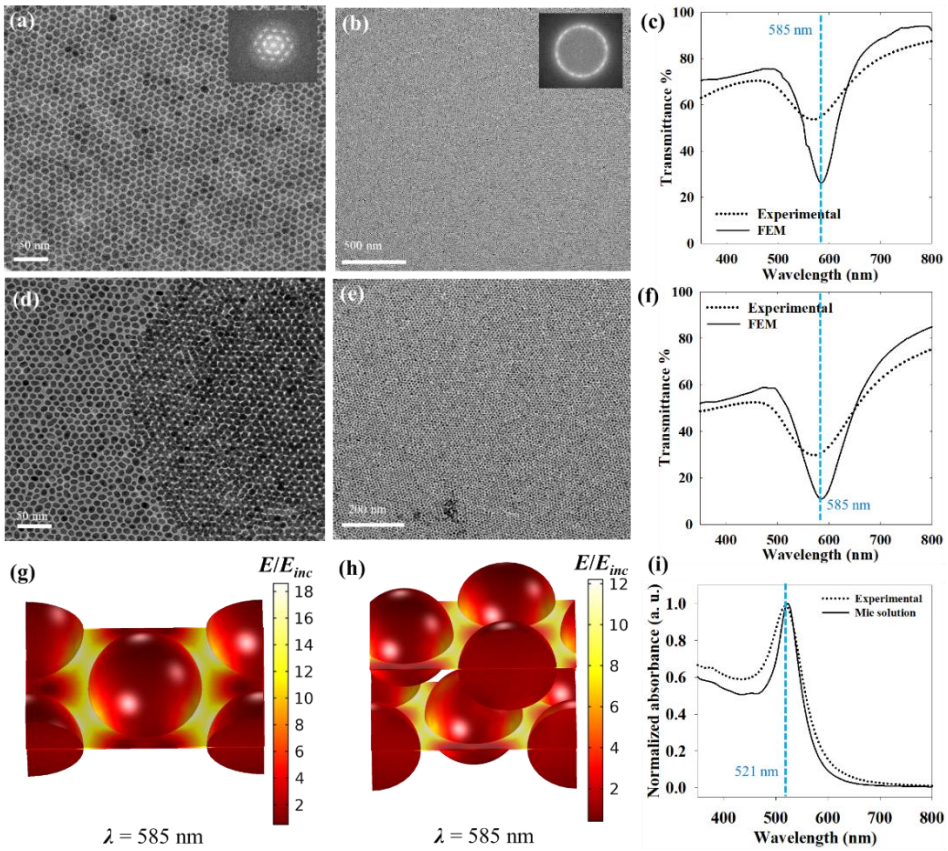

Figure 6.3 (a, b) TEM images of a Au nanoparticle monolayer with fast Fourier transformation (FFT) in the inset. (c) Comparison of experimental and computed transmission spectra of the Au nanoparticle monolayer. (d, e) TEM images of a respective Au nanoparticle bilayer. In (d), the contrast between bilayer and monolayer is visible. (f) Comparison of experimental and computed transmission spectra of the Au nanoparticle bilayer. (g, h) Near-field enhancement at the resonance of monolayer and bilayer films *w.r.t.* the incident field indicating the strength of plasmonic coupling by near-field overlap. (i) UV-Vis absorbance spectra of the Au nanoparticles as aqueous colloids compared with the Mie analytical extinction spectrum for spherical Au nanoparticles (10 nm).

As shown in **Figures 6.3 (g)** and **(h)**, for an interparticle gap of 2 nm, the near-field coupling is quite strong as indicated by the enhancement maps with respect to the

incident electric field. This strong near-field enhancement of up to 18 and 12 times with respect to the incident field for the monolayer and the bilayer, respectively, also implies the applicability of these films in surface-enhanced processes such as SERS, SEIRA, Fluorescence, *etc*. Despite the same interparticle distance, the weaker near-field enhancement for the bi-layer film compared to the monolayer is due to the fact that the wave transmitted through the top layer is reflected back by the bottom layer to destructively interfere with the top layer field.[253]

6.3.4 Refractive index sensitivity of optical response

For the optical characterization and further sensing experiments, a part of a nanoparticle film as shown in **Figure 6.1** was transferred to a glass slide of 3 cm^2 area. A large film area is beneficial for these measurements so that the entire beam of the ellipsometer can interact with plasmonic nanoparticles for better sensitivity. Absorbance, reflectance, and transmittance spectra for the normal incidence from the top were collected to show the agreement with the predicted plasmon resonance (**Figure 6.4 (a)** and **(b)**). Individually non-scattering ~10 nm Au nanoparticles packed as a film now exhibit strong reflection by coherent scattering at the lattice plasmon resonance. The film's theoretical refractive index sensitivity of 250 nm/RIU in the normal incidence indicated by the red-shift of the lattice resonance (optical intensity mode) is expectedly similar to the sensitivity of a diffraction grating coupler, **Figure 6.4 (c)**.[308] This is not surprising as the diffraction grating couplers are also periodic metal nanostructures that facilitate resonant energy transfer from the electromagnetic wave to diffractively coupled surface plasmons.[309] It is important to note that the refractive index of the entire embedding medium outside of the prism is varied in the computations.

In the Kretschmann *i.e*. ATR configuration, the evanescent wave outside the prism coupler excites the plasmons in the nanoparticle film. A unique feature of the ATR geometry is that the maximum intensity of the incident beam, regardless of its polarisation, is localised at the interface which attenuates with the distance from the interface.[310] In **Figure 6.4 (d, e)**, the optical responses of the Au nanoparticle film to *p*- and *s*-polarized incident beams are significantly different as obtained from the numerical model. The reflectance dip in both the cases indicates the lattice resonance by the excitation of the lattice plasmon modes by the evanescent wave. However, the lattice resonance band is weaker for the *s*-polarized beam. Usually, the depth of penetration of the evanescent wave, which is dependent on the wavelength of incidence, is more than twice as pronounced for a *p*-polarized incident beam as compared to an *s*-polarized incident beam.[311] Also, the polarization of the evanescent field due to *s*-polarized incident field is confined to the plane of the dielectric interface in contrast to the evanescent field by *p*-polarized beam with both in-plane and out-of-plane components. Hence, such differences in the optical response by the two directions of polarization arise from the differences in the evanescent fields. Regardless of the polarization, the refractive index sensitivity of the film in the Kretschmann configuration in **Figure 6.4 (d, e)** is similar to that for the normal incidence in **Figure 6.4 (c)** as in both the cases, the lattice resonance modes are excited in three different

ways. Generally, in SPR or LSPR based sensing, the shift in the plasmon resonance wavelength or angle is correlated with the refractive index change induced by the target molecules in the surrounding environment. In the optical intensity mode as discussed so far, the wavelength interrogation in the Kretschmann configuration has been shown to be more sensitive than the direct incidence configuration for nanostructured arrays such as a diffraction grating.[312]

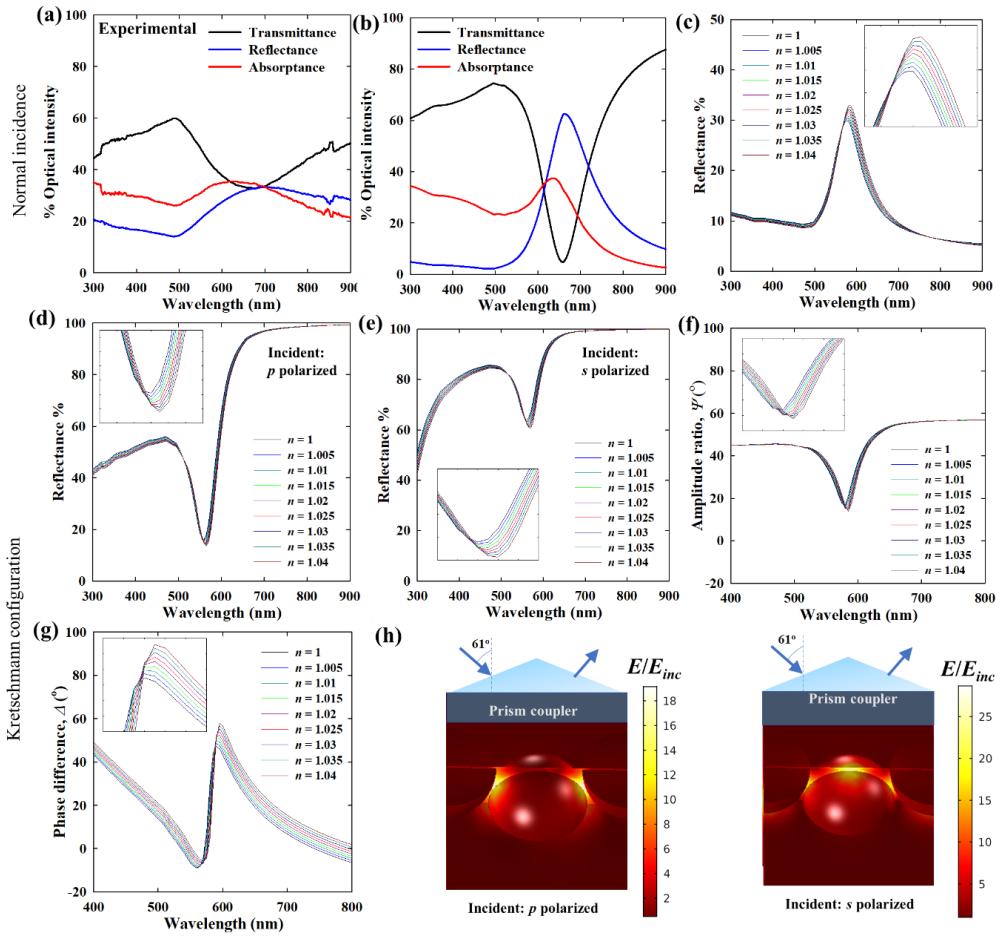

Figure 6.4 (a) Experimental transmittance, reflectance, and absorptance spectra of a self-assembled film of ~10 nm Au nanoparticles. (b) Computed optical spectra of the films for comparison. (c) Computed refractive index sensitivity of the Au nanoparticle film used in the sensing experiment under normal direct incidence. Computed reflectance spectra and refractive index sensitivity of *p*-polarized incident light (d) and *s*-polarized incident light (e) in the Kretschmann *i.e.* ATR configuration. Computed (f) ψ and (g) Δ spectra from ellipsometry and their refractive index sensitivity for the Au nanoparticle film in the Kretschmann configuration. (h) Near-field enhancement around the self-assembled nanoparticles by *p*- and *s*-polarized incident beam in the Kretschmann configuration. (incident angle for the Kretschmann configuration: 61°).

In contrast to intensity spectra, ellipsometry provides the relative amplitude and phase difference between the optical responses of the nanoparticle films to *p*- and *s*-polarized incident beams. In ellipsometric measurements, ψ and Δ are the amplitude ratio and the phase difference of the *p*- and *s*- polarized components (normalized to the incident wave) of the reflected beam respectively. The differences in the polarization of the nanoparticles by *p*- and *s*-polarized incident beams is evident from the near-field maps in **Figure 6.4 (h)**. The ψ spectra obtained from the complex reflectivity values for the two polarization indicates the lattice resonance by a characteristic dip in **Figure 6.4 (f)**, in line with the intensities in Figure (d) and (e) indicating the difference in amplitudes. The Δ spectra in **Figure 6.4 (g)** indicate that close to the lattice resonance, an abrupt change in the phase difference takes place due to the difference in the plasmonic excitations by the two orthogonal polarization modes. The theoretical refractive index sensitivity study of the amplitude ratio ψ shows that similar to intensity spectra, increasing refractive index of the air (or vacuum) medium results in a red-shift of the plasmon band with an enhancement in the absolute value. The Δ spectra also show a similar response to refractive index changes, however, with a significantly higher sensitivity than ψ in the absolute values. It has been shown that for a thin Au film, the ψ and Δ response from ellipsometry are 10 times more sensitive than conventional intensity-based spectroscopy. Further, the phase parameter Δ is also an order of magnitude more sensitive than the amplitude ratio ψ.[313] It is to be noted that in the above discussion for computational models, the refractive index change is homogeneous around the nanoparticles in the interparticle gaps as well as the rest of the medium. In most sensing applications, when the adsorption of the probed molecules takes place at only one side of the nanoparticles, such asymmetries are supposed to result in stronger variation in the polarization specific optical responses as discussed in later sections.

6.3.5 Methanol sensing experiments with in-situ spectroscopy

It is clear from **Figure 6.4** that the spectroscopic response of the nanoparticle films based on intensity has a similar refractive index sensitivity in both normal and Kretschmann configuration regardless of the mode of polarization. Also, the choice of reflectance or transmittance is immaterial as the plasmon band in the spectra in both the cases originates from the same lattice resonance. Since the Au nanoparticles are capped by the oleylamine ligands, it is also useful to discuss the effect of this dielectric ligand shell on the refractive index sensitivity. As shown in **Figure A6.7**, the presence of a 2 nm dielectric shell (n = 1.5) is not detrimental to the refractive index sensitivity of 20 nm Au nanoparticles. In fact, due to the metal-dielectric electromagnetic coupling, there is a slight enhancement in the refractive index sensitivity of the nanoparticles with a thin dielectric shell. When the refratice index of the medium is varied from n = 1 to n = 1.07, the optical intensity at the resonance wavelength increases by ~11% for the nanoparticle with a shell as compared to the bare nanoparticles. Thus, the presence of the oleylamine shell fundamentally has no detrimental effect on the refractive index sensitivity of the Au nanoparticles.

The methanol dosing experiments to systematically vary the bulk gas phase refractive index or local refractive index (by molecular adsorption) were set-up with *in-situ* spectroscopy in the normal incidence mode to continuously measure the transmittance spectra, **Figure 6.5 (a)**. The methanol vapor dosing varies the bulk as well as the local refractive index near the nanoparticle film as the organic ligand-nanoparticles network serves as adsorption sites for the vapor phase methanol. As shown in **Figure 6.5 (b)**, the red-shift of the plasmon resonance for the refractive index changes induced by methanol dosing is too small to be quantified. However, the intensity changes can be exploited to track the refractive index changes by methanol vapor with time as shown in **Figure 6.5 (c)** and **(d)**. The sensitivity and reversibility of the signal is clearly illustrated in the dosing experiment (P/P_0 from 0% to 65.58%) in **Figure 6.5 (c)**. The sensitivity (with reversibility) to as low as 4.63% methanol vapor indicates that methanol adsorption in the organic ligand network contributes strongly to the refractive index enhancement in the vicinity of the Au nanoparticles. Also, **Figure 6.4** shows that the evanescent near-field is confined very close to the nanoparticles and in the interparticle gaps. Thus, the near-field can interact with the local dielectric environment only within a short range, so that the changes only within that range are detected in the far-field response. The adsorption of methanol molecules for an equilibrium vapor phase concentration takes place reversibly on/in the nanoparticle-ligand network. **Figure 6.5 (d)** indicates a correlation between the transmittance and the vapor phase methanol concentration.

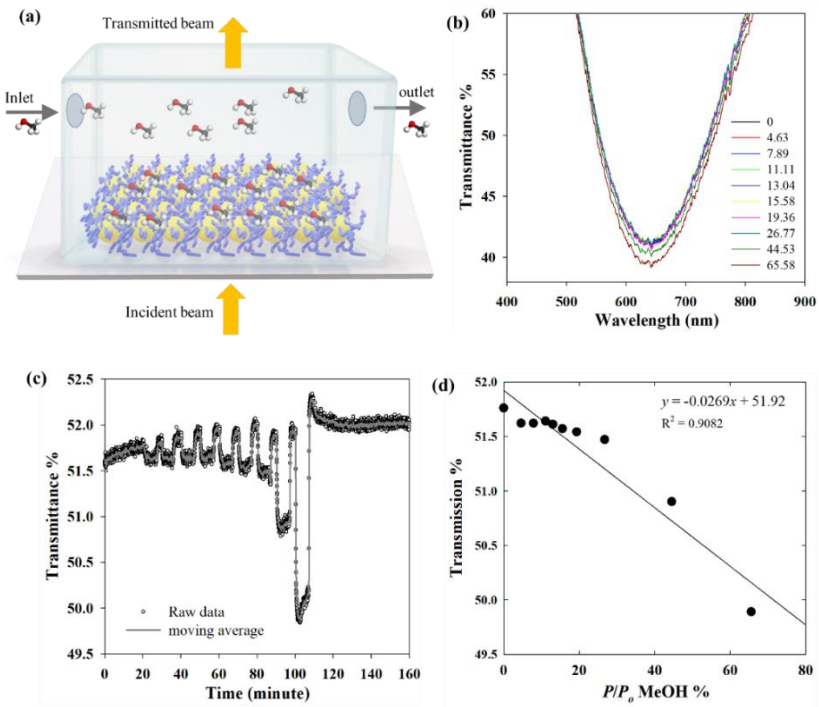

Figure 6.5 (a) A representative schematic of the methanol vapor dosing set-up with in-situ transmission spectroscopy with illumination from the bottom (yellow spheres: Au nanoparticles, blue wires: oleylamine ligand). (b) Transmittance at the resonance wavelength for increasing methanol concentration (relative saturation, % P/P_o). Time

evolution of the transmittance at wavelength: 650 nm during the methanol dosing experiment with step-wise increasing concentration, showing the transient variation of the optical signal with concentration. (d) Isotherm showing the dependence of the % transmittance *vs*. methanol concentration.

6.3.6 Methanol sensing in the Kretschmann configuration with in-situ ellipsometry

As evident from **Figure 6.4**, the plasmonic response of the nanoparticle films to *p*- and *s*-polarized light are significantly different in both amplitude and phase. The use of ellipsometry instead of transmission intensity-based probing enables access to the polarization-specific amplitude (amplitude ratio: ψ) and phase information (phase difference: Δ) of the film. By exploiting the polarization dependence of the plasmonic response to refractive index changes in the nanostructure surrounding, higher sensitivity can be obtained with ψ and Δ.[314] In the methanol vapor dosing experiments, in contrast to the computational models where the refractive index is varied uniformly over the entire medium, the local refractive index changes due to molecular adsorption on the ligand-nanoparticle network is non-uniform. As shown in **Figure 6.6 (a)**, the open side of the film facing the gas phase naturally has a higher concentration of the methanol molecules than the interstitial gaps. Thus, a greater contrast in the optical response of the film to *p*-and *s*-polarized incident beams is expected as the polarizing evanescent electric fields for the two orthogonal modes of polarization have completely different directions. In the Kretschmann configuration, it has been shown that while the *p*-polarized incident infra-red beam can probe the vibration modes parallel and perpendicular to the sample film, the *s*-polarized beam probes solely the components of the vibrational modes parallel within the plane of the sample film sample film.[315] The *in-situ* ellipsometry set-up in this chapter elucidates the effect of the adsorption of methanol molecules in the plasmonic nanoparticle-organic ligand network by means of the relative optical response to the in-plane (plane of the nanoparticle film) and out-of-plane polarized evanescent fields due to the two orthogonal incident polarization modes. In the set-up, the self-assembled Au nanoparticle film was combined with a smaller (bottom face area: 20 cm^2) prism coupler to construct the Kretschmann configuration inside an environmental chamber where the methanol vapor was dosed systematically, **Figure 6.6 (a)**.

Figure 6.6 (b) shows the ψ and Δ spectra of the nanoparticle film in the Kretschmann geometry. The dip in ψ around ~640 nm representing the plasmon resonance indicates the variation of the *p*-polarized intensity with respect to the *s*-polarized intensity as a result of the plasmon excitation by the two components of the resulting evanescent wave. In the Δ, a corresponding jump at ~700 nm is observed. The characteristic ψ and Δ spectra of the film as shown in **Figure 6.6 (b)** agrees with the computed spectra in **Figure 6.4**. The dip in ψ and the jump in Δ at around 640 nm and 700 nm, respectively, signifies the lattice plasmon resonance in the Kretschmann configuration. The difference in the electric fields of the exciting evanescent fields, thus, results in the characteristic ψ and Δ spectra indicating the difference between the plasmonic responses by the two incident fields. Thus, in the *in-situ* methanol dosing experiments, ψ and Δ

indicate the relative response of the two incident polarizations to the local refractive index changes by the adsorption/absorption of methanol molecules.[316] The variation of ψ and Δ with increasing concentration of methanol vapor indicates the changes in the refractive index close to the nanoparticle film, **Figure 6.6 (c, d)**. Although the red-shift of the plasmon band in the ψ spectra is rather weak, the intensity has a strong variation with methanol vapor concentration similar to the computed trends in **Figure 6.4 (f)**. In contrast, Δ experiences a strong red-shift of ~20 nm for the methanol vapor concentration variation from 0 to 65.58 % (P/P_o). Due to the non-uniform refractive index change around the nanoparticles (in the network of oleylamine ligands), the experimental ψ and Δ spectra variation with different methanol concentration is expectedly different from the computed results shown for the model nanoparticle film. Still, a general agreement between the experiments in **Figure 6.6** and the models in **Figure 6.4** is clear. **Figure 6.4** also shows how the near-field enhancement of the film, *i.e*. the polarization of the nanoparticles, is distributed and the sensitivity to refractive index is strongly dependent on the polarization.[316] The high sensitivity of ψ and Δ signal of Au thin films has also been reported in literature.[313 314] As shown in **Figure 6.6 (e)**, the intensity variation of the dip in the ψ spectra around 640 nm with increasing methanol vapor concentration allows any wavelength on the right of the resonance to be used for continuous measurements. The time evolution of the ψ intensity with varying methanol concentration in **Figure 6.6 (e)** shows the reversibility of the equilibrium adsorption/desorption process.

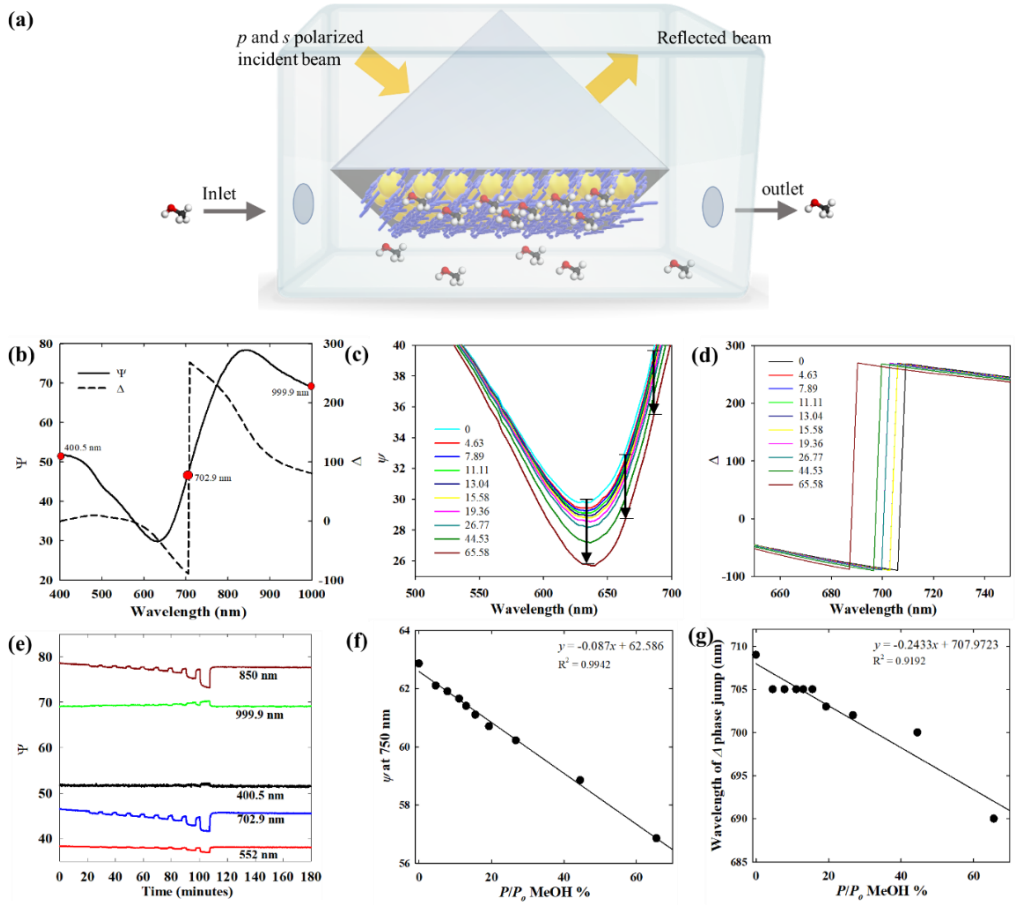

Figure 6.6 (a) A representative schematic of the *in-situ* ellipsometry set-up used for the methanol dosing experiment. (b) Experimental ellipsometric ψ and Δ spectra at 61° incidence angle. (c) ψ at the resonance wavelength for increasing Methanol concentration (relative saturation, % P/P_o). (d) Time evolution of ψ during the methanol dosing experiment at different wavelengths showing the transient variation of the optical signal with concentration. (e) Isotherm showing the dependence of the ψ *vs*. methanol concentration. (f) Isotherm exported from ψ intensity at different concentrations. (g) Isotherm obtained from wavelength position of phase Δ jump at different concentrations.

Compared to the transmission mode experiments, an improvement in the noise can be observed, especially at wavelengths close to the resonance. The sensitivity is the highest close to the resonance at ~ 640 nm which gradually decreases as one moves away from the resonance wavelength. The concentration vs. ψ data in **Figure 6.6 (f)** indicate a linear relationship. A similar linearity is also observed in the concentration vs. Δ position data in **Figure 6.6 (g)**, the clarity of which however suffers from the resolution of the measurements. Clearly, while the lattice resonances in 2D Au nanostructure arrays as studied here can also be excited by normal incidence, the Kretschmann configuration for ellipsometric measurement is particularly advantageous. Compared to

the transmission mode experiments, an improvement in the noise can be observed, especially at wavelengths close to the resonance. The improved lowered noise can be attributed to the fact that the plasmonic excitation in the Kretschmann geometry is driven by the evanescent wave, while the incident beam is reflected by total internal reflection with no transmission. Thus, unlike the transmission mode where the signal intensity results from the combination of absorbance and reflectance, the reflectance in the Kretschmann configuration facilitates the collection of the entire light signal that is not absorbed by the nanoparticle film by the plasmonic enhancement. Also, ψ and Δ being relative parameters are free from the noise arising from the fluctuations in the light source.

6.4 Conclusion

Self-assembly of nanoparticles is a simple method to obtain functional thin films. When self-assembled into close-packed films, oleylamine capped plasmonic Au nanoparticles exhibit collective optical properties through plasmonic coupling. At the ethylene glycol-air interface, colloidal nanoparticles can be self-assembled over large areas up to several cm^2 by controlled evaporation of the solvent phase. Such nanoparticle films exhibit a strong lattice resonance by the near-field coupling, as shown by electromagnetic modeling. Due to the periodicity of nanoparticle arrangement, the lattice plasmon modes of self-assembled Au nanoparticle films can be excited by normally incident electromagnetic waves. However, the lattice resonance can also be excited in the Kretschmann (*i.e* ATR) configuration by the interaction of the evanescent field with the nanoparticles at the low refractive index side. The refractive index sensitivity of the intensity spectra (*i.e*., transmittance, absorptance, or reflectance) of the self-assembled films in both normal incidence and Kretschmann configuration, is similar to grating-based plasmonic sensing platforms reported in literature. The oleylamine capped nanoparticle assembly creates a ligand-nanoparticle network that facilitates adsorption of molecules from the gas phase. When *in-situ* ellipsometry and *in-situ* spectroscopy are compared, amplitude ratio (ψ) and phase difference (Δ) measurements for differently polarized incident light provide higher sensitivity and improved signal quality. The results shown here establish the feasibility of VOC sensing by plasmonic nanoparticle films, with experiments performed for methanol concentrations of ~2000 ppm and higher. However, to achieve high sensitivity at low concentrations (<50 ppm), it is important to integrate a material (for example, a metal organic framework) with the nanoparticles that can facilitate the adsorption and concentration of the probe molecules near the film. Another important aspect is the selectivity of the sensing process towards a certain molecule. For high selectivity, further adaptation of the surface chemistry for selective adsorption/absorption of the probe molecule is necessary.

Chapter 7

Phase transfer and self-assembly of metal oxide nanoparticles at the air-water interface: towards functional interfaces

Based on:

Rituraj Borah, Rajesh Reddy Ninakanti, Gert Nuyts, Hannelore Peeters, Pedrazo-Tardajos, Silvia Nuti, Christophe Vande Velde, Karolien De Wael, Silvia Lenaerts, Sara Bals, Sammy W. Verbruggen, Selectivity in the Ligand Functionalization of Photocatalytic Metal Oxide Nanoparticles for Phase Transfer and Self-Assembly Applications. Chemistry – A European Journal 2021, 27 (35), 9011–9021.

Contribution:

R.B. performed the experiments (except TGA and SEM imaging) and wrote the manuscript.

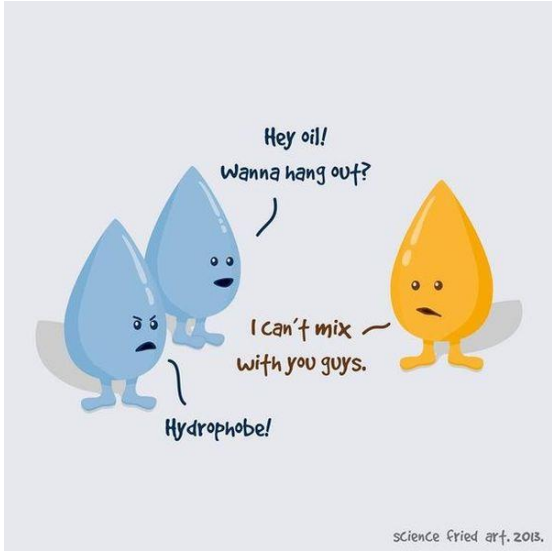

Courtesy: from the twitter feed of ACSReactions.

7.1 Introduction

Up to **Chapter 6**, the main theme of discussion has been plasmonic metal nanoparticles, their self-assembly, optical properties and their application in, for instance, refractive index-based sensing. **Chapter 7** includes experimental results on metal oxide nanoparticles and their self-assembly. Apart from the novelty of these results as a separate study on metal oxides, the insights from this part of the investigation pave way for the application of hybrid plasmonic-metal oxide nanostructures, e.g. metal@semiconductor core-shell nanostructures, towards self-assembled functional interfaces.

Nanoparticles of semiconductor oxides such as TiO_2, ZnO, WO_3 and CuO have gained considerable attention over the years for their proven usefulness in important applications such as photocatalysis, water splitting, CO_2 reduction, solar cells, super-capacitors, sensing applications, amongst others.[317] [318] [319] Many of these applications require functionalization of the nanoparticles with organic ligands with desired functionalities.[320] For instance, bio-functionalization of nanoparticles is essential for *in-vitro/in-vivo* medical applications in order to render them bio-compatible, target-specific[321] and stable.[322] Other applications of the functionalization of nanoparticles include molecular imaging[323], click-chemistry mediated conjugation[324], selective self-assembly of nanoparticles[325], ligand accelerated catalysis,[326] and many more. For nanoparticles synthesized in an aqueous medium, hydrophobic functionalization is often necessary to stably disperse the nanoparticles in a non-polar medium. Therefore, it is important to have hydrophobic functionalization strategies available that enable phase transfer of nanoparticles from an aqueous to non-polar organic phase, for follow-up reactions in this non-polar phase[327], coating of hydrophobic substrates[328], self-assembly as thin films[329], and so on.

The efficacy of the functionalization is dependent on the affinity of functional head groups towards the nanoparticles' surface.[320] Chemisorption by the formation of a covalent-like bond results in stable functionalization, while electrostatic or hydrophobic interactions result in a weaker attachment for which the surface coverage is subject to the equilibrium concentration of the ligand in the solution. The exact nature of these bonds is still an important topic of investigation even for an extensively explored case of Au and thiol-functionalized ligands.[330] [331] Recently for instance, Inkpen *et al*. challenged the widely accepted view that the Au-thiol linkage is covalent showing that the nature of the bond is mainly physisorption.[332]

Nonetheless, the strong bonding of thiols to both metal and metal-oxide nanoparticles is overall well known. Similarly, amines also bind strongly with metal as well as metal oxide nanoparticles. In heterogeneous catalysis, thiols and amines have therefore been the most explored anchoring ligands. However, the binding affinity of ligands to a metal or metal oxide varies depending on the functional group. In ligand exchange processes,

the relative affinity of different functional groups to bind to the nanoparticles determines whether the existing ligands on the nanoparticle surface can be replaced by a new ligand. Naturally, the new ligands must have a stronger affinity to bind in comparison to the existing surface ligand.[333] [334] It is also important to note that while the binding affinity may determine the thermodynamic feasibility of ligand exchange, the kinetics of the process are also important to observe the process in a realistic timeframe. Due to the stronger affinity, oleylamine capping on Au nanoparticles can be effectively replaced by thiol ligands by simply introducing the thiol ligands to the nanoparticle colloid in a thiol-for-amine ligand exchange process.[335] Similarly, thiol-for-phosphine ligand exchange has also been achieved at room temperature due to such relative binding affinity.[336] This kind of strong variation in the binding affinities of different ligands on a metal is naturally expected for metal oxides as well. As the nanoparticles investigated in **Chapter 7** are ligand free, an initial ligand exchange step is not required for their functionalization. However, the variation of the binding affinity of different ligands leads to different outcomes in the further colloidal processing steps of the nanoparticles such as water to oil phase transfer.

As discussed above, while functionalization of metal nanoparticles with different ligands is well-explored, metal–oxide nanoparticles are far less studied in this context. **Chapter 7** provides a comparative picture of the functionalization of semiconductor oxide nanoparticles, namely TiO_2, ZnO, WO_3 and CuO with amine (oleylamine) and thiol (1-dodecanethiol) ligands in identical chemical environments. While the study is limited to only two kinds of commonly used ligands and four common metal oxides in order to delineate the trends for the possible ligand-metal oxide combinations, the general fundamental aspects can be extrapolated to other combinations as well. In this study, the selectivity of a functional group towards a specific oxide becomes clear and is further consolidated by the fact that the efficacy of phase transfer of these nanoparticles from aqueous to non-polar (hexane or chloroform) phase is in direct correspondence with the ability of the ligand, *i.e*. the head group, to chemically attach on to the nanoparticles' surface. The ligand-capped nanoparticles' surface chemistry has been probed by (ATR-) FTIR with respect to dissociative and molecularly adsorbed H_2O on active sites, in order to understand to what extent the different ligands occupy the active sites on the various metal oxide surfaces. It has been shown that the alkyl chain length for a specific head group is also important in facilitating polar to non-polar phase transfer of nanoparticles.[337] [338] A too long alkyl chain may lead to steric hindrance in the fast ligand attachment process during the phase-transfer resulting in insufficient coverage of the nanoparticles. A short alkyl chain on the other hand may not be able to sufficiently hydrophobize the nanoparticles. Soliwoda *et al*. showed that for thiols, 1-octadecanethiol with 18-C alkyl chains form disordered assemblies on the nanoparticle surface which results in poor phase transfer.[338] While, for amines, it takes longer 18-C chains to facilitate stable and efficient phase transfer of nanoparticles.[337] In the phase transfer experiments, 18-C and 12-C alkyl chains of oleylamine and 1-dodecanethiol,

respectively, are found to be effective for the phase transfer of the respective metal oxide nanoparticles. Whether the optimal alkyl chain length of a ligand for phase transfer is dependent on the type of the headgroup is not immediately clear in this study. As an application of the functionalization, the hydrophobized nanoparticles are self-assembled at the air-water interface for the formation of nanoparticle thin-films. Such nanoparticle films can be promising as functional interfaces in (photo)catalytic, (photo)electrochemical, sensing, anti-fogging as well as other applications.

7.2 Experimental section

7.2.1 Materials

The chemicals were purchased from the following suppliers and used without further purification: P25 TiO_2 nanoparticles (Aeroxide, size <25 nm), ZnO nanoparticles (Sigma Aldrich), WO_3 nanoparticles (Sigma Aldrich), CuO nanoparticles (Sigma Aldrich), oleylamine (70%, Sigma Aldrich), 1-dodecanethiol (Sigma Aldrich), absolute ethanol (Sigma Aldrich), hexane (VWR Chemicals). Deionized water with conductivity <0.1 $\mu S\ cm^{-1}$ was used. 10 mL borosilicate glass vials were used for the phase transfer.

7.2.2 Ligand adsorption experiments

Well-mixed solutions of oleylamine and 1-dodecanethiol were prepared by mixing 400 mg of each ligand in 20 mL ethanol. Colloidal solutions of TiO_2, ZnO, WO_3 and CuO Nanoparticles were prepared by mixing 50 mg of each type of nanoparticle with 10 mL of ethanol. For adsorption, 2 mL of the ligand solution were added to the nanoparticle colloids to be sonicated for 30 minutes. The colloid-ligand mixture was then left still in dark for 4 hours for adsorption. After 4 hours, the colloids were centrifuged (5000 rpm for 10 minutes) and re-washed repeatedly up to 4 cycles to remove any access unbound ligand. To obtain powders, the nanoparticles were dried in an oven at 60^{o}C.

7.2.3 Phase transfer experiments

A colloidal solution was prepared with 15 mg of a given type of nanoparticle (TiO_2/ZnO/WO_3/CuO) in 20 mL of water, followed by sonication for 20 minutes for uniform mixing and breaking down of agglomerates. 1 mL of this solution was mixed with 3 mL of a ligand (oleylamine or 1-dodecanethiol) solution in ethanol (200 mg in 20 mL), in a glass vial, followed by one minute of vortex mixing and 20 minutes of sonication. Now, 4 mL of pure hexane were poured onto this mixture, which remains above the water/ethanol phase as a separate phase. The glass vial was then shaken vigorously in a vortex mixture for one minute for the phase transfer of the nanoparticles to the hexane phase to occur. Upon resting the glass vial for a few minutes, the two phases separate, the water/ethanol mixture phase becomes fully transparent, and the hexane phase attains the colloidal colour. The as-obtained nanoparticle in hexane colloid was centrifuged at 5000 rpm for 15 minutes to remove the excess ligands and

again redispersed in pure hexane. The experiment was repeated for different initial concentrations of the nanoparticle and the same oleylamine/1-dodecanethiol concentration in ethanol in order to test the efficacy.

7.2.4 Self-assembly at air-water interface and immobilization on substrate

TiO_2, ZnO, WO_3 nanoparticles were dispersed in ethanol (50 mg in 20 mL) by sonication for 15 minutes to form a stable colloid. Then, 2 mL of oleylamine in ethanol (400 mg in 20 mL) solution were added to the TiO_2 and WO_3 colloids. Similarly, 2 mL of 1-dodecanethiol in ethanol (400 mg in 20 ml) solution were added to the ZnO colloid. After addition, the colloids were subjected to 30 minutes of sonication followed by four washing steps with ethanol (500 rpm for 10 minutes). After the 4^{th} step, the nanoparticles were re-dispersed in 1 mL of ethanol. 200 μL of these nanoparticles were then introduced along the walls of a beaker of 5.3 cm in diameter, filled for 80% with water so that the nanoparticles flow down along the wall and get trapped at the air-water interface. This step was carried on until the entire surface was covered with a nanoparticle film. In order to immobilize the self-assembled nanoparticle film on a glass or silicon surface, a dip coating method with a slow upward velocity was implemented. The films were then calcined at 450°C for two hours at a heating rate of 3 °C/min, for the removal of the oleylamine or 1-dodecanethiol ligands. Alternatively, the films were subjected to UV light (Philips Cleo 25 W fluorescent light bulbs, λ_{max} at 365 nm) for the degradation of the oleylamine via a photocatalytic route. Trials were also performed with CuO nanoparticles for which the self-assembly could not be achieved efficiently following the same procedure, as the nanoparticles tended to form agglomerates at the interface.

7.2.5 Preparation of nanoparticle films on glass for contact angle measurements

For the measurement of sessile-drop contact angles, nanoparticle films were prepared by drop-casting 200 μL of nanoparticle colloids (50 mg in 1 mL ethanol) on glass pieces(1.5 cm^2) previously cleaned with piranha solution. The ligand functionalized nanoparticles were also dispersed in ethanol in a similar way for drop-casting. The drop-casted films were dried in oven for one hour at 80°C.

7.2.6 Characterization

The scanning transmission electron microscopy (STEM) images were obtained using a FEI Osiris TEM operated at 200 kV. The samples were prepared by drop casting a small drop of the colloidal solutions onto a carbon coated copper grid. The SEM characterization was done with a scanning electron microscope (SEM) equipped with secondary electron and multisegmented backscattered electron detector (EVO10, Carl Zeiss Microscopy GmbH), using an accelerating voltage of 10kV, a take-off angle of 35°. In order to characterize the organic ligand attached to nanoparticles, a Thermo

Fisher Scientific NicoletTM 380 FTIR spectrometer was used to record the infrared spectra in a wavenumber range of 3600 – 400 cm^{-1} in both transmission and Attenuated Total Reflection (ATR) mode. The thermogravimetric analysis (TGA) measurements were performed on a TA Instruments Q5000 thermogravimetric analyzer with a sample heating rate of 10 °C min^{-1} in the temperature range of 30 to 800 °C. During the photocatalytic experiments, the samples were illuminated with UVA fluorescent lamps (Philips Cleo 25 W, incident intensity of 0.87 mW cm^{-2} at a distance of 7.5 cm) and visible lamps (Van-cliff minilight, 1.6 mW cm^{-2} at a distance of 7.5 cm). The contact angle measurements were done with an Ossila sessile drop-based contact angle goniometer with a high-resolution camera (1920 x 1080). The droplet volume used was 4 μL. For the film thickness measurements, a Bruker DektakXT stylus profilometer was used. The measurements were done for 2 mm long sliding steps of the stylus (needle) starting from a bare surface area to the films. The powder X-ray diffraction (XRD) analysis was performed on a Bruker D8 Advance Eco (40kV, 25 mA, Cu Kα wavelength =1.5406 Å). A Low background Si sample holder was used for all XRD measurements. The scan rate was 0.04° with total time per step of 96 seconds for a 2-theta scan range of 20° to 90°.

7.3 Results and discussion

7.3.1 Functionalization and phase-transfer of nanoparticles

The FTIR spectra in **Figure 7.1** compare the presence of the two organic ligands on the different nanoparticle powders after surface adsorption and repeated washing. The intensity of the general ν_s(-CH_2-), ν_{as}(-CH_2-), and ν_{as}(-CH_3) stretches of the alkyl chain in the 2850-3000 cm^{-1} region indicates the amount of both oleylamine and 1-dodecanethiol ligand present in the dry powder. The weaker bands at 1466 and 1377 cm^{-1} arising from the asymmetric and symmetric bending vibration of the methyl group, δ_{as}(-CH_3) and δ_s(-CH_3), respectively, also represent the ligands. Repeated washing steps ensure that any weakly physisorbed species will be removed due to mass action upon introduction of fresh solvent. Clearly, oleylamine remains bound to TiO_2 and WO_3, while 1-dodecanethiol remains on ZnO and CuO nanoparticles. It is, however, difficult to comment on the true chemical nature of the bond on the basis of the stability through washing steps. In the transmission mode, due to the higher opacity of WO_3, the WO_3 sample amount had to be kept at a minimum level yet sufficient as the spectra become too noisy for sample amounts similar to the other materials.[339]

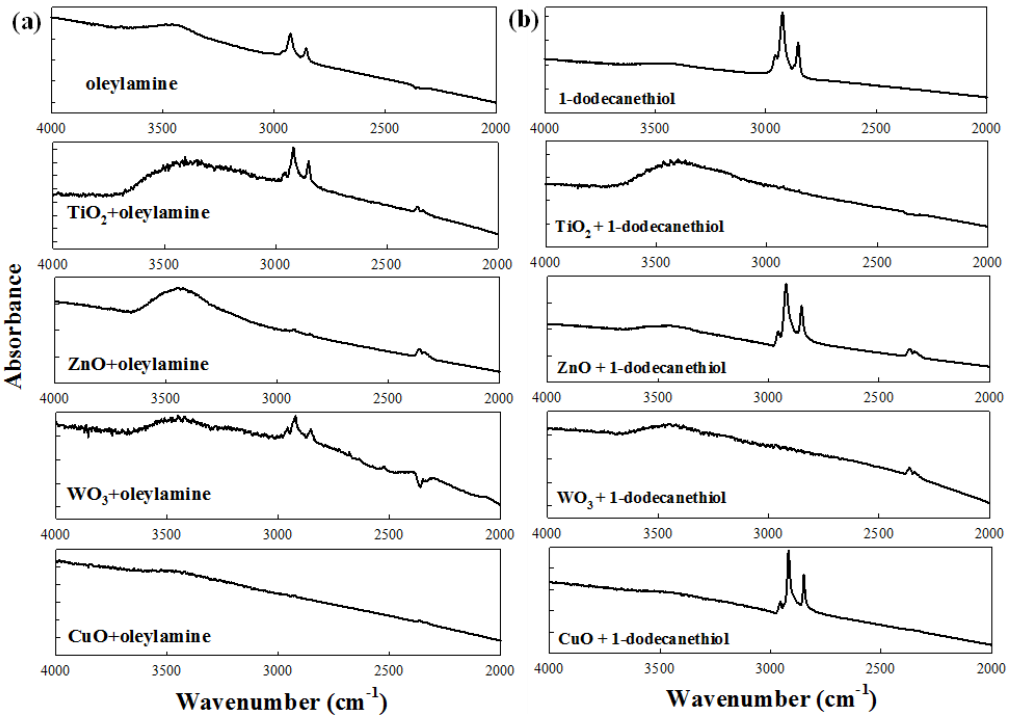

Figure 7.1 FTIR (transmission) spectra comparing $\nu_s(-CH_2-)$, $\nu_{as}(-CH_2-)$, and $\nu_{as}(-CH_3)$ stretches of the alkyl chain of ligand functionalized nanoparticles after four washing cycles: (a) oleylamine and oleylamine + nanoparticles (b) 1-dodecanethiol and 1-dodecanethiol + nanoparticles.

The nanoparticle-ligand interaction becomes clear in the discussion of phase transfer experiments and hydrophobicity by water contact angle measurement later in this study. The broad absorption band in the 3200-3800 cm^{-1} region corresponds to different bands of H_2O adsorbed both dissociatively and in molecular form.[340] This broad absorption band is significantly weakened by adsorption of 1-dodecanethiol on ZnO nanoparticles. However, absorption of oleylamine does not suppress this absorption band in TiO_2 and WO_3 nanoparticles. Since water is adsorbed in many forms, it is important to differentiate those in order to derive further information, as discussed in **section 7.3.2**. Usually, the bands for amine and thiols are difficult to detect due to their relative weakness.[341 342]

Both thiol-metal and amine-metal bonding have been known to be strong interactions, while metal oxide-thiol or metal oxide-amine bonding has not been explored extensively.[343 341] In ligand-exchange studies, thiol often successfully replaces other functional groups under ambient conditions.[320 334] For instance, it has been shown that octadecanethiol can effectively replace oleylamine on Au nanoparticle surfaces by ligand-exchange.[345] Generally, reports on controlled experiments comparing binding tendencies of thiols and amines on metal or metal oxide nanoparticle surfaces are

scant.[346] However, considering the known strong dependence of ligand interaction on the crystal planes[347], Lewis- Brønsted acid sites[348], *etc*., the selectivity of both oleylamine and 1-dodecanethiol to these four metal-oxides in **Figure 7.1** is an expected occurrence. It has been hypothesized that ligands can coordinate as an anion to excess metal atoms on the surface to balance charge and terminate the lattice (X-type), such as oleic acid, dodecanethiol, or phosphonic acids, or as a neutral dative bond (L-type, Lewis basic), as in oleylamine, trioctylphosphine oxide, and trioctylphosphine.[349] To explain the reciprocity in the trend shown in this study, deeper insight into the atomistic interaction is required to explain the tendency of a certain functional group to a certain surface, which is a subject of ongoing theoretical/computational investigations.[350]

This selectivity of one type of functional group to a certain metal oxide observed in the adsorption experiments explains success of the phase transfer experiments of nanoparticles with a specific ligand only, as illustrated in **Figure 7.2**, and with the results of the different metal oxide-ligand phase transfer experiments summarized in **Table 7.1**. Very clearly, phase transfer with oleylamine only works for TiO_2 and WO_3, while 1-dodecanethiol only works for ZnO and CuO. **Figure A7.1** shows the inability of the non-attaching ligands to successfully transfer nanoparticles from a water/ethanol phase to a hexane phase. The phase transfer process requires strong nanoparticle-ligand bonding in order for the nanoparticles to cross the interfacial barrier between the polar and the non-polar phases.[351] [352]Apparently, the amine-ZnO or -CuO and thiol-TiO_2 or -WO_3 interactions are too weak to permanently hydrophobize the nanoparticle surfaces for the interfacial transfer. The thiol-ZnO or CuO bond are strong, resulting in smooth phase transfer and very pronounced infrared absorption bands even after repeated washing steps. It has been shown with XPS analysis that both Zn- and O-terminated nanoparticles of ZnO bind quite strongly with thiol groups and these bonds are thermally stable up to 350^{o}C.[350] Interestingly, on ZnO nanoparticles, an even stronger affinity of phosphonic acid functional groups as compared to thiols has been reported.[351] While certain reports on amine functionalization of ZnO and CuO nanoparticles can also be found in literature[355] [356], it is clear from our experiments that the interaction is not strong enough for phase transfer. On the other hand, the strong interaction between oleylamine and TiO_2 or WO_3 easily enables phase transfer. It is important to note that a ligand that binds strongly to TiO_2 and WO_3 does not necessarily have to be an ineffective binder to ZnO or CuO surfaces. It is known that organic ligands with phosphonic acid functional head groups bind strongly to both TiO_2 and ZnO.[351] [354] [357] [358] This consolidates the fact that the nature of the ligand-nanoparticle interaction varies case by case and the selectivity is determined by both the ligand and the nanoparticle surface chemistry. It is, however, also important to have a sufficiently high ligand concentration as the contact time needed for effective attachment is inversely proportional to this concentration.[359] [360]

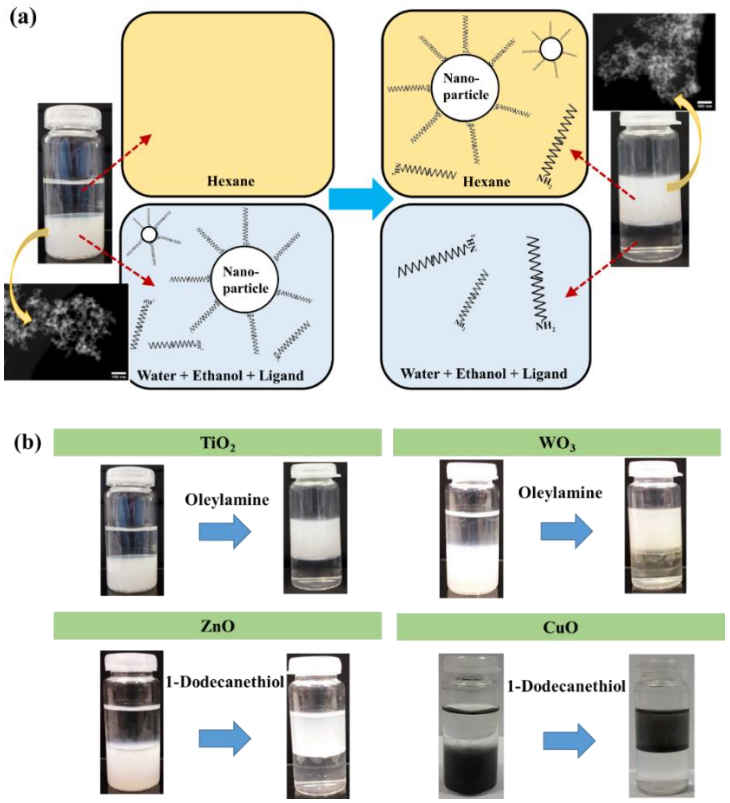

Figure 7.2 (a) Schematic explanation of the polar to non-polar phase transfer procedure of nanoparticles (inset: HAADF-STEM images of TiO_2 nanoparticles before and after phase transfer with 100 nm scale bar). (b) Successful phase transfer of each nanoparticle with its specific ligand. In the unsuccessful experiments, the nanoparticles remain in the bottom ethanol-water phase even after ligand addition and vigorous mixing, as indicated by the color.

Table 7.1 Summary of phase transfer experiments of each metal-oxide nanoparticle with oleylamine and 1-dodecanethiol.

	oleylamine	1-dodecanethiol
TiO_2	**successful**	unsuccessful
WO_3	**successful**	unsuccessful
ZnO	unsuccessful	**successful**
CuO	unsuccessful	**successful**

The selectivity of ligands to bind to a given oxide also prompts experimentation to selectively transfer a particular oxide nanoparticle from a mixture of two. The trial experiment in **Figure A7.2** shows that 1-dodecanethiol can selectively transfer CuO and ZnO nanoparticles from a mixture of CuO-TiO_2 and ZnO-TiO_2, respectively. However, selective phase transfer of TiO_2 using oleylamine was not possible possibly due to the

lack of a relative binding tendency as strong as in the case of thiol. It indicates that thiol-binding is more chemically selective.

7.3.2 Surface chemistry of nanoparticle powders

Since adsorption of H_2O on metal oxide surfaces, especially TiO_2 and ZnO, is well known, comparison of pure nanoparticle powders with ligand functionalized powders with FTIR provides important insight into the ligand binding on the surface. Since the transmission mode includes the H_2O bands possibly due to capillary condensation in the pores, the attenuated total reflectance (ATR) mode is more appropriate for such surface chemistry characterization. In general, ATR-FTIR is a rather simple yet efficient method for surface characterization, especially in the case of WO_3 that yields poor spectral information in the transmission mode due to its opacity. The broad absorption band in the FTIR spectrum of both pure TiO_2 and ZnO powders in the region 3000-3700 cm^{-1} is commonly assigned to the stretching vibration modes of H_2O molecules, **Figure 7.3 (a)**.[361 362] In the context of surface chemistry, the band at 3695 cm^{-1} is of particular interest as it represents isolated non-hydrogen-bonded OH groups on TiO_2, as shown in the HREELS study by Henderson, indicating availability or unavailability of active sites.[363]Similarly, the absorption band around 1637 cm^{-1} is known to be from the scissoring modes of molecularly adsorbed H_2O, **Figure 7.3(b)**. In contrast, the surfaces of WO_3 and CuO nanoparticles are free from adsorbed water. It has been shown by Albanese *et al*. with the help of DFT calculations that H_2O preferably adsorbs on WO_3 in its non-dissociated form due to the presence of ions at the surface that act as Lewis acid sites and this interaction per H_2O molecule is not strong.[364] Lu *et al*. attribute the absence of the H_2O bands on commercial WO_3 to low surface area.[365] Similarly, a number of DFT studies has shown the possibility of both molecular and dissociative adsorption of H_2O on CuO surfaces[366 367], in contrast to the FTIR spectra in **Figure 7.3**, which can in fact be attributed to low surface area. Although surface adsorbed water on WO_3 and CuO is not apparent from the ATR-FTIR spectra, the presence of trapped moisture in the pores has been indicated in the transmission spectra in **Figure 7.1** and TGA analysis in **Figure 7.4**. Nevertheless, comparison with respect to the surface adsorbed H_2O is possible only in the cases of TiO_2 and ZnO.

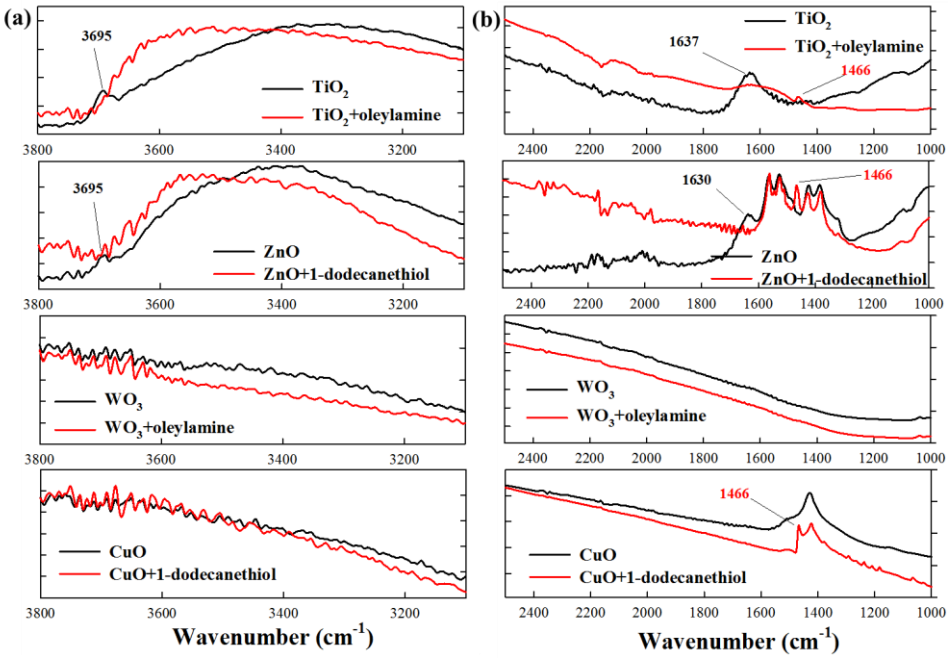

Figure 7.3 ATR-FTIR spectra of ligand functionalized nanoparticles (red) compared with their pure powders (black) in the (a) 3800-3100 cm^{-1} (b) 2500-1000 cm^{-1} regions in terms of H_2O adsorption bands. The bands originating from the dissociative and molecular adsorption of H_2O molecules are marked.

Since H_2O adsorption on TiO_2 and ZnO has been studied extensively, it is useful to discuss these cases with respect to the ATR-FTIR results in order to understand the ligand-nanoparticle interaction. On the (101) surface of anatase TiO_2, which is dominating in this form, molecular adsorption of H_2O is energetically favorable in comparison to dissociative adsorption as shown by Vittadini *et al*.[368] This stability is thought to be due to the hydrogen bonding between the H atoms of the adsorbed H_2O molecules with bridging O atoms on TiO_2. On the (001) surface, dissociative adsorption is favored up to half coverage of the Ti sites beyond which molecular adsorption is more likely.[368] Physical adsorption of H_2O on the first layer via hydrogen bonding has also been shown to be an energetically favorable occurrence. Similarly, on the energetically favorable $(10\bar{1}0)$ surface of ZnO, H_2O adsorbs both dissociatively and as molecules.[369] [362] In the 3100-3800 cm^{-1} region of broad band H_2O absorption in **Figure 7.3 (a)**, as discussed already, the shoulder at 3695 cm^{-1} in both pure TiO_2 and ZnO distinctly signifies dissociatively adsorbed water to the surface.[363] [340] [370] The absence of this shoulder in the spectra of oleylamine-TiO_2 and 1-dodecanethiol-ZnO nanoparticles indicates unavailability of these sites for dissociative chemisorption of H_2O. Similarly, the bands at 1637 and 1630 cm^{-1} in pure TiO_2 and ZnO, respectively, indicate these molecular adsorbed water bands are broadened or hidden in the ligand capped TiO_2 and ZnO. This also indicates occupation of these adsorption sites by the ligands. The 1466

cm^{-1} band for the, $\delta_{as}(-CH_3)$ asymmetric vibrations in both oleylamine and 1-dodecanethiol is also quite clear on ligand grafted nanoparticles. This band is particularly strong in 1-dodecanethiol-capped ZnO and CuO nanoparticles in contrast to the weak intensity in oleylamine-capped TiO_2 and WO_3 nanoparticles. As these experiments were conducted in the dark without any chance of photo-degradation, this indicates weaker oleylamine-nanoparticle interaction and partial removal of surface-ligands due to mass action of washing steps.

Thermogravimetric analysis was carried out to gain further insight into the ligand-functionalization of the nanoparticles, **Figure 7.4**. 1-dodecanethiol starts to burn off at a lower temperature (~150^{o}C) than oleylamine (200^{o}C) below which both the compounds remain at their fixed initial weight, **Figure A7.3**. For the dry powders, the weight loss due to moisture loss starts at around 50^{o}C in all the samples. Also, for the oleylamine capped TiO_2 and WO_3, the weight loss already begins at >50^{o}C, hence the presence of significant trapped moisture despite ligand functionalization is evident. In the transmission FTIR spectra in **Figure 7.1**, this trapped water also contributes substantially to the 3000-3500 cm^{-1} broad absorption band. In contrast, such an early weight loss is not observed in 1-dodecanethiol capped ZnO and CuO nanoparticles, meaning that moisture is present in lower amounts, which is in line with the FTIR spectra of thiol-capped ZnO and CuO nanoparticles where the H_2O band intensity is significantly reduced as compared to uncapped (as oleylamine is not present) ones. This has as a possible implication that 1-dodecanethiol is able to cover ZnO and CuO nanoparticles more stably and extensively. In **Figure 7.4**, both oleylamine and 1-dodecanethiol attached on the nanoparticles start burning off at a temperature higher than their pure forms implying strong ligand-nanoparticle bonding. This elevation of the thermal decomposition temperature is again particularly well-defined for 1-dodecanethiol-capped CuO and ZnO nanoparticles due to strong binding. Importantly, for the same ligand functionalization procedure, CuO nanoparticles carry a considerably high weight % (>50%) of 1-dodecanethiol. A possible implication of this may be the formation of ligand-nanoparticle networks, as a gel-like consistency was observed for ligand-capped CuO nanoparticles. For TiO_2 and WO_3, the transition from the moisture-loss phase to oleylamine decomposition phase is smooth. It indicates that oleylamine-nanoparticle bonding is not as strong as that in the case of 1-dodecanethiol-nanoparticle. A relatively weaker interaction between TiO_2/WO_3 and oleylamine has already been evident from the FTIR spectra comparisons.

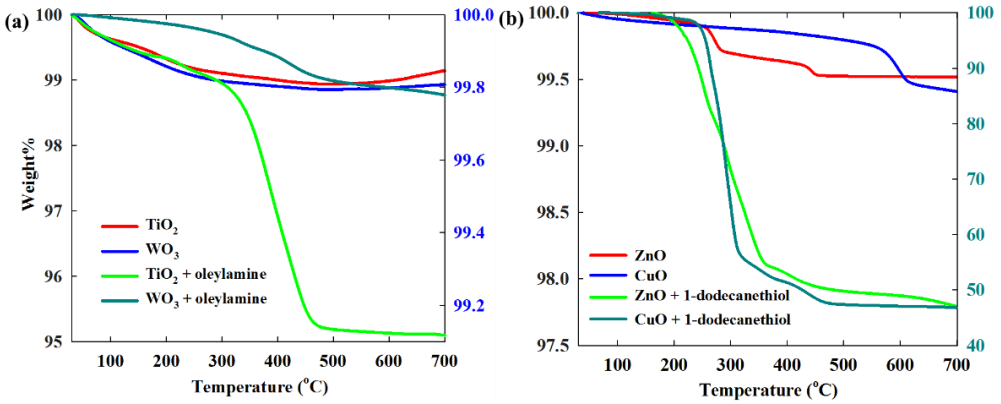

Figure 7.4 Thermogravimetric analysis (TGA) of (a) oleylamine functionalized nanoparticles (b) 1-dodecanethiol functionalized nanoparticles. Right y-axis in Figure (a): WO_3 powder, right y-axis in Figure (b): CuO + 1-dodecanethiol.

7.3.3 Photo-stability of ligand capped nanoparticles

Given that the semiconductor metal-oxide nanoparticles of TiO_2, ZnO, WO_3 and CuO are known to show photocatalytic activity, the photo-stability of the ligand-capped nanoparticles under UV and visible light is an important aspect in any possible application. Conversely, as a positive side-effect of such high photo-instability, *i.e.* fast photodegradation of the ligands, implies high self-cleaning tendencies of the nanoparticles, which in turn opens up various application opportunities. The photo-stability of the ligand capped nanoparticles was tested by monitoring the ν_s(-CH_2-), ν_{as}(-CH_2-), and ν_{as}(-CH_3) bands of the ligands in the 2850-3000 cm^{-1} region under illumination with UV and visible light, **Figure 7.5**. After 24 hours of UV illumination, TiO_2 completely degrades the oleylamine ligands, while WO_3 degrades 45%, with further degradation up to 85% after 48 hours. In contrast, ZnO and CuO nanoparticles could not degrade the ligands to any considerable extent. Similarly, also under visible light (using a white fluorescent lamp), both TiO_2 and WO_3 nanoparticles degrade the ligands effectively, while ZnO and CuO are unable to do the same. As expected, the photocatalytic activity of TiO_2 is lower under visible light with 62% degradation in 24 hours, while WO_3 is equally active under both UV and visible light over the 24 h time span (48% degradation in 24 hours). It is important to note that TiO_2 degrades the ligands under UV within an hour (**Figure 7.6**); thus, the visible light activity of TiO_2 is negligibly low in comparison to the UV light activity. The inactivity of ZnO, which is also a known photocatalytic material, is counterintuitive. It is reasonable to assume that the strong interaction of thiol ligands results in poisoning of the catalyst surface. Therefore, selectivity enhancements with thiol ligands are accompanied by a loss of activity.[371] To understand whether it is the inactivity of ZnO itself or a strong thiol-ZnO binding that prohibits the degradation mechanistically, degradation studies were conducted for both oleylamine and 1-dodecanethiol on TiO_2 and ZnO films on Si

wafers, **Figure 7.6**. Instead of pre-functionalizing the nanoparticles with the ligands, oleylamine and 1-dodecanethiol was spin coated on the surface of both the TiO_2 and ZnO films. Clearly, TiO_2 degrades both oleylamine and 1-dodecanethiol rapidly within an hour. In the case of ZnO nanoparticles, both the ligands remain almost unaffected even after 4 hours of illumination. The fitting of the data points to a first order kinetic model shows that the rate constant for ZnO is two orders of magnitude smaller than that for TiO_2. Thus, the inactivity of ZnO is not due to a particularly strong thiol-ZnO bond hindering a degradation pathway. Similarly, any effect of the shift of band-edge positions due to ligand grafting can be tentatively ruled out by this experiment. Considering their known activity in aqueous medium, the low photocatalytic activity of ZnO and CuO nanoparticles in gas phase may also be related to different surface states and hence, band-edges. While, the concrete postulation of an explanation is difficult in the scope of this study, it could be that the degradation kinetics by ZnO and CuO is slowed down by either charge and/or mass transfer processes.

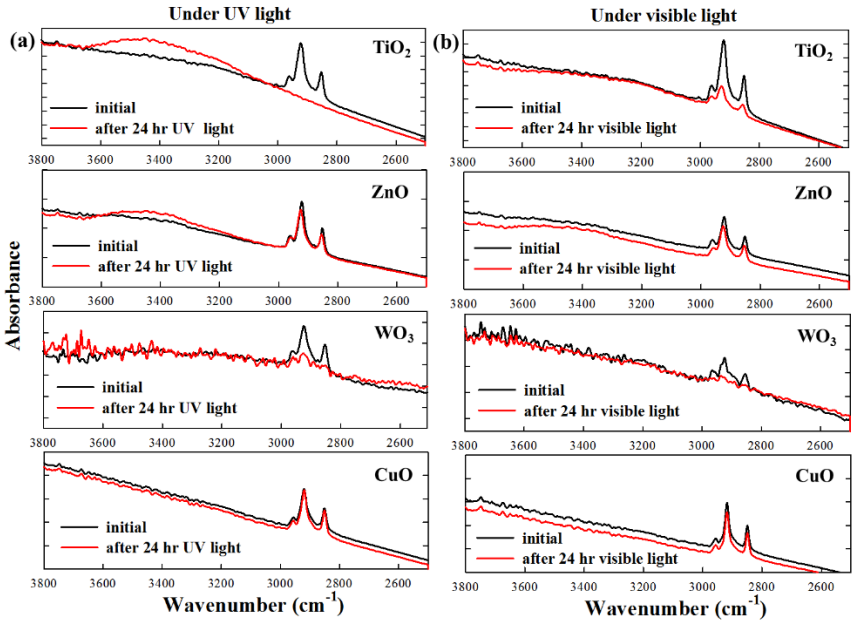

Figure 7.5 FTIR spectra (v_s(-CH_2-), v_{as}(-CH_2-), and v_{as}(-CH_3) bands in the 2800-3000 cm^{-1} region) of ligand capped nanoparticle films on a Si substrate showing photo-stability of the ligands on the nanoparticles under (a) UV (b) visible light irradiance. The intensity of the bands in the 2800-3000 cm^{-1} region indicates the concentration of the ligand molecules. The irradiances are 0.87 mW cm^{-2} and 1.6 mW cm^{-2} for the UV and visible light respectively.

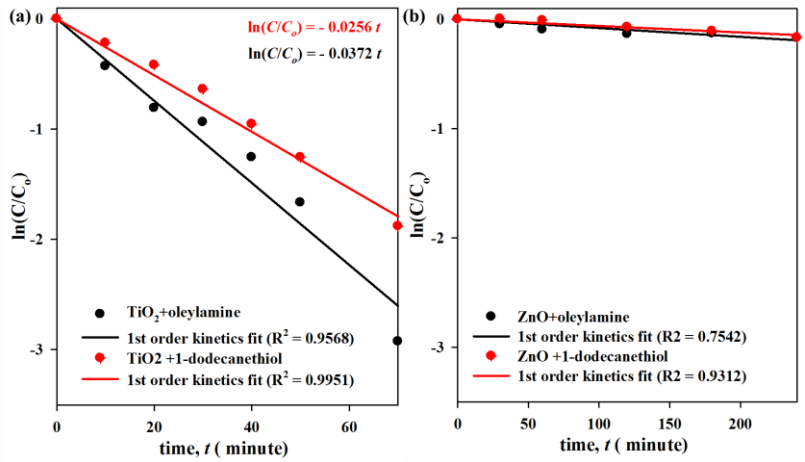

Figure 7.6 Degradation curves of oleylamine and 1-dodecanethiol on (a) TiO_2 and (b) ZnO films respectively fitted to a first order kinetic model. The relative concentrations are estimated from the area of the ν_s(-CH_2-), ν_{as}(-CH_2-), and ν_{as}(-CH_3) bands in the 2800-3000 cm^{-1} region.

7.3.4 Wettability and self-assembly

High wettability, *i.e.* super-hydrophilicity of TiO_2,[372] ZnO, WO_3[373]and CuO[371 374] is known and hydrophobization of these surfaces is important in many applications. This super-hydrophilicity has mostly been attributed to a photo-induced effect explained by several surface chemistry mechanisms. [372] For more details on these mechanisms, the reader is encouraged to consult the comprehensive review by Fujishima *et al.*[375] In addition, the switching between hydrophilic and oleophilic behavior is unique to TiO_2. Photo-induced hydrophilicity (PIH) has also been studied for ZnO, WO_3, and CuO. Like in the case of TiO_2, numerous studies have shown induction of hydrophilicity in ZnO and WO_3 films within a couple of minutes to an hour, while CuO has not been found to show any photo-induced hydrophilicity.[376 377 378] On nanoparticle films such as P25 (TiO_2), where the morphological irregularity may help hydrophobicity, photo-induced super-hydrophilicity can nonetheless be achieved rapidly, as also verified by our experiments.[379]

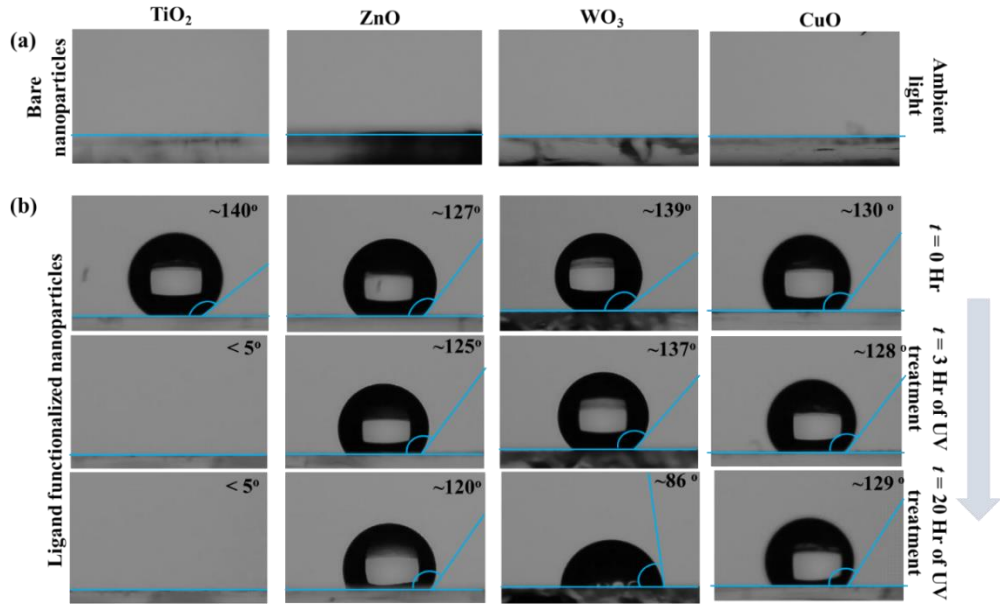

Figure 7.7 Water contact angle obtained by sessile drop technique on drop-casted ligand capped nanoparticle films: (a) ligand free bare nanoparticles (b) hydrophobic functionalized nanoparticles, also showing the effect of UV irradiation. The contact angles are average of five measurements and the blue lines marking the angles are for representation. The irradiances are 0.87 mW cm^{-2} and 1.6 mW cm^{-2} for the UV and visible light respectively.

So, the wettability of the ligand-capped nanoparticles of TiO_2, ZnO, WO_3 and CuO is an important aspect as the presence of the hydrophobic alkyl chains alters the surface chemistry. First, the water contact angle on drop-casted films of non-functionalized bare nanoparticle films of all four oxides were found to be close to 0°, **Figure 7.7 (a)**. This may be a photo-induced process as the films were prepared under ambient light. While PIH is not observed in the case of CuO, it also appears highly hydrophilic in nature. The hydrophilicity of all the different nanoparticles is confirmed by contact angle measurements which also explains easy dispersion of these nanoparticles in water to form stable colloids. In contrast, all the ligand capped nanoparticle films are strongly hydrophobic with an average water contact angle >120°, **Figure 7.7 (b)**. From the experiments in **Figures 7.5** and **7.6**, the irradiation of UV light is supposed to degrade the ligands especially on TiO_2 and WO_3 to revert the surfaces back to their hydrophilic ground state, at a rate corresponding to the photocatalytic self-cleaning rate. Thus, the super-hydrophilicity of TiO_2 film after 3 hours of irradiation is consistent with our photo-stability experiments showing that the ligands are completely degraded under UV within that time period. Similarly, since 24 hours of UV treatment only partially decomposed the ligands on WO_3 nanoparticles (**Figure 7.7 (b)**), the water contact angle is still 86° after 20 hours of illumination. For both ZnO and CuO, the nanoparticle films

remain hydrophobic throughout the UV treatment showing consistency with the photo-stability experiments. To confirm the effect of ligand photo-degradation on the water contact angle, contact angle measurements were taken after keeping the samples in dark for 24 hours, **Figure A7.4**. Importantly, while the correlation holds in this particular case, in general photocatalytic activity cannot always be directly related to photo-induced hydrophilicity as it has been shown that despite comparable photocatalytic activity of $SrTiO_3$, photo-induced hydrophilicity was not observed like in the case of TiO_2.[380]

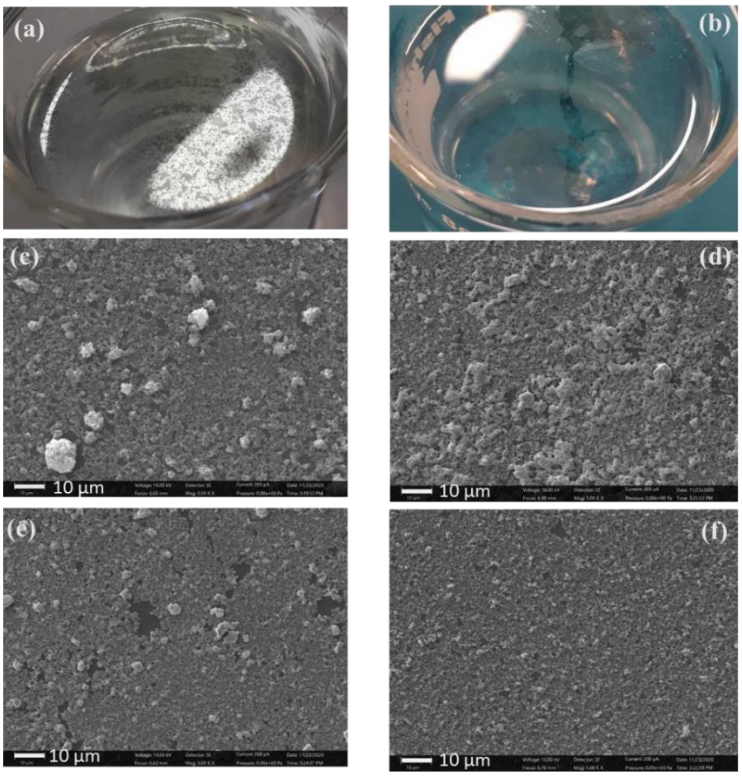

Figure 7.8 Images of assembly of ZnO (a) and TiO_2 (b) nanoparticles at the air-water interface obtained simply over a water surface in a beaker. (c, d, e, f) are SEM images of self-assembled films of TiO_2, WO_3, ZnO (sample 1) and ZnO (sample 2). Sample 1: film after incomplete surface coverage; sample 2: film after complete surface coverage.

The contact angle measurement show that the ligand capping renders the nanoparticles hydrophobic. Thus, self-assembly of these nanoparticles on a water surface is possible by trapping them at the air-water interface, which is otherwise not possible, **Figure A7.5**. In **Figure 7.8 (a)**, a partially covered water surface with ZnO nanoparticles is shown. As more nanoparticles are introduced, the self-assembled islands rearrange and eventually develop a continuous film. The self-assembled films obtained with ZnO nanoparticles as shown in **Figure 7.8 (e)** and **(f)** have high uniformity. Self-assembled films of TiO_2 and WO_3 nanoparticles, **Figure 7.8 (c)** and **(d)**, however, are not as

uniform due to the presence of agglomerates. While there is high surface coverage in all the cases, the uniformity of the self-assembled films is subject to the morphological uniformity of individual nanoparticles. In all these three cases of TiO_2, WO_3 and ZnO, the morphological and dimensional irregularities of the nanoparticles limit the quality of the films in terms of uniformity. **Table 7.2** summarizes the nanoparticle average sizes as provided by the manufacturer data, crystallite size and self-assembled film thicknesses. Due to the size and morphological irregularities, estimating an average size from TEM images (**Figure 7.2**) or dynamic light scattering is not ideal. Thus, the primary crystallite size from Scherrer equation (**Figure A7.8**) by considering the peaks of significant intensity (greater than 20% of maximum intensity peaks) is provided in **Table 7.2** as an indication of the lower limit of the particle size which matches with the manufacturer data. Film thickness profiles were acquired by stylus profilometry (**Figure A7.6**), which captures the transition as the stylus slides from the bare substrate to the film. The profilometry results capture the surface morphology only to an extent as the contact between the needle and the film leads to unavoidable displacement of some particles due to the softness of the assembled layer, hence the relatively large experimental error. Still, the measured average layer thicknesses correspond very well to the expected thickness based on a self-assembled monolayer of the corresponding particles. Even with these irregular nanoparticles, such self-assembled films can be useful in many applications. As an example, **Figure 7.9** demonstrates the use of such a self-assembled TiO_2 nanoparticle film for antifogging applications.

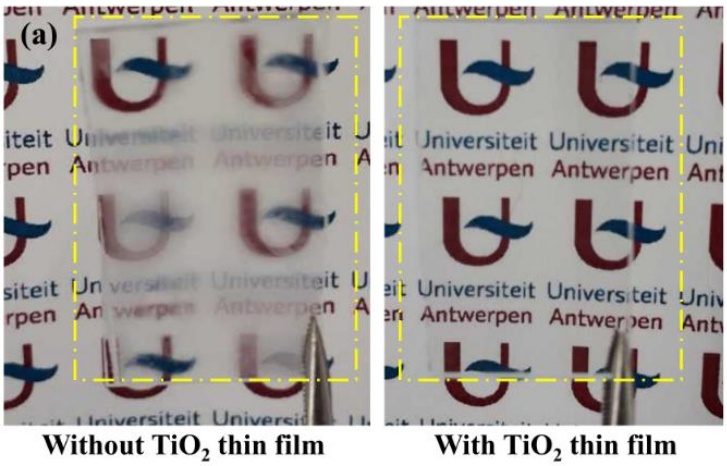

Figure 7.9 Antifogging property of a self-assembled TiO_2 nanoparticle film immobilized on a glass slide held above boiling water. Left: un-treated glass, right: glass with self-assembled TiO_2 nanoparticle film.

Table 7.2 Summary of nanoparticle sizes from manufacturer, crystallite sizes and self-assembled film thicknesses obtained from stylus profilometry.

Material	Avg. Particle size (nm), manufacturer	Avg. crystallite size (nm) (from XRD)	Approx. Film thickness (nm) (from profilometry)
TiO_2	≤25 nm	25.8± 0.4	21.2 ± 4.3
WO_3	≤50 nm	48.4 ± 7.6	67.9 ± 13.2
ZnO	≤40 nm	44.3 ± 5.7	59.3 ± 3.1

7.4 Conclusion

Functionalization of TiO_2, ZnO, WO_3, CuO nanoparticles with alkyl-amine (oleylamine) and alkyl-thiol (1-dodecanethiol) ligands was studied under ambient conditions. It was observed that oleylamine binds strongly to TiO_2 and WO_3, but not to ZnO and CuO. Conversely, 1-dodecanethiol strongly attaches to ZnO and CuO, but not to TiO_2 and WO_3. Polar to non-polar phase transfer experiments confirm these trends. The ligand attachment is stable through the impact of mass action in the washing steps, and confirmed by FTIR data. In the case of TiO_2 and ZnO, it could be shown that oleylamine and 1-dodecanethiol effectively occupy the active sites that are otherwise occupied by OH groups in the pristine powders resulting from dissociative adsorption of ambient H_2O. Under UV and visible light, the stability of the surface ligands on the nanoparticles was found to be dependent not only on the intrinsic photocatalytic activity of the material, but also on the ligand bond strength. While TiO_2 degrades oleylamine within two hours and WO_3 takes more than a day, ZnO and CuO appeared to be quite inactive in degrading the thiol-ligands even after 48 hours of illumination by UV or visible light. Similarly, the hydrophobicity attained by the nanoparticles can be removed by photocatalytic degradation of the amine ligands on TiO_2 and WO_3, while 1-dodecanethiol functionalized ZnO and CuO nanoparticles remain stable and hydrophobic under UV and visible light illumination over an extended period of time (>48 hours). The functionalized nanoparticles can be easily self-assembled at the air-water interface to obtain nanoparticle films for various applications, such as antifogging layers as a demonstrated proof-of-principle in this chapter. While the ligand selectivity of different metal oxide nanoparticles and the corresponding phase transfer processes shown in this chapter is an important aspect relevant to various application scenarios, the demonstration of the use of these hydrophobic functionalized nanoparticles for self-assembled films is potentially valuable to future research on photocatalytic surfaces, photo-electrochemical and photovoltaic applications. Especially in view of the ongoing research on hybrid multifunctional nanoparticles, self-assembly methods are important for obtaining films in a nonintrusive way.

Chapter 8

General conclusions and future outlook

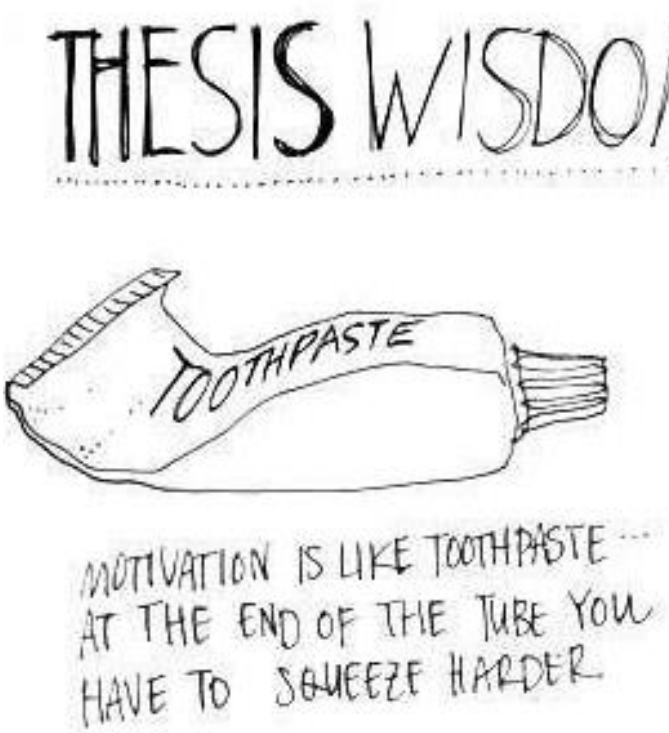

Courtesy: www.inktales.me

8.1 General conclusions: Objectives

In the course of this PhD project, the following **3 main objectives** were investigated:

Objective 1: To gain fundamental insight into plasmonic noble metal nanostructures through computational electromagnetic models, going from individual nanoparticles to infinite particle assemblies, and bridging the gap between theoretical and experimental optical properties of plasmonic nanostructures.

Objective 2: To bridge the gap between theoretical and experimental optical properties of plasmonic nanostructure arrays by investigating the self-assembly of plasmonic nanoparticles and their applications.

Objective 3: To experimentally study the functionalization of metal oxide nanoparticles for self-assembly and related applications.

In **Chapter 1** a general overview of all the relevant topics with regard to the research work reported in this dissertation has been provided. Since this project involves investigation of photoactive nanostructures including plasmonic and metal oxide nanoparticles, a brief introduction has been provided on both classes of nanoparticles. As a major portion of the project is based on computation investigation of the plasmonic nanostructures, the theoretical background based on the classical electromagnetic theory has been introduced. In line with the experimental results, an introduction to self-assembly of nanoparticles has been provided with the recent trends and potential applications.

8.1.1 Objective 1: To gain fundamental insight into plasmonic noble metal nanostructures through computational electromagnetic models, going from individual nanoparticles to infinite particle assemblies, and bridging the gap between theoretical and experimental optical properties of plasmonic nanostructures.

The first objective is a broad one which is achieved in **Chapter 2**, **3**, **4**, **5** and **6** combined. In **Chapter 2**, **3**, **4** and **5**, the important gaps in literature were identified and these unexplored yet important aspects were investigated with regard to the current application focus areas. Specifically, **Chapter 2** compared the plasmonic properties of isolated Ag−Au alloy and core−shell bimetallic nanoparticles. The comparison included spherical as well as anisotropic nanoparticles (rods and triangles) to cover structures with and without the contribution of interband transitions of Au, respectively. The insights obtained from these results are relevant in many different applications such as surface enhanced spectroscopy (SEIRA, SERS, etc.), photothermal applications, hot-electron mediated chemical processes, and so on. Firstly, it was shown that the spectra of core-shell and alloy nanoparticles are qualitatively different with varying features, but quantitatively, the intensity values remain in the same range. Importantly, the interband transition, which is present in Au but not in Ag within the visible range, plays

a big role here. Thus, because anisotropic nanoparticles have their plasmon band in the near-infrared region where interband transitions do no longer occur for Au, the difference between the plasmonic properties of alloy and core-shell structures becomes less prominent. From an application perspective, the differences in core-shell and alloy nanoparticles do not all have equally strong implication. Generally, inclusion of Au, even at a low amount (~20%), was shown to be detrimental for the plasmonic enhancement of spherical Ag nanoparticles. In anisotropic nanoparticles, however, inclusion of Au showed a far lesser impact, especially in core-shell architectures. Because inclusion of Au can reduce the scattering losses of large (>50 nm) Ag nanoparticles and increase the absorption, higher photothermal temperatures can be achieved by incorporating small amount of Au in such larger Ag nanoparticles. Anisotropic nanoparticles are generally highly absorbing, also in the near-infrared region. Such structures are therefore generally better for therapeutic photothermal applications.

The problem tackled in **Chapter 3** was invoked during the investigation of **Chapter 2** while comparing the theoretical and experimental spectra of colloidal plasmonic nanoparticles. The gap between theory and experiment, especially in the case of Ag nanoparticles, posed the question how different statistical and structural aspects of colloidal nanoparticles actually influence the optical response. In **Chapter 3**, the ambiguity surrounding the role of particle size distribution, *i.e*. polydispersity and skewness, intrinsic optical properties and particle surface morphology in determining the collective optical response of colloidal plasmonic nanoparticles has been resolved. Firstly, the results clearly demonstrated that it is the mean nanoparticle size that largely determines the plasmon band or LSPR position. This is true even for a highly polydisperse population of nanoparticles for which the volume distribution is strongly shifted to large particle sizes. The skewness also does not have a significant effect on the LSPR position. Upon clarification of these aspects, the optical properties of Ag nanoparticle colloids could be predicted with Palik's optical constants with significantly improved agreement. Also, for larger nanoparticles (>100 nm), it was apparent that the polydispersity only had a partial role in dampening of the higher order LSPR modes (for instance, the quadrupolar mode). It became clear that mainly the accuracy of the optical constant data largely determines the agreement between theory and experiments. Finally, some important implications of the size distribution on the interpretation of dynamic light scattering data were discussed.

Chapter 4 provided a transition from isolated/individual nanoparticles to nanoparticle assemblies or clusters. It is well-known that closely separated plasmonic nanoparticles couple together through their electrodynamic response which is called the plasmonic coupling. This plasmonic coupling strongly influences the individual optical properties of the nanoparticles in the cluster, and in many ways, enhances the optical response. Thus, in **Chapter 4** the coupled plasmonic response of isolated Au nanoparticle clusters

of different sizes was studied. The collective optical response has been analyzed in terms of near-field and far-field coupling among constituent nanoparticles in the cluster. Otherwise weakly radiative 20 nm Au nanoparticles, when coupled through overlapping of the near-fields in a close packed 2D cluster, started exhibiting an optical response as an integrated structure, resulting in strong absorption and scattering with a spectral shift. The plasmonic coupling in clusters consisting of 20 nm and 40 nm nanoparticles was discussed in terms of near-field and far-field interactions among adjacent nanoparticles. For 20 nm nanoparticles, a 19 nanoparticle cluster was identified as an optimal structure for the highest per-particle absorption and consequent higher photothermal temperature. Also, it was shown that the photothermal temperature can be controlled by varying the interparticle distance. The enhancement in the photothermal properties of nanoparticles in clusters and the dependence of this property on the nanoparticle position withing the cluster, as well as the interparticle distance provides a scope for new applications.

Chapter 5 extended the study of the finite nanoparticle clusters from **Chapter 4** to infinitely extended nanoparticle films (film dimensions >> incident wavelength) with an experimental demonstration of the self-assembly of Au and Ag nanoparticles. For the numerical computations of the infinite film's optical response, a new approach had to be taken with unit-cell computational domains with periodic boundary conditions. Also, in contrast to the scattered field solution in the previous chapters, full-field solutions were obtained by excitation of the incoming wave at the inlet at the top of the computational domain. These models were validated with the experimental optical spectra of self-assembled Au and Ag nanoparticles. The findings from **Chapter 3** were helpful here, especially for Ag nanoparticles. The optical properties of self-assembled films were investigated in the direct normal incidence and Kretschmann (*i.e.* ATR) configuration. Like **Chapter 4**, the individual optical properties of nanoparticles in infinite films were compared with isolated nanoparticles. It was found that the plasmon damping mechanism changes strongly as the interparticle distance decreases, *i.e*. the plasmon coupling becomes stronger. Isolated 20 nm Au nanoparticles that characteristically experience only non-radiative damping, were shown to experience strong reflection, *i.e* radiative damping, when assembled in a close packed film. In the ATR configuration, in the absence of any transmission, high absorption by the nanoparticle films was also demonstrated. The optical properties of the nanoparticles films for *p*-polarized (TM) and *s*-polarized (TE) incidence in the ATR configuration were starkly different. The strong near-field enhancement in the ATR configuration shows great potential for surface enhanced spectroscopy techniques.

While **Chapter 6** is primarily based on the application of self-assembled Au nanoparticle films for volatile organic compound (VOC) sensing, the electromagnetic modelling provided further insight into the polarization specific response of the nanoparticle films. It was shown that the ellipsometric response of the nanoparticle films in the ATR configuration is determined by the difference in the evanescent fields arising

from *p* and *s*-polarized incident beams. The difference in the polarization of the nanoparticles by the two modes of incidence thus give rise to the ψ (amplitude ratio) and Δ (phase difference) spectra, that can be exploited for a highly sensitive sensing strategy.

8.1.2 Objective 2: To bridge the gap between theoretical and experimental optical properties of plasmonic nanostructure arrays by investigating the self-assembly of plasmonic nanoparticles and their applications.

For the validation of the computational models of the infinite nanoparticle films, experimental nanoparticle self-assemblies were fabricated (**Chapter 5**). The nanoparticles were self-assembled at an air-ethylene glycol interface. Before self-assembly, the nanoparticles were transferred from an aqueous phase to a non-polar toluene phase by oleylamine ligand functionalization. Since literature on Ag nanoparticle self-assembly is scant, different trials were carried out to optimize the procedure. These films were characterized by TEM to ensure the homogeneity and obtaining dimensional information to be used in the models.

In **Chapter 6**, an existing method for the self-assembly of Au nanoparticles was further extended towards larger areas of several cm^2. **Chapter 6** demonstrated the application of such films in refractive index-based sensing of volatile organic compounds, methanol in particular. As revealed under Objective 1 , when self-assembled into close-packed films, oleylamine-capped plasmonic Au nanoparticles exhibit collective optical properties through plasmonic coupling, giving rise to lattice resonances. Importantly, the ligand capped nanoparticles form a nanoparticle-ligand network that can facilitate adsorption of the probe molecules from the gas phase. Thus, by tracking the changes in the optical response as a result of a change in the refractive index of the dielectric medium in the vicinity of the nanoparticles due to the adsorption of the molecules, gas phase sensing is enabled. Also shown in **Chapter 5**, due to the periodicity of nanoparticle arrangement, the lattice plasmon modes of self-assembled Au nanoparticle films can be excited by normally incident electromagnetic waves. This is in contrast to planar Au thin films, for which, the excitation of surface plasmon resonance requires a special arrangement like the Kretschmann (ATR) or Otto configuration. Still, it was shown that the lattice resonance of Au nanoparticle films could also be very effectively excited in the Kretschmann configuration by the interaction of the evanescent field with the nanoparticles at the low refractive index side. The refractive index sensitivity of the intensity spectra (*i.e.*, transmittance, absorptance, or reflectance) of the self-assembled films in both normal incidence and Kretschmann configuration was shown to be similar to grating-based plasmonic sensing platforms reported in literature. Moreover, when *in-situ* ellipsometry and *in-situ* spectroscopy are compared, ψ and Δ measurements, especially probing Δ can provide up to a 10-fold better sensitivity, which paves the way toward improved plasmonic-based sensing applications.

8.1.3 Objective 3: To experimentally study the functionalization of metal oxide nanoparticles for self-assembly and related applications.

Metal oxide nanoparticle thin films also have numerous applications. In particular, metal oxide nanoparticles can be hybridized with plasmonic nanostructures (e.g. in core-shell configurations) for plasmon-enhanced thin film applications. In this regard, functionalization of TiO_2, ZnO, WO_3, CuO nanoparticles with alkyl-amine (oleylamine) and alkyl-thiol (1-dodecanethiol) ligands was studied under ambient conditions in **Chapter 7**. Through this functionalization, it was shown that the nanoparticles dispersed in a polar phase (aqueous or other polar solvents) could be transferred to a non-polar phase (hexane). Further, these nanoparticles were self-assembled at the air-water interface to obtain thin nanoparticle films. The selectivity study showed that oleylamine binds strongly to TiO_2 and WO_3, but not to ZnO and CuO. Conversely, 1-dodecanethiol strongly attached to ZnO and CuO, but not to TiO_2 and WO_3. The ligand attachment resisted the impact of mass action during washing steps, which was also confirmed by FTIR data. In the case of TiO_2 and ZnO, it could be shown that oleylamine and 1-dodecanethiol effectively occupy the active sites that are otherwise occupied by OH groups in the pristine powders resulting from dissociative adsorption of ambient H_2O. Under UV and visible light, the stability of the surface ligands on the nanoparticles was found to be dependent not only on the intrinsic photocatalytic activity of the material, but also on the ligand bond strength. While TiO_2 degrades oleylamine almost within one hour and WO_3 takes more than a day, ZnO and CuO appeared to be quite inactive in degrading the thiol-ligands even after 48 hours of illumination by UV or visible light. Similarly, the hydrophobicity attained by the nanoparticles can be removed by photocatalytic degradation of the amine ligands on TiO_2 and WO_3, while 1-dodecanethiol functionalized ZnO and CuO nanoparticles remain stable and hydrophobic under UV and visible light illumination over an extended period of time (>48 hours). The functionalized nanoparticles were easily self-assembled at the air-water interface to obtain nanoparticle films for various applications, such as antifogging layers as was a demonstrated proof-of-principle in this chapter. While the ligand selectivity of different metal oxide nanoparticles and the corresponding phase transfer processes shown in this chapter is an important aspect relevant to various application scenarios, the demonstration of the use of these hydrophobic functionalized nanoparticles for self-assembled films is potentially valuable to future research on photocatalytic surfaces, photo-electrochemical and photovoltaic applications. Especially in view of the ongoing research on hybrid multifunctional nanoparticles, self-assembly methods are important for obtaining films in a nonintrusive way.

8.2 Future outlook

Research is creating new knowledge.. (Neil Armstrong) and there is no end to this creative process. Given the time and resources, it is important for the author to set the scope of the research, and define a beginning and an end of the PhD project. In this final

discussion of this dissertation, it is thus useful to provide a perspective on the possible future developments based on the research carried out in the course of this PhD.

Firstly, based on the theoretical insights into core-shell and alloy nanoparticles that were gathered using the techniques in **Chapter 2**, it will be interesting to study spherical and anisotropic nanoparticles in real applications. For instance, how the incorporation of Au in Ag in these two kinds of nanostructures impacts the activity in hot electron mediated processes is an important research question to address. Also, in photothermal therapy, the application of Ag nanoparticles with a thin Au shell will be interesting for future developments as the Au shell not only protects Ag chemically, it also increases the absorption intensity. Extension of the alloy *vs*. core shell comparison for isolated nanoparticles in **Chapter 2** to close packed arrays of nanoparticles poses an interesting research problem as plasmonic nanoparticles have significantly different optical behaviour as arrays when compared with isolated nanoparticles. The experimental validation of the results in **Chapter 4** also remains as an important future objective as significant enhancement of the photothermal properties is shown in clusters as compared to isolated nanoparticles. In fact, by combining colloidal synthesis with lithographic techniques, several research groups have shown the feasibility of obtaining finite 2D nanoparticle cluster arrays over large areas. To exploit the dependence of the photothermal temperature on the interparticle gap, nanoscale control of the photothermal temperature of the clusters by the variation of the interparticle gap is also an interesting future objective relevant to sensing applications. In addition, further theoretical as well as experimental work on 3D clusters will be interesting as such clusters can be synthesized by colloidal techniques like DNA origami, emulsion mediated self-assembly, *etc*., with great controllability. As in 3D clusters, since the heat retainment is more effective in the nanoparticles at the interior of the cluster, a higher photothermal temperature can be expected. Also, the broadening of the plasmon band enhances the amount of light absorbed from the solar spectrum.

The air-liquid interfacial self-assembly of nanoparticles has been a topic of growing interest in the area of functional nanomaterials. Since the optical interaction of plasmonic nanoparticles is enhanced by plasmonic coupling, the integration of the self-assembled plasmonic nanoparticle films (as experimentally demonstrated in **Chapter 5)** in photocatalytic, photoelectrochemical and photovoltaic applications merits further investigations. Future experimental study of the application of Au or Ag nanoparticle self-assembled films in surface-enhanced spectroscopy (SEIRA, SERS, etc.), especially in the Kretschmann configuration, is an important lead for analytical research.

Based on the VOC sensing experiments shown in **Chapter 6**, there lies great scope towards further development for higher sensitivity and selectivity. One promising strategy is integrating the self-assembled nanoparticle films with ultra-porous materials (for example, microporous metal organic frameworks or MOFs) for selective adsorption and concentration of the probe molecules . The challenge in integrating the two systems

lies in the modification of the surface chemistry of the material for selective adsorption. A similar approach can also be adopted for biosensing applications where selective adsorption of the probe molecules on the nanoparticle can be mediated by surface chemistry. In all the sensing applications, ATR configuration can provide a convenient arrangement for improved sensitivity. Again, application of Ag nanoparticles instead of Au nanoparticles in such sensing applications can yield better results due to better plasmonic properties of Ag. However, in the applications with Ag nanoparticles, an additional challenge has to be tackled as Ag nanoparticles are not chemically stable. Thus, strategies for the stabilization of Ag nanoparticles with a protecting material such as silica, polymer, *etc*., is a parallel research problem that is already being studied by our group and collaborators. **Chapter 7** indicates the future development opportunities with metal oxide nanoparticles. An application area of the as-shown self-assembled metal oxide nanoparticle films to be explored, is gas sensing with nanoparticle thin films. While the colloidally synthesized nanoparticles provide high surface area for interfacial processes, the self-assembled monolayer films have very low thickness for efficient charge carrier transport in a circuit. Finally, self-assembly techniques hold great promise towards the application of hybrid colloidal nanoparticles. For instance, plasmonic core-metal oxide shell nanoparticles are such hybrids where the light driven processes in the metal oxide are enhanced by the plasmonic core. To obtain functional interfaces from such nanoparticles, self-assembly is a promising strategy that requires further investigation.

Curriculum vitae

Personal Information

Name	Rituraj Borah
Date of Birth	26.10.1990
Address	Sint-Sebastiaanstraat 45, Wilrijk, Antwerp, Belgium – 2610.
Permanent address	By lane 2, Chandan Nagar, Club road, Jorhat, India - 785001
Nationality	Indian
Contact number	+32 4658 68831
e-mail	*rituraj386@gmail.com* *rituraj.borah@uantwerpen.be*

Education

Nov. 2018 - present	PhD at Department of Bioscience Engineering, University of Antwerp, Belgium
July 2016 – May 2018	Masters in Chemical Engineering, Indian Institute of Technology Kanpur, India
July 2010 – May 2014	Bachelors in Chemical Engineering National Institute of Technology Rourkela, India

Professional Experience

Sept. 2014 – June 2016	Chemical Process Engineer (Technical Services and Production), Paradeep Phosphates Limited (Adventz Group), India

Research stays/Industrial internships

February 2022 – March 2022 (research stay)	Leibniz Institute for Interactive Materials, RWTH Aachen, Germany
June 2018 – August 2018 (research stay)	Department of Engineering and System Sciences, National Tsing Hua University, Taiwan

May 2013 - July 2013 (industrial internship)	Numaligarh Refinery Limited (NRL), Assam, India
May 2012 - July 2012 (summer research internship)	Council of Scientific and Industrial Research (NEIST), Jorhat, India

Publications

1. **Borah, R**.; Verbruggen, S. W. Effect of Size Distribution, Skewness and Roughness on the Optical Properties of Colloidal Plasmonic Nanoparticles. *Colloids and Surfaces A: Physicochemical and Engineering Aspects* 2022, *640*, 128521.

2. **Borah, R**.; Ninakanti, R.; Nuyts, G.; Peeters, H.; Pedrazo-Tardajos, A.; Nuti, S.; Velde, C. V.; Wael, K. D.; Lenaerts, S.; Bals, S.; Verbruggen, S. W. Selectivity in the Ligand Functionalization of Photocatalytic Metal Oxide Nanoparticles for Phase Transfer and Self-Assembly Applications. *Chemistry – A European Journal* 2021, *27* (35), 9011–9021.

3. **Borah, R**.; Verbruggen, S. W. Silver–Gold Bimetallic Alloy versus Core–Shell Nanoparticles: Implications for Plasmonic Enhancement and Photothermal Applications. *J. Phys. Chem. C* 2020, *124* (22), 12081–12094.

4. **Borah, R**.; Verbruggen, S. W. Coupled Plasmon Modes in 2D Gold Nanoparticle Clusters and Their Effect on Local Temperature Control. *J. Phys. Chem. C* 2019, *123* (50), 30594–30603.

5. Ninakanti, R.; Dingenen, F.; **Borah, R.**; Peeters, H.; Verbruggen, S. W.; Plasmonic Hybrid Nanostructures in Photocatalysis: Structures, Mechanisms and Applications. (Accepted in *Topics in Current Chemistry*)

6. Blommaerts, N.; Hoeven, N.; Arenas Esteban, D.; Campos, R.; Mertens, M.; **Borah, R**.; Glisenti, A.; De Wael, K.; Bals, S.; Lenaerts, S.; Verbruggen, S. W.; Cool, P. Tuning the Turnover Frequency and Selectivity of Photocatalytic CO2 Reduction to CO and Methane Using Platinum and Palladium Nanoparticles on Ti-Beta Zeolites. *Chemical Engineering Journal* 2021, *410*, 128234.

7. Dingenen, F.; Blommaerts, N.; Van Hal, M.; **Borah, R**.; Arenas-Esteban, D.; Lenaerts, S.; Bals, S.; Verbruggen, S. W. Layer-by-Layer-Stabilized Plasmonic Gold-Silver Nanoparticles on TiO2: Towards Stable Solar Active Photocatalysts. *Nanomaterials* 2021, *11* (10), 2624.

8. **Borah, R**.; Gupta, S.; Mishra, L.; Chhabra, R. P.; Heating of Liquid Foods in Cans: Effects of Can Geometry, Orientation, and Food Rheology. *Journal of Food Process Engineering* 2020, *43* (7), e13420.

9. Dasgupta, N.; **Borah, R**.; Mishra, P.; Gupta, A. K.; Chhabra, R. P. Combined Effects of Blockage and Yield Stress on Drag and Heat Transfer from an In-Line Array of Three Spheres. *Journal of Dispersion Science and Technology* 2019, *40* (6), 855–873.

10. Purbia, R.; **Borah, R**.; Paria S.; Carbon-Doped Mesoporous Anatase TiO2 Multi-Tubes Nanostructures for Highly Improved Visible Light Photocatalytic Activity. *Inorg. Chem.* 2017, *56* (16), 10107–10116.

Submitted Articles

1. Dingenen, F.; **Borah**, **R**.; Ninakanti, R.; Verbruggen, S. W., Probing oxygen activation on plasmonic photocatalysts.
2. **Borah, R**.; Smets, J.; Ninakanti, R.; Tietze, M. L.; Ameloot, R.; Bals, S.; Lenaerts, S.; Verbruggen, S. W.; Self-assembled Ligand-capped Plasmonic (Au) Nanoparticle Films in the Kretschmann Configuration: Towards Sensing of Volatile Organic Compounds.

Articles in preparation/to be submitted

1. **Borah, R.**; Ninakanti, R.; Bals, S.; Verbruggen, S. W.; Plasmonic Lattice Resonances in Self-assembled Arrays of Silver and Gold Nanoparticles: Normal *vs*. ATR (Kretschmann) Configuration.
2. **Borah, R.**; Verbruggen, S. W.; Self-Assembly of Colloidal Nanoparticles into Clusters, Patterns and Films: Methods and Applications.

Patent(s)

1. **Borah, R.**; A. G., Karthick Raj; Verbruggen, S. W.; Electrolysis reactor (in process).

Conference contributions

1) 24th National Symposium for Biological Sciences (NSABS), 4th February, 2019, Ghent, Belgium: Poster presentation.

2) 2nd Chemical Research in Flanders (CRF 2) conference, 14th - 16th October 2019, Blankenberghe, Belgium: Oral presentation.

3) The Belgian Photonics Conference (bePOM), 11th September 2020, online: Poster presentation.

4) International Conference on Frontiers in Chemical Engineering (ICFCE-2013), 9th – 11th December, 2013, NIT Rourkela, Odisha, India: Oral presentation.

Scholarships/Awards and Grants

1) Encouraging grant 2021 'Rosa Blanckaert' for young researchers: Exact and Applied Sciences.

2) Taiwan International Graduate Program IIP grant (2018).

3) Full scholarship from the Government of India for pursuing post graduate education (2016).

Bibliography

(1) Mansoori, G.; Soelaiman, T. A. F. Nanotechnology — An Introduction for the Standards Community. **2005**. https://doi.org/10.1520/JAI13110.

(2) Bayda, S.; Adeel, M.; Tuccinardi, T.; Cordani, M.; Rizzolio, F. The History of Nanoscience and Nanotechnology: From Chemical–Physical Applications to Nanomedicine. *Molecules* **2020**, *25* (1), 112. https://doi.org/10.3390/molecules25010112.

(3) Barchiesi, D.; Otto, A. Excitations of Surface Plasmon Polaritons by Attenuated Total Reflection, Revisited. *Rivista del Nuovo Cimento* **2013**, *36* (5), 173. https://doi.org/10.1393/ncr/i2013-10088-9.

(4) Zhang, Y. Theory of Plasmonic Hot-Carrier Generation and Relaxation. *J. Phys. Chem. A* **2021**, *125* (41), 9201–9208. https://doi.org/10.1021/acs.jpca.1c05837.

(5) Horvath, H. Gustav Mie and the Scattering and Absorption of Light by Particles: Historic Developments and Basics. *Journal of Quantitative Spectroscopy and Radiative Transfer* **2009**, *110* (11), 787–799. https://doi.org/10.1016/j.jqsrt.2009.02.022.

(6) Mie, G. Beiträge Zur Optik Trüber Medien, Speziell Kolloidaler Metallösungen. *Annalen der Physik* **1908**, *330* (3), 377–445. https://doi.org/10.1002/andp.19083300302.

(7) Bozzola, A.; Perotto, S.; Angelis, F. D. Hybrid Plasmonic–Photonic Whispering Gallery Mode Resonators for Sensing: A Critical Review. *Analyst* **2017**, *142* (6), 883–898. https://doi.org/10.1039/C6AN02693A.

(8) Freestone, I.; Meeks, N.; Sax, M.; Higgitt, C. The Lycurgus Cup — A Roman Nanotechnology. *Gold Bull* **2007**, *40* (4), 270–277. https://doi.org/10.1007/BF03215599.

(9) Haes, A. J.; Stuart, D. A.; Nie, S.; Van Duyne, R. P. Using Solution-Phase Nanoparticles, Surface-Confined Nanoparticle Arrays and Single Nanoparticles as Biological Sensing Platforms. *Journal of Fluorescence* **2004**, *14* (4), 355–367. https://doi.org/10.1023/B:JOFL.0000031817.35049.1f.

(10) Sadler, P. J. Gold—Progress in Chemistry, Biochemistry and Technology. H. Schmidbaur (Ed.) John Wiley & Sons, Chichester, 1999 908 Pages. £250 ISBN 0-471-97369-6. *Applied Organometallic Chemistry* **2000**, *14* (3), 171–171. https://doi.org/10.1002/(SICI)1099-0739(200003)14:3<171::AID-AOC921>3.0.CO;2-O.

(11) Schlather, A. E.; Gieri, P.; Robinson, M.; Centeno, S. A.; Manjavacas, A. Nineteenth-Century Nanotechnology: The Plasmonic Properties of Daguerreotypes. *PNAS* **2019**, *116* (28), 13791–13798. https://doi.org/10.1073/pnas.1904331116.

(12) Brazil, R. Plasmonic Color Makes a Comeback. *ACS Cent. Sci.* **2020**, *6* (3), 332–335. https://doi.org/10.1021/acscentsci.0c00259.

(13) Edwards, P. P.; Thomas, J. M. Gold in a Metallic Divided State—From Faraday to Present-Day Nanoscience. *Angewandte Chemie International Edition* **2007**, *46* (29), 5480–5486. https://doi.org/10.1002/anie.200700428.

(14) Loos, M. Chapter 1 - Nanoscience and Nanotechnology. In *Carbon Nanotube Reinforced Composites*; Loos, M., Ed.; William Andrew Publishing: Oxford, 2015; pp 1–36. https://doi.org/10.1016/B978-1-4557-3195-4.00001-1.

(15) Yu, H.; Peng, Y.; Yang, Y.; Li, Z.-Y. Plasmon-Enhanced Light–Matter Interactions and Applications. *npj Comput Mater* **2019**, *5* (1), 1–14. https://doi.org/10.1038/s41524-019-0184-1.

(16) Ye, H.; Liu, Y.; Zhan, L.; Liu, Y.; Qin, Z. Signal Amplification and Quantification on Lateral Flow Assays by Laser Excitation of Plasmonic Nanomaterials. *Theranostics* **2020**, *10* (10), 4359–4373. https://doi.org/10.7150/thno.44298.

(17) Svedendahl, M.; Chen, S.; Käll, M. An Introduction to Plasmonic Refractive Index Sensing. In *Nanoplasmonic Sensors*; Dmitriev, A., Ed.; Integrated Analytical Systems; Springer: New York, NY, 2012; pp 1–26. https://doi.org/10.1007/978-1-4614-3933-2_1.

(18) Guo, L.; Jackman, J. A.; Yang, H.-H.; Chen, P.; Cho, N.-J.; Kim, D.-H. Strategies for Enhancing the Sensitivity of Plasmonic Nanosensors. *Nano Today* **2015**, *10* (2), 213–239. https://doi.org/10.1016/j.nantod.2015.02.007.

(19) Langer, J.; Jimenez de Aberasturi, D.; Aizpurua, J.; Alvarez-Puebla, R. A.; Auguié, B.; Baumberg, J. J.; Bazan, G. C.; Bell, S. E. J.; Boisen, A.; Brolo, A. G.; Choo, J.; Cialla-May, D.; Deckert, V.; Fabris, L.; Faulds, K.; García de Abajo, F. J.; Goodacre, R.; Graham, D.; Haes, A. J.; Haynes, C. L.; Huck, C.; Itoh, T.; Käll, M.; Kneipp, J.; Kotov, N. A.; Kuang, H.; Le Ru, E. C.; Lee, H. K.; Li, J.-F.; Ling, X. Y.; Maier, S. A.; Mayerhöfer, T.; Moskovits, M.; Murakoshi, K.; Nam, J.-M.; Nie, S.; Ozaki, Y.; Pastoriza-Santos, I.; Perez-Juste, J.; Popp, J.; Pucci, A.; Reich, S.; Ren, B.; Schatz, G. C.; Shegai, T.; Schlücker, S.; Tay, L.-L.; Thomas, K. G.; Tian, Z.-Q.; Van Duyne, R. P.; Vo-Dinh, T.; Wang, Y.; Willets, K. A.; Xu, C.; Xu, H.; Xu, Y.; Yamamoto, Y. S.; Zhao, B.; Liz-Marzán, L. M. Present and Future of Surface-Enhanced Raman Scattering. *ACS Nano* **2020**, *14* (1), 28–117. https://doi.org/10.1021/acsnano.9b04224.

(20) Kawasaki, H.; Suzuki, H.; Maekawa, M.; Hariyama, T. Combination of the NanoSuit Method and Gold/Platinum Particle-Based Lateral Flow Assay for Quantitative and Highly Sensitive Diagnosis Using a Desktop Scanning Electron Microscope. *Journal of Pharmaceutical and Biomedical Analysis* **2021**, *196*, 113924. https://doi.org/10.1016/j.jpba.2021.113924.

(21) Li, L.; Wu, S.; Li, L.; Zhou, Z.; Ding, H.; Xiao, C.; Li, X. Gap-Mode Excitation, Manipulation, and Refractive-Index Sensing Application by Gold Nanocube Arrays. *Nanoscale* **2019**, *11* (12), 5467–5473. https://doi.org/10.1039/C8NR09073D.

(22) Seh, Z. W.; Liu, S.; Low, M.; Zhang, S.-Y.; Liu, Z.; Mlayah, A.; Han, M.-Y. Janus Au-TiO2 Photocatalysts with Strong Localization of Plasmonic Near-Fields for Efficient Visible-Light Hydrogen Generation. *Advanced Materials* **2012**, *24* (17), 2310–2314. https://doi.org/10.1002/adma.201104241.

(23) Elmoula, M. A.; Panaitescu, E.; Phan, M.; Yin, D.; Richter, C.; Lewis, L. H.; Menon, L. Controlled Attachment of Gold Nanoparticles on Ordered Titania Nanotube Arrays. *J. Mater. Chem.* **2009**, *19* (26), 4483–4487. https://doi.org/10.1039/B903197A.

(24) Zhou, L.; Tan, Y.; Wang, J.; Xu, W.; Yuan, Y.; Cai, W.; Zhu, S.; Zhu, J. 3D Self-Assembly of Aluminium Nanoparticles for Plasmon-Enhanced Solar Desalination. *Nature Photon* **2016**, *10* (6), 393–398. https://doi.org/10.1038/nphoton.2016.75.

(25) Liu, T.; Li, Y. Plasmonic Solar Desalination. *Nature Photon* **2016**, *10* (6), 361–362. https://doi.org/10.1038/nphoton.2016.97.

(26) Hackett, L. P.; Goddard, L. L.; Liu, G. L. Plasmonic Nanocone Arrays for Rapid and Detailed Cell Lysate Surface Enhanced Raman Spectroscopy Analysis. *Analyst* **2017**, *142* (23), 4422–4430. https://doi.org/10.1039/C7AN00630F.

(27) Govorov, A. O.; Zhang, H.; Demir, H. V.; Gun'ko, Y. K. Photogeneration of Hot Plasmonic Electrons with Metal Nanocrystals: Quantum Description and Potential Applications. *Nano Today* **2014**, *9* (1), 85–101. https://doi.org/10.1016/j.nantod.2014.02.006.

(28) George, J. M.; Antony, A.; Mathew, B. Metal Oxide Nanoparticles in Electrochemical Sensing and Biosensing: A Review. *Microchim Acta* **2018**, *185* (7), 358. https://doi.org/10.1007/s00604-018-2894-3.

(29) Korotcenkov, G. *Colloidal Metal Oxide Nanoparticles: Synthesis, Characterization and Applications*, 1st edition.; Thomas, S., Sunny, A. T., V, P., Eds.; Elsevier: Amsterdam, 2019.

(30) Li, W.; Walther, C. F. J.; Kuc, A.; Heine, T. Density Functional Theory and Beyond for Band-Gap Screening: Performance for Transition-Metal Oxides and Dichalcogenides. *J. Chem. Theory Comput.* **2013**, *9* (7), 2950–2958. https://doi.org/10.1021/ct400235w.

(31) Haque, F.; Daeneke, T.; Kalantar-zadeh, K.; Ou, J. Z. Two-Dimensional Transition Metal Oxide and Chalcogenide-Based Photocatalysts. *Nano-Micro Lett.* **2018**, *10* (2), 1–27. https://doi.org/10.1007/s40820-017-0176-y.

(32) *Surfaces and Interfaces of Metal Oxide Thin Films, Multilayers, Nanoparticles and Nano-Composites: In Memory of Prof. Dr. Hanns-Ulrich Habermeier*; Roca, A. G., Mele, P., Kijima-Aoki, H., Fantechi, E., Vejpravova, J. K., Kalbac, M., Kaneko, S., Endo, T., Eds.; Springer, 2021.

(33) Lu, Y.; Yin, W.-J.; Peng, K.-L.; Wang, K.; Hu, Q.; Selloni, A.; Chen, F.-R.; Liu, L.-M.; Sui, M.-L. Self-Hydrogenated Shell Promoting Photocatalytic H2 Evolution on Anatase TiO2. *Nat Commun* **2018**, *9* (1), 2752. https://doi.org/10.1038/s41467-018-05144-1.

(34) Nishiyama, H.; Yamada, T.; Nakabayashi, M.; Maehara, Y.; Yamaguchi, M.; Kuromiya, Y.; Nagatsuma, Y.; Tokudome, H.; Akiyama, S.; Watanabe, T.; Narushima, R.; Okunaka, S.; Shibata, N.; Takata, T.; Hisatomi, T.; Domen, K. Photocatalytic Solar Hydrogen Production from Water on a 100-M2 Scale. *Nature* **2021**, *598* (7880), 304–307. https://doi.org/10.1038/s41586-021-03907-3.

(35) Huang, F.-C.; Chen, Y.-Y.; Wu, T.-T. A Room Temperature Surface Acoustic Wave Hydrogen Sensor with Pt Coated ZnO Nanorods. *Nanotechnology* **2009**, *20* (6), 065501. https://doi.org/10.1088/0957-4484/20/6/065501.

(36) Ji, H.; Zeng, W.; Li, Y. Gas Sensing Mechanisms of Metal Oxide Semiconductors: A Focus Review. *Nanoscale* **2019**, *11* (47), 22664–22684. https://doi.org/10.1039/C9NR07699A.

(37) Bishop, K. J. M.; Wilmer, C. E.; Soh, S.; Grzybowski, B. A. Nanoscale Forces and Their Uses in Self-Assembly. *Small* **2009**, *5* (14), 1600–1630. https://doi.org/10.1002/smll.200900358.

(38) Rogers, W. B.; Shih, W. M.; Manoharan, V. N. Using DNA to Program the Self-Assembly of Colloidal Nanoparticles and Microparticles. *Nat Rev Mater* **2016**, *1* (3), 1–14. https://doi.org/10.1038/natrevmats.2016.8.

(39) Zhao, Y.; Shi, L.; Kuang, H.; Xu, C. DNA-Driven Nanoparticle Assemblies for Biosensing and Bioimaging. *Top Curr Chem (Z)* **2020**, *378* (1), 18. https://doi.org/10.1007/s41061-020-0282-z.

(40) Singamaneni, S.; Bliznyuk, V. N.; Binek, C.; Tsymbal, E. Y. Magnetic Nanoparticles: Recent Advances in Synthesis, Self-Assembly and Applications. *J. Mater. Chem.* **2011**, *21* (42), 16819–16845. https://doi.org/10.1039/C1JM11845E.

(41) Hughes, R. A.; Menumerov, E.; Neretina, S. When Lithography Meets Self-Assembly: A Review of Recent Advances in the Directed Assembly of Complex Metal Nanostructures on Planar and Textured Surfaces. *Nanotechnology* **2017**, *28* (28), 282002. https://doi.org/10.1088/1361-6528/aa77ce.

(42) Hu, L.; Chen, M.; Fang, X.; Wu, L. Oil–Water Interfacial Self-Assembly: A Novel Strategy for Nanofilm and Nanodevice Fabrication. *Chem. Soc. Rev.* **2012**, *41* (3), 1350–1362. https://doi.org/10.1039/C1CS15189D.

(43) G. Zarbin, A. J. Liquid–Liquid Interfaces: A Unique and Advantageous Environment to Prepare and Process Thin Films of Complex Materials. *Materials Horizons* **2021**, *8* (5), 1409–1432. https://doi.org/10.1039/D0MH01676D.

(44) Blodgett, K. B. Films Built by Depositing Successive Monomolecular Layers on a Solid Surface. *J. Am. Chem. Soc.* **1935**, *57* (6), 1007–1022. https://doi.org/10.1021/ja01309a011.

(45) Hussain, S. A.; Dey, B.; Bhattacharjee, D.; Mehta, N. Unique Supramolecular Assembly through Langmuir – Blodgett (LB) Technique. *Heliyon* **2018**, *4* (12), e01038. https://doi.org/10.1016/j.heliyon.2018.e01038.

(46) Tao, A.; Sinsermsuksakul, P.; Yang, P. Tunable Plasmonic Lattices of Silver Nanocrystals. *Nature Nanotech* **2007**, *2* (7), 435–440. https://doi.org/10.1038/nnano.2007.189.

(47) Ye, X.; Chen, J.; Engel, M.; Millan, J. A.; Li, W.; Qi, L.; Xing, G.; Collins, J. E.; Kagan, C. R.; Li, J.; Glotzer, S. C.; Murray, C. B. Competition of Shape and Interaction Patchiness for Self-Assembling Nanoplates. *Nature Chem* **2013**, *5* (6), 466–473. https://doi.org/10.1038/nchem.1651.

(48) Dong, A.; Chen, J.; Vora, P. M.; Kikkawa, J. M.; Murray, C. B. Binary Nanocrystal Superlattice Membranes Self-Assembled at the Liquid–Air Interface. *Nature* **2010**, *466* (7305), 474–477. https://doi.org/10.1038/nature09188.

(49) Cargnello, M.; Johnston-Peck, A. C.; Diroll, B. T.; Wong, E.; Datta, B.; Damodhar, D.; Doan-Nguyen, V. V. T.; Herzing, A. A.; Kagan, C. R.; Murray, C. B. Substitutional Doping in Nanocrystal Superlattices. *Nature* **2015**, *524* (7566), 450–453. https://doi.org/10.1038/nature14872.

(50) Mueller, N. S.; Okamura, Y.; Vieira, B. G. M.; Juergensen, S.; Lange, H.; Barros, E. B.; Schulz, F.; Reich, S. Deep Strong Light–Matter Coupling in

Plasmonic Nanoparticle Crystals. *Nature* **2020**, *583* (7818), 780–784. https://doi.org/10.1038/s41586-020-2508-1.

(51) Liu, Y.; Deng, K.; Yang, J.; Wu, X.; Fan, X.; Tang, M.; Quan, Z. Shape-Directed Self-Assembly of Nanodumbbells into Superstructure Polymorphs. *Chem. Sci.* **2020**, *11* (16), 4065–4073. https://doi.org/10.1039/D0SC00592D.

(52) Griesemer, S. D.; You, S. S.; Kanjanaboos, P.; Calabro, M.; Jaeger, H. M.; Rice, S. A.; Lin, B. The Role of Ligands in the Mechanical Properties of Langmuir Nanoparticle Films. *Soft Matter* **2017**, *13* (17), 3125–3133. https://doi.org/10.1039/C7SM00319F.

(53) Nie, H.-L.; Dou, X.; Tang, Z.; Jang, H. D.; Huang, J. High-Yield Spreading of Water-Miscible Solvents on Water for Langmuir–Blodgett Assembly. *J. Am. Chem. Soc.* **2015**, *137* (33), 10683–10688. https://doi.org/10.1021/jacs.5b06052.

(54) Morag, A.; Philosof-Mazor, L.; Volinsky, R.; Mentovich, E.; Richter, S.; Jelinek, R. Self-Assembled Transparent Conductive Electrodes from Au Nanoparticles in Surfactant Monolayer Templates. *Advanced Materials* **2011**, *23* (37), 4327–4331. https://doi.org/10.1002/adma.201101290.

(55) Schulz, F.; Pavelka, O.; Lehmkühler, F.; Westermeier, F.; Okamura, Y.; Mueller, N. S.; Reich, S.; Lange, H. Structural Order in Plasmonic Superlattices. *Nat Commun* **2020**, *11* (1), 3821. https://doi.org/10.1038/s41467-020-17632-4.

(56) Kim, F.; Kwan, S.; Akana, J.; Yang, P. Langmuir−Blodgett Nanorod Assembly. *J. Am. Chem. Soc.* **2001**, *123* (18), 4360–4361. https://doi.org/10.1021/ja0059138.

(57) Song, H.; Kim, F.; Connor, S.; Somorjai, G. A.; Yang, P. Pt Nanocrystals: Shape Control and Langmuir−Blodgett Monolayer Formation. *J. Phys. Chem. B* **2005**, *109* (1), 188–193. https://doi.org/10.1021/jp0464775.

(58) Martin, M. N.; Basham, J. I.; Chando, P.; Eah, S.-K. Charged Gold Nanoparticles in Non-Polar Solvents: 10-Min Synthesis and 2D Self-Assembly. *Langmuir* **2010**, *26* (10), 7410–7417. https://doi.org/10.1021/la100591h.

(59) Moon, G. D.; Lee, T. I.; Kim, B.; Chae, G.; Kim, J.; Kim, S.; Myoung, J.-M.; Jeong, U. Assembled Monolayers of Hydrophilic Particles on Water Surfaces. *ACS Nano* **2011**, *5* (11), 8600–8612. https://doi.org/10.1021/nn202733f.

(60) Xiong, S.; Dunphy, D. R.; Wilkinson, D. C.; Jiang, Z.; Strzalka, J.; Wang, J.; Su, Y.; de Pablo, J. J.; Brinker, C. J. Revealing the Interfacial Self-Assembly Pathway of Large-Scale, Highly-Ordered, Nanoparticle/Polymer Monolayer Arrays at an Air/Water Interface. *Nano Lett.* **2013**, *13* (3), 1041–1046. https://doi.org/10.1021/nl304253y.

(61) Dumur, F.; Reculusa, S.; Mruczkiewicz, M.; Perrin, M.; Vignau, L.; Fasquel, S. Multilayer Langmuir-Blodgett Films as Diffractive External 3D Photonic Crystal in Blue OLEDs. *Opt. Express, OE* **2016**, *24* (24), 27184–27198. https://doi.org/10.1364/OE.24.027184.

(62) Dong, A.; Chen, J.; Vora, P. M.; Kikkawa, J. M.; Murray, C. B. Binary Nanocrystal Superlattice Membranes Self-Assembled at the Liquid–Air Interface. *Nature* **2010**, *466* (7305), 474–477. https://doi.org/10.1038/nature09188.

(63) Stolarczyk, J. K.; Deak, A.; Brougham, D. F. Nanoparticle Clusters: Assembly and Control Over Internal Order, Current Capabilities, and Future Potential. *Advanced Materials* **2016**, *28* (27), 5400–5424. https://doi.org/10.1002/adma.201505350.

(64) Zhang, M.; Ettelaie, R.; Dong, L.; Li, X.; Li, T.; Zhang, X.; Binks, B. P.; Yang, H. Pickering Emulsion Droplet-Based Biomimetic Microreactors for Continuous Flow Cascade Reactions. *Nat Commun* **2022**, *13* (1), 475. https://doi.org/10.1038/s41467-022-28100-6.

(65) Burdyny, T.; Riordon, J.; Dinh, C.-T.; Sargent, E. H.; Sinton, D. Self-Assembled Nanoparticle-Stabilized Photocatalytic Reactors. *Nanoscale* **2016**, *8* (4), 2107–2115. https://doi.org/10.1039/C5NR05859G.

(66) Kaewsaneha, C.; Tangboriboonrat, P.; Polpanich, D.; Eissa, M.; Elaissari, A. Preparation of Janus Colloidal Particles via Pickering Emulsion: An Overview. *Colloids and Surfaces A: Physicochemical and Engineering Aspects* **2013**, *439*, 35–42. https://doi.org/10.1016/j.colsurfa.2013.01.004.

(67) Yoon, S. J.; Murthy, A.; Johnston, K. P.; Sokolov, K. V.; Emelianov, S. Y. Thermal Stability of Biodegradable Plasmonic Nanoclusters in Photoacoustic Imaging. *Opt. Express, OE* **2012**, *20* (28), 29479–29487. https://doi.org/10.1364/OE.20.029479.

(68) Wu, S.-H.; Mou, C.-Y.; Lin, H.-P. Synthesis of Mesoporous Silica Nanoparticles. *Chem. Soc. Rev.* **2013**, *42* (9), 3862–3875. https://doi.org/10.1039/C3CS35405A.

(69) Suematsu, K.; Shin, Y.; Hua, Z.; Yoshida, K.; Yuasa, M.; Kida, T.; Shimanoe, K. Nanoparticle Cluster Gas Sensor: Controlled Clustering of SnO2 Nanoparticles for Highly Sensitive Toluene Detection. *ACS Appl. Mater. Interfaces* **2014**, *6* (7), 5319–5326. https://doi.org/10.1021/am500944a.

(70) Sun, Y.; Zhao, Z.; Zhou, R.; Li, P.; Zhang, W.; Suematsu, K.; Hu, J. Synthesis of In2O3 Nanocubes, Nanocube Clusters, and Nanocubes-Embedded Au Nanoparticles for Conductometric CO Sensors. *Sensors and Actuators B: Chemical* **2021**, *345*, 130433. https://doi.org/10.1016/j.snb.2021.130433.

(71) Fraire, J. C.; Pérez, L. A.; Coronado, E. A. Cluster Size Effects in the Surface-Enhanced Raman Scattering Response of Ag and Au Nanoparticle Aggregates: Experimental and Theoretical Insight. *J. Phys. Chem. C* **2013**, *117* (44), 23090–23107. https://doi.org/10.1021/jp3123709.

(72) Ait-Touchente, Z.; Falah, S.; Scavetta, E.; Chehimi, M. M.; Touzani, R.; Tonelli, D.; Taleb, A. Different Electrochemical Sensor Designs Based on Diazonium Salts and Gold Nanoparticles for Pico Molar Detection of Metals. *Molecules* **2020**, *25* (17), 3903. https://doi.org/10.3390/molecules25173903.

(73) Dhar, J.; Patil, S. Self-Assembly and Catalytic Activity of Metal Nanoparticles Immobilized in Polymer Membrane Prepared via Layer-by-Layer Approach. *ACS Appl. Mater. Interfaces* **2012**, *4* (3), 1803–1812. https://doi.org/10.1021/am300068e.

(74) Krasteva, N.; Besnard, I.; Guse, B.; Bauer, R. E.; Müllen, K.; Yasuda, A.; Vossmeyer, T. Self-Assembled Gold Nanoparticle/Dendrimer Composite Films for Vapor Sensing Applications. *Nano Lett.* **2002**, *2* (5), 551–555. https://doi.org/10.1021/nl020242s.

(75) Wu, Y.; Yu, W.; Yang, B.; Li, P. Self-Assembled Two-Dimensional Gold Nanoparticle Film for Sensitive Nontargeted Analysis of Food Additives with

Surface-Enhanced Raman Spectroscopy. *Analyst* **2018**, *143* (10), 2363–2368. https://doi.org/10.1039/C8AN00540K.

(76) Karg, M.; König, T. A. F.; Retsch, M.; Stelling, C.; Reichstein, P. M.; Honold, T.; Thelakkat, M.; Fery, A. Colloidal Self-Assembly Concepts for Light Management in Photovoltaics. *Materials Today* **2015**, *18* (4), 185–205. https://doi.org/10.1016/j.mattod.2014.10.036.

(77) Yadav, A.; Gerislioglu, B.; Ahmadivand, A.; Kaushik, A.; Cheng, G. J.; Ouyang, Z.; Wang, Q.; Yadav, V. S.; Mishra, Y. K.; Wu, Y.; Liu, Y.; RamaKrishna, S. Controlled Self-Assembly of Plasmon-Based Photonic Nanocrystals for High Performance Photonic Technologies. *Nano Today* **2021**, *37*, 101072. https://doi.org/10.1016/j.nantod.2020.101072.

(78) West, P. R.; Ishii, S.; Naik, G. V.; Emani, N. K.; Shalaev, V. M.; Boltasseva, A. Searching for Better Plasmonic Materials. *Laser & Photonics Reviews* **2010**, *4* (6), 795–808. https://doi.org/10.1002/lpor.200900055.

(79) Valenti, M.; Venugopal, A.; Tordera, D.; Jonsson, M. P.; Biskos, G.; Schmidt-Ott, A.; Smith, W. A. Hot Carrier Generation and Extraction of Plasmonic Alloy Nanoparticles. *ACS Photonics* **2017**, *4* (5), 1146–1152. https://doi.org/10.1021/acsphotonics.6b01048.

(80) Mahmoud, M. A.; El-Sayed, M. A. Different Plasmon Sensing Behavior of Silver and Gold Nanorods. *J. Phys. Chem. Lett.* **2013**, *4* (9), 1541–1545. https://doi.org/10.1021/jz4005015.

(81) Verbruggen, S. W.; Keulemans, M.; Goris, B.; Blommaerts, N.; Bals, S.; Martens, J. A.; Lenaerts, S. Plasmonic 'Rainbow' Photocatalyst with Broadband Solar Light Response for Environmental Applications. *Applied Catalysis B: Environmental* **2016**, *188*, 147–153. https://doi.org/10.1016/j.apcatb.2016.02.002.

(82) Ristig, S.; Chernousova, S.; Meyer-Zaika, W.; Epple, M. Synthesis, Characterization and in Vitro Effects of 7 Nm Alloyed Silver–Gold Nanoparticles. *Beilstein J. Nanotechnol.* **2015**, *6* (1), 1212–1220. https://doi.org/10.3762/bjnano.6.124.

(83) Qiu, G.; Ng, S. P.; Wu, C.-M. L. Bimetallic Au-Ag Alloy Nanoislands for Highly Sensitive Localized Surface Plasmon Resonance Biosensing. *Sensors and Actuators B: Chemical* **2018**, *265*, 459–467. https://doi.org/10.1016/j.snb.2018.03.066.

(84) Yang, Y.; Shi, J.; Kawamura, G.; Nogami, M. Preparation of Au–Ag, Ag–Au Core–Shell Bimetallic Nanoparticles for Surface-Enhanced Raman Scattering. *Scripta Materialia* **2008**, *58* (10), 862–865. https://doi.org/10.1016/j.scriptamat.2008.01.017.

(85) Link, S.; Wang, Z. L.; El-Sayed, M. A. Alloy Formation of Gold−Silver Nanoparticles and the Dependence of the Plasmon Absorption on Their Composition. *J. Phys. Chem. B* **1999**, *103* (18), 3529–3533. https://doi.org/10.1021/jp990387w.

(86) Verbruggen, S. W.; Keulemans, M.; Martens, J. A.; Lenaerts, S. Predicting the Surface Plasmon Resonance Wavelength of Gold–Silver Alloy Nanoparticles. *J. Phys. Chem. C* **2013**, *117* (37), 19142–19145. https://doi.org/10.1021/jp4070856.

(87) Verbruggen, S. W.; Keulemans, M.; Filippousi, M.; Flahaut, D.; Van Tendeloo, G.; Lacombe, S.; Martens, J. A.; Lenaerts, S. Plasmonic Gold–

Silver Alloy on TiO2 Photocatalysts with Tunable Visible Light Activity. *Applied Catalysis B: Environmental* **2014**, *156–157*, 116–121. https://doi.org/10.1016/j.apcatb.2014.03.027.

(88) Gilroy, K. D.; Ruditskiy, A.; Peng, H.-C.; Qin, D.; Xia, Y. Bimetallic Nanocrystals: Syntheses, Properties, and Applications. *Chem. Rev.* **2016**, *116* (18), 10414–10472. https://doi.org/10.1021/acs.chemrev.6b00211.

(89) Shankar, C.; Dao, A. T. N.; Singh, P.; Higashimine, K.; Mott, D. M.; Maenosono, S. Chemical Stabilization of Gold Coated by Silver Core–Shell Nanoparticles via Electron Transfer. *Nanotechnology* **2012**, *23* (24), 245704. https://doi.org/10.1088/0957-4484/23/24/245704.

(90) Sutter, E. A.; Sutter, P. W. In Situ Liquid Cell Electron Microscopy of Ag–Au Galvanic Replacement Reactions. *Nanoscale* **2017**, *9* (3), 1271–1278. https://doi.org/10.1039/C6NR07293C.

(91) Yang, Y.; Liu, J.; Fu, Z.-W.; Qin, D. Galvanic Replacement-Free Deposition of Au on Ag for Core–Shell Nanocubes with Enhanced Chemical Stability and SERS Activity. *J. Am. Chem. Soc.* **2014**, *136* (23), 8153–8156. https://doi.org/10.1021/ja502472x.

(92) Zhang, Z.; Bando, K.; Taguchi, A.; Mochizuki, K.; Sato, K.; Yasuda, H.; Fujita, K.; Kawata, S. Au-Protected Ag Core/Satellite Nanoassemblies for Excellent Extra-/Intracellular Surface-Enhanced Raman Scattering Activity. *ACS Appl. Mater. Interfaces* **2017**, *9* (50), 44027–44037. https://doi.org/10.1021/acsami.7b14976.

(93) Liu, H.; Liu, T.; Zhang, L.; Han, L.; Gao, C.; Yin, Y. Etching-Free Epitaxial Growth of Gold on Silver Nanostructures for High Chemical Stability and Plasmonic Activity. *Advanced Functional Materials* **2015**, *25* (34), 5435–5443. https://doi.org/10.1002/adfm.201502366.

(94) Blommaerts, N.; Vanrompay, H.; Nuti, S.; Lenaerts, S.; Bals, S.; Verbruggen, S. W. Unraveling Structural Information of Turkevich Synthesized Plasmonic Gold–Silver Bimetallic Nanoparticles. *Small 0* (0), 1902791. https://doi.org/10.1002/smll.201902791.

(95) Blommaerts, N.; Vanrompay, H.; Nuti, S.; Lenaerts, S.; Bals, S.; Verbruggen, S. W. Unraveling Structural Information of Turkevich Synthesized Plasmonic Gold–Silver Bimetallic Nanoparticles. *Small* **2019**, *15* (42), 1902791. https://doi.org/10.1002/smll.201902791.

(96) Wang, C.; Peng, S.; Chan, R.; Sun, S. Synthesis of AuAg Alloy Nanoparticles from Core/Shell-Structured Ag/Au. *Small* **2009**, *5* (5), 567–570. https://doi.org/10.1002/smll.200801169.

(97) Shore, M. S.; Wang, J.; Johnston-Peck, A. C.; Oldenburg, A. L.; Tracy, J. B. Synthesis of Au(Core)/Ag(Shell) Nanoparticles and Their Conversion to AuAg Alloy Nanoparticles. *Small* **2011**, *7* (2), 230–234. https://doi.org/10.1002/smll.201001138.

(98) Sanyal, U.; Davis, D. T.; Jagirdar, B. R. Bimetallic Core–Shell Nanocomposites Using Weak Reducing Agent and Their Transformation to Alloy Nanostructures. *Dalton Trans.* **2013**, *42* (19), 7147–7157. https://doi.org/10.1039/C3DT33086A.

(99) Rioux, D.; Vallières, S.; Besner, S.; Muñoz, P.; Mazur, E.; Meunier, M. An Analytic Model for the Dielectric Function of Au, Ag, and Their Alloys.

Advanced Optical Materials **2014**, *2* (2), 176–182. https://doi.org/10.1002/adom.201300457.

(100) Prodan, E.; Radloff, C.; Halas, N. J.; Nordlander, P. A Hybridization Model for the Plasmon Response of Complex Nanostructures. *Science* **2003**, *302* (5644), 419–422. https://doi.org/10.1126/science.1089171.

(101) Espinosa, A.; Curcio, A.; Cabana, S.; Radtke, G.; Bugnet, M.; Kolosnjaj-Tabi, J.; Péchoux, C.; Alvarez-Lorenzo, C.; Botton, G. A.; Silva, A. K. A.; Abou-Hassan, A.; Wilhelm, C. Intracellular Biodegradation of Ag Nanoparticles, Storage in Ferritin, and Protection by a Au Shell for Enhanced Photothermal Therapy. *ACS Nano* **2018**, *12* (7), 6523–6535. https://doi.org/10.1021/acsnano.8b00482.

(102) Liu, X.; Shan, G.; Yu, J.; Yang, W.; Ren, Z.; Wang, X.; Xie, X.; Chen, H.; Chen, X. Laser Heating of Metallic Nanoparticles for Photothermal Ablation Applications. *AIP Advances* **2017**, *7* (2), 025308. https://doi.org/10.1063/1.4977554.

(103) Cathcart, N.; Chen, J. I. L.; Kitaev, V. LSPR Tuning from 470 to 800 Nm and Improved Stability of Au–Ag Nanoparticles Formed by Gold Deposition and Rebuilding in the Presence of Poly(Styrenesulfonate). *Langmuir* **2018**, *34* (2), 612–621. https://doi.org/10.1021/acs.langmuir.7b03537.

(104) Qi, Y.; Xing, T.; Zhao, J.; Weng, G.; Li, J.; Zhu, J.; Zhao, J. Tuning the Surface Enhanced Raman Scattering Performance of Anisotropic Au Core−Ag Shell Hetero-Nanostructure: The Effect of Core Geometry. *Journal of Alloys and Compounds* **2019**, *776*, 934–947. https://doi.org/10.1016/j.jallcom.2018.10.321.

(105) Kluczyk, K.; Jacak, W. Damping-Induced Size Effect in Surface Plasmon Resonance in Metallic Nano-Particles: Comparison of RPA Microscopic Model with Numerical Finite Element Simulation (COMSOL) and Mie Approach. *Journal of Quantitative Spectroscopy and Radiative Transfer* **2016**, *168*, 78–88. https://doi.org/10.1016/j.jqsrt.2015.08.021.

(106) Borah, R.; Gupta, S.; Mishra, L.; Chhabra, R. P. Heating of Liquid Foods in Cans: Effects of Can Geometry, Orientation, and Food Rheology. *Journal of Food Process Engineering n/a* (n/a), e13420. https://doi.org/10.1111/jfpe.13420.

(107) Dasgupta, N.; Borah, R.; Mishra, P.; Gupta, A. K.; Chhabra, R. P. Combined Effects of Blockage and Yield Stress on Drag and Heat Transfer from an In-Line Array of Three Spheres. *Journal of Dispersion Science and Technology* **2019**, *40* (6), 855–873. https://doi.org/10.1080/01932691.2018.1485581.

(108) Donner, J. S.; Baffou, G.; McCloskey, D.; Quidant, R. Plasmon-Assisted Optofluidics. *ACS Nano* **2011**, *5* (7), 5457–5462. https://doi.org/10.1021/nn200590u.

(109) Baffou, G.; Quidant, R.; García de Abajo, F. J. Nanoscale Control of Optical Heating in Complex Plasmonic Systems. *ACS Nano* **2010**, *4* (2), 709–716. https://doi.org/10.1021/nn901144d.

(110) Chen, X.; Chen, Y.; Yan, M.; Qiu, M. Nanosecond Photothermal Effects in Plasmonic Nanostructures. *ACS Nano* **2012**, *6* (3), 2550–2557. https://doi.org/10.1021/nn2050032.

(111) Mkhatshwa, M.; Motsa, S.; Sibanda, P. Overlapping Multi-Domain Spectral Method for Conjugate Problems of Conduction and MHD Free Convection

Flow of Nanofluids over Flat Plates. *Mathematical and Computational Applications* **2019**, *24* (3), 75. https://doi.org/10.3390/mca24030075.

(112) Fukutani, H. Optical Constants of Silver-Gold Alloys. *J. Phys. Soc. Jpn.* **1971**, *30* (2), 399–403. https://doi.org/10.1143/JPSJ.30.399.

(113) Ripken, K. Die optischen Konstanten von Au, Ag und ihren Legierungen im Energiebereich 2,4 bis 4,4 eV. *Z. Physik* **1972**, *250* (3), 228–234. https://doi.org/10.1007/BF01387459.

(114) Mulvaney, P. Surface Plasmon Spectroscopy of Nanosized Metal Particles. *Langmuir* **1996**, *12* (3), 788–800. https://doi.org/10.1021/la9502711.

(115) Etchegoin, P. G.; Le Ru, E. C.; Meyer, M. An Analytic Model for the Optical Properties of Gold. *J. Chem. Phys.* **2006**, *125* (16), 164705. https://doi.org/10.1063/1.2360270.

(116) Etchegoin, P. G.; Le Ru, E. C.; Meyer, M. Erratum: "An Analytic Model for the Optical Properties of Gold" [J. Chem. Phys. 125, 164705 (2006)]. *J. Chem. Phys.* **2007**, *127* (18), 189901. https://doi.org/10.1063/1.2802403.

(117) Nishijima, Y.; Akiyama, S. Unusual Optical Properties of the Au/Ag Alloy at the Matching Mole Fraction. *Opt. Mater. Express, OME* **2012**, *2* (9), 1226–1235. https://doi.org/10.1364/OME.2.001226.

(118) Peña-Rodríguez, O.; Caro, M.; Rivera, A.; Olivares, J.; Perlado, J. M.; Caro, A. Optical Properties of Au-Ag Alloys: An Ellipsometric Study. *Opt. Mater. Express, OME* **2014**, *4* (2), 403–410. https://doi.org/10.1364/OME.4.000403.

(119) Gong, C.; Leite, M. S. Noble Metal Alloys for Plasmonics. *ACS Photonics* **2016**, *3* (4), 507–513. https://doi.org/10.1021/acsphotonics.5b00586.

(120) Patskovsky, S.; Bergeron, E.; Rioux, D.; Simard, M.; Meunier, M. Hyperspectral Reflected Light Microscopy of Plasmonic Au/Ag Alloy Nanoparticles Incubated as Multiplex Chromatic Biomarkers with Cancer Cells. *Analyst* **2014**, *139* (20), 5247–5253. https://doi.org/10.1039/C4AN01063A.

(121) Palik, E. D. *Handbook of Optical Constants of Solids*, 1 edition.; Academic Press: San Diego, Calif., 1997.

(122) Zhang, A.-Q.; Qian, D.-J.; Chen, M. Simulated Optical Properties of Noble Metallic Nanopolyhedra with Different Shapes and Structures. *Eur. Phys. J. D* **2013**, *67* (11), 231. https://doi.org/10.1140/epjd/e2013-40240-1.

(123) Yang, Y.; Liu, J.; Fu, Z.-W.; Qin, D. Galvanic Replacement-Free Deposition of Au on Ag for Core–Shell Nanocubes with Enhanced Chemical Stability and SERS Activity. *J. Am. Chem. Soc.* **2014**, *136* (23), 8153–8156. https://doi.org/10.1021/ja502472x.

(124) Johnson, P. B.; Christy, R. W. Optical Constants of the Noble Metals. *Phys. Rev. B* **1972**, *6* (12), 4370–4379. https://doi.org/10.1103/PhysRevB.6.4370.

(125) Zheng, B. Y.; Zhao, H.; Manjavacas, A.; McClain, M.; Nordlander, P.; Halas, N. J. Distinguishing between Plasmon-Induced and Photoexcited Carriers in a Device Geometry. *Nature Communications* **2015**, *6* (1), 1–7. https://doi.org/10.1038/ncomms8797.

(126) Li, X.-H.; Chou, J. B.; Kwan, W. L.; Elsharif, A. M.; Kim, S.-G. Effect of Anisotropic Electron Momentum Distribution of Surface Plasmon on Internal Photoemission of a Schottky Hot Carrier Device. *Opt. Express, OE* **2017**, *25* (8), A264–A273. https://doi.org/10.1364/OE.25.00A264.

(127) Manjavacas, A.; Liu, J. G.; Kulkarni, V.; Nordlander, P. Plasmon-Induced Hot Carriers in Metallic Nanoparticles. *ACS Nano* **2014**, *8* (8), 7630–7638. https://doi.org/10.1021/nn502445f.

(128) Huang, Y.; Lin, D.; Li, M.; Yin, D.; Wang, S.; Wang, J. Ag@Au Core–Shell Porous Nanocages with Outstanding SERS Activity for Highly Sensitive SERS Immunoassay. *Sensors* **2019**, *19* (7), 1554. https://doi.org/10.3390/s19071554.

(129) Gonzalez, C. M.; Martin, B.; Betancourt, T. Photochemical Synthesis of Bimetallic and Anisotropic Au-Containing Nanoparticles Using a One-Step Protocol. *J. Mater. Chem. A* **2014**, *2* (41), 17574–17585. https://doi.org/10.1039/C4TA03974B.

(130) Hodak, J. H.; Henglein, A.; Giersig, M.; Hartland, G. V. Laser-Induced Inter-Diffusion in AuAg Core−Shell Nanoparticles. *J. Phys. Chem. B* **2000**, *104* (49), 11708–11718. https://doi.org/10.1021/jp002438r.

(131) Lim, D.-K.; Kim, I.-J.; Nam, J.-M. DNA-Embedded Au/Ag Core–Shell Nanoparticles. *Chem. Commun.* **2008**, No. 42, 5312–5314. https://doi.org/10.1039/B810195G.

(132) Banerjee, M.; Sharma, S.; Chattopadhyay, A.; Ghosh, S. S. Enhanced Antibacterial Activity of Bimetallic Gold-Silver Core–Shell Nanoparticles at Low Silver Concentration. *Nanoscale* **2011**, *3* (12), 5120–5125. https://doi.org/10.1039/C1NR10703H.

(133) Rioux, D.; Vallières, S.; Besner, S.; Muñoz, P.; Mazur, E.; Meunier, M. An Analytic Model for the Dielectric Function of Au, Ag, and Their Alloys. *Advanced Optical Materials* **2014**, *2* (2), 176–182. https://doi.org/10.1002/adom.201300457.

(134) Albrecht, W.; Hoeven, J. E. S. van der; Deng, T.-S.; Jongh, P. E. de; Blaaderen, A. van. Fully Alloyed Metal Nanorods with Highly Tunable Properties. *Nanoscale* **2017**, *9* (8), 2845–2851. https://doi.org/10.1039/C6NR08484B.

(135) Yang, L.; Zhou, Z.; Song, J.; Chen, X. Anisotropic Nanomaterials for Shape-Dependent Physicochemical and Biomedical Applications. *Chem. Soc. Rev.* **2019**, *48* (19), 5140–5176. https://doi.org/10.1039/C9CS00011A.

(136) Ren, Y.; Qi, H.; Chen, Q.; Wang, S.; Ruan, L. Localized Surface Plasmon Resonance of Nanotriangle Dimers at Different Relative Positions. *Journal of Quantitative Spectroscopy and Radiative Transfer* **2017**, *199*, 45–51. https://doi.org/10.1016/j.jqsrt.2017.05.003.

(137) Fu, L.; Liu, Y.; Wang, W.; Wang, M.; Bai, Y.; Chronister, E. L.; Zhen, L.; Yin, Y. A Pressure Sensor Based on the Orientational Dependence of Plasmonic Properties of Gold Nanorods. *Nanoscale* **2015**, *7* (34), 14483–14488. https://doi.org/10.1039/C5NR03450G.

(138) Chang, W.-S.; Ha, J. W.; Slaughter, L. S.; Link, S. Plasmonic Nanorod Absorbers as Orientation Sensors. *PNAS* **2010**, *107* (7), 2781–2786. https://doi.org/10.1073/pnas.0910127107.

(139) Biswas, S.; Nepal, D.; Park, K.; Vaia, R. A. Orientation Sensing with Color Using Plasmonic Gold Nanorods and Assemblies. *J. Phys. Chem. Lett.* **2012**, *3* (18), 2568–2574. https://doi.org/10.1021/jz3009908.

(140) Gherman, A. M. M.; Boca, S.; Vulpoi, A.; Cristea, M. V.; Farcau, C.; Tosa, V. Plasmonic Photothermal Heating of Gold Nanostars in a Real-Size

Container: Multiscale Modelling and Experimental Study. *Nanotechnology* **2020**, *31* (12), 125701. https://doi.org/10.1088/1361-6528/ab5d83.

(141) Borah, R.; Verbruggen, S. W. Coupled Plasmon Modes in 2D Gold Nanoparticle Clusters and Their Effect on Local Temperature Control. *J. Phys. Chem. C* **2019**. https://doi.org/10.1021/acs.jpcc.9b09048.

(142) Du, M.; Tang, G. H. Plasmonic Nanofluids Based on Gold Nanorods/Nanoellipsoids/Nanosheets for Solar Energy Harvesting. *Solar Energy* **2016**, *137*, 393–400. https://doi.org/10.1016/j.solener.2016.08.029.

(143) Verbruggen, S. W. TiO2 Photocatalysis for the Degradation of Pollutants in Gas Phase: From Morphological Design to Plasmonic Enhancement. *Journal of Photochemistry and Photobiology C: Photochemistry Reviews* **2015**, *24*, 64–82. https://doi.org/10.1016/j.jphotochemrev.2015.07.001.

(144) Guo, L.; Jackman, J. A.; Yang, H.-H.; Chen, P.; Cho, N.-J.; Kim, D.-H. Strategies for Enhancing the Sensitivity of Plasmonic Nanosensors. *Nano Today* **2015**, *10* (2), 213–239. https://doi.org/10.1016/j.nantod.2015.02.007.

(145) Ali, M. R. K.; Wu, Y.; El-Sayed, M. A. Gold-Nanoparticle-Assisted Plasmonic Photothermal Therapy Advances Toward Clinical Application. *J. Phys. Chem. C* **2019**, *123* (25), 15375–15393. https://doi.org/10.1021/acs.jpcc.9b01961.

(146) Borah, R.; Verbruggen, S. W. Coupled Plasmon Modes in 2D Gold Nanoparticle Clusters and Their Effect on Local Temperature Control. *J. Phys. Chem. C* **2019**, *123* (50), 30594–30603. https://doi.org/10.1021/acs.jpcc.9b09048.

(147) Lu, X.; Rycenga, M.; Skrabalak, S. E.; Wiley, B.; Xia, Y. Chemical Synthesis of Novel Plasmonic Nanoparticles. *Annual Review of Physical Chemistry* **2009**, *60* (1), 167–192. https://doi.org/10.1146/annurev.physchem.040808.090434.

(148) Wuithschick, M.; Birnbaum, A.; Witte, S.; Sztucki, M.; Vainio, U.; Pinna, N.; Rademann, K.; Emmerling, F.; Kraehnert, R.; Polte, J. Turkevich in New Robes: Key Questions Answered for the Most Common Gold Nanoparticle Synthesis. *ACS Nano* **2015**, *9* (7), 7052–7071. https://doi.org/10.1021/acsnano.5b01579.

(149) Bastús, N. G.; Merkoçi, F.; Piella, J.; Puntes, V. Synthesis of Highly Monodisperse Citrate-Stabilized Silver Nanoparticles of up to 200 Nm: Kinetic Control and Catalytic Properties. *Chem. Mater.* **2014**, *26* (9), 2836–2846. https://doi.org/10.1021/cm500316k.

(150) Lérondel, G.; Kostcheev, S.; Plain, J. Nanofabrication for Plasmonics. In *Plasmonics: From Basics to Advanced Topics*; Enoch, S., Bonod, N., Eds.; Springer Series in Optical Sciences; Springer: Berlin, Heidelberg, 2012; pp 269–316.

(151) Luo, Z.; Yuan, X.; Yu, Y.; Zhang, Q.; Leong, D. T.; Lee, J. Y.; Xie, J. From Aggregation-Induced Emission of Au(I)–Thiolate Complexes to Ultrabright Au(0)@Au(I)–Thiolate Core–Shell Nanoclusters. *J. Am. Chem. Soc.* **2012**, *134* (40), 16662–16670. https://doi.org/10.1021/ja306199p.

(152) Dong, J. X.; Gao, Z. F.; Zhang, Y.; Li, B. L.; Zhang, W.; Lei, J. L.; Li, N. B.; Luo, H. Q. The PH-Switchable Agglomeration and Dispersion Behavior of Fluorescent Ag Nanoclusters and Its Applications in Urea and Glucose

Biosensing. *NPG Asia Materials* **2016**, *8* (12), e335–e335. https://doi.org/10.1038/am.2016.184.

(153) Huang, H.; Toit, H. du; Besenhard, M. O.; Ben-Jaber, S.; Dobson, P.; Parkin, I.; Gavriilidis, A. Continuous Flow Synthesis of Ultrasmall Gold Nanoparticles in a Microreactor Using Trisodium Citrate and Their SERS Performance. *Chemical Engineering Science* **2018**, *189*, 422–430. https://doi.org/10.1016/j.ces.2018.06.050.

(154) Lin, X. Z.; Terepka, A. D.; Yang, H. Synthesis of Silver Nanoparticles in a Continuous Flow Tubular Microreactor. *Nano Lett.* **2004**, *4* (11), 2227–2232. https://doi.org/10.1021/nl0485859.

(155) Thanh, N. T. K.; Maclean, N.; Mahiddine, S. Mechanisms of Nucleation and Growth of Nanoparticles in Solution. *Chem. Rev.* **2014**, *114* (15), 7610–7630. https://doi.org/10.1021/cr400544s.

(156) Shih, C.-Y.; Wu, C.; Shugaev, M. V.; Zhigilei, L. V. Atomistic Modeling of Nanoparticle Generation in Short Pulse Laser Ablation of Thin Metal Films in Water. *Journal of Colloid and Interface Science* **2017**, *489*, 3–17. https://doi.org/10.1016/j.jcis.2016.10.029.

(157) Reich, S.; Schönfeld, P.; Wagener, P.; Letzel, A.; Ibrahimkutty, S.; Gökce, B.; Barcikowski, S.; Menzel, A.; dos Santos Rolo, T.; Plech, A. Pulsed Laser Ablation in Liquids: Impact of the Bubble Dynamics on Particle Formation. *Journal of Colloid and Interface Science* **2017**, *489*, 106–113. https://doi.org/10.1016/j.jcis.2016.08.030.

(158) Bastús, N. G.; Comenge, J.; Puntes, V. Kinetically Controlled Seeded Growth Synthesis of Citrate-Stabilized Gold Nanoparticles of up to 200 Nm: Size Focusing versus Ostwald Ripening. *Langmuir* **2011**, *27* (17), 11098–11105. https://doi.org/10.1021/la201938u.

(159) Rodriguez-Lorenzo, L.; Rothen-Rutishauser, B.; Petri-Fink, A.; Balog, S. Nanoparticle Polydispersity Can Strongly Affect In Vitro Dose. *Particle & Particle Systems Characterization* **2015**, *32* (3), 321–333. https://doi.org/10.1002/ppsc.201400079.

(160) Borah, R.; Ninakanti, R.; Nuyts, G.; Peeters, H.; Pedrazo-Tardajos, A.; Nuti, S.; Vande Velde, C.; De Wael, K.; Lenaerts, S.; Bals, S.; Verbruggen, S. W. Selectivity in the Ligand Functionalization of Photocatalytic Metal Oxide Nanoparticles for Phase Transfer and Self-Assembly Applications. *Chemistry – A European Journal* **2021**, *27* (35), 9011–9021. https://doi.org/10.1002/chem.202100029.

(161) Gudjonson, H.; Kats, M. A.; Liu, K.; Nie, Z.; Kumacheva, E.; Capasso, F. Accounting for Inhomogeneous Broadening in Nano-Optics by Electromagnetic Modeling Based on Monte Carlo Methods. *PNAS* **2014**, *111* (6), E639–E644. https://doi.org/10.1073/pnas.1323392111.

(162) Peña, O.; Rodríguez-Fernández, L.; Rodríguez-Iglesias, V.; Kellermann, G.; Crespo-Sosa, A.; Cheang-Wong, J. C.; Silva-Pereyra, H. G.; Arenas-Alatorre, J.; Oliver, A. Determination of the Size Distribution of Metallic Nanoparticles by Optical Extinction Spectroscopy. *Appl. Opt., AO* **2009**, *48* (3), 566–572. https://doi.org/10.1364/AO.48.000566.

(163) Tserkezis, C.; Maack, J. R.; Liu, Z.; Wubs, M.; Mortensen, N. A. Robustness of the Far-Field Response of Nonlocal Plasmonic Ensembles. *Sci Rep* **2016**, *6* (1), 28441. https://doi.org/10.1038/srep28441.

(164) Sancho-Parramon, J. Surface Plasmon Resonance Broadening of Metallic Particles in the Quasi-Static Approximation: A Numerical Study of Size Confinement and Interparticle Interaction Effects. *Nanotechnology* **2009**, *20* (23), 235706. https://doi.org/10.1088/0957-4484/20/23/235706.

(165) Qin, Z.; Wang, Y.; Randrianalisoa, J.; Raeesi, V.; Chan, W. C. W.; Lipiński, W.; Bischof, J. C. Quantitative Comparison of Photothermal Heat Generation between Gold Nanospheres and Nanorods. *Sci Rep* **2016**, *6* (1), 29836. https://doi.org/10.1038/srep29836.

(166) Blommaerts, N.; Vanrompay, H.; Nuti, S.; Lenaerts, S.; Bals, S.; Verbruggen, S. W. Unraveling Structural Information of Turkevich Synthesized Plasmonic Gold–Silver Bimetallic Nanoparticles. *Small* **2019**, *15* (42), 1902791. https://doi.org/10.1002/smll.201902791.

(167) Asapu, R.; Ciocarlan, R.-G.; Claes, N.; Blommaerts, N.; Minjauw, M.; Ahmad, T.; Dendooven, J.; Cool, P.; Bals, S.; Denys, S.; Detavernier, C.; Lenaerts, S.; Verbruggen, S. W. Plasmonic Near-Field Localization of Silver Core–Shell Nanoparticle Assemblies via Wet Chemistry Nanogap Engineering. *ACS Appl. Mater. Interfaces* **2017**, *9* (47), 41577–41585. https://doi.org/10.1021/acsami.7b13965.

(168) Ross, M. B.; Ku, J. C.; Blaber, M. G.; Mirkin, C. A.; Schatz, G. C. Defect Tolerance and the Effect of Structural Inhomogeneity in Plasmonic DNA-Nanoparticle Superlattices. *PNAS* **2015**, *112* (33), 10292–10297. https://doi.org/10.1073/pnas.1513058112.

(169) Borah, R.; Verbruggen, S. W. Silver–Gold Bimetallic Alloy versus Core–Shell Nanoparticles: Implications for Plasmonic Enhancement and Photothermal Applications. *J. Phys. Chem. C* **2020**, *124* (22), 12081–12094. https://doi.org/10.1021/acs.jpcc.0c02630.

(170) Palik, E. D. *Handbook of Optical Constants of Solids*, 1st edition.; Academic Press: Orlando, 1997.

(171) Johnson, P. B.; Christy, R. W. Optical Constants of the Noble Metals. *Phys. Rev. B* **1972**, *6* (12), 4370–4379. https://doi.org/10.1103/PhysRevB.6.4370.

(172) Yang, H. U.; D'Archangel, J.; Sundheimer, M. L.; Tucker, E.; Boreman, G. D.; Raschke, M. B. Optical Dielectric Function of Silver. *Phys. Rev. B* **2015**, *91* (23), 235137. https://doi.org/10.1103/PhysRevB.91.235137.

(173) Wu, Y.; Zhang, C.; Estakhri, N. M.; Zhao, Y.; Kim, J.; Zhang, M.; Liu, X.-X.; Pribil, G. K.; Alù, A.; Shih, C.-K.; Li, X. Intrinsic Optical Properties and Enhanced Plasmonic Response of Epitaxial Silver. *Advanced Materials* **2014**, *26* (35), 6106–6110. https://doi.org/10.1002/adma.201401474.

(174) Rioux, D.; Vallières, S.; Besner, S.; Muñoz, P.; Mazur, E.; Meunier, M. An Analytic Model for the Dielectric Function of Au, Ag, and Their Alloys. *Advanced Optical Materials* **2014**, *2* (2), 176–182. https://doi.org/10.1002/adom.201300457.

(175) Gong, C.; Dias, M. R. S.; Wessler, G. C.; Taillon, J. A.; Salamanca-Riba, L. G.; Leite, M. S. Near-Field Optical Properties of Fully Alloyed Noble Metal Nanoparticles. *Advanced Optical Materials* **2017**, *5* (1), 1600568. https://doi.org/10.1002/adom.201600568.

(176) Pabisch, S.; Feichtenschlager, B.; Kickelbick, G.; Peterlik, H. Effect of Interparticle Interactions on Size Determination of Zirconia and Silica Based Systems – A Comparison of SAXS, DLS, BET, XRD and TEM. *Chemical*

Physics Letters **2012**, *521*, 91–97. https://doi.org/10.1016/j.cplett.2011.11.049.

(177) Bohren, C. F.; Huffman, D. R. *Absorption and Scattering of Light by Small Particles*, New edition.; Wiley-VCH: New York, 1998.

(178) Haiss, W.; Thanh, N. T. K.; Aveyard, J.; Fernig, D. G. Determination of Size and Concentration of Gold Nanoparticles from UV−Vis Spectra. *Anal. Chem.* **2007**, *79* (11), 4215–4221. https://doi.org/10.1021/ac0702084.

(179) Amendola, V.; Meneghetti, M. Size Evaluation of Gold Nanoparticles by UV−vis Spectroscopy. *J. Phys. Chem. C* **2009**, *113* (11), 4277–4285. https://doi.org/10.1021/jp8082425.

(180) Mafuné, Fumitaka; Kohno, J.; Takeda, Y.; Kondow, T.; Sawabe, H. Formation and Size Control of Silver Nanoparticles by Laser Ablation in Aqueous Solution. *J. Phys. Chem. B* **2000**, *104* (39), 9111–9117. https://doi.org/10.1021/jp001336y.

(181) Heidarzadeh, H.; Mehrfar, F. Effect of Size Non-Uniformity on Performance of a Plasmonic Perovskite Solar Cell: An Array of Embedded Plasmonic Nanoparticles with the Gaussian Distribution Radiuses. *Plasmonics* **2018**, *13* (6), 2305–2312. https://doi.org/10.1007/s11468-018-0753-z.

(182) Akimov, Yu. A.; Koh, W. S. Tolerance Study of Nanoparticle Enhancement for Thin-Film Silicon Solar Cells. *Appl. Phys. Lett.* **2011**, *99* (6), 063102. https://doi.org/10.1063/1.3623483.

(183) Hansen, J. C.; Maier, D.; Honerkamp, J.; Richtering, W.; Horn, F. M.; Senff, H. Size Distributions out of Static Light Scattering: Inclusion of Distortions from the Experimental Setup, e.g., a SOFICA-Type Goniometer. *Journal of Colloid and Interface Science* **1999**, *215* (1), 72–84. https://doi.org/10.1006/jcis.1999.6229.

(184) Derkachova, A.; Kolwas, K. Size Dependence of Multipolar Plasmon Resonance Frequenciesand Damping Rates in Simple Metal Spherical Nanoparticles. *Eur. Phys. J. Spec. Top.* **2007**, *144* (1), 93–99. https://doi.org/10.1140/epjst/e2007-00112-1.

(185) Burrows, C. P.; Barnes, W. L. Large Spectral Extinction Due to Overlap of Dipolar and Quadrupolar Plasmonic Modes of Metallic Nanoparticles in Arrays. *Opt. Express, OE* **2010**, *18* (3), 3187–3198. https://doi.org/10.1364/OE.18.003187.

(186) Kreibig, U.; Vollmer, M. *Optical Properties of Metal Clusters*, 1995th edition.; Springer: Berlin, 1995.

(187) Suzuki, A.; Ho, N. F. H.; Higuchi, W. I. Predictions of the Particle Size Distribution Changes in Emulsions and Suspensions by Digital Computation. *Journal of Colloid and Interface Science* **1969**, *29* (3), 552–564. https://doi.org/10.1016/0021-9797(69)90140-4.

(188) Ziff, R. M.; McGrady, E. D.; Meakin, P. On the Validity of Smoluchowski's Equation for Cluster–Cluster Aggregation Kinetics. *J. Chem. Phys.* **1985**, *82* (11), 5269–5274. https://doi.org/10.1063/1.448600.

(189) Kiss, L. B.; Söderlund, J.; Niklasson, G. A.; Granqvist, C. G. New Approach to the Origin of Lognormal Size Distributions of Nanoparticles. *Nanotechnology* **1999**, *10* (1), 25–28. https://doi.org/10.1088/0957-4484/10/1/006.

(190) Thomas, J.; Periakaruppan, P.; Thomas, V.; John, J.; S, M.; Thomas, T.; Jose, J.; I, R.; A, M. Morphology Dependent Nonlinear Optical and Photocatalytic Activity of Anisotropic Plasmonic Silver. *RSC Advances* **2018**, *8* (72), 41288–41298. https://doi.org/10.1039/C8RA08893D.

(191) González, A. L.; Noguez, C.; Beránek, J.; Barnard, A. S. Size, Shape, Stability, and Color of Plasmonic Silver Nanoparticles. *J. Phys. Chem. C* **2014**, *118* (17), 9128–9136. https://doi.org/10.1021/jp5018168.

(192) Ringe, E.; Langille, M. R.; Sohn, K.; Zhang, J.; Huang, J.; Mirkin, C. A.; Van Duyne, R. P.; Marks, L. D. Plasmon Length: A Universal Parameter to Describe Size Effects in Gold Nanoparticles. *J. Phys. Chem. Lett.* **2012**, *3* (11), 1479–1483. https://doi.org/10.1021/jz300426p.

(193) Wu, L.; E. Kolmeijer, K.; Zhang, Y.; An, H.; Arnouts, S.; Bals, S.; Altantzis, T.; P. Hofmann, J.; Figueiredo, M. C.; M. Hensen, E. J.; M. Weckhuysen, B.; Stam, W. van der. Stabilization Effects in Binary Colloidal Cu and Ag Nanoparticle Electrodes under Electrochemical CO 2 Reduction Conditions. *Nanoscale* **2021**, *13* (9), 4835–4844. https://doi.org/10.1039/D0NR09040A.

(194) Agnihotri, S.; Mukherji, S.; Mukherji, S. Size-Controlled Silver Nanoparticles Synthesized over the Range 5–100 Nm Using the Same Protocol and Their Antibacterial Efficacy. *RSC Adv.* **2013**, *4* (8), 3974–3983. https://doi.org/10.1039/C3RA44507K.

(195) Amirjani, A.; Firouzi, F.; Haghshenas, D. F. Predicting the Size of Silver Nanoparticles from Their Optical Properties. *Plasmonics* **2020**, *15* (4), 1077–1082. https://doi.org/10.1007/s11468-020-01121-x.

(196) Nobbmann, U.; Morfesis, A. Light Scattering and Nanoparticles. *Materials Today* **2009**, *12* (5), 52–54. https://doi.org/10.1016/S1369-7021(09)70164-6.

(197) Wang, W.; Ramezani, M.; Väkeväinen, A. I.; Törmä, P.; Rivas, J. G.; Odom, T. W. The Rich Photonic World of Plasmonic Nanoparticle Arrays. *Materials Today* **2018**, *21* (3), 303–314. https://doi.org/10.1016/j.mattod.2017.09.002.

(198) Kravets, V. G.; Kabashin, A. V.; Barnes, W. L.; Grigorenko, A. N. Plasmonic Surface Lattice Resonances: A Review of Properties and Applications. *Chem Rev* **2018**, *118* (12), 5912–5951. https://doi.org/10.1021/acs.chemrev.8b00243.

(199) Alù, A.; Engheta, N. The Quest for Magnetic Plasmons at Optical Frequencies. *Opt. Express, OE* **2009**, *17* (7), 5723–5730. https://doi.org/10.1364/OE.17.005723.

(200) Mirin, N. A.; Bao, K.; Nordlander, P. Fano Resonances in Plasmonic Nanoparticle Aggregates. *J. Phys. Chem. A* **2009**, *113* (16), 4028–4034. https://doi.org/10.1021/jp810411q.

(201) Punj, D.; Regmi, R.; Devilez, A.; Plauchu, R.; Moparthi, S. B.; Stout, B.; Bonod, N.; Rigneault, H.; Wenger, J. Self-Assembled Nanoparticle Dimer Antennas for Plasmonic-Enhanced Single-Molecule Fluorescence Detection at Micromolar Concentrations. *ACS Photonics* **2015**, *2* (8), 1099–1107. https://doi.org/10.1021/acsphotonics.5b00152.

(202) Kuttner, C. Plasmonics in Sensing: From Colorimetry to SERS Analytics. *Plasmonics* **2018**. https://doi.org/10.5772/intechopen.79055.

(203) Luk'yanchuk, B.; Zheludev, N. I.; Maier, S. A.; Halas, N. J.; Nordlander, P.; Giessen, H.; Chong, C. T. The Fano Resonance in Plasmonic Nanostructures

and Metamaterials. *Nature Materials* **2010**, *9* (9), 707–715. https://doi.org/10.1038/nmat2810.

(204) Hopkins, B.; Poddubny, A. N.; Miroshnichenko, A. E.; Kivshar, Y. S. Revisiting the Physics of Fano Resonances for Nanoparticle Oligomers. *Phys. Rev. A* **2013**, *88* (5), 053819. https://doi.org/10.1103/PhysRevA.88.053819.

(205) Zohar, N.; Chuntonov, L.; Haran, G. The Simplest Plasmonic Molecules: Metal Nanoparticle Dimers and Trimers. *Journal of Photochemistry and Photobiology C: Photochemistry Reviews* **2014**, *21*, 26–39. https://doi.org/10.1016/j.jphotochemrev.2014.10.002.

(206) Klinkova, A.; Choueiri, R. M.; Kumacheva, E. Self-Assembled Plasmonic Nanostructures. *Chem. Soc. Rev.* **2014**, *43* (11), 3976–3991. https://doi.org/10.1039/C3CS60341E.

(207) Zhang, Y.; Wen, F.; Zhen, Y.-R.; Nordlander, P.; Halas, N. J. Coherent Fano Resonances in a Plasmonic Nanocluster Enhance Optical Four-Wave Mixing. *PNAS* **2013**, *110* (23), 9215–9219. https://doi.org/10.1073/pnas.1220304110.

(208) Dahmen, C.; Schmidt, B.; von Plessen, G. Radiation Damping in Metal Nanoparticle Pairs. *Nano Lett.* **2007**, *7* (2), 318–322. https://doi.org/10.1021/nl062377u.

(209) Hao, E.; Schatz, G. C. Electromagnetic Fields around Silver Nanoparticles and Dimers. *J. Chem. Phys.* **2003**, *120* (1), 357–366. https://doi.org/10.1063/1.1629280.

(210) Zhu, W.; Esteban, R.; Borisov, A. G.; Baumberg, J. J.; Nordlander, P.; Lezec, H. J.; Aizpurua, J.; Crozier, K. B. Quantum Mechanical Effects in Plasmonic Structures with Subnanometre Gaps. *Nature Communications* **2016**, *7*, 11495. https://doi.org/10.1038/ncomms11495.

(211) Asapu, R.; Ciocarlan, R.-G.; Claes, N.; Blommaerts, N.; Minjauw, M.; Ahmad, T.; Dendooven, J.; Cool, P.; Bals, S.; Denys, S.; Detavernier, C.; Lenaerts, S.; Verbruggen, S. W. Plasmonic Near-Field Localization of Silver Core–Shell Nanoparticle Assemblies via Wet Chemistry Nanogap Engineering. *ACS Appl. Mater. Interfaces* **2017**, *9* (47), 41577–41585. https://doi.org/10.1021/acsami.7b13965.

(212) Nordlander, P.; Oubre, C.; Prodan, E.; Li, K.; Stockman, M. I. Plasmon Hybridization in Nanoparticle Dimers. *Nano Lett.* **2004**, *4* (5), 899–903. https://doi.org/10.1021/nl049681c.

(213) Baur, S.; Sanders, S.; Manjavacas, A. Hybridization of Lattice Resonances. *ACS Nano* **2018**, *12* (2), 1618–1629. https://doi.org/10.1021/acsnano.7b08206.

(214) Tira, C.; Tira, D.; Simon, T.; Astilean, S. Finite-Difference Time-Domain (FDTD) Design of Gold Nanoparticle Chains with Specific Surface Plasmon Resonance. *Journal of Molecular Structure* **2014**, *1072*, 137–143. https://doi.org/10.1016/j.molstruc.2014.04.086.

(215) Zhong, Z.; Patskovskyy, S.; Bouvrette, P.; Luong, J. H. T.; Gedanken, A. The Surface Chemistry of Au Colloids and Their Interactions with Functional Amino Acids. *J. Phys. Chem. B* **2004**, *108* (13), 4046–4052. https://doi.org/10.1021/jp037056a.

(216) Modinos, A. Scattering of Electromagnetic Waves by a Plane of Spheres-Formalism. *Physica A: Statistical Mechanics and its Applications* **1987**, *141* (2), 575–588. https://doi.org/10.1016/0378-4371(87)90184-1.

(217) Stafanou, N.; Modinos, A. Scattering of Light from a Two-Dimensional Array of Spherical Particles on a Substrate. *J. Phys.: Condens. Matter* **1991**, *3* (41), 8135–8148. https://doi.org/10.1088/0953-8984/3/41/012.

(218) Stefanou, N.; Yannopapas, V.; Modinos, A. MULTEM 2: A New Version of the Program for Transmission and Band-Structure Calculations of Photonic Crystals. *Computer Physics Communications* **2000**, *132* (1), 189–196. https://doi.org/10.1016/S0010-4655(00)00131-4.

(219) Moroz, A.; Sommers, C. Photonic Band Gaps of Three-Dimensional Face-Centred Cubic Lattices. *J. Phys.: Condens. Matter* **1999**, *11* (4), 997–1008. https://doi.org/10.1088/0953-8984/11/4/007.

(220) Moroz, A. Metallo-Dielectric Diamond and Zinc-Blende Photonic Crystals. *Phys. Rev. B* **2002**, *66* (11), 115109. https://doi.org/10.1103/PhysRevB.66.115109.

(221) Zundel, L.; Manjavacas, A. Finite-Size Effects on Periodic Arrays of Nanostructures. *J. Phys. Photonics* **2018**, *1* (1), 015004. https://doi.org/10.1088/2515-7647/aae8a2.

(222) Liu, N.; Mukherjee, S.; Bao, K.; Li, Y.; Brown, L. V.; Nordlander, P.; Halas, N. J. Manipulating Magnetic Plasmon Propagation in Metallic Nanocluster Networks. *ACS Nano* **2012**, *6* (6), 5482–5488. https://doi.org/10.1021/nn301393x.

(223) Cui, Y.; Zhou, J.; Tamma, V. A.; Park, W. Dynamic Tuning and Symmetry Lowering of Fano Resonance in Plasmonic Nanostructure. *ACS Nano* **2012**, *6* (3), 2385–2393. https://doi.org/10.1021/nn204647b.

(224) Pazos-Perez, N.; Wagner, C. S.; Romo-Herrera, J. M.; Liz-Marzán, L. M.; García de Abajo, F. J.; Wittemann, A.; Fery, A.; Alvarez-Puebla, R. A. Organized Plasmonic Clusters with High Coordination Number and Extraordinary Enhancement in Surface-Enhanced Raman Scattering (SERS). *Angewandte Chemie International Edition* **2012**, *51* (51), 12688–12693. https://doi.org/10.1002/anie.201207019.

(225) Matricardi, C.; Hanske, C.; Garcia-Pomar, J. L.; Langer, J.; Mihi, A.; Liz-Marzán, L. M. Gold Nanoparticle Plasmonic Superlattices as Surface-Enhanced Raman Spectroscopy Substrates. *ACS Nano* **2018**, *12* (8), 8531–8539. https://doi.org/10.1021/acsnano.8b04073.

(226) Greybush, N. J.; Liberal, I.; Malassis, L.; Kikkawa, J. M.; Engheta, N.; Murray, C. B.; Kagan, C. R. Plasmon Resonances in Self-Assembled Two-Dimensional Au Nanocrystal Metamolecules. *ACS Nano* **2017**, *11* (3), 2917–2927. https://doi.org/10.1021/acsnano.6b08189.

(227) Le, F.; Brandl, D. W.; Urzhumov, Y. A.; Wang, H.; Kundu, J.; Halas, N. J.; Aizpurua, J.; Nordlander, P. Metallic Nanoparticle Arrays: A Common Substrate for Both Surface-Enhanced Raman Scattering and Surface-Enhanced Infrared Absorption. *ACS Nano* **2008**, *2* (4), 707–718. https://doi.org/10.1021/nn800047e.

(228) Ali, M. R. K.; Wu, Y.; El-Sayed, M. A. Gold-Nanoparticle-Assisted Plasmonic Photothermal Therapy Advances Toward Clinical Application. *J. Phys. Chem. C* **2019**, *123* (25), 15375–15393. https://doi.org/10.1021/acs.jpcc.9b01961.

(229) Baffou, G.; Ureña, E. B.; Berto, P.; Monneret, S.; Quidant, R.; Rigneault, H. Deterministic Temperature Shaping Using Plasmonic Nanoparticle

Assemblies. *Nanoscale* **2014**, *6* (15), 8984–8989. https://doi.org/10.1039/C4NR01644K.

(230) Hatef, A.; Fortin-Deschênes, S.; Boulais, E.; Lesage, F.; Meunier, M. Photothermal Response of Hollow Gold Nanoshell to Laser Irradiation: Continuous Wave, Short and Ultrashort Pulse. *International Journal of Heat and Mass Transfer* **2015**, *89*, 866–871. https://doi.org/10.1016/j.ijheatmasstransfer.2015.05.071.

(231) Alali, F.; Karampelas, I. H.; Kim, Y. H.; Furlani, E. P. Photonic and Thermofluidic Analysis of Colloidal Plasmonic Nanorings and Nanotori for Pulsed-Laser Photothermal Applications. *J. Phys. Chem. C* **2013**, *117* (39), 20178–20185. https://doi.org/10.1021/jp406986y.

(232) Baffou, G.; Berto, P.; Bermúdez Ureña, E.; Quidant, R.; Monneret, S.; Polleux, J.; Rigneault, H. Photoinduced Heating of Nanoparticle Arrays. *ACS Nano* **2013**, *7* (8), 6478–6488. https://doi.org/10.1021/nn401924n.

(233) Wang, S.; Fu, L.; Zhang, Y.; Wang, J.; Zhang, Z. Quantitative Evaluation and Optimization of Photothermal Bubble Generation around Overheated Nanoparticles Excited by Pulsed Lasers. *J. Phys. Chem. C* **2018**, *122* (42), 24421–24435. https://doi.org/10.1021/acs.jpcc.8b07672.

(234) Ren, Y.; Chen, Q.; Qi, H.; Ruan, L.; Dai, J. Phase Transition Induced by Localized Surface Plasmon Resonance of Nanoparticle Assemblies. *International Journal of Heat and Mass Transfer* **2018**, *127*, 244–252. https://doi.org/10.1016/j.ijheatmasstransfer.2018.07.049.

(235) Baffou, G.; Quidant, R.; Girard, C. Thermoplasmonics Modeling: A Green's Function Approach. *Phys. Rev. B* **2010**, *82* (16), 165424. https://doi.org/10.1103/PhysRevB.82.165424.

(236) Baffou, G.; Polleux, J.; Rigneault, H.; Monneret, S. Super-Heating and Micro-Bubble Generation around Plasmonic Nanoparticles under Cw Illumination. *J. Phys. Chem. C* **2014**, *118* (9), 4890–4898. https://doi.org/10.1021/jp411519k.

(237) Johnson, P. B.; Christy, R. W. Optical Constants of the Noble Metals. *Phys. Rev. B* **1972**, *6* (12), 4370–4379. https://doi.org/10.1103/PhysRevB.6.4370.

(238) Barrow, S. J.; Wei, X.; Baldauf, J. S.; Funston, A. M.; Mulvaney, P. The Surface Plasmon Modes of Self-Assembled Gold Nanocrystals. *Nature Communications* **2012**, *3*, 1275. https://doi.org/10.1038/ncomms2289.

(239) McCabe, W.; Smith, J.; Harriott emeritus, P. *Unit Operations of Chemical Engineering*, 7 edition.; McGraw-Hill Education: Boston, 2004.

(240) Amendola, V.; Meneghetti, M. Size Evaluation of Gold Nanoparticles by UV−vis Spectroscopy. *J. Phys. Chem. C* **2009**, *113* (11), 4277–4285. https://doi.org/10.1021/jp8082425.

(241) Fan, J. A.; Wu, C.; Bao, K.; Bao, J.; Bardhan, R.; Halas, N. J.; Manoharan, V. N.; Nordlander, P.; Shvets, G.; Capasso, F. Self-Assembled Plasmonic Nanoparticle Clusters. *Science* **2010**, *328* (5982), 1135–1138. https://doi.org/10.1126/science.1187949.

(242) Dutta-Gupta, S.; Martin, O. J. F. Insight into the Eigenmodes of Plasmonic Nanoclusters Based on the Green’s Tensor Method. *J. Opt. Soc. Am. B, JOSAB* **2015**, *32* (2), 194–200. https://doi.org/10.1364/JOSAB.32.000194.

(243) Brandl, D. W.; Mirin, N. A.; Nordlander, P. Plasmon Modes of Nanosphere Trimers and Quadrumers. *J. Phys. Chem. B* **2006**, *110* (25), 12302–12310. https://doi.org/10.1021/jp0613485.

(244) Rechberger, W.; Hohenau, A.; Leitner, A.; Krenn, J. R.; Lamprecht, B.; Aussenegg, F. R. Optical Properties of Two Interacting Gold Nanoparticles. *Optics Communications* **2003**, *220* (1), 137–141. https://doi.org/10.1016/S0030-4018(03)01357-9.

(245) Halas, N. J.; Lal, S.; Chang, W.-S.; Link, S.; Nordlander, P. Plasmons in Strongly Coupled Metallic Nanostructures. *Chem. Rev.* **2011**, *111* (6), 3913–3961. https://doi.org/10.1021/cr200061k.

(246) Manjavacas, A.; Zundel, L.; Sanders, S. Analysis of the Limits of the Near-Field Produced by Nanoparticle Arrays. *ACS Nano* **2019**. https://doi.org/10.1021/acsnano.9b05031.

(247) Fan, J. A.; Bao, K.; Wu, C.; Bao, J.; Bardhan, R.; Halas, N. J.; Manoharan, V. N.; Shvets, G.; Nordlander, P.; Capasso, F. Fano-like Interference in Self-Assembled Plasmonic Quadrumer Clusters. *Nano Lett.* **2010**, *10* (11), 4680–4685. https://doi.org/10.1021/nl1029732.

(248) Dhiman, M.; Maity, A.; Das, A.; Belgamwar, R.; Chalke, B.; Lee, Y.; Sim, K.; Nam, J.-M.; Polshettiwar, V. Plasmonic Colloidosomes of Black Gold for Solar Energy Harvesting and Hotspots Directed Catalysis for CO2 to Fuel Conversion. *Chem. Sci.* **2019**, *10* (27), 6594–6603. https://doi.org/10.1039/C9SC02369K.

(249) Baffou, G.; Quidant, R.; García de Abajo, F. J. Nanoscale Control of Optical Heating in Complex Plasmonic Systems. *ACS Nano* **2010**, *4* (2), 709–716. https://doi.org/10.1021/nn901144d.

(250) Kim, J. Y.; Kim, H.; Kim, B. H.; Chang, T.; Lim, J.; Jin, H. M.; Mun, J. H.; Choi, Y. J.; Chung, K.; Shin, J.; Fan, S.; Kim, S. O. Highly Tunable Refractive Index Visible-Light Metasurface from Block Copolymer Self-Assembly. *Nat Commun* **2016**, *7* (1), 1–9. https://doi.org/10.1038/ncomms12911.

(251) Hamajima, S.; Mitomo, H.; Tani, T.; Matsuo, Y.; Niikura, K.; Naya, M.; Ijiro, K. Nanoscale Uniformity in the Active Tuning of a Plasmonic Array by Polymer Gel Volume Change. *Nanoscale Adv.* **2019**, *1* (5), 1731–1739. https://doi.org/10.1039/C8NA00404H.

(252) Lio, G. E.; Palermo, G.; Caputo, R.; De Luca, A. Opto-Mechanical Control of Flexible Plasmonic Materials. *Journal of Applied Physics* **2019**, *125* (8), 082533. https://doi.org/10.1063/1.5055370.

(253) Kravets, V. G.; Kabashin, A. V.; Barnes, W. L.; Grigorenko, A. N. Plasmonic Surface Lattice Resonances: A Review of Properties and Applications. *Chem. Rev.* **2018**, *118* (12), 5912–5951. https://doi.org/10.1021/acs.chemrev.8b00243.

(254) Yang, K.; Yao, X.; Liu, B.; Ren, B. Metallic Plasmonic Array Structures: Principles, Fabrications, Properties, and Applications. *Advanced Materials* **2021**, *33* (50), 2007988. https://doi.org/10.1002/adma.202007988.

(255) Stratakis, E.; Kymakis, E. Nanoparticle-Based Plasmonic Organic Photovoltaic Devices. *Materials Today* **2013**, *16* (4), 133–146. https://doi.org/10.1016/j.mattod.2013.04.006.

(256) Wang, H.; Yao, L.; Mao, X.; Wang, K.; Zhu, L.; Zhu, J. Gold Nanoparticle Superlattice Monolayer with Tunable Interparticle Gap for Surface-Enhanced Raman Spectroscopy. *Nanoscale* **2019**, *11* (29), 13917–13923. https://doi.org/10.1039/C9NR03590G.

(257) Pang, J. S.; Theodorou, I. G.; Centeno, A.; Petrov, P. K.; Alford, N. M.; Ryan, M. P.; Xie, F. Tunable Three-Dimensional Plasmonic Arrays for Large Near-Infrared Fluorescence Enhancement. *ACS Appl. Mater. Interfaces* **2019**, *11* (26), 23083–23092. https://doi.org/10.1021/acsami.9b08802.

(258) Mayerhöfer, T. G.; Popp, J. Periodic Array-Based Substrates for Surface-Enhanced Infrared Spectroscopy. *Nanophotonics* **2018**, *7* (1), 39–79. https://doi.org/10.1515/nanoph-2017-0005.

(259) Piltan, S.; Sievenpiper, D. Plasmonic Nano-Arrays for Enhanced Photoemission and Photodetection. *J. Opt. Soc. Am. B, JOSAB* **2018**, *35* (2), 208–213. https://doi.org/10.1364/JOSAB.35.000208.

(260) Grzelczak, M.; Vermant, J.; Furst, E. M.; Liz-Marzán, L. M. Directed Self-Assembly of Nanoparticles. *ACS Nano* **2010**, *4* (7), 3591–3605. https://doi.org/10.1021/nn100869j.

(261) Thorkelsson, K.; Bai, P.; Xu, T. Self-Assembly and Applications of Anisotropic Nanomaterials: A Review. *Nano Today* **2015**, *10* (1), 48–66. https://doi.org/10.1016/j.nantod.2014.12.005.

(262) Lei, Y.; Chim, W.-K. Highly Ordered Arrays of Metal/Semiconductor Core−Shell Nanoparticles with Tunable Nanostructures and Photoluminescence. *J. Am. Chem. Soc.* **2005**, *127* (5), 1487–1492. https://doi.org/10.1021/ja043969m.

(263) Zhu, H.; Fan, Z.; Yu, L.; Wilson, M. A.; Nagaoka, Y.; Eggert, D.; Cao, C.; Liu, Y.; Wei, Z.; Wang, X.; He, J.; Zhao, J.; Li, R.; Wang, Z.; Grünwald, M.; Chen, O. Controlling Nanoparticle Orientations in the Self-Assembly of Patchy Quantum Dot-Gold Heterostructural Nanocrystals. *J. Am. Chem. Soc.* **2019**, *141* (14), 6013–6021. https://doi.org/10.1021/jacs.9b01033.

(264) Deng, K.; Luo, Z.; Tan, L.; Quan, Z. Self-Assembly of Anisotropic Nanoparticles into Functional Superstructures. *Chem. Soc. Rev.* **2020**, *49* (16), 6002–6038. https://doi.org/10.1039/D0CS00541J.

(265) Dong, A.; Chen, J.; Vora, P. M.; Kikkawa, J. M.; Murray, C. B. Binary Nanocrystal Superlattice Membranes Self-Assembled at the Liquid–Air Interface. *Nature* **2010**, *466* (7305), 474–477. https://doi.org/10.1038/nature09188.

(266) Elbert, K. C.; Zygmunt, W.; Vo, T.; Vara, C. M.; Rosen, D. J.; Krook, N. M.; Glotzer, S. C.; Murray, C. B. Anisotropic Nanocrystal Shape and Ligand Design for Co-Assembly. *Science Advances* **2021**. https://doi.org/10.1126/sciadv.abf9402.

(267) Mejía-Salazar, J. R.; Oliveira, O. N. Plasmonic Biosensing. *Chem. Rev.* **2018**, *118* (20), 10617–10625. https://doi.org/10.1021/acs.chemrev.8b00359.

(268) Bastús, N. G.; Merkoçi, F.; Piella, J.; Puntes, V. Synthesis of Highly Monodisperse Citrate-Stabilized Silver Nanoparticles of up to 200 Nm: Kinetic Control and Catalytic Properties. *Chem. Mater.* **2014**, *26* (9), 2836–2846. https://doi.org/10.1021/cm500316k.

(269) Lau, C. Y.; Duan, H.; Wang, F.; He, C. B.; Low, H. Y.; Yang, J. K. W. Enhanced Ordering in Gold Nanoparticles Self-Assembly through Excess Free Ligands. *Langmuir* **2011**, *27* (7), 3355–3360. https://doi.org/10.1021/la104786z.

(270) Huang, S.; Minami, K.; Sakaue, H.; Shingubara, S.; Takahagi, T. Effects of the Surface Pressure on the Formation of Langmuir−Blodgett Monolayer of

Nanoparticles. *Langmuir* **2004**, *20* (6), 2274–2276. https://doi.org/10.1021/la0302293.

(271) Ross, M. B.; Ku, J. C.; Blaber, M. G.; Mirkin, C. A.; Schatz, G. C. Defect Tolerance and the Effect of Structural Inhomogeneity in Plasmonic DNA-Nanoparticle Superlattices. *PNAS* **2015**, *112* (33), 10292–10297. https://doi.org/10.1073/pnas.1513058112.

(272) Sani, E.; Dell'Oro, A. Optical Constants of Ethylene Glycol over an Extremely Wide Spectral Range. *Optical Materials* **2014**, *37*, 36–41. https://doi.org/10.1016/j.optmat.2014.04.035.

(273) Johnson, P. B.; Christy, R. W. Optical Constants of the Noble Metals. *Phys. Rev. B* **1972**, *6* (12), 4370–4379. https://doi.org/10.1103/PhysRevB.6.4370.

(274) Palik, E. D. *Handbook of Optical Constants of Solids*; Academic Press: San Diego, Calif., 1998.

(275) Borah, R.; Verbruggen, S. Effect of Size Distribution, Skewness and Roughness on the Optical Properties of Colloidal Plasmonic Nanoparticles. *Colloids and Surfaces A: Physicochemical and Engineering Aspects* **2022**, *640*, 128521. https://doi.org/10.1016/j.colsurfa.2022.128521.

(276) Brown, A. M.; Sundararaman, R.; Narang, P.; Goddard, W. A.; Atwater, H. A. Nonradiative Plasmon Decay and Hot Carrier Dynamics: Effects of Phonons, Surfaces, and Geometry. *ACS Nano* **2016**, *10* (1), 957–966. https://doi.org/10.1021/acsnano.5b06199.

(277) Valenti, M.; Venugopal, A.; Tordera, D.; Jonsson, M. P.; Biskos, G.; Schmidt-Ott, A.; Smith, W. A. Hot Carrier Generation and Extraction of Plasmonic Alloy Nanoparticles. *ACS Photonics* **2017**, *4* (5), 1146–1152. https://doi.org/10.1021/acsphotonics.6b01048.

(278) Prodan, E.; Lee, A.; Nordlander, P. The Effect of a Dielectric Core and Embedding Medium on the Polarizability of Metallic Nanoshells. *Chemical Physics Letters* **2002**, *360* (3), 325–332. https://doi.org/10.1016/S0009-2614(02)00850-3.

(279) Zhou, X.; Li, H.; Xie, S.; Fu, S.; Xu, H.; Liu, Z. Effects of Dielectric Core and Embedding Medium on Plasmonic Coupling of Gold Nanoshell Arrays. *Solid State Communications* **2011**, *151* (14), 1049–1052. https://doi.org/10.1016/j.ssc.2011.04.014.

(280) Khurgin, J.; Tsai, W.-Y.; Tsai, D. P.; Sun, G. Landau Damping and Limit to Field Confinement and Enhancement in Plasmonic Dimers. *ACS Photonics* **2017**, *4* (11), 2871–2880. https://doi.org/10.1021/acsphotonics.7b00860.

(281) Huang, Y.; Ma, L.; Hou, M.; Li, J.; Xie, Z.; Zhang, Z. Hybridized Plasmon Modes and Near-Field Enhancement of Metallic Nanoparticle-Dimer on a Mirror. *Sci Rep* **2016**, *6* (1), 30011. https://doi.org/10.1038/srep30011.

(282) Zong, C.; Premasiri, R.; Lin, H.; Huang, Y.; Zhang, C.; Yang, C.; Ren, B.; Ziegler, L. D.; Cheng, J.-X. Plasmon-Enhanced Stimulated Raman Scattering Microscopy with Single-Molecule Detection Sensitivity. *Nat Commun* **2019**, *10* (1), 5318. https://doi.org/10.1038/s41467-019-13230-1.

(283) Rahmani, M.; Yoxall, E.; Hopkins, B.; Sonnefraud, Y.; Kivshar, Y.; Hong, M.; Phillips, C.; Maier, S. A.; Miroshnichenko, A. E. Plasmonic Nanoclusters with Rotational Symmetry: Polarization-Invariant Far-Field Response vs Changing Near-Field Distribution. *ACS Nano* **2013**, *7* (12), 11138–11146. https://doi.org/10.1021/nn404869c.

(284) Pluchery, O.; Vayron, R.; Van, K.-M. Laboratory Experiments for Exploring the Surface Plasmon Resonance. *Eur. J. Phys.* **2011**, *32* (2), 585–599. https://doi.org/10.1088/0143-0807/32/2/028.

(285) Ras, R. H. A.; Schoonheydt, R. A.; Johnston, C. T. Relation between S-Polarized and p-Polarized Internal Reflection Spectra: Application for the Spectral Resolution of Perpendicular Vibrational Modes. *J. Phys. Chem. A* **2007**, *111* (36), 8787–8791. https://doi.org/10.1021/jp073108a.

(286) Bruno, O. P.; Fernandez-Lado, A. G. Rapidly Convergent Quasi-Periodic Green Functions for Scattering by Arrays of Cylinders—Including Wood Anomalies. *Proceedings of the Royal Society A: Mathematical, Physical and Engineering Sciences* **2017**, *473* (2199), 20160802. https://doi.org/10.1098/rspa.2016.0802.

(287) Fernandez-Lado, A. G. Wave-Scattering by Periodic Media. phd, California Institute of Technology, 2020. https://doi.org/10.7907/G7XQ-RT85.

(288) Darweesh, A. A.; Bauman, S. J.; Debu, D. T.; Herzog, J. B. The Role of Rayleigh-Wood Anomalies and Surface Plasmons in Optical Enhancement for Nano-Gratings. *Nanomaterials* **2018**, *8* (10), 809. https://doi.org/10.3390/nano8100809.

(289) Manera, M. G.; Colombelli, A.; Taurino, A.; Martin, A. G.; Rella, R. Magneto-Optical Properties of Noble-Metal Nanostructures: Functional Nanomaterials for Bio Sensing. *Sci Rep* **2018**, *8* (1), 12640. https://doi.org/10.1038/s41598-018-30862-3.

(290) Kravets, V. G.; Schedin, F.; Grigorenko, A. N. Extremely Narrow Plasmon Resonances Based on Diffraction Coupling of Localized Plasmons in Arrays of Metallic Nanoparticles. *Phys. Rev. Lett.* **2008**, *101* (8), 087403. https://doi.org/10.1103/PhysRevLett.101.087403.

(291) Kanie, K.; Matsubara, M.; Zeng, X.; Liu, F.; Ungar, G.; Nakamura, H.; Muramatsu, A. Simple Cubic Packing of Gold Nanoparticles through Rational Design of Their Dendrimeric Corona. *J. Am. Chem. Soc.* **2012**, *134* (2), 808–811. https://doi.org/10.1021/ja2095816.

(292) Lee, S.; Sim, K.; Moon, S. Y.; Choi, J.; Jeon, Y.; Nam, J.-M.; Park, S.-J. Controlled Assembly of Plasmonic Nanoparticles: From Static to Dynamic Nanostructures. *Advanced Materials* **2021**, *33* (46), 2007668. https://doi.org/10.1002/adma.202007668.

(293) Cersonsky, R. K.; Anders, G. van; Dodd, P. M.; Glotzer, S. C. Relevance of Packing to Colloidal Self-Assembly. *PNAS* **2018**, *115* (7), 1439–1444. https://doi.org/10.1073/pnas.1720139115.

(294) Willets, K. A.; Van Duyne, R. P. Localized Surface Plasmon Resonance Spectroscopy and Sensing. *Annual Review of Physical Chemistry* **2007**, *58* (1), 267–297. https://doi.org/10.1146/annurev.physchem.58.032806.104607.

(295) Li, M.; Cushing, S. K.; Wu, N. Plasmon-Enhanced Optical Sensors: A Review. *Analyst* **2014**, *140* (2), 386–406. https://doi.org/10.1039/C4AN01079E.

(296) Nguyen, H. H.; Park, J.; Kang, S.; Kim, M. Surface Plasmon Resonance: A Versatile Technique for Biosensor Applications. *Sensors* **2015**, *15* (5), 10481–10510. https://doi.org/10.3390/s150510481.

(297) Kretschmann, E.; Raether, H. Notizen: Radiative Decay of Non Radiative Surface Plasmons Excited by Light. *Zeitschrift für Naturforschung A* **1968**, *23* (12), 2135–2136. https://doi.org/10.1515/zna-1968-1247.

(298) Schulz, F.; Pavelka, O.; Lehmkühler, F.; Westermeier, F.; Okamura, Y.; Mueller, N. S.; Reich, S.; Lange, H. Structural Order in Plasmonic Superlattices. *Nat Commun* **2020**, *11* (1), 3821. https://doi.org/10.1038/s41467-020-17632-4.

(299) Yu, J.; Zheng, L.; Geng, C.; Wang, X.; Yan, Q.; Wang, X.; Shen, G.; Shen, D. Colloidal Monolayer at the Air/Water Interface: Large-Area Self-Assembly and in-Situ Annealing. *Thin Solid Films* **2013**, *544*, 557–561. https://doi.org/10.1016/j.tsf.2012.12.069.

(300) Dai, Z.; Dai, H.; Zhou, Y.; Liu, D.; Duan, G.; Cai, W.; Li, Y. Monodispersed Nb2O5 Microspheres: Facile Synthesis, Air/Water Interfacial Self-Assembly, Nb2O5-Based Composite Films, and Their Selective NO2 Sensing. *Advanced Materials Interfaces* **2015**, *2* (11), 1500167. https://doi.org/10.1002/admi.201500167.

(301) Lau, C. Y.; Duan, H.; Wang, F.; He, C. B.; Low, H. Y.; Yang, J. K. W. Enhanced Ordering in Gold Nanoparticles Self-Assembly through Excess Free Ligands. *Langmuir* **2011**, *27* (7), 3355–3360. https://doi.org/10.1021/la104786z.

(302) Wang, B.; Yu, P.; Wang, W.; Zhang, X.; Kuo, H.-C.; Xu, H.; Wang, Z. M. High-Q Plasmonic Resonances: Fundamentals and Applications. *Advanced Optical Materials* **2021**, *9* (7), 2001520. https://doi.org/10.1002/adom.202001520.

(303) Zhang, J.; Zhang, L.; Xu, W. Surface Plasmon Polaritons: Physics and Applications. *J. Phys. D: Appl. Phys.* **2012**, *45* (11), 113001. https://doi.org/10.1088/0022-3727/45/11/113001.

(304) Sikdar, D.; Kornyshev, A. A. Theory of Tailorable Optical Response of Two-Dimensional Arrays of Plasmonic Nanoparticles at Dielectric Interfaces. *Sci Rep* **2016**, *6* (1), 33712. https://doi.org/10.1038/srep33712.

(305) Milosevic, M. On the Nature of the Evanescent Wave. *Appl Spectrosc* **2013**, *67* (2), 126–131. https://doi.org/10.1366/12-06707.

(306) Mueller, N. S.; Vieira, B. G. M.; Schulz, F.; Kusch, P.; Oddone, V.; Barros, E. B.; Lange, H.; Reich, S. Dark Interlayer Plasmons in Colloidal Gold Nanoparticle Bi- and Few-Layers. *ACS Photonics* **2018**, *5* (10), 3962–3969. https://doi.org/10.1021/acsphotonics.8b00898.

(307) Vohnsen, B.; Valente, D. Surface-Plasmon-Based Wavefront Sensing. *Optica, OPTICA* **2015**, *2* (12), 1024–1027. https://doi.org/10.1364/OPTICA.2.001024.

(308) Homola, J.; Koudela, I.; Yee, S. S. Surface Plasmon Resonance Sensors Based on Diffraction Gratings and Prism Couplers: Sensitivity Comparison. *Sensors and Actuators B: Chemical* **1999**, *54* (1), 16–24. https://doi.org/10.1016/S0925-4005(98)00322-0.

(309) Kravets, V. G.; Schedin, F.; Grigorenko, A. N. Extremely Narrow Plasmon Resonances Based on Diffraction Coupling of Localized Plasmons in Arrays of Metallic Nanoparticles. *Phys. Rev. Lett.* **2008**, *101* (8), 087403. https://doi.org/10.1103/PhysRevLett.101.087403.

(310) Ryu, M.; Ng, S. H.; Anand, V.; Lundgaard, S.; Hu, J.; Katkus, T.; Appadoo, D.; Vilagosh, Z.; Wood, A. W.; Juodkazis, S.; Morikawa, J. Attenuated Total Reflection at THz Wavelengths: Prospective Use of Total Internal Reflection and Polariscopy. *Applied Sciences* **2021**, *11* (16), 7632. https://doi.org/10.3390/app11167632.

(311) Averett, L. A.; Griffiths, P. R.; Nishikida, K. Effective Path Length in Attenuated Total Reflection Spectroscopy. *Anal. Chem.* **2008**, *80* (8), 3045–3049. https://doi.org/10.1021/ac7025892.

(312) Homola, J.; Yee, S. S.; Gauglitz, G. Surface Plasmon Resonance Sensors: Review. *Sensors and Actuators B: Chemical* **1999**, *54* (1), 3–15. https://doi.org/10.1016/S0925-4005(98)00321-9.

(313) Nabok, A.; Tsargorodskaya, A. The Method of Total Internal Reflection Ellipsometry for Thin Film Characterisation and Sensing. *Thin Solid Films* **2008**, *516* (24), 8993–9001. https://doi.org/10.1016/j.tsf.2007.11.077.

(314) Abelès, F. Surface Electromagnetic Waves Ellipsometry. *Surface Science* **1976**, *56*, 237–251. https://doi.org/10.1016/0039-6028(76)90450-7.

(315) Ras, R. H. A.; Schoonheydt, R. A.; Johnston, C. T. Relation between S-Polarized and p-Polarized Internal Reflection Spectra: Application for the Spectral Resolution of Perpendicular Vibrational Modes. *J. Phys. Chem. A* **2007**, *111* (36), 8787–8791. https://doi.org/10.1021/jp073108a.

(316) Wang, H. Plasmonic Refractive Index Sensing Using Strongly Coupled Metal Nanoantennas: Nonlocal Limitations. *Sci Rep* **2018**, *8* (1), 9589. https://doi.org/10.1038/s41598-018-28011-x.

(317) Huang, Z.-F.; Song, J.; Pan, L.; Zhang, X.; Wang, L.; Zou, J.-J. Tungsten Oxides for Photocatalysis, Electrochemistry, and Phototherapy. *Advanced Materials* **2015**, *27* (36), 5309–5327. https://doi.org/10.1002/adma.201501217.

(318) Medhi, R.; Marquez, M. D.; Lee, T. R. Visible-Light-Active Doped Metal Oxide Nanoparticles: Review of Their Synthesis, Properties, and Applications. *ACS Appl. Nano Mater.* **2020**, *3* (7), 6156–6185. https://doi.org/10.1021/acsanm.0c01035.

(319) Verbruggen, S. W. TiO2 Photocatalysis for the Degradation of Pollutants in Gas Phase: From Morphological Design to Plasmonic Enhancement. *Journal of Photochemistry and Photobiology C: Photochemistry Reviews* **2015**, *24*, 64–82. https://doi.org/10.1016/j.jphotochemrev.2015.07.001.

(320) Sperling, R. A.; Parak, W. J. Surface Modification, Functionalization and Bioconjugation of Colloidal Inorganic Nanoparticles. *Philosophical Transactions of the Royal Society A: Mathematical, Physical and Engineering Sciences* **2010**, *368* (1915), 1333–1383. https://doi.org/10.1098/rsta.2009.0273.

(321) Pollinger, K.; Hennig, R.; Ohlmann, A.; Fuchshofer, R.; Wenzel, R.; Breunig, M.; Tessmar, J.; Tamm, E. R.; Goepferich, A. Ligand-Functionalized Nanoparticles Target Endothelial Cells in Retinal Capillaries after Systemic Application. *Proceedings of the National Academy of Sciences* **2013**, *110* (15), 6115–6120. https://doi.org/10.1073/pnas.1220281110.

(322) Conde, J.; Dias, J. T.; Grazú, V.; Moros, M.; Baptista, P. V.; de la Fuente, J. M. Revisiting 30 Years of Biofunctionalization and Surface Chemistry of Inorganic Nanoparticles for Nanomedicine. *Frontiers in Chemistry* **2014**, *2*.

(323) Thiruppathi, R.; Mishra, S.; Ganapathy, M.; Padmanabhan, P.; Gulyás, B. Nanoparticle Functionalization and Its Potentials for Molecular Imaging. *Advanced Science* **2017**, *4* (3), 1600279. https://doi.org/10.1002/advs.201600279.

(324) Poonthiyil, V.; Lindhorst, T. K.; Golovko, V. B.; Fairbanks, A. J. Recent Applications of Click Chemistry for the Functionalization of Gold Nanoparticles and Their Conversion to Glyco-Gold Nanoparticles. *Beilstein J. Org. Chem.* **2018**, *14* (1), 11–24. https://doi.org/10.3762/bjoc.14.2.

(325) Weller, L.; Thacker, V. V.; Herrmann, L. O.; Hemmig, E. A.; Lombardi, A.; Keyser, U. F.; Baumberg, J. J. Gap-Dependent Coupling of Ag–Au Nanoparticle Heterodimers Using DNA Origami-Based Self-Assembly. *ACS Photonics* **2016**, *3* (9), 1589–1595. https://doi.org/10.1021/acsphotonics.6b00062.

(326) Berrisford, D. J.; Bolm, C.; Sharpless, K. B. Ligand-Accelerated Catalysis. *Angewandte Chemie International Edition in English* **1995**, *34* (10), 1059–1070. https://doi.org/10.1002/anie.199510591.

(327) Sadeghmoghaddam, E.; Gu, H.; Shon, Y.-S. Pd Nanoparticle-Catalyzed Isomerization vs Hydrogenation of Allyl Alcohol: Solvent-Dependent Regioselectivity. *ACS Catal.* **2012**, *2* (9), 1838–1845. https://doi.org/10.1021/cs300270d.

(328) Chen, B. T. Investigation of the Solvent-Evaporation Effect on Spin Coating of Thin Films. *Polymer Engineering & Science* **1983**, *23* (7), 399–403. https://doi.org/10.1002/pen.760230706.

(329) Sriramulu, D.; Reed, E. L.; Annamalai, M.; Venkatesan, T. V.; Valiyaveettil, S. Synthesis and Characterization of Superhydrophobic, Self-Cleaning NIR-Reflective Silica Nanoparticles. *Sci Rep* **2016**, *6* (1), 35993. https://doi.org/10.1038/srep35993.

(330) Reimers, J. R.; Ford, M. J.; Halder, A.; Ulstrup, J.; Hush, N. S. Gold Surfaces and Nanoparticles Are Protected by Au(0)–Thiyl Species and Are Destroyed When Au(I)–Thiolates Form. *Proceedings of the National Academy of Sciences* **2016**, *113* (11), E1424–E1433. https://doi.org/10.1073/pnas.1600472113.

(331) Xue, Y.; Li, X.; Li, H.; Zhang, W. Quantifying Thiol–Gold Interactions towards the Efficient Strength Control. *Nat Commun* **2014**, *5* (1), 4348. https://doi.org/10.1038/ncomms5348.

(332) Inkpen, M. S.; Liu, Z.-F.; Li, H.; Campos, L. M.; Neaton, J. B.; Venkataraman, L. Non-Chemisorbed Gold–Sulfur Binding Prevails in Self-Assembled Monolayers. *Nat. Chem.* **2019**, *11* (4), 351–358. https://doi.org/10.1038/s41557-019-0216-y.

(333) Hostetler, M. J.; Templeton, A. C.; Murray, R. W. Dynamics of Place-Exchange Reactions on Monolayer-Protected Gold Cluster Molecules. *Langmuir* **1999**, *15* (11), 3782–3789. https://doi.org/10.1021/la981598f.

(334) Dewi, M. R.; Laufersky, G.; Nann, T. A Highly Efficient Ligand Exchange Reaction on Gold Nanoparticles: Preserving Their Size, Shape and Colloidal Stability. *RSC Adv.* **2014**, *4* (64), 34217–34220. https://doi.org/10.1039/C4RA05035E.

(335) Yang, Y.; Serrano, L. A.; Guldin, S. A Versatile AuNP Synthetic Platform for Decoupled Control of Size and Surface Composition. *Langmuir* **2018**, *34* (23), 6820–6826. https://doi.org/10.1021/acs.langmuir.8b00353.

(336) Woehrle, G. H.; Brown, L. O.; Hutchison, J. E. Thiol-Functionalized, 1.5-Nm Gold Nanoparticles through Ligand Exchange Reactions: Scope and Mechanism of Ligand Exchange. *J. Am. Chem. Soc.* **2005**, *127* (7), 2172–2183. https://doi.org/10.1021/ja0457718.

(337) Soliwoda, K.; Tomaszewska, E.; Tkacz-Szczesna, B.; Rosowski, M.; Celichowski, G.; Grobelny, J. The Influence of the Chain Length and the Functional Group Steric Accessibility of Thiols on the Phase Transfer Efficiency of Gold Nanoparticles from Water to Toluene. *Polish Journal of Chemical Technology* **2014**, *16* (1), 86–91.

(338) Soliwoda, K.; Tomaszewska, E.; Tkacz-Szczesna, B.; Mackiewicz, E.; Rosowski, M.; Bald, A.; Blanck, C.; Schmutz, M.; Novák, J.; Schreiber, F.; Celichowski, G.; Grobelny, J. Effect of the Alkyl Chain Length of Secondary Amines on the Phase Transfer of Gold Nanoparticles from Water to Toluene. *Langmuir* **2014**, *30* (23), 6684–6693. https://doi.org/10.1021/la501135q.

(339) Xin, Y.; Zhou, H.; Ni, X.; Pan, Y.; Zhang, X.; Zheng, J.; Bao, S.; Jin, P. The Optical Properties of Low Infrared Transmittance WO3−x Nanocrystal Thin Films Prepared by DC Magnetron Sputtering under Different Oxygen Ratios. *RSC Adv.* **2015**, *5* (71), 57757–57763. https://doi.org/10.1039/C5RA09518B.

(340) Litke, A.; Su, Y.; Tranca, I.; Weber, T.; Hensen, E. J. M.; Hofmann, J. P. Role of Adsorbed Water on Charge Carrier Dynamics in Photoexcited TiO2. *J. Phys. Chem. C* **2017**, *121* (13), 7514–7524. https://doi.org/10.1021/acs.jpcc.7b00472.

(341) Miller, B. J.; Howard, D. L.; Lane, J. R.; Kjaergaard, H. G.; Dunn, M. E.; Vaida, V. SH-Stretching Vibrational Spectra of Ethanethiol and Tert-Butylthiol. *J. Phys. Chem. A* **2009**, *113* (26), 7576–7583. https://doi.org/10.1021/jp9017162.

(342) Berti, I. O. P. D.; Cagnoli, M. V.; Pecchi, G.; Alessandrini, J. L.; Stewart, S. J.; Bengoa, J. F.; Marchetti, S. G. Alternative Low-Cost Approach to the Synthesis of Magnetic Iron Oxide Nanoparticles by Thermal Decomposition of Organic Precursors. *Nanotechnology* **2013**, *24* (17), 175601. https://doi.org/10.1088/0957-4484/24/17/175601.

(343) Heinz, H.; Pramanik, C.; Heinz, O.; Ding, Y.; Mishra, R. K.; Marchon, D.; Flatt, R. J.; Estrela-Lopis, I.; Llop, J.; Moya, S.; Ziolo, R. F. Nanoparticle Decoration with Surfactants: Molecular Interactions, Assembly, and Applications. *Surface Science Reports* **2017**, *72* (1), 1–58. https://doi.org/10.1016/j.surfrep.2017.02.001.

(344) Pujari, S. P.; Scheres, L.; Marcelis, A. T. M.; Zuilhof, H. Covalent Surface Modification of Oxide Surfaces. *Angewandte Chemie International Edition* **2014**, *53* (25), 6322–6356. https://doi.org/10.1002/anie.201306709.

(345) Kluenker, M.; Mondeshki, M.; Nawaz Tahir, M.; Tremel, W. Monitoring Thiol–Ligand Exchange on Au Nanoparticle Surfaces. *Langmuir* **2018**, *34* (4), 1700–1710. https://doi.org/10.1021/acs.langmuir.7b04015.

(346) Rao, X.; Tatoulian, M.; Guyon, C.; Ognier, S.; Chu, C.; Abou Hassan, A. A Comparison Study of Functional Groups (Amine vs. Thiol) for Immobilizing

AuNPs on Zeolite Surface. *Nanomaterials* **2019**, *9* (7), 1034. https://doi.org/10.3390/nano9071034.

(347) Hoft, R. C.; Ford, M. J.; McDonagh, A. M.; Cortie, M. B. Adsorption of Amine Compounds on the Au(111) Surface: A Density Functional Study. *J. Phys. Chem. C* **2007**, *111* (37), 13886–13891. https://doi.org/10.1021/jp072494t.

(348) Harima, Y.; Fujita, T.; Kano, Y.; Imae, I.; Komaguchi, K.; Ooyama, Y.; Ohshita, J. Lewis-Acid Sites of TiO2 Surface for Adsorption of Organic Dye Having Pyridyl Group as Anchoring Unit. *J. Phys. Chem. C* **2013**, *117* (32), 16364–16370. https://doi.org/10.1021/jp405835y.

(349) Turo, M. J.; Macdonald, J. E. Crystal-Bound vs Surface-Bound Thiols on Nanocrystals. *ACS Nano* **2014**, *8* (10), 10205–10213. https://doi.org/10.1021/nn5032164.

(350) Malola, S.; Nieminen, P.; Pihlajamäki, A.; Hämäläinen, J.; Kärkkäinen, T.; Häkkinen, H. A Method for Structure Prediction of Metal-Ligand Interfaces of Hybrid Nanoparticles. *Nat Commun* **2019**, *10* (1), 3973. https://doi.org/10.1038/s41467-019-12031-w.

(351) Schmitt Pauly, C.; Genix, A.-C.; Alauzun, J. G.; Guerrero, G.; Appavou, M.-S.; Pérez, J.; Oberdisse, J.; Mutin, P. H. Simultaneous Phase Transfer and Surface Modification of TiO2 Nanoparticles Using Alkylphosphonic Acids: Optimization and Structure of the Organosols. *Langmuir* **2015**, *31* (40), 10966–10974. https://doi.org/10.1021/acs.langmuir.5b02833.

(352) Yang, J.; Lee, J. Y.; Ying, J. Y. Phase Transfer and Its Applications in Nanotechnology. *Chem. Soc. Rev.* **2011**, *40* (3), 1672–1696. https://doi.org/10.1039/B916790K.

(353) Sadik, P. W.; Pearton, S. J.; Norton, D. P.; Lambers, E.; Ren, F. Functionalizing Zn- and O-Terminated ZnO with Thiols. *Journal of Applied Physics* **2007**, *101* (10), 104514. https://doi.org/10.1063/1.2736893.

(354) Perkins, C. L. Molecular Anchors for Self-Assembled Monolayers on ZnO: A Direct Comparison of the Thiol and Phosphonic Acid Moieties. *J. Phys. Chem. C* **2009**, *113* (42), 18276–18286. https://doi.org/10.1021/jp906013r.

(355) Nasrollahi, N.; Aber, S.; Vatanpour, V.; Mahmoodi, N. M. The Effect of Amine Functionalization of CuO and ZnO Nanoparticles Used as Additives on the Morphology and the Permeation Properties of Polyethersulfone Ultrafiltration Nanocomposite Membranes. *Composites Part B: Engineering* **2018**, *154*, 388–409. https://doi.org/10.1016/j.compositesb.2018.09.027.

(356) Ranjith Kumar, D.; Manoj, D.; Santhanalakshmi, J. Optimization of Site Specific Adsorption of Oleylamine Capped CuO Nanoparticles on MWCNTs for Electrochemical Determination of Guanosine. *Sensors and Actuators B: Chemical* **2013**, *188*, 603–612. https://doi.org/10.1016/j.snb.2013.07.067.

(357) Quiñones, R.; Rodriguez, K.; Iuliucci, R. J. Investigation of Phosphonic Acid Surface Modifications on Zinc Oxide Nanoparticles under Ambient Conditions. *Thin Solid Films* **2014**, *565*, 155–164. https://doi.org/10.1016/j.tsf.2014.06.057.

(358) Bhandary, R.; Alauzun, J. G.; Hesemann, P.; Stocco, A.; In, M.; Mutin, P. H. Phase Transfer of TiO2 Nanoparticles from Water to Ionic Liquid Triggered by Phosphonic Acid Grafting. *Soft Matter* **2017**, *13* (44), 8023–8026. https://doi.org/10.1039/C7SM01424D.

(359) Bensebaa, F.; Voicu, R.; Huron, L.; Ellis, T. H.; Kruus, E. Kinetics of Formation of Long-Chain n-Alkanethiolate Monolayers on Polycrystalline Gold. *Langmuir* **1997**, *13* (20), 5335–5340. https://doi.org/10.1021/la970052a.

(360) Love, J. C.; Estroff, L. A.; Kriebel, J. K.; Nuzzo, R. G.; Whitesides, G. M. Self-Assembled Monolayers of Thiolates on Metals as a Form of Nanotechnology. *Chem. Rev.* **2005**, *105* (4), 1103–1170. https://doi.org/10.1021/cr0300789.

(361) Takeuchi, M.; Martra, G.; Coluccia, S.; Anpo, M. Investigations of the Structure of H2O Clusters Adsorbed on TiO2 Surfaces by Near-Infrared Absorption Spectroscopy. *J. Phys. Chem. B* **2005**, *109* (15), 7387–7391. https://doi.org/10.1021/jp040630d.

(362) Noei, H.; Qiu, H.; Wang, Y.; Löffler, E.; Wöll, C.; Muhler, M. The Identification of Hydroxyl Groups on ZnO Nanoparticles by Infrared Spectroscopy. *Phys. Chem. Chem. Phys.* **2008**, *10* (47), 7092–7097. https://doi.org/10.1039/B811029H.

(363) Henderson, M. A. An HREELS and TPD Study of Water on TiO2(110): The Extent of Molecular versus Dissociative Adsorption. *Surface Science* **1996**, *355* (1), 151–166. https://doi.org/10.1016/0039-6028(95)01357-1.

(364) Albanese, E.; Di Valentin, C.; Pacchioni, G. H2O Adsorption on WO3 and WO3–x (001) Surfaces. *ACS Appl. Mater. Interfaces* **2017**, *9* (27), 23212–23221. https://doi.org/10.1021/acsami.7b06139.

(365) Lu, Z.; Kanan, S. M.; Tripp, C. P. Synthesis of High Surface Area Monoclinic WO3 Particles Using Organic Ligands and Emulsion Based Methods. *J. Mater. Chem.* **2002**, *12* (4), 983–989. https://doi.org/10.1039/B107993J.

(366) Fronzi, M.; Nolan, M. First-Principles Analysis of the Stability of Water on Oxidised and Reduced CuO(111) Surfaces. *RSC Adv.* **2017**, *7* (89), 56721–56731. https://doi.org/10.1039/C7RA11854F.

(367) Yu, X.; Zhang, X.; Wang, H.; Feng, G. High Coverage Water Adsorption on the CuO(111) Surface. *Applied Surface Science* **2017**, *425*, 803–810. https://doi.org/10.1016/j.apsusc.2017.07.086.

(368) Vittadini, A.; Selloni, A.; Rotzinger, F. P.; Grätzel, M. Structure and Energetics of Water Adsorbed at ${\mathrm{TiO}}_{2}$ Anatase \(101\) and \(001\) Surfaces. *Phys. Rev. Lett.* **1998**, *81* (14), 2954–2957. https://doi.org/10.1103/PhysRevLett.81.2954.

(369) Wöll, C. The Chemistry and Physics of Zinc Oxide Surfaces. *Progress in Surface Science* **2007**, *82* (2), 55–120. https://doi.org/10.1016/j.progsurf.2006.12.002.

(370) Sheng, H.; Zhang, H.; Song, W.; Ji, H.; Ma, W.; Chen, C.; Zhao, J. Activation of Water in Titanium Dioxide Photocatalysis by Formation of Surface Hydrogen Bonds: An In Situ IR Spectroscopy Study. *Angewandte Chemie International Edition* **2015**, *54* (20), 5905–5909. https://doi.org/10.1002/anie.201412035.

(371) Kunz, S. Supported, Ligand-Functionalized Nanoparticles: An Attempt to Rationalize the Application and Potential of Ligands in Heterogeneous Catalysis. *Top Catal* **2016**, *59* (19), 1671–1685. https://doi.org/10.1007/s11244-016-0687-7.

(372) Wang, R.; Hashimoto, K.; Fujishima, A.; Chikuni, M.; Kojima, E.; Kitamura, A.; Shimohigoshi, M.; Watanabe, T. Light-Induced Amphiphilic Surfaces. *Nature* **1997**, *388* (6641), 431–432. https://doi.org/10.1038/41233.

(373) Gondal, M. A.; Sadullah, M. S.; Qahtan, T. F.; Dastageer, M. A.; Baig, U.; McKinley, G. H. Fabrication and Wettability Study of WO3 Coated Photocatalytic Membrane for Oil-Water Separation: A Comparative Study with ZnO Coated Membrane. *Sci Rep* **2017**, *7* (1), 1686. https://doi.org/10.1038/s41598-017-01959-y.

(374) He, Y.; Fishman, Z. S.; Yang, K. R.; Ortiz, B.; Liu, C.; Goldsamt, J.; Batista, V. S.; Pfefferle, L. D. Hydrophobic CuO Nanosheets Functionalized with Organic Adsorbates. *J. Am. Chem. Soc.* **2018**, *140* (5), 1824–1833. https://doi.org/10.1021/jacs.7b11654.

(375) Fujishima, A.; Zhang, X.; Tryk, D. A. TiO2 Photocatalysis and Related Surface Phenomena. *Surface Science Reports* **2008**, *63* (12), 515–582. https://doi.org/10.1016/j.surfrep.2008.10.001.

(376) Miyauchi, M. Photocatalysis and Photoinduced Hydrophilicity of WO3 Thin Films with Underlying Pt Nanoparticles. *Phys. Chem. Chem. Phys.* **2008**, *10* (41), 6258–6265. https://doi.org/10.1039/B807426G.

(377) Sun, R.-D.; Nakajima, A.; Fujishima, A.; Watanabe, T.; Hashimoto, K. Photoinduced Surface Wettability Conversion of ZnO and TiO2 Thin Films. *J. Phys. Chem. B* **2001**, *105* (10), 1984–1990. https://doi.org/10.1021/jp002525j.

(378) Miyauchi, M.; Nakajima, A.; Watanabe, T.; Hashimoto, K. Photocatalysis and Photoinduced Hydrophilicity of Various Metal Oxide Thin Films. *Chem. Mater.* **2002**, *14* (6), 2812–2816. https://doi.org/10.1021/cm020076p.

(379) Kameya, Y.; Yabe, H. Optical and Superhydrophilic Characteristics of TiO2 Coating with Subwavelength Surface Structure Consisting of Spherical Nanoparticle Aggregates. *Coatings* **2019**, *9* (9), 547. https://doi.org/10.3390/coatings9090547.

(380) Miyauchi, M.; Nakajima, A.; Fujishima, A.; Hashimoto, K.; Watanabe, T. Photoinduced Surface Reactions on TiO2 and SrTiO3 Films: Photocatalytic Oxidation and Photoinduced Hydrophilicity. *Chem. Mater.* **2000**, *12* (1), 3–5. https://doi.org/10.1021/cm990556p.

Appendix

A1. Supporting information of Chapter 1

Not applicable.

A2. Supporting information of Chapter 2

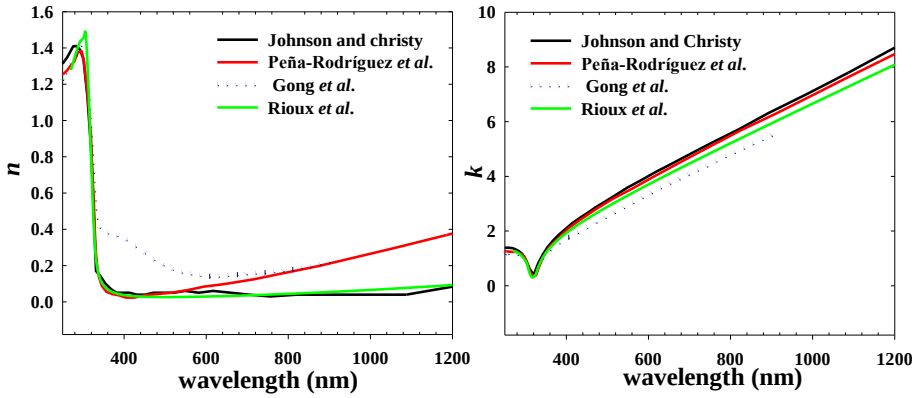

Figure A2.1 Comparison of optical constants of Ag from different literature. (References in the main text)

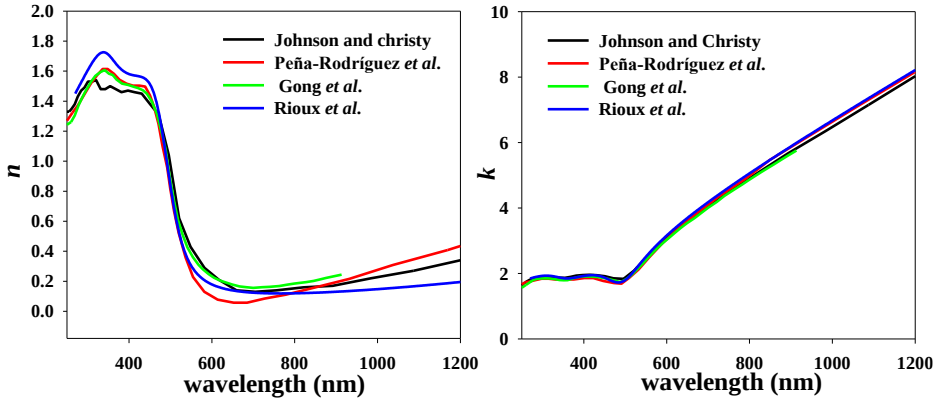

Figure A2.2. Comparison of optical constants of Au from different literature. (References in the main text)

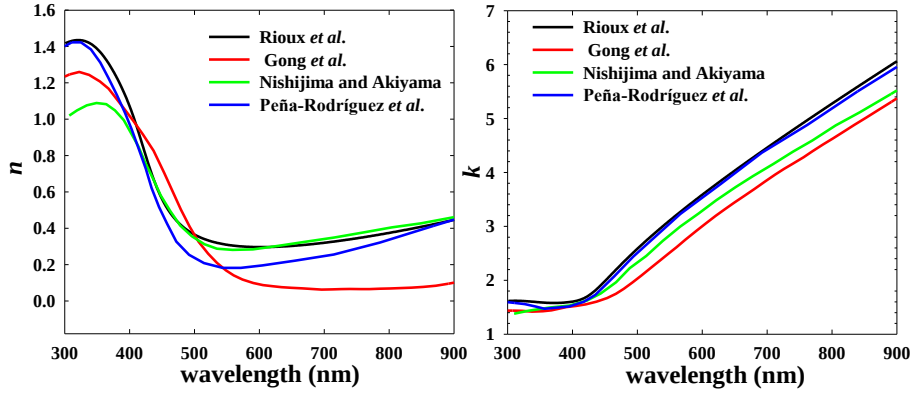

Figure A2.3. Comparison of optical constants of 50% Ag- 50% Au alloy from different literature. Exception: the composition for Peña-Rodríguez *et al*. is 48:50. (References in the main text)

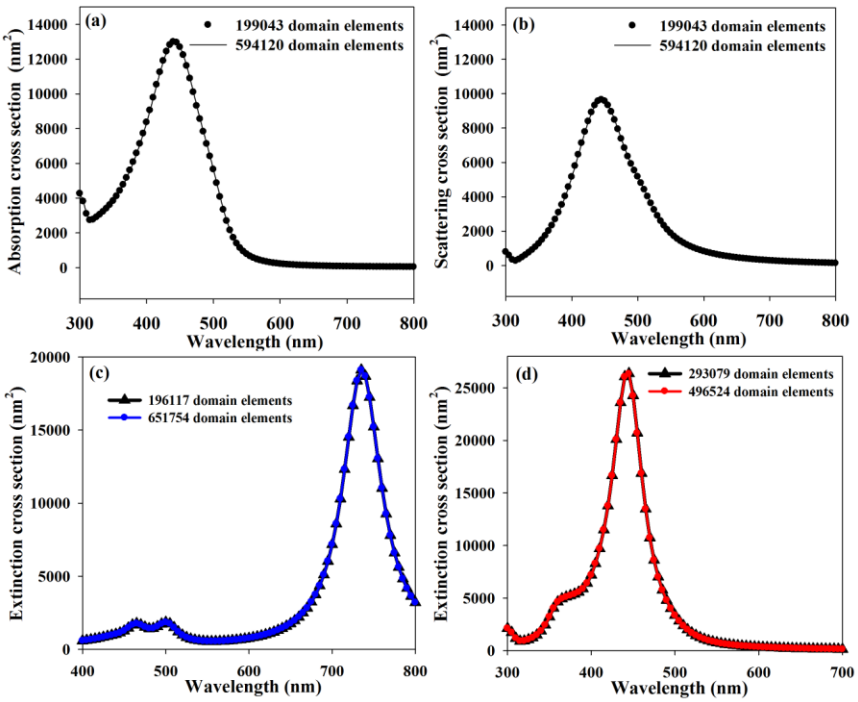

Figure A2.4. (a, b) Grid-independence test for 60 nm core-shell Ag@Au nanoparticles with 2.14 nm thin Au shell. (c) Grid independence test for Ag-Au alloy nanotriangle of 80:20 composition. (d) Grid-independence test for the validation of Ag@Au nanocube with 0.5 nm thin Au shell in Figure 2.

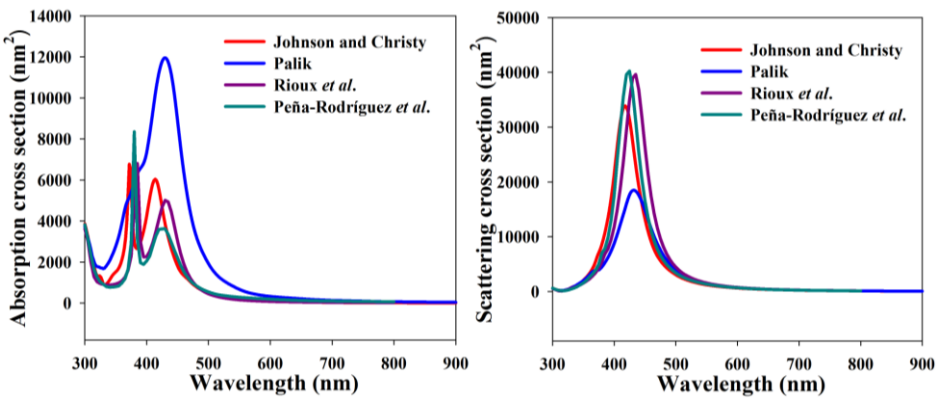

Figure A2.5. Absorption and scattering cross section of 60 nm Ag nanoparticle calculated with optical constants from different literature. (References in the main text)

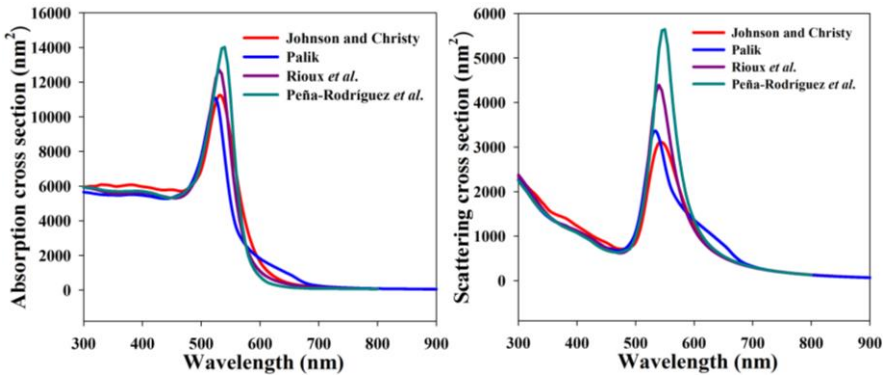

Figure A2.6. Absorption and scattering cross section of 60 nm Au nanoparticle calculated with optical constants from different literature. (References in the main text)

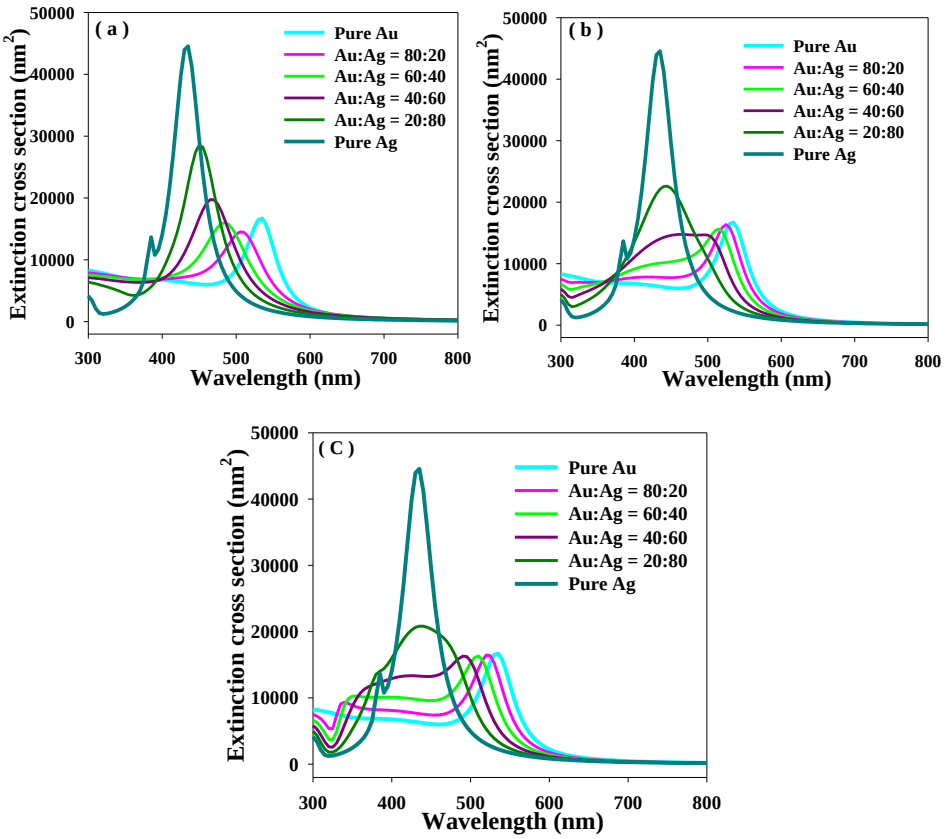

Figure A2.7. Extinction cross section of 60 nm Bimetallic Ag-Au nanoparticles constituted as (a) alloy (b) Ag@Au core-shell (c) Au@Ag core-shell.

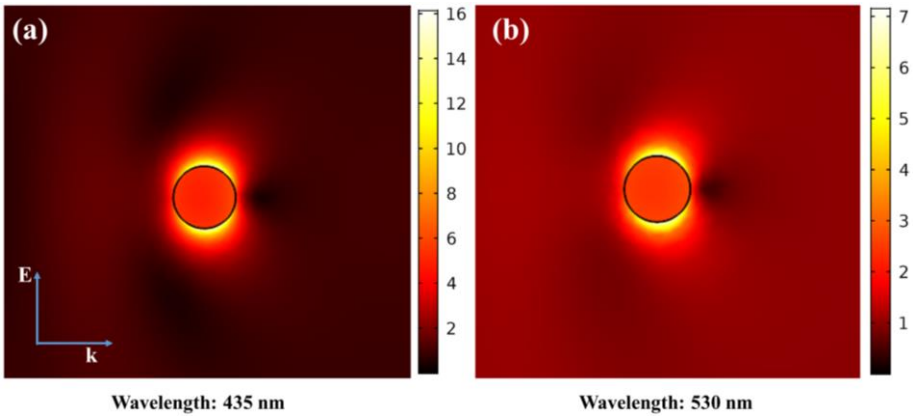

Figure A2.8. Near field enhancement around 60 nm (a) Ag and (b) Au nanoparticle at their respective dipolar plasmon resonance modes.

A3. Supporting information of Chapter 3

MATLAB code

For simplicity, three separate functions are written within one file so that one function can be called in the scripts of other functions. **AgMieScattering1** returns the Mie solution for any size, wavelength and medium refractive index, while **AgindexReadPalik** is defined for piecewise interpolation of experimental complex refractive data to obtain the optical constants at any wavelength. **AgDoit1** evaluates the optical spectra for a particle size distribution by using **AgMieScattering1** iteratively over the whole distribution.

1) The following is the MATLAB script for the function **AgMieScattering1** that returns the extinction, scattering and absorption cross section for three inputs: wavelength, nanoparticle radius and refractive index of dielectric medium. The script calls a separate function **AgindexReadPalik** (in the following section) that returns the complex refractive index for the given wavelength by piecewise interpolation.

```
%% SCATTERING BY A SPHERICAL GOLD NANOPARTICLE USING MIE
THEORY
%% inputs
%n_m         optical index of the medium
%lambda0     wavelength in nm
%r0          radius of the particle in nm
%N=5         maximum n-pole

function
[Qext,Qsca,Qabs]=AgMieScattering1(lambda0,r0,n_m);

%% parameters
n_Au=AgindexReadPalik(lambda0); %any function that
returns the optical index of gold
m=n_Au/n_m;
k=2*pi*n_m/lambda0;
x=k*r0;
z=m*x;
N=round(2+x+4*x^(1/3))

%% computation

j=(1:N);
sqr=sqrt(pi*x/2);
```

```
sqrm=sqrt(pi*z/2);

phi=sqr.*besselj(j+0.5,x);
xi=sqr.*(besselj(j+0.5,x)+i*bessely(j+0.5,x));
phim=sqrm.*besselj(j+0.5,z);
phi1=[sin(x), phi(1:N-1)];
phi1m=[sin(z), phim(1:N-1)];
y=sqr*bessely(j+0.5,x);
y1=[-cos(x), y(1:N-1)];

phip=(phi1-j/x.*phi);
phimp=(phi1m-j/z.*phim);
xip=(phi1+i*y1)-j/x.*(phi+i*y);
aj=(m*phim.*phip-phi.*phimp)./(m*phim.*xip-xi.*phimp);
bj=(phim.*phip-m*phi.*phimp)./(phim.*xip-m*xi.*phimp);

Qsca=sum( (2*j+1).*(abs(aj).*abs(aj)+abs(bj).*abs(bj)) );
Qext=sum( (2*j+1).*real(aj+bj) );

Qext=Qext*2*pi/(k*k);
Qsca=Qsca*2*pi/(k*k);
Qabs=Qext-Qsca;
end
```

2) In the script above, another function **AgindexReadPalik** is incorporated, which gives the complex refractive index for any arbitrary wavelength from the optical constant data of Palik (or any other source) by piecewise interpolation:

```
function Ri = AgindexReadPalik(lambda0)


%% complex refractive index

%% column 1:wavelength, column 2:n, column 3:k

RI = [124   1.241   0.568
127.8   1.229   0.566
134.8   1.182   0.55
137.8   1.149   0.552
140.9   1.112   0.563
```

144.2 1.073 0.581
147.6 1.032 0.61
151.2 0.993 0.653
155 0.962 0.706
159 0.94 0.77
163.1 0.935 0.832
167.5 0.936 0.892
172.2 0.942 0.951
177.1 0.953 1.01
182.3 0.969 1.07
187.9 0.995 1.13
193.7 1.028 1.18
196.8 1.048 1.21
200 1.072 1.24
203.3 1.098 1.26
206.6 1.125 1.27
213.8 1.173 1.29
221.4 1.208 1.3
229.6 1.238 1.31
238.4 1.265 1.33
248 1.298 1.35
253 1.32 1.35
258.3 1.343 1.35
263.8 1.372 1.35
269.5 1.404 1.33
275.5 1.441 1.31
281.8 1.476 1.26
288.3 1.502 1.19
295.2 1.519 1.08
298.8 1.522 0.992
302.4 1.496 0.882
306.1 1.432 0.766
310 1.323 0.647
311.5 1.246 0.586
313.9 1.149 0.54
315.5 1.044 0.514
317.9 0.932 0.504
319.5 0.815 0.526
322 0.708 0.565
323.7 0.616 0.609
326.3 0.526 0.663
330.6 0.371 0.813

```
332.4   0.321   0.902
335.1   0.294   0.986
339.7   0.259   1.12
344.4   0.238   1.24
354.2   0.209   1.44
364.7   0.186   1.61
375.7   0.2 1.67
387.5   0.192   1.81
400 0.173   1.95
413.3   0.173   2.11
427.5   0.16    2.26
442.8   0.157   2.4
459.2   0.144   2.56
476.9   0.132   2.72
495.9   0.13    2.88
516.6   0.13    3.07
539.1   0.129   3.25
563.6   0.12    3.45
590.4   0.121   3.66
619.9   0.131   3.88
652.6   0.14    4.15
688.8   0.14    4.44
729.3   0.148   4.74
774.9   0.143   5.09
826.6   0.145   5.5
885.6   0.163   5.95
953.7   0.198   6.43
1033    0.226   6.99
1127    0.251   7.67
1240    0.329   8.49];

C1 = RI(:,1);
X1 = length(find(C1<lambda0));
X2 = X1+1;
x1 = C1(X1);
x2 = C1(X2);

n = RI(X1,2) + (lambda0 - x1)*((RI(X2,2)-RI(X1,2))/(x2-
x1));
k = RI(X1,3) + (lambda0 - x1)*((RI(X2,3)-RI(X1,3))/(x2-
x1));
CR =  [n+k*i];
```

```
Ri = CR(1,1);
end
```

3) In order to obtain the optical cross sections for a complete particle distribution (in this case $\mu = 60$, $\sigma = 15$), the **AgMieScattering1** function shown above is used in the function **AgDoit1** iteratively as given below:

```
%% Implementation of the AgMieScattering1 function

function Mie2 = AgDoit1

Mie2 = [0,0,0];

%% wavelength range
X = [300:1:800];
L = transpose(X);


%% Particle size distribution within 3 standard
deviations
SD  = [15   56582553.49
15.1    57724314.11
15.2    58886496.71
15.3    60069408.11
15.4    61273358.49
15.5    62498661.46
15.6    63745634
15.7    65014596.52
15.8    66305872.85
...
...
...
...


103.8   71700713.26
103.9   70316874.57
104     68956679.44
104.1   67619790.25
104.2   66305872.85
104.3   65014596.52
104.4   63745634
104.5   62498661.46
```

```
104.6   61273358.49
104.7   60069408.11
104.8   58886496.71
104.9   57724314.11
105 56582553.49];

for i = 1:length(L)
    Sum = [0,0,0];
    for j = 1:length(SD)
        [A,B,C] =
AgMieScattering1(L(i,1),(SD(j,1)/2),1.33);
        G = SD(j,2)*[A,B,C];
        Sum = Sum+G;
    end
    Mie2 = [Mie2; Sum];
end
```

Additional Figures

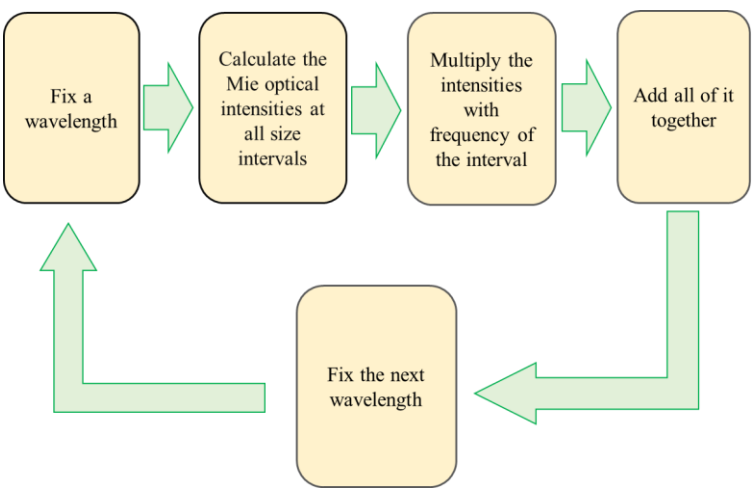

Figure A3.1. Flow chart describing the steps for the calculation of the optical spectra for a distribution of nanoparticles.

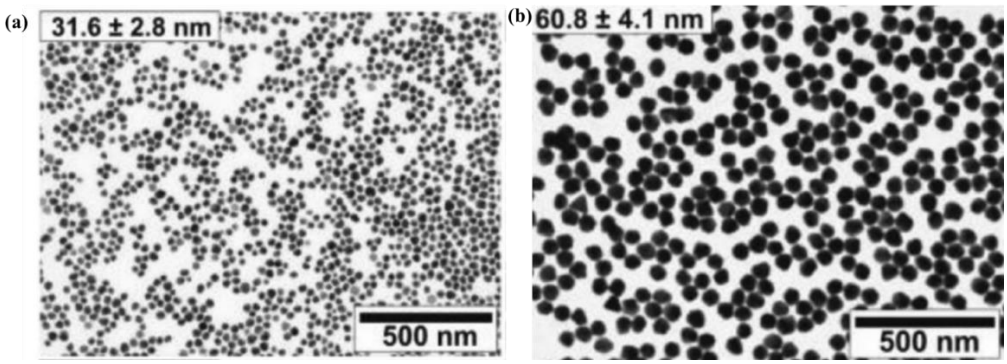

Figure A3.2. TEM images of nanoparticles reported by Bastus *et al*. Figure adapted and reproduced from with permission from the American Chemical Society (Copyright 2014).

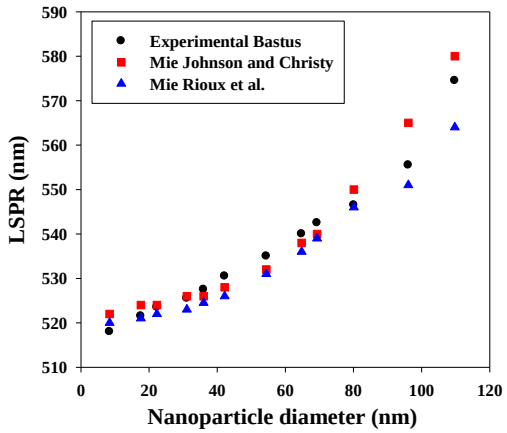

Figure A3.3. Comparison between experimental and theoretically predicted LSPR wavelength for Au nanoparticles.

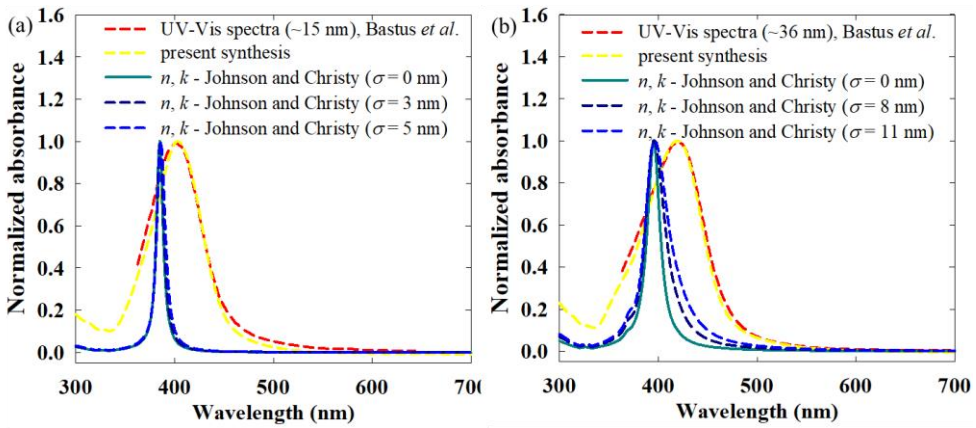

Figure A3.4. Comparison between experimental and theoretically spectra for two different mean sizes (a) 15 nm and (b) 36 nm. The theoretical spectra were calculated

using the optical data of Johnson and Christy. The means were fixed and the standard deviation was varied.

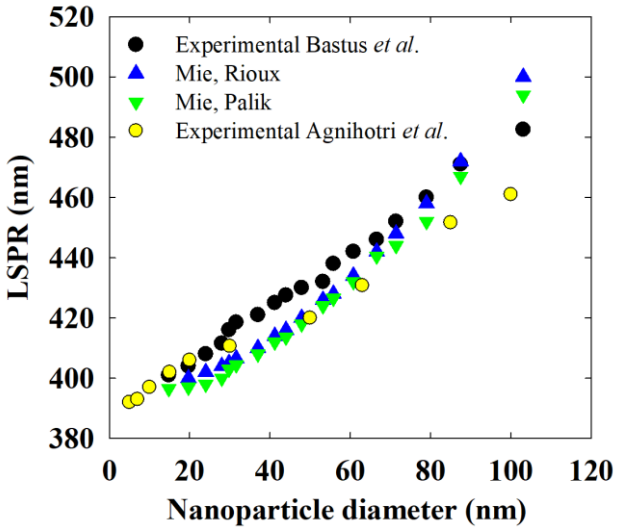

Figure A3.5. Comparison of the mean size vs. LSPR data from two different sources: Bastus *et al*. and Agnihotri *et al*. The theoretical predictions using the optical constants of Rioux *et al*. and Palik *et al*. are also added.

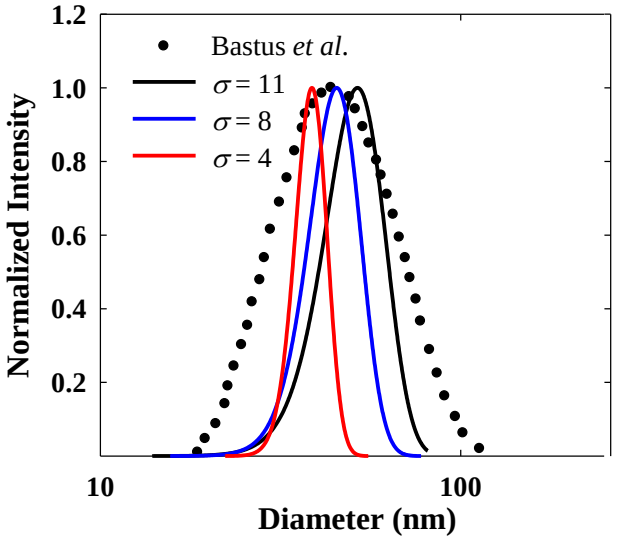

Figure A3.6. The theoretical scattering intensity distributions for a fixed mean 36 nm and varying standard deviation compared with experimental DLS intensity distribution data from Bastus *et al*.

Table A3.1. Fitting parameters with statistics correlating right-HWHM and σ for the distributions in Figure 3.3, 3.4 and 3.5. (For 100 mean size, only 5 points were taken as a clear maximum does not exist.)

	Parameters					Statistics	
Mean size, μ	c_o	c_1	c_2	c_3	c_4	R^2	Adj. R^2
20	1.1347	1.052	0.2726	-0.4026	2.3519	0.9994	0.9987
60	2.81	2.8739	2.2126	-0.1096	2.3384	0.9992	0.9981
100	24.7715	5.1987	3.2165	-0.0831	2.9937	0.9999	0.9999

A4. Supporting information for Chapter 4

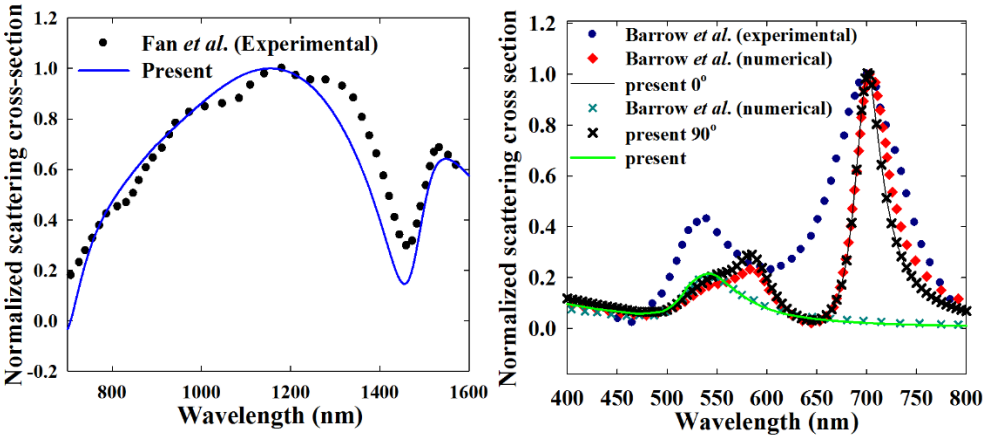

Figure A4.1 Validation of numerical model by comparison with Fan *et al*.[241] and Barrow *et al*.[238]

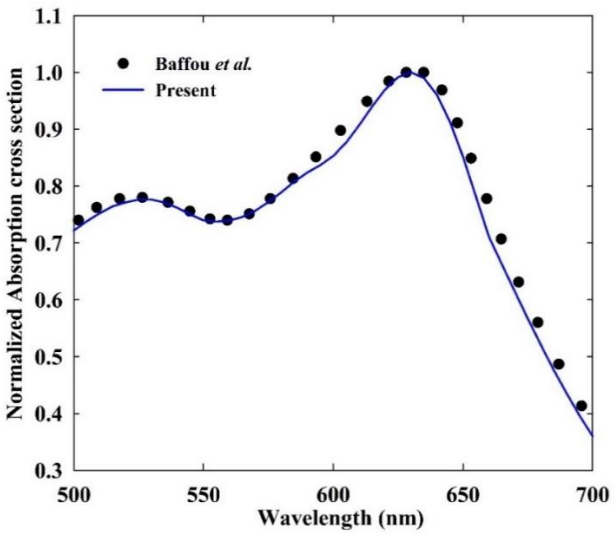

Figure A4.2 Validation of Baffou *et al*. for a linear array of 15 nanospheres.

Table A4.1 Sensitivity analysis for thermal conductivity of gold.

Nanosphere from schematic	Thermal conductivity k = 110 W/m. K	Thermal conductivity k = 317 W/m. K
Nanosphere **1**	378.72	378.54
Nanosphere **2**	378.41	378.24

Nanosphere **3**	376.48	376.35
Nanosphere **4**	370.88	370.85
Nanosphere **5**	375.37	375.29
Nanosphere **6**	373.61	373.55
Nanosphere **7**	365.80	365.84
Nanosphere **8**	365.07	365.12

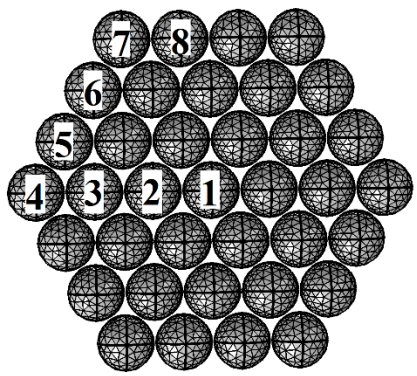

Figure A4.3 Nanoparticle cluster schematic corresponding to Table S1.

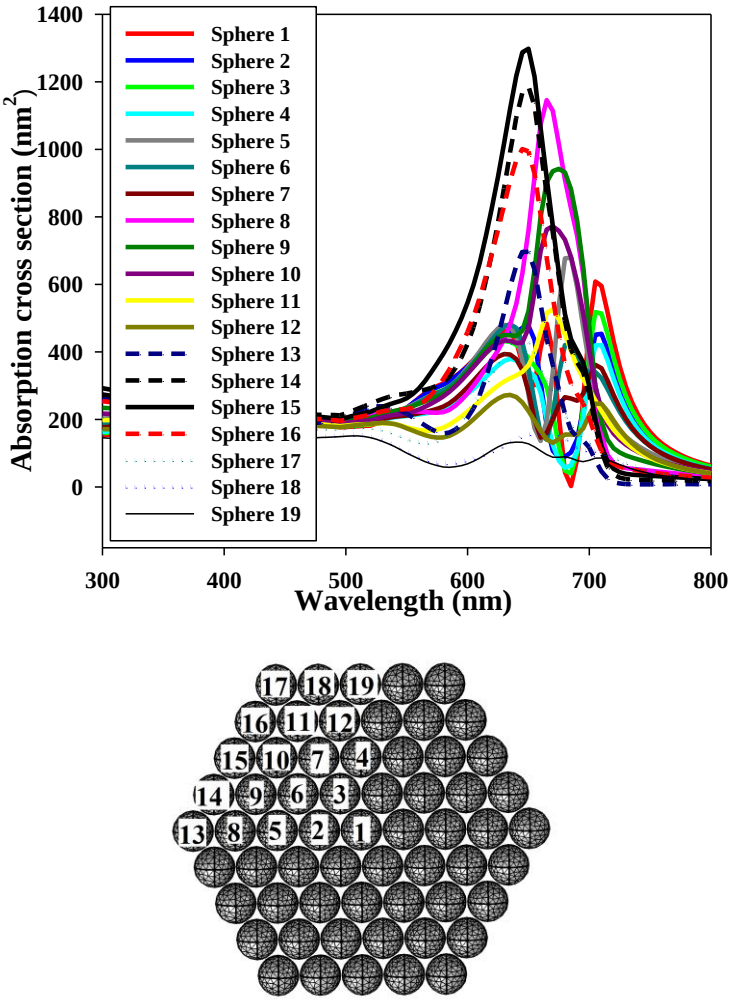

Figure A4.4 Individual absorption spectra of nanoparticles in 61 nanoparticle spectra (top). Below: The nanoparticle numbering in correspondence to the top figure.

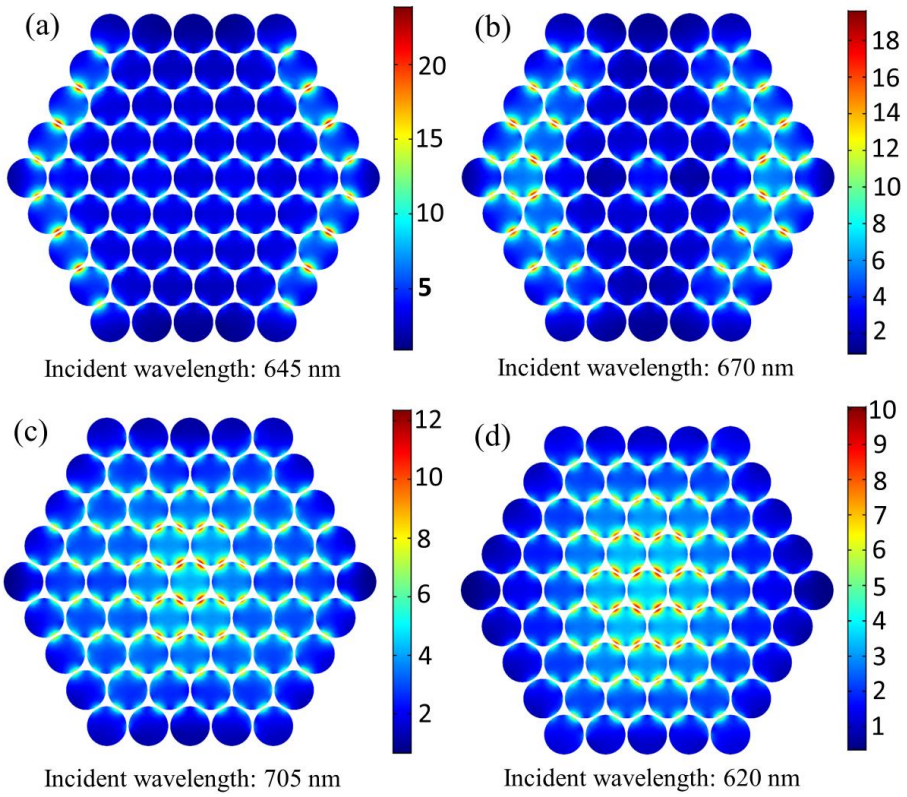

Figure A4.5 Near-field enhancement in 61 nanoparticle cluster at different incident wavelengths showing spatial variation of field magnitiude.

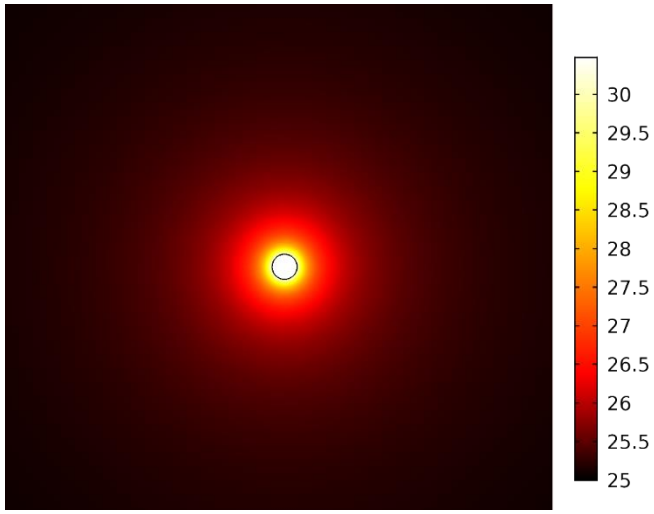

Figure A4.6 Temperature field around an isolated nanoparticle in ^{o}C.

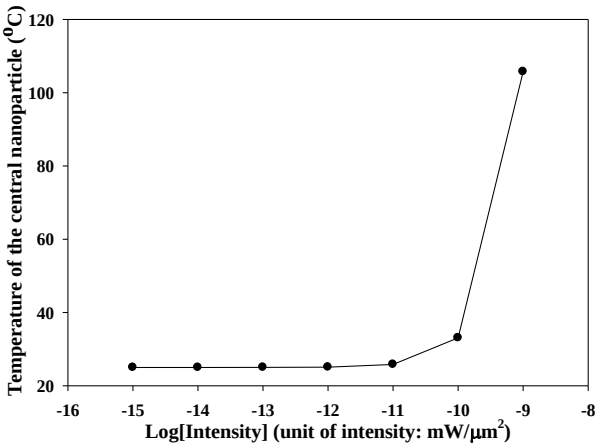

Figure A4.7 Temperature of central nanoparticle in a 37 particle cluster as function of incident intensity.

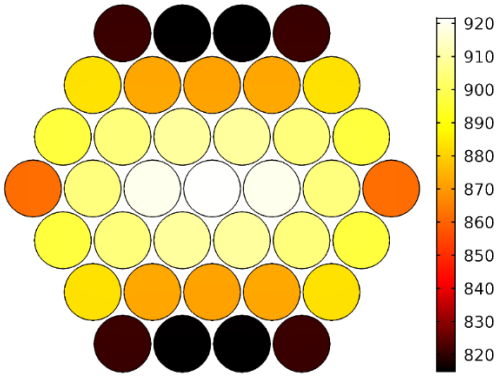

Figure A4.8 Steady state temperatures (°C) of nanoparticles in a cluster of 37 nanoparticles upon EM irradiation of respective peak wavelength in air medium. The intensity of incident radiation is 1 mW/μm^2 for all the cases.

A5. Supporting information for Chapter 5

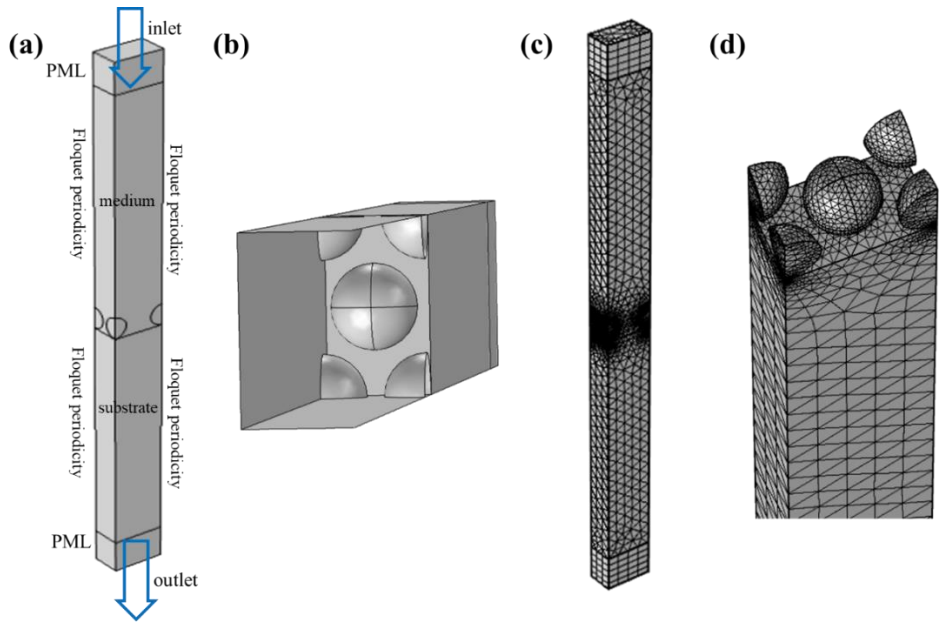

Figure A5.1. Size distribution of Au nanoparticles (average diameter: 9.56 nm from 45 data points, average interparticle gap: 2 nm from 18 data points).

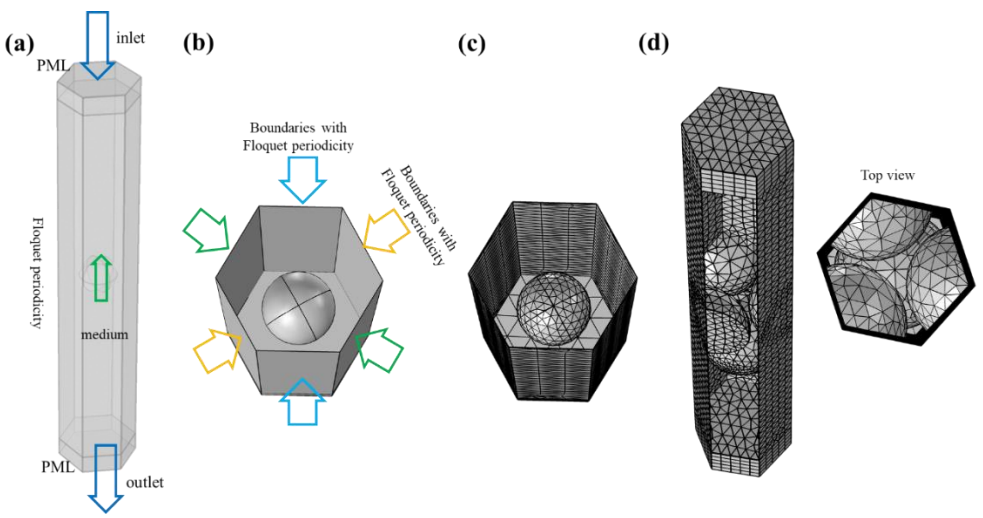

Figure A5.2. Size distribution of Au nanoparticles (average diameter: 9.56 nm from 45 data points, average interparticle gap: 2 nm from 18 data points).

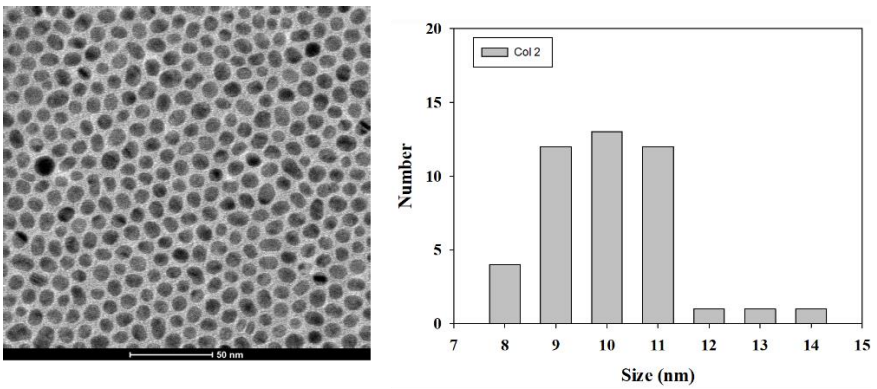

Figure A5.3. Size distribution of Au nanoparticles (average diameter: 9.56 nm from 45 data points, average interparticle gap: 2.1 nm from 18 data points).

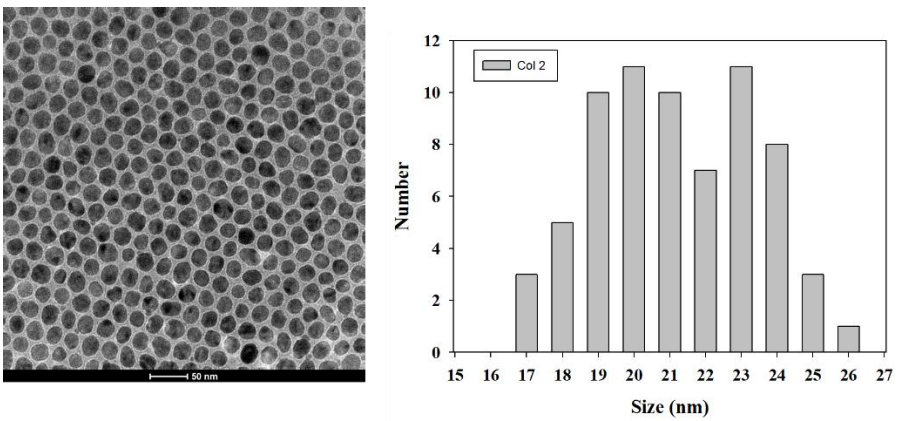

Figure A5.4. Size distribution of Ag nanoparticles (average diameter: 20.76 nm from 70 data points, average interparticle gap: 2.98 nm from 20 data points).

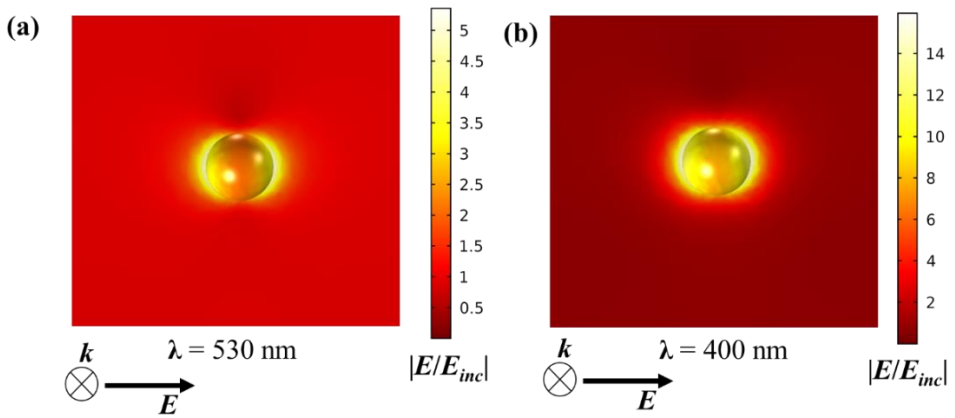

Figure A5.5. Near-field enhancement of 20 nm large Au and Ag nanoparticles in dielectric medium (n = 1.33) when isolated.

A6. Supporting information for Chapter 6

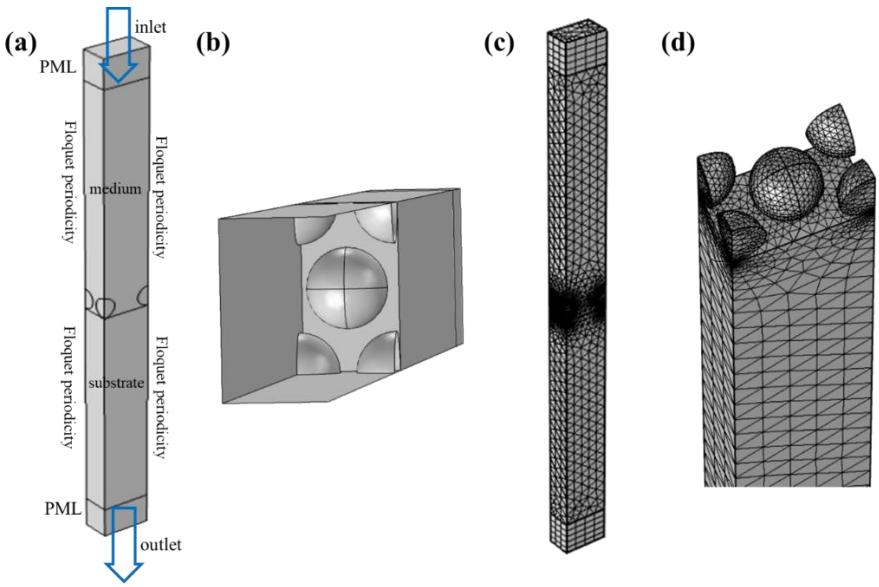

Figure A6.1 Rectangular unit cell computational domain used for the computation: (a) complete view (b) top view. (c, d) Meshing scheme with tetrahedral grid elements in the physical domain and prismatic elements in the PML.

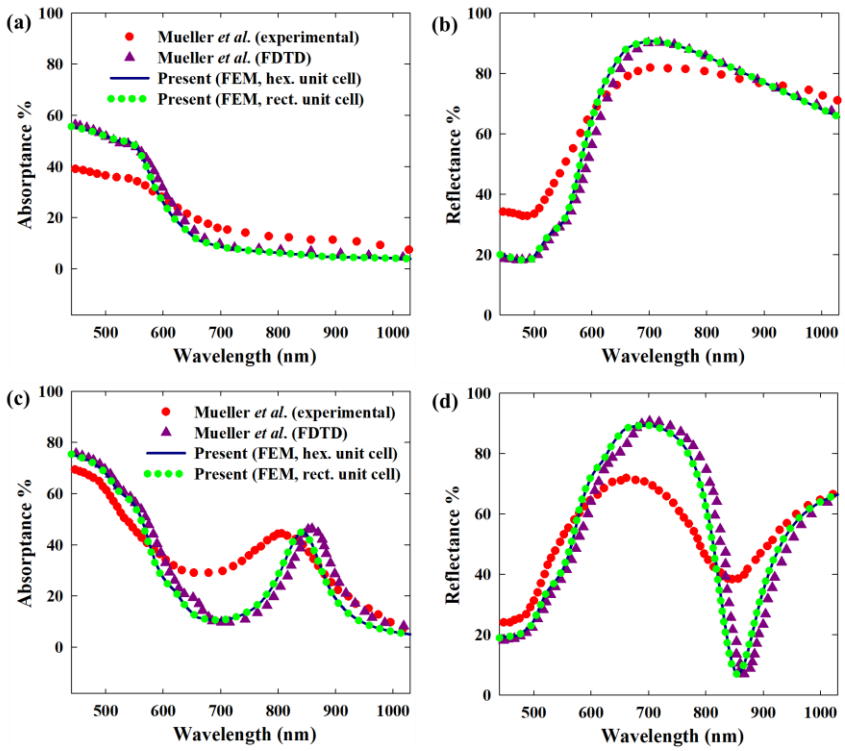

Figure A6.2 Validation of the present numerical models of the self-assembled films by comparison with the experimental and FDTD results of 46 nm Au nanoparticle self-assembled films: (a,b) monolayer (c,d) bilayer.

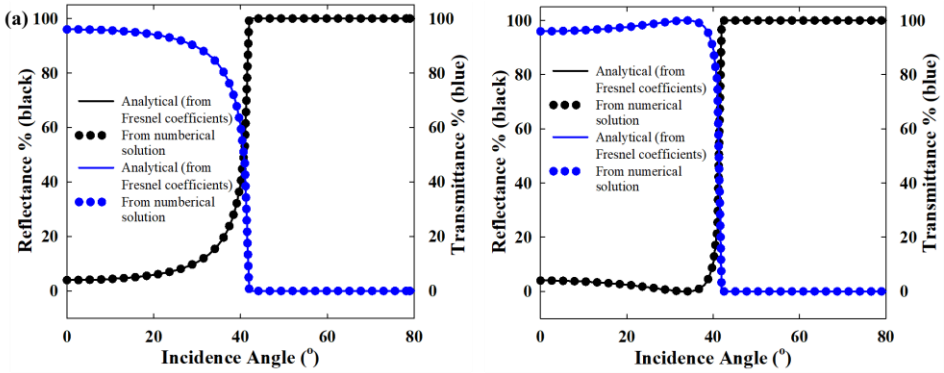

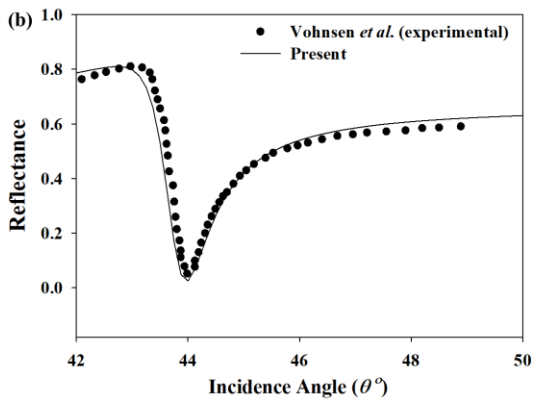

Figure A6.3. Validation of the present computational model for the Kretschmann geometry by comparison with (a) Analytical reflectance/transmittance from Fresnel coefficients (without any plasmonic nanoparticles or films) (b) the experimental incident angle sweep reflectance data of Vohnsen *et al*. for a 50 nm Au thin film in the Kretschmann configuration.

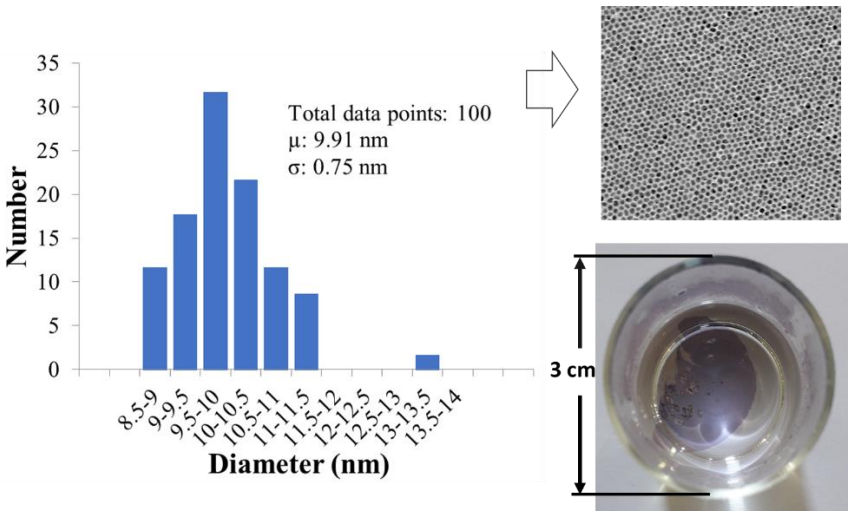

Figure A6.4. Size distrubution of Au nanoparticles in the self assembled film obtained over the ethylene glycol surface contained in a smaller glass container. The optical spectra of this film with the corresponding data from from the TEM characterization was used for the simulation results in Figure 3.

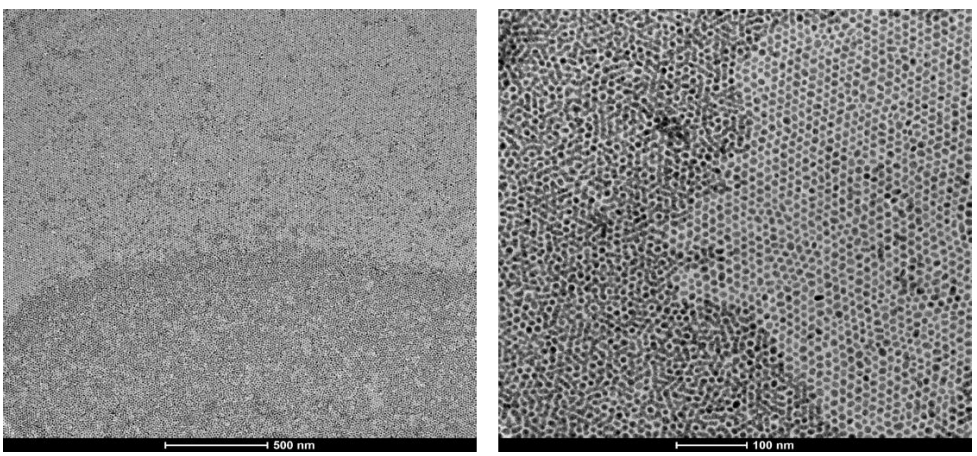

Figure A6.5. TEM images of the self-assmelbed films with both monolayer and bilayer regions.

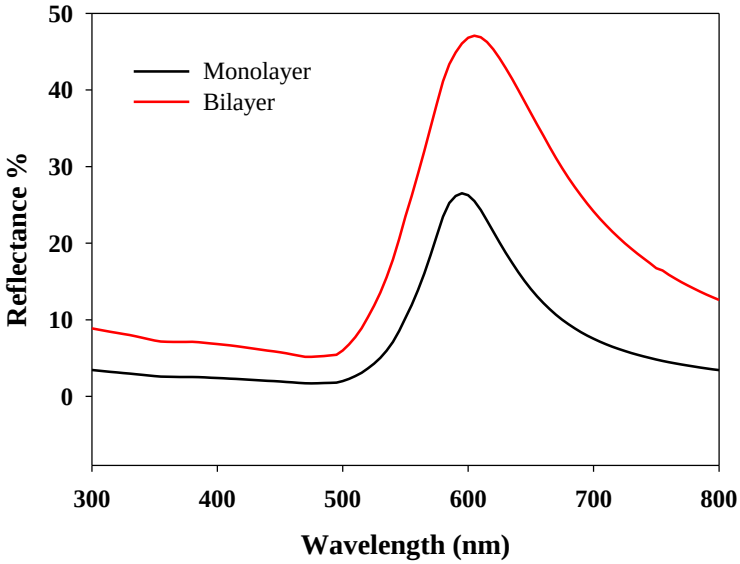

Figure A6.6. Reflectance for the bilayer and monolayer films.

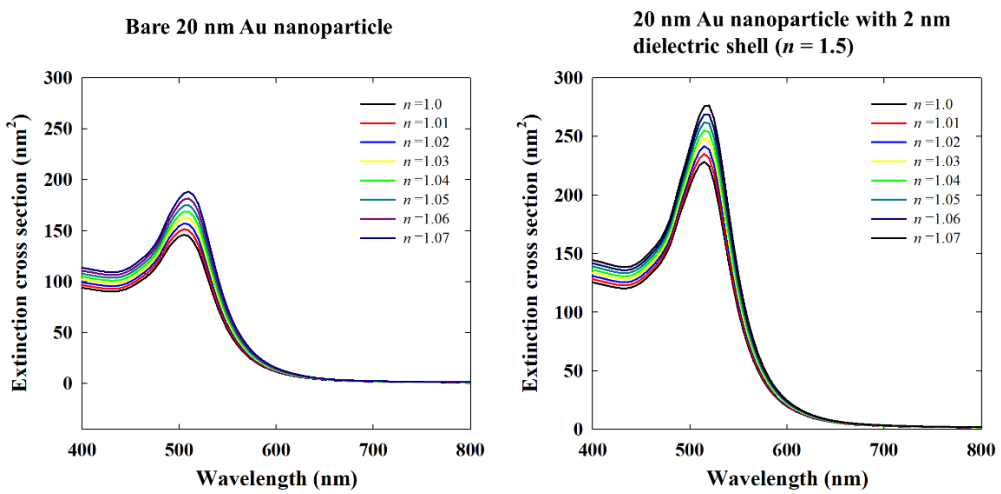

Figure A6.7. Medium refractive index sensitivity of a bare 20 nm Au nanoparticle vs. a 20 nm Au nanoparticle with a 2 nm of dielectric shell (n = 1.5).

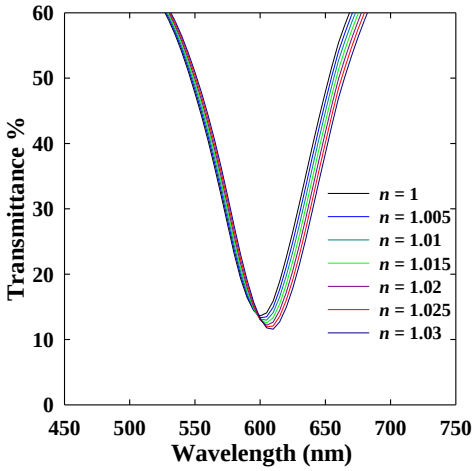

Figure A6.8. Effect of refractive index of the vapor phase on transmittance obtained from electromagnetic models.

A7. Supporting information for Chapter 7

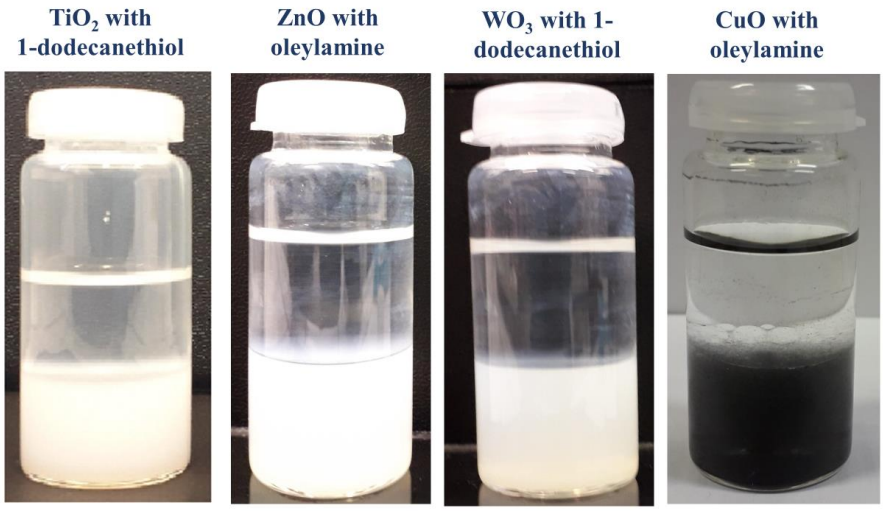

Figure A7.1. Phase-transfer trials of metal oxide nanoparticles with ligands that do not attach stably on the nanoparticle surface: nanoparticles fail to get transferred to the hexane phase above after vigorous shaking.

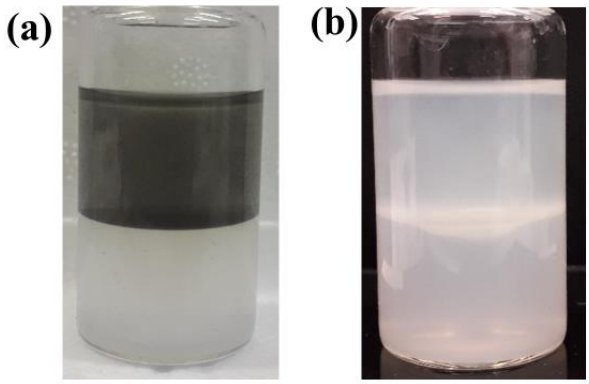

Figure A7.2. Selective phase-transfer of CuO (a) and ZnO (b) nanoparticles from colloidal mixtures of CuO/TiO_2 and ZnO/TiO_2 nanoparticles respectively using 1-dodecanethiol.

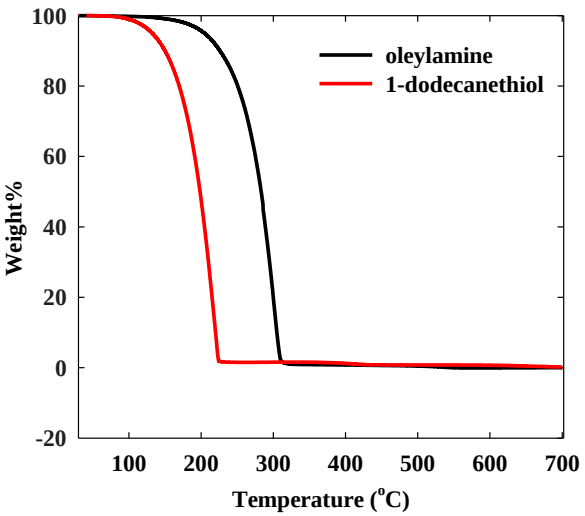

Figure A7.3. Thermogravimetric analysis (TGA) of oleylamine and 1-dodecanethiol.

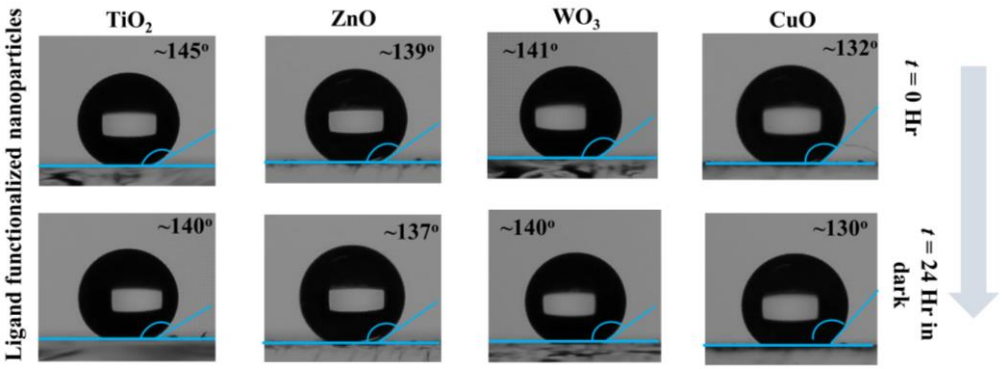

Figure A7.4. Wettability of ligand functionalized nanoparticles after keeping in the dark without photocatalytic degradation.

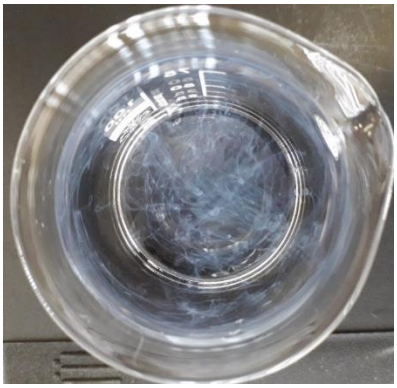

Figure A7.5. TiO_2 nanoparticles without ligand functionalization do not get trapped in the air-water interface.

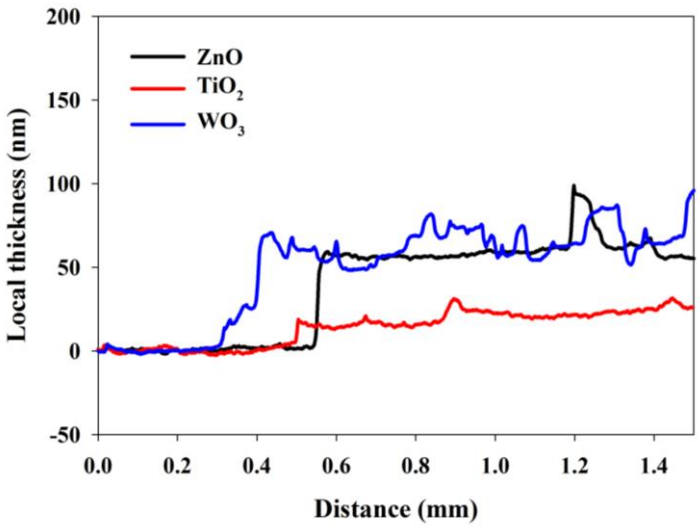

Figure A7.6. DektakXT profilometer local film thickness of different samples along the needle sliding distance.

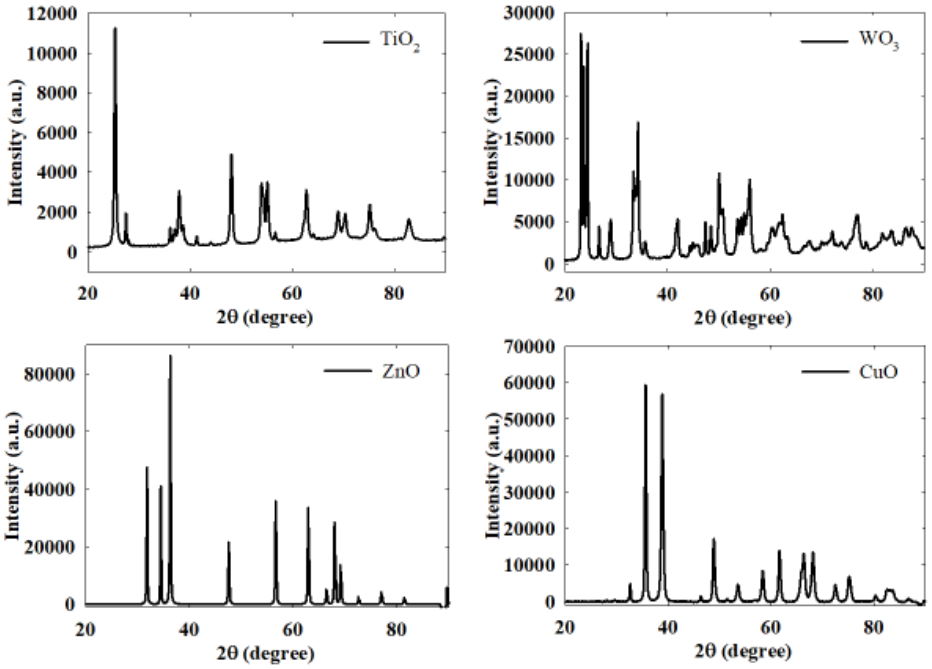

Figure A7.7. XRD patterns of different nanoparticle powders.

Crystallite size calculation

Using XRD average crystallite size of different materials is estimated using Scherrer equation:

$$D = \frac{K.\lambda}{\beta.cos\theta}$$

D is the crystal size of the particle.

K is the Debye Scherrer constant (K=0.94)

ʎ is the wavelength of the CuKa radiation (0.154 nm)

β is the Full width at half maximum (FWHM)

θ is the Bragg angle